
Doctoral Dissertations

Student Theses and Dissertations

Summer 2012

Measuring the orientations of hidden subvertical joints in highways rock cuts using ground penetrating radar in combination with LIDAR

Adnan Mohammed Aqeel

Follow this and additional works at: https://scholarsmine.mst.edu/doctoral_dissertations



Part of the [Geological Engineering Commons](#)

Department: Geosciences and Geological and Petroleum Engineering

Recommended Citation

Aqeel, Adnan Mohammed, "Measuring the orientations of hidden subvertical joints in highways rock cuts using ground penetrating radar in combination with LIDAR" (2012). *Doctoral Dissertations*. 2022.
https://scholarsmine.mst.edu/doctoral_dissertations/2022

This thesis is brought to you by Scholars' Mine, a service of the Missouri S&T Library and Learning Resources. This work is protected by U. S. Copyright Law. Unauthorized use including reproduction for redistribution requires the permission of the copyright holder. For more information, please contact scholarsmine@mst.edu.

**MEASURING THE ORIENTATIONS OF HIDDEN SUBVERTICAL JOINTS IN
HIGHWAYS ROCK CUTS USING GROUND PENETRATING RADAR IN
COMBINATION WITH LIDAR**

by

ADNAN MOHAMMED AQEEL

A DISSERTATION

**Presented to the Faculty of the Graduate School of the
MISSOURI UNIVERSITY OF SCIENCE AND TECHNOLOGY**

In Partial Fulfillment of the Requirements for the Degree

DOCTOR OF PHILOSOPHY

in

GEOLOGICAL ENGINEERING

2012

Approved by

Norbert H. Maerz, Advisor

Neil L. Anderson, Co-advisor

David J. Rogers, Co-advisor

Mohamed Abdelsalam

Jeffrey Cawfield

Kwame Awuah-Offei

© 2012
Adnan Mohammed Aqeel
All Rights Reserved

ABSTRACT

Mapping discontinuities in rock cuts and measuring their orientations is crucial in assessing the stability of rock masses. This can be done usually using manual methods such as scanline or advanced techniques such as LIDAR. However, these methods are used only to map exposed discontinuities which may cause underestimation for slope stability. Accordingly, ground penetrating radar (GPR) has been recently used to detect such hidden discontinuities.

The used 400 MHz monostatic GPR antenna was significantly able to detect and map hidden subvertical joints within 4 m depths in five sandstone highways rock cuts and within 3 m depths in two ignimbrite highways rock cuts in the State of Missouri. Manual 2D migration was done to estimate, in 2D and 3D radiograms, “the slope face-perpendicular depths” which was measured from three coplanar etched points, “the three index points”, at each rock cut surface to the corresponding points on each plane of the detected subvertical joints.

The orientations of the detected hidden joints were then determined based on the 3-point equation and using the calibrated LIDAR coordinates. Some of these measurements were confirmed by very close-results of field verification measurements. The results of this GPR-and-LIDAR based investigation demonstrate that our new proposed approach using these techniques is straightforward, understandable, and can be valuable in some rock engineering applications and rock cuts design in terms of the orientations of joints, in addition to the number of joint sets which may build a more clear view about the rock cut stability than before.

ACKNOWLEDGMENT

First, my deep praise and thanks go to my Lord, ALLAH, for his guidance for me through all those successful steps and plans in my life including the stages of doing this research that would not be accomplished without his will. Then I would love to express deeply my sincere gratitude, appreciations, and thanks to my advisor, Dr. Norbert Maerz, my co-advisors, Prof. Neil Anderson and Dr. David Rogers, and the other advisory members: Prof. Mohamed Abdelsalam, Dr. Jeffery Cawlfeld, and Dr. Kwame Awuah-Offei for their valuable suggestions, discussions, and continuous encouragements during all the phases of this research. I would like also to thank my colleagues: Adel Elkrry, Evgeniy Torgashov, Essam Dawed, James Otoo, and Travis Kassebaum for their great help during the field work. In addition, I would like to thank the faculties and staff of the Department of Geological Sciences and Engineering who made my study in the university fruitful and enjoyable; especially, Ms. Paula Cochran and Ms. Patricia Robertson who had been kindly helping me managing the routine paper work. I would like to thank Sana'a University for their partial support and the Geological Engineering Program for supporting me financially and being a graduate teaching assistant. My gratitude and thanks go also to the Graduate Office and the International Student Office, and specially to Dr. Venkata Allada , Ms. Susan Potrafka, and Ms. Buffi White for their kindness, guidance, and help particularly during those the rainy days I faced.

Finally, my sincere appreciations go to my family and my brother Abdulmajeed in Yemen for their patience and encouragement for me during all my studies abroad. I respectfully dedicated this work to the memory of my most beloved ones, my parents who passed away during a year and half ago; may Allah have mercy on them.

TABLE OF CONTENTS

	Page
ABSTRACT.....	iii
ACKNOWLEDGMENT.....	iv
LIST OF ILLUSTRATIONS.....	ix
LIST OF TABLES.....	xviii
 SECTION	
1. INTRODUCTION	1
1.1 OVERVIEW.....	1
1.2 RESEARCH OBJECTIVES	6
1.3 PLAN OF ACTION	8
1.3.1 Phase I - Reconnaissance Survey and Literature Review for the Study Area....	8
1.3.2 Phase II - Field Work, Sampling, and Testing	9
1.3.3 Phase III- Data Analysis and Interpretation (Office Work)	9
1.4 STRUCTURE OF THE DISSERTATION	11
2. LITERATURE REVIEW	13
2.1 OVERVIEW.....	13
2.2 GEOMETRY OF DISCONTINUITIES	14
2.3 MAPPING DISCONTINUITIES.....	15
2.3.1 Scanline Method.....	16
2.3.2 Light Detection And Ranging (LIDAR or LiDAR)	17
2.3.3 Geophysical Techniques.....	19
2.3.3.1 Ground penetrating radar	21
2.4 SLOPE STABILITY ANALYSIS	24
2.4.1 Rock Failure Types.....	26
2.4.2 Kinematic Analysis for Rock Failures.....	27
2.4.2.1 Kinematic analysis for plane failure	29

2.4.2.2 Kinematic analysis for toppling failure.....	31
2.4.2.3 Kinematic analysis for wedge failure	33
2.5 STUDY AREA LOCATION	34
2.6 GEOLOGY OF THE STUDY AREA	38
3. BACKGROUND AND THEORY OF GROUND PENETRATING RADAR (GPR) 42	
3.1 OVERVIEW.....	42
3.2 THEORY OF ELECTROMAGNETIC ENERGY	43
3.2.1 Maxwell’s Equations	45
3.2.2 Constitutive Equations.....	46
3.3 ELECTROMAGNETIC PROPERTIES OF EARTH MATERIALS.....	47
3.4 FUNDAMENTALS OF GPR TECHNOLOGY	51
3.4.1 GPR System Components	51
3.4.2 Principals of GPR Operating.....	54
3.4.3 Estimation of Target Depth	59
3.5 GPR PULSE RESOLUTION.....	61
3.5.1 Vertical GPR Resolution	62
3.5.2 Horizontal GPR Resolution.....	63
3.6 GPR DATA ACQUISITION MODES (GPR FIELD SURVEY MTHODS)	64
3.6.1 Continuous Common Offset Profiling (GPR Reflection Profiling)	65
3.6.2 Wide-Angle Reflection and Refraction (WARR) Profiling (Common Source Profiling).....	67
3.6.3 Common Midpoint Profiling (CMP)	69
3.6.4 Trans-illumination Profiling (GPR Tomography Profiling).....	70
3.7 GPR DATA PROCESSING, ANALYSIS, AND INTERPRETATION	72
3.7.1 Filtering	73
3.7.2 Deconvolution	74
3.7.3 Time Gain	74
3.7.4 Migration	75
4. BACKGROUND AND PRINCIPLES OF LIGHT DETECTION AND RANGING SYSTEM (LIDAR).....	83
4.1 OVERVIEW.....	83

4.2 LIDAR SCANNER COMPONENTS.....	84
4.2.1 Point Cloud Produced by LIDAR.....	84
4.3 CLASSIFICATION OF LIDAR SCANNERS	87
4.4 TECHNIQUES OF LIDAR SURVEY	89
4.5 ADVANTAGES AND LIMITATIONS OF USING LIDAR	91
4.5.1 Advantage of LIDAR	91
4.5.2 Limitations of LIDAR	91
4.6 SPECIFICATIONS OF LEICA AND RIEGL LIDAR SCANNERS.....	93
5. METHODOLOGY	99
5.1 OVERVIEW.....	99
5.2 FIELD SURVEY.....	102
5.2.1 Scanline Method	102
5.2.2 Ground Penetrating Radar Field Measurements.....	105
5.2.2.1 Estimation of GPR pulse velocities	107
5.2.2.1.1 Estimation of GPR pulse velocity through sandstone sample of site 1	112
5.2.2.1.2 Estimation of GPR pulses velocity through ignimbrite sample of site 2	116
5.2.2.2 Modes of GPR survey.....	121
5.2.2.2.1 GPR distance mode survey	122
5.2.2.3 GPR data processing	130
5.2.2.3.1 Migration.....	130
5.2.3 LIDAR Field Measurements	134
5.2.3.1 Calibration and geometry of rock slope face measurements using LIDAR	138
5.2.3.1.1 Three point equation and the conversion to spherical coordinates ...	140
5.2.3.1.2 The geometry of the detected hidden subvertical joints using LIDAR.....	144
6. RESULTS AND DISCUSSION	148
6.1 OVERVIEW.....	148
6.2 RESULTS OF THE STATIONS OF SITE 1.....	149

6.2.1 Station 1	149
6.2.2 Station 2	155
6.2.3 Station 3	160
6.2.4 Station 4	164
6.2.5 Station 5	168
6.3 RESULTS OF THE STATIONS OF SITE 2	172
6.3.1 Station 6	172
6.3.2 Station 7	176
6.4 DISCUSSION	182
7. CONCLUSIONS AND RECOMMENDATIONS	187
7.1 OVERVIEW	187
7.2 GPR AS A TOOL FOR DISCONTINUITY MAPPING	189
7.3 LIDAR AS A TOOL TO ESTIMATE THE ORIENTATIONS OF THE HIDDEN SUBVERTICAL JOINTS	190
7.4 RECOMMENDATION FOR FUTURE WORK	192
APPENDIX	195
REFERENCES	249
VITA	261

LIST OF ILLUSTRATIONS

	Page
Figure 1.1: (A) A rock cut; (B) The same rock cut showing both joint traces (red lines) and facets (yellow polygons).	3
Figure 1.2: A rock failure along a hidden sub-vertical joint resulting in the death of a truck driver on Highway 401, Brockville, Ontario, Canada. Dr. Norbert Mazerz, the advisor of this research, is standing beside the sub-vertical joint trace after removal the failed materials (dashed yellow line)	6
Figure 2.1: A 2-D diagram shows the primary geometrical and non-geometrical properties of discontinuities in a rock mass.	15
Figure 2.2: A Catastrophic rock slide destroyed tens of houses and killed 65 persons in Al-Dhafir village in Sana'a Governorate, Yemen, in December 28th 2008.....	25
Figure 2.3: A traffic accident happened due to a rock fall incident on a highway; Canada.....	25
Figure 2.4: Raveling, undercutting, and rolling failures along Highway 70 road cuts, respectively, Colorado State, USA.	28
Figure 2.5: Example of toppling, planar, and wedge rock failures respectively along highway rock cuts.	28
Figure 2.6: A potential plane failure on a single sliding discontinuity plane (ψ_p - dashed yellow line), Italy. Note that the dip angle of that sliding plane is less than the dip angle of the rock slope face (ψ_f - dashed red line).....	30
Figure 2.7: Kinematic analysis for plane failure.....	30
Figure 2.8: A potential toppling failure at station 7 in site 2 of the study area. Notice that the potential sliding planes of some discontinuities (dashed yellow lines) are dipping steeply into the rock slope.	32
Figure 2.9: Kinematic analysis for toppling failure	32
Figure 2.10: A wedge failure along two intersecting planes of discontinuities both of which daylight in the slope face in a limestone quarry.....	33
Figure 2.11: Kinematic analysis for wedge failure	34

Figure 2.12: The study area (red-dashed line square) shows the locations of the two selected sites. Site 1 is in the central part of Missouri while site 2 is in the southeast part	35
Figure 2.13: Location of site No.1 in Phelps County, MO. Site 1 was divided into five stations to conduct field work. Google Earth program was used to locate the stations of the study area.....	36
Figure 2.14: Location of site No.2 in Madison County, MO. Site 2 was divided into two stations to conduct field work. Google Earth program was used to locate the stations of the study area.....	37
Figure 2.15: The geology of the study area at site 1.....	39
Figure 2.16: The geology of the study area at site 2.....	40
Figure 3.1: The main components of the electromagnetic fields (EM) and the direction of the propagation of the EM waves along only Y-axis for the electric field (E) and the magnetic field (H).	44
Figure 3.2: A simple diagram shows the basic components of GPR system.....	52
Figure 3.3: (A) Shielded 400 MHz monostatic GPR antenna, which was used in this research, and (B) a bistatic GPR antenna.....	53
Figure 3.4: The GPR – GSSI control unit which was used in this research. This equipment is manufactured by Geophysical Survey Systems, Inc. (GSSI).....	53
Figure 3.5: The concept of electromagnetic energy propagation as a wavefront related to the EM rays from a local source or GPR antenna.....	55
Figure 3.6: The reflection and refraction or transmission of electromagnetic waves at a planar interface of two different materials.	57
Figure 3.7: Normal incident, reflected, and transmitted GPR pulse related to their amplitudes through two different subsurface media using monostatic antenna. ..	58
Figure 3.8: The concept of estimation the GPR velocity and then target depth based on the two way travel time of GPR pulses through a subsurface medium to known depth discontinuity plane.	61
Figure 3.9: Vertical and horizontal GPR resolution.	62
Figure 3.10: The GPR horizontal resolution in terms of Fresnel Zone. The target cross-sectional area is equivalent to the area of the first Fresnel Zone.	64

- Figure 3.11: A shielded monostatic GPR antenna is towed along a survey line on a study area of interest, and the data is interpreted to be normal incidence reflection signals. 66
- Figure 3.12: A bistatic GPR antenna which consists of two separate transmitter and receiver antennae. The two antennae placed at fixed offset distance along survey line on the study area of interest, and the data is interpreted to be near-normal incidence reflection signals 67
- Figure 3.13: WARR method or common source survey profiling method using only bistatic GPR antenna where the transmitter antenna (Tx) is fixed while the receiver antenna (Rx) is towed away so the offset distance increases..... 68
- Figure 3.14: Common Midpoint GPR survey method using a bistatic antenna. The transmitter (Tx) and the receiver antennae are moved away to keep the same position of reflection point..... 69
- Figure 3.15: Common midpoint GPR profiling using a monostatic antenna over a point in-homogeneity in subsurface..... 70
- Figure 3.16: Trans-illumination and cross-hole GPR method of data acquisition: (A) between galleries in a mine, (B) between boreholes or hole-surface, and (C) through a concrete pillar. In all cases the distance between the transmitter and receiver is known 71
- Figure 3.17: (A) GPR pulses of a horizontal survey line can be treated as a perpendicular plane to the rock slope face. The intersection between the plane of the penetrating GPR pulses and the plane of detected hidden joint results in a linear feature can be considered as the strike line of that detected hidden joint. 76
- Figure 3.18: A top view of the linear feature “the strike direction line” of a subvertical hidden joint shows the apparent location and the true location of that joint. β is the true declination angle of the strike direction line while α is its apparent declination angle. 77
- Figure 3.19: Top view illustrates the concepts of manual migration for the strike line of a dipping discontinuity. The apparent location of the strike line (green line) has a declination angle (α) less than the true declination angle (β) of the true location of the strike direction line (red line)..... 79
- Figure 4.1: The more scanned points are the more resolution and more details. (A) A scanned rock cut which has 9.5 million points while (B) is the same rock cut but with less details, 8.2 million points..... 85
- Figure 4.2: The orientation of rock mass discontinuities can be extracted from LIDAR points cloud..... 86

Figure 4.3: The principles of range measurement in the phase-based survey and time-of-flight survey using LIDAR scanners	90
Figure 4.4: shows that when the scanner beams directed in the same direction of the extension of the discontinuity this may cause orientations bias. Also when the beam of the scanner is directed upwards at an angle steeper than a discontinuity, occlusion results in a shadow zone.	93
Figure 4.5: A back view for the Leica-ScanStation2 which was in this research.....	94
Figure 4.6: Field view of Leica HDS3000 LIDAR scanner system, which was used in this research, with associated software programs (Cyclone6 was used in this research) for LIDAR data set processing.....	96
Figure 4.7: Riegl LMS-Z390i scanner (Adopted from http://www.geographica.hr).....	96
Figure 5.1: (A) a side of Site No.1 where is divided into three stations (St.1, St.2, and St.3); (B) and (C) show the other side of Site No.1 where St.4 and St.5 are located.	100
Figure 5.2: (A) Station 6 (St.6) and (B) St. 7 in site 2, Madison County-MO.	101
Figure 5.3: Proposed classification for planes based on dipping angle (θ). The shaded yellow area shows the planes of interest in this research.....	103
Figure 5.4: Shows the location (blue circle) of where the tape measurement should be for scanline survey at St.1. Notice that the scanline did not intersect with more than three joints on the rock face which push us to measure manually the orientation of all accessible joints without relying on the scanline itself.	104
Figure 5.5: The used SIR 3000-GPR system (A), and the used 400 MHz shielded monostatic antenna (B).	106
Figure 5.6: Monostatic antennae 270 MHz, 400 MHz, and 1500 MHz respectively. With increasing the frequency, the resolution of data increases but the penetration of depth decreases and as well as the size of the antenna.	107
Figure 5.7: Raw time-domain GPR data acquired using 400 MHz antenna (A) and 1500 MHz antenna (B) at St.1. The higher frequency antenna (1500 MHz) has the higher resolution but lower penetration depth.	108
Figure 5.8: The sandstone sample from Phelps County-MO and the trimmed two blocks of the sample in order to conduct a lab measurement for the velocity of the GPR pulses that travel through this type of sedimentary rock. The thickness of the top block is 10.60 cm.....	109
Figure 5.9: The ignimbrite rock sample from Madison County-MO and the trimmed two blocks of the sample in order to conduct a lab measurement for the	

- velocity of the GPR pulses that travel through this type of igneous rock. The Thickness of the top block is 7.40 cm..... 109
- Figure 5.10: The two blocks of sandstone rock sample were positioned on top of each other to create an artificial joint with a filled-air aperture of 1.8 cm wide. 111
- Figure 5.11: The two blocks of ignimbrite rock sample were positioned on top of each other to create an artificial joint with a filled-air aperture of 0.8 cm wide. 111
- Figure 5.12: The thickness of the top block is 10.50 cm which means the true perpendicular (vertical) depth to the created discontinuity is 10.50 cm. The separation between the two blocks was 1.80 cm. 113
- Figure 5.13: The radiogram image shows the two way travel time (TWTT) from the surface of top block (block 1) to the discontinuity plane location (dashed line). The TWTT was 2ns as shown in image A; while the perpendicular (vertical) depth to the discontinuity was 10.50 cm as shown in image B. The zero correction and display gain process were applied to the radiogram images to enhance the resolution and the clarity of the images. 114
- Figure 5.14: The geometry of the used two blocks to measure the GPR pulses velocity in the laboratory of geophysics in Missouri University of Science and Technology..... 115
- Figure 5.15: (A) The true perpendicular depth (d) from the surface of the top block to the created discontinuity or separation, which is 7.40 cm. (B) The apparent perpendicular depth (z) from the surface of the top block to the created discontinuity or separation, which was 12.20 cm, in radiogram before correcting the used relative dielectric permittivity of the ignimbrite rock. The zero correction and display gain process were applied to the radiogram images to enhance the resolution and clarity of the images..... 118
- Figure 5.16: The two travel time of GPR pulses from the surface of the top ignimbrite block to the created discontinuity is 2 ns. The zero correction and display gain process were applied to enhance the resolution and clarity of the radiogram images..... 119
- Figure 5.17: The radiogram image shows true perpendicular depth to the created discontinuity after adjusting the relative dielectric permittivity of ignimbrite in GPR data set. The resulting perpendicular depth from the radiogram ($d = 7.50$ cm) is almost the same as the measured perpendicular (vertical) depth in the lab ($d \approx 7.50$ cm). The zero correction and display gain process were applied to enhance the resolution and clarity of the radiogram images..... 120
- Figure 5.18: The produced radiograms from GPR data acquired using 400 MHz antenna in time-mode (left image) and distance-mode (right image) surveys at Station.3 (St.3). In time mode (left image), the data will be acquired regardless the antenna is towed or not which results in exaggerated

- horizontal distance that will have to be normalized before any further GPR data processing steps..... 121
- Figure 5.19: A 400 MHz antenna with no attached wheel (A), and with an attached wheel (B) to be used in a distance mode survey..... 122
- Figure 5.20: Creating three different locations on each rock slope face (rock slope face of station no.1) by using a hammer to create the three index points as reference to measure perpendicular depths from the surface of the rock face to detected hidden discontinuities..... 124
- Figure 5.21: Identifying the three index points locations by colors on the radiogram images. The small blue circle represents index point.1, while the small red and the orange circles represent the index points 2 and 3 respectively. 124
- Figure 5.22: The location of the GPR survey lines including the two index lines (dashed lines) at St.1. The colored circles are the locations of the three index points. The small blue circle represents the index point.1, while the small red and the orange circles represent the index points 2 and 3 respectively. 125
- Figure 5.23: The locations of the two index GPR survey line (the two dashed lines) at station 3, which passed through the three index points..... 126
- Figure 5.24: The location of the GPR survey lines vary from one station to another based on the extensions and the surface condition of the rock cut. (A) Shows St.2 as it seems small but (B) shows its real dimensions while (C) shows the locations of the GPR survey lines at this station..... 127
- Figure 5.25: A wooden panel was used as a try to create a smooth surface on which the GPR antenna was towed at St.1 (left image), while the right image shows the process of drawing using chalk the location of the GPR survey lines on the rock slope face 128
- Figure 5.26: The multiple reflections resulted from using a panel during acquiring GPR data at St.1 (A), and a good radiogram image (B) when acquiring the data with no using the wooden panel..... 129
- Figure 5.27: Parallel horizontal GPR survey lines (dashed lines are the two index lines) which are parallel to the strike direction of the plane of the rock face of station 3. The left image shows a linear trace of only one joint (joint no.1) which was detected in radiogram image as shown in Figure 5.28..... 132
- Figure 5.28: The radiogram of profile 1 at St.1. Raw radiogram (A), processed radiogram (B), and the detected hidden subvertical joints (yellow lines) (C). The strike of joint No.1 has an apparent declination angle (α) is 17° and so a true declination angle (β) is 17.80° 132

- Figure 5.29: The created 3D image of St. 3 using RADAN software (above) and the 3D-image for the detected hidden subvertical joints with apparent and true strike directions. 135
- Figure 5.30: A Leica ScanStation II (LIDAR scanner) which was used in this study. .. 136
- Figure 5.31: Station 1 before (A) and after (B), respectively, removing the grass to create a clean view for using the LIDAR. Notice that the locations of the three index..... 137
- Figure 5.32: The location of both the reference object (the blue circle) and the three index points (red circles) at St. 1. The below image is a point cloud image using LIDAR..... 139
- Figure 5.33: Cartesian coordinates are related to spherical coordinates..... 142
- Figure 5.34: The 3D image of St.1 showing the apparent and true geometry of the detected hidden subvertical joints..... 144
- Figure 5.35: The depth vector at St.1 was resolved to: $Y' = Y - d \cos 26^\circ$; and $X' = X - d \cos 64^\circ$ 146
- Figure 5.36: Equal area projection shows that the three detected hidden subvertical joints in station 1 represent an individual joint set (blue circle). 147
- Figure 6.1: Front view and side view of the rock slope of the station 1 at site 1. 150
- Figure 6.2: Projections of vectors normal to exposed joints and rock face planes (poles) on a unit lower hemisphere- Lambert stereonet at St.1. The poles of these exposed joints can be clustered into three sets. 152
- Figure 6.3: (A) True 3D GPR image for St.1 showing the location of the detected hidden subvertical joint. (B) Field verification was done by investigation some discontinuities whose planes extend parallel inside St.1, in the surrounding rock blocks..... 153
- Figure 6.4: The poles of the three detected hidden joints at station 1 can be represented as a separate joint set (blue circle)..... 154
- Figure 6.5: A front view of the rock slope of St.2 in site 1. 155
- Figure 6.6: The Lambert stereonet projections of the normal vectors (the poles) of the measured exposed joints as well as the rock slope face of the station (St.2). The poles of these exposed joints can be clustered into three sets (red circles). 157
- Figure 6.7: The position of the linear traces of the two detected hidden joints exposed on the side of the slope verifies the accuracy of the resulting true 3D GPR

image of station 2. Note that the true perpendicular depths (d) of these two hidden joints in the 3D image were verified by field measurements.....	158
Figure 6.8: The poles of the two detected hidden joints at station 2 can be represented as a separate joint set (blue circle).....	159
Figure 6.9.: A front view of the rock slope of St.3 in site 1.	160
Figure 6.10: The poles of the measured exposed joints at St.3 can be clustered into six joint sets (red circles).....	162
Figure 6.11: True 3D GPR image of station 2. Note that the true perpendicular depth (d) to the linear trace of the detected hidden joint (joint 1) in the 3D image was verified by field measurements.....	162
Figure 6.12: The poles of the two detected hidden joints can be represented as a separate joint set (blue circle) at station 3.....	163
Figure 6.13: A front view of the rock slope of St.4 in site 1.	164
Figure 6.14: The Lambert stereonet projections of the normal vectors (the poles) of the measured exposed joints of St. 4 can be clustered into five joint sets (red circles).....	166
Figure 6.15: True 3D GPR image for St.4 showing the location of the detected hidden subvertical joint. Field verification was not possible for this station.	166
Figure 6.16: The detected hidden subvertical joint at St.4 can be represented as a separate joint set (blue circle).	167
Figure 6.17: A front view of the rock slope of St.5 in site 1.	168
Figure 6.18: The Lambert stereonet projections of the normal vectors (the poles) of the measured exposed joints St.5 can be clustered into four joint sets (red circles).....	170
Figure 6.19: True 3D GPR image for St.5 showing the location of the detected hidden subvertical joint. Field verification was not possible in this station.	170
Figure 6.20: The normal vectors (the poles) of the four detected hidden subvertical joints at station 5 can be represented as a separate joint set (blue circle).....	171
Figure 6.21: A front view of the rock slope of St.2 in site 2 (Madison County).	172
Figure 6.22: The Lambert stereonet projections of the normal vectors (the poles) of the measured exposed joints of St.6 can be clustered into four joint sets (red circles).....	173

- Figure 6.23: The position of the linear traces of only four of the six detected hidden joints are exposed on the side of the slope verifies the accuracy of the resulting true 3D GPR image of station 2. Note that the true perpendicular depths (d) of these four hidden joints in the 3D image match those in the field. Joint 4 dips steeply into the slope face as indicated from the LIDAR measurements..... 174
- Figure 6.24: The two sets of the poles (blue circles) represented the six detected hidden subvertical joints at station 6..... 176
- Figure 6.25: A front view of the rock slope of St.7 in site 2 (Madison County)..... 177
- Figure 6.26: A side view of St.7 in site 2 is showing some discontinuities dipping steeply into the slope face which may cause toppling failure in the future (Madison County). 177
- Figure 6.27: The Lambert stereonet projections of the normal vectors (the poles) of the measured exposed joints of St.7 can be clustered into three joint sets (red circles)..... 178
- Figure 6.28: The position of the linear traces of the three detected hidden subvertical joints are exposed on the side of the slope which verifies the accuracy of the resulting true 3D GPR image of station 2. Note that the true perpendicular depths (d) of these three detected hidden subvertical joints in the 3D image match almost those in the field. 179
- Figure 6.29: The normal vectors (the poles) to the three detected hidden subvertical joints at station 7 can be a separate joint set (blue circle)..... 181
- Figure 6.30: In terms of resolution and so the number of detected hidden joints, the penetration depth of the GPR pulses was less in station 7 (A) than in station 6 (B). 181

LIST OF TABLES

	Page
Table 3.1: Typical values of relative dielectric permittivity for some common earth materials	50
Table 3.2: The apparent declination angle (ϕ) and the true declination angle (β) of the detected hidden subvertical joint which is shown as a linear event or interface in radiogram images.....	81
Table 4.1: A summary of Leica HDS3000 LIDAR scanner.....	95
Table 4.2: Specifications of Riegl LMS-Z390i terrestrial laser scanner according to manufacture datasheet.....	97
Table 5.1: Manual measurements results for the measured exposed discontinuities at station 1 (St.1).....	105
Table 5.2: The parameters which were entered into the GPR system of the 1500 GHz monostatic antenna to estimate the velocity of the GPR pulses in sandstone sample collected from Roubidoux Outcrop, Rolla-MO.....	113
Table 5.3: The parameters which were entered into the GPR system of the used 1500 GHz monostatic antenna to estimate the velocity of the GPR pulses in ignimbrite rock sample collected from Madison County-MO.....	117
Table 5.4: The values of the apparent and true perpendicular depths of the detected hidden subvertical joint No.1 at St.3.....	133
Table 5.5: The field measurements using a Brunton compass for both the reference object and the rock slope face at station 1.	139
Table 5.6: The coordinates of the three points of the reference object at station 1 at site 1 using Cyclone 6 program.	140
Table 5.7: The coordinates of the three index points of the rock slope face at station 1 using Cyclone 6 program.	140
Table 5.8: The coordinate values and the geometry of the reference object for LIDAR measurements calibration at the rock slope face of St.1.....	143
Table 5.9: Geometrical measurements of the rock slope face at St.1 after the calibration process for LIDAR measurements.....	144

Table 5.10: The apparent and true perpendicular depths from the three index point on the rock slope face of St.1 to the detected hidden subvertical joints.....	145
Table 5.11: Geometrical measurements using LIDAR for the detected hidden subvertical joints at St.1.....	146
Table 6.1: The dip direction (D.D.) and the dip angle (θ) of the rock slope face of station 1 resulting from the manual method and the LIDAR technique.....	150
Table 6.2: The manual geometrical measurements for dip direction (D.D.) and dip angle (θ) of the measured exposed discontinuities at the rock slope of St.1.	151
Table 6.3: Some field verification measurements for the detected hidden subvertical joints at station 1.	154
Table 6.4: The geometrical measurements for the rock slope face of St.2.....	156
Table 6.5: Manual measurements for dip direction (D.D.) and dip angle (θ) of exposed discontinuities at St.2.....	156
Table 6.6: The orientations of the two detected hidden joints measured by LIDAR at St.2 in addition to the field verification measurements.	157
Table 6.7: The geometrical measurements for the rock slope face of St.3.....	161
Table 6.8: Manual measurements for dip direction (D.D.) and dip angle (θ) of exposed discontinuities at St.3.....	161
Table 6.9: The orientations of the three detected hidden joints measured by LIDAR at St.3 in addition to the field verification measurements.	163
Table 6.10: The geometrical measurements for the rock slope face of St.4.....	165
Table 6.11: Manual measurements for dip direction (D.D.) and dip angle (θ) of exposed discontinuities at St.4.....	165
Table 6.12: The orientations of only the one detected hidden subvertical joint measured by LIDAR at station 4.	167
Table 6.13: The geometrical measurements for the rock slope face of St.5.....	169
Table 6.14: Manual measurements for dip direction (D.D.) and dip angle (θ) of the measured exposed discontinuities at St.5.....	169
Table 6.15: The orientations of the four detected hidden joints measured by LIDAR at St.5 in addition to the field verification measurements.	171
Table 6.16: The geometrical measurements for the rock slope face of St.6.....	172

Table 6.17: Manual measurements for dip direction and dip angle of exposed discontinuities at St.6.....	173
Table 6.18: The orientations of the six detected hidden subvertical joints measured by LIDAR at St.6 in addition to some field verification measurements.....	175
Table 6.19: The geometry of the rock slope face of St.7.....	178
Table 6.20: Manual measurements for dip direction (D.D.) and dip angle (θ) of the measured exposed discontinuities at St.7.....	178
Table 6.21: The orientations of the three detected hidden joints measured by LIDAR and the field verification measurements at St.7.....	180

1. INTRODUCTION

1.1 OVERVIEW

Slope stability can be defined as the resistance of an inclined surface of rock or soil mass to failure by either sliding or collapsing (Kliche, 1999). In both engineering and geological concepts, the term slope includes human-made slopes, such as rock/road cuts, open pits, and excavations as well as natural slopes, such as cliffs and valleys. Slope stability analysis is routinely performed and directed toward assessing the safe and the functional and economic design of either human-made or natural slopes and/or their equilibrium conditions (Abramson et al., 2002; & Eberhardt, 2003).

Slope stability analysis for rock mass requires a good understanding of its nature and what factors control its stability. A rock mass is usually characterized by the presence of many discontinuities that divide the rock mass into different sizes of rock blocks which are known as intact rocks. Discontinuities occur naturally in every rock mass (Scheidegger, 1978). The term discontinuity is a general term which suggests a break in the continuity of a rock fabric without an implied genetic origin (Otoo et al., 2011a).

A discontinuity can be defined as a significant mechanical break, or fracture of negligible tensile strength. It has both a low shear strength and high fluid conductivity when compared to the intact rock itself (Chernyshev and Dearman, 1991; & Priest, 1993).

When a discontinuity is exposed in an outcrop or cut of a rock mass, it manifests itself in one of two ways, often in both ways on the same exposure (Figure 1.1):

- Either as a fracture trace (a visible line) on the rock cut surface due to the intersection of the plane of the discontinuity and the planar rock slope face.
- Or as an exposed plane or face on the rock cut surface on which can be considered to be like “facet” on a precious cut stone (Otto et al., 2011a; and Duan et al., 2011).

In general, discontinuities are planes of weakness occurring in three dimensions in space, such as joints, faults, bedding planes, and fractures upon which both movement and sliding of intact rocks can take place (Kliche, 1999). Consequently, for the consideration to engineering properties of the intact rocks, the rock slope stability analysis requires detailed information about the geometry and the properties of those discontinuities which surely control to a large extent the mechanical and hydrological behavior of the rock mass (Bieniawski, 1989; Kilche, 1999; and Otto et al., 2011b).

Nearly all rock slope stability studies should involve two steps. The first step is to determine the geometrical properties of the discontinuities, which involves mapping outcrops and existing cuts. The second step is to determine the influence of the discontinuities on the rock slope stability based on the relationship between both the geometry of those discontinuities and the geometry of the rock slope face (Wyllie and Mah, 2004).

Currently, mapping discontinuities at rock cuts is generally conducted by using a geological compass and measuring tape. These measurements are documented by recording information on a notebook and photographing using a camera.



Figure 1.1: (A) A rock cut; (B) The same rock cut showing both joint traces (red lines) and facets (yellow polygons).

This traditional method is well known as the scanline method and is a traditional method still used in most rock slope stability analysis techniques. This method is cheap and easy to use, but it is time consuming and applied only to exposed discontinuities at accessible rock slope areas. In addition, considerable safety risks are involved, as measurements are sometimes carried out at the base of existing slopes or during quarrying, tunneling or mining operations or along busy highways and there is difficulty gotten direct access to rock faces (Otoo et al., 2011b).

Accordingly, to overcome the drawbacks of tradition methods, new techniques have been developed for in-situ geometrical data collection. From such techniques, photogrammetry (Coe, 1995), total station (Bulut and Tudes, 1996), image processing (Post et al., 2001), and the Three Dimensions Terrestrial Laser Scanner (3D TLS) (Slob et al., 2004 & 2005; and Feng and Röshoff, 2004) have been tested and used for mapping and extracting geometrical data from the exposed discontinuities at rock slope faces. In general, these methods are fast in terms of data acquisition, data accuracy, and accessibility to rock slope face areas.

Among these techniques, the 3D TLS, or what is called in some references as Light Detection And Ranging scanner (LIDAR), has shown a great potential to acquire and extract a large amount of geometrical data of discontinuities within a short time and with a high level of accuracy (Slob et al., 2004 & 2005). All of the methods mentioned to this point are used for mapping exposed discontinuities. In contrast, ground penetrating radar (GPR) has been used to map hidden discontinuities in the slope stability analysis field. GPR is a rapid, non-destructive, non-invasive and high resolution geophysical tool which can provide vital subsurface structural information about the hidden discontinuities

in the rock mass. GPR plays a significant role in terms of mapping discontinuities and identifying the mechanism of the potential rock failure. Consequently the geometrical data acquired by GPR can be then integrated into rock slope stability analysis.

Both horizontal and sub-horizontal discontinuities will intersect the exposed rock cut and, therefore, can be projected back into the rock mass. In addition, vertical and sub-vertical discontinuities striking obliquely to the rock mass will also be exposed, and can also be easily mapped (Maerz and Kim, 2000). However, both vertical and subvertical discontinuities which strike parallel or semi-parallel to the rock slope face do not daylight into the slope face, and thereby they will not be exposed and observed. This leads to underestimating risks and hazards of potential slope failures (Figure 1.2).

Even though these discontinuities should daylight above the road cut, they are typically obscured by a layer of soil, and are not visible unless a significant effort is made to remove this layer of soil and clean the top of the rock. As this is a costly and environmentally unfriendly undertaking, the removal of overburden above the rock cut is rarely attempted. Consequently, when vertical to subvertical discontinuities occur parallel to a rock cut they are typically not identified utilizing traditional methods and cannot therefore be incorporated into the rock slope stability analysis.

Ground Penetrating Radar (GPR) has the ability to detect hidden vertical to subvertical discontinuities that are parallel or semi-parallel to the rock cut, and accordingly, to avoid failures, reduce property damage and avoid injury and loss of lives. (Maerz and Kim, 2000).



Figure 1.2: A rock failure along a hidden sub-vertical joint resulting in the death of a truck driver on Highway 401, Brockville, Ontario, Canada. Dr. Norbert Maerz, the advisor of this research, is standing beside the sub-vertical joint trace after removal the failed materials (dashed yellow line) (Adopted from Maerz and Kim, 2000).

1.2 RESEARCH OBJECTIVES

The main objective is to develop a methodology for the purpose of determining the geometry and orientation of hidden discontinuities in rock slopes. This approach will help to localize and evaluate the hazards of subvertical discontinuities hidden behind the rock slope walls, and give an image about the potential rock failures and its

consequences; therefore, significantly help in the design of efficient and proactive conservation measurements for the rock slope.

The other specific objectives are as follows:

- To assess the slope stability utilizing the scanline method for exposed discontinuities on rock cuts.
- To locate hidden vertical to subvertical discontinuities (joints) using processed GPR data two dimensions (2-D) images. Since the difference between a vertical joint and a subvertical joint is could be a few degrees in dip, the term “subvertical joint” will imply both of vertical and/or subvertical joints in the context of this research to avoid repeating writing the words and any other potential confusion.
- To create a 3-D image for each rock slope face, station, showing the detected hidden subvertical joints related to the rock slope face.
- To depict the apparent geometry of the detected hidden subvertical joints in 3-D views related to rock slope faces.
- To estimate “the slope face - perpendicular depth” which can be defined as the depth vector that is perpendicular to the plane of the surveyed rock slope face, and which must be measured horizontally in the Y- axis direction from any selected point on the plane of the rock face to the corresponding point on any plane of the detected hidden joints behind the slope face. This “the slope face - perpendicular depth” is known commonly in geophysics and GPR literatures as a vertical depth denoted d .
- To depict the true geometry of the detected hidden subvertical joints in 3-D views related to rock slope faces.

- To determine the true geometry and orientations, dip direction and dip angle, of each detected hidden joint using the 3-point equation results derived from the LIDAR and GPR data in a combination.
- To validate our new approach, detecting and measuring the orientation of the detected hidden vertical to subvertical joints, with some ground truths measurements.

Our approach has been basically built based on the combination of GPR data and LIDAR to extract the orientations of the detected hidden subvertical joints in some highways rock cuts and, thus, to provide a better understanding for the surface and subsurface characteristics of the rock cuts or the rock slopes. This approach may help to evaluate more accurately the instability or the degree of fractioning of the rock slope.

1.3 PLAN OF ACTION

The plan of this research, in order to achieving its goals and the objectives, consists mainly of three phases are summarized as follows:

1.3.1 Phase I - Reconnaissance Survey and Literature Review for the Study

Area. This preliminary phase includes the following tasks:

- Walking reconnaissance of potential site and other nearby rocks to:
 - i. Identify the regional geology of the study area.
 - ii. Determine the lithology of the study area.
 - iii. Determine the geometry of the rock slope and its condition.
 - iv. Investigate the history of the slope stability of the study area.

- Identify and determine the appropriate sites (stations) of rock slopes where the new method may be applied.
- Conduct a literature review related to the subject of this dissertation.
- Search for topographic and geological maps and reports relevant to the study area and the field of interest.
- Use satellite images study to identify some the geological structures and patterns in the study area where it is necessary.
- Write and summarize what have been found through the above steps and prepare for the next plan (Phase II).

1.3.2 Phase II - Field Work, Sampling, and Testing. This phase has included the following tasks:

- Conducting scanline method measurements in the field.
- Collecting rock samples to determine the velocity of GPR electromagnetic waves through the rock samples and to determine the dielectric constant value of the rocks from which slopes composed of.
- Conducting several parallel horizontal GPR survey lines at each station of the study area in the purpose of to create 2D and 3D radiograms images for the detected hidden joints.
- Conducting the LIDAR survey in the area with a respect to conduct a calibration for the LIDAR geometrical measurements based on field measurements using a geological compass.

1.3.3 Phase III- Data Analysis and Interpretation (Office Work). In this phase, the following tasks will be done:

- Processing of GPR data and interpretation using GSSI - RADAN 6.5 software.
- Generation 3D images from 3D-TLS using Cyclone 7.0 software, and extract the geometrical and orientation data for exposed discontinuities using 3-Points equation after calibrating the measurements of the 3D TLS based on the taken field measurements by a geological compass. These geometrical and orientation data include: strike direction, dip direction, and dip angle for each exposed joint/discontinuity.
- Extracting geometrical and orientation data for hidden discontinuities from the 2D and/or 3D GPR data based on the location of the selected 3 points on the slope face surface which two of these points have to be coplanar and no co-linear at all.
- Stereonet projection and analysis for the scanline method measurements using OpenStereo software.
- Stereonet projection and analysis for the measured geometries of the detected hidden subvertical joints which are resulted from using GPR and LIDAR in a combinations.
- Comparison between the resultant stereonet projections before detecting the hidden subvertical joints and after detecting them, so such results could be used to strengthen any further slope stability analysis for the study area.
- Final results, discussion, conclusions, and recommendations.

1.4 STRUCTURE OF THE DISSERTATION

Since discontinuities play an important role in rock slope stability analysis, chapter one focuses on how these discontinuities can be detected using some well-known techniques. Then this chapter lists briefly the main objective of this research and how can be achieved through the plan of action.

Chapter 2, details and information about the art of mapping discontinuities and the used techniques are presented through a comprehensive literature review. This chapter will give the reader a general view about what has been done for many years in the field of slope stability analysis by mapping discontinuities and extraction the geometrical data of the rock slope.

Following that chapter 3, where the author points out the study area location and geology, then a detailed description for the scientific systematic steps that have been used during field and laboratory work including all the details of our new approach to detect and map the hidden discontinuities in rock slope, and how their geometry and orientations have been extracted.

Then in chapter 4, the required fundamentals and theory of using the 3D Terrestrial Laser Scanning technique for mapping exposed discontinuities in the support of slope stability analysis are written with an emphasis on our new approach's concepts and requirements and also at a level that is required for anyone who works in the field of rock engineering.

And in chapter 5, in the same way that previous chapter, chapter 4, was written, a background and all the required fundamentals and theory of use the GPR technique for

mapping hidden discontinuities in the support of slope stability analysis are written with an emphasis on our new approach's concepts and requirements.

In chapter 6, all the results and data analysis of the used techniques (scanline, 3D-TLS, and GPR techniques) are outlined and discussed.

Finally in chapter 7, the most important points are discussed with a respect to some important recommendations and suggestions for any proposed study in the art of slope stability analysis using a similar or semi-similar approach to ours. The appendices, bibliography, and VITA follow to end the contents of this dissertation.

2. LITERATURE REVIEW

2.1 OVERVIEW

The stability of rock slopes is often significantly controlled and governed by the structural geology of the rock mass in which the slope is excavated. Structural geology refers generally to naturally occurring breaks in the rock masses (Wyllie & Mah, 2004). These breaks are known as discontinuities which control the mechanical and hydrogeological behavior of rock masses (Hoek, 2006). A discontinuity is any type of defect in the rock fabric or a surface which marks a change in the physical or chemical characteristics in rock material (Hack et al., 2003; and Kliche, 1999). Discontinuities are, in general, planes of weakness controlling the engineering properties of the rock mass. Based on the geological process by which discontinuities are formed, discontinuities can be any plane of weakness such as joints, faults, bedding planes, foliation plane, cleavage, etc (Torres, 2008). Joints are fractures along which essentially no shear displacement has occurred and formed due to the change of stress conditions by geological process. Joints are the most common defect and weakness planes in rock masses while faults are the most serious, and thus this is why we used the term joint in our research rather than any other type of discontinuities. All discontinuities have the following physical properties: orientation, spacing, intensity, aperture (width of opening), and wall roughness, and in some cases filling materials (Kliche, 1999; and Torres, 2008).

Basically, mapping discontinuity orientations on rock slope faces and then identifying the probable mechanisms and the modes of failure are the two first main steps

in rock slope stability analysis. On other words, the mapping of discontinuities is ultimately required before a rock slope stability analysis can be undertaken.

2.2 GEOMETRY OF DISCONTINUITIES

The mechanical and hydrological behavior of this rock mass is controlled and governed by the nature of these discontinuities (joints, fractures, faults, etc). Therefore, it is of paramount of importance to accurately collect, map, and analysis the data of discontinuities occur in the rock mass slopes for a slope stability analysis. The International Society for Rock Mechanics, ISRM, has pointed out the basic required descriptions for such discontinuities which have to include all or some of the following characteristics, based on the objectives of the research and the used technology and methods for mapping the discontinuities,: orientation, spacing, persistence, roughness, wall strength, aperture, filling materials, number of sets, block size, and seepage (Figure 2.1).

Discontinuity properties can be classified into geometrical and non-geometrical properties. Geometric properties include orientation, persistence, spacing, rock block size and discontinuity aperture size. Non-geometrical properties include wall strength, roughness, filling materials and seepage or water conductivity. The most important discontinuity property is orientation. Orientation, which implies dip direction and dip angle of a discontinuity, influences significantly the potential of the intact rocks in rock masses to slide or fall, the direction of this sliding or falling or movement and the volume of material to be moved (Donovan et al., 2005). Orientation is so important that it is

ultimately used in every kind of slope stability analysis, either numerical or non numerical modeling (Otoo et al. 2011b).

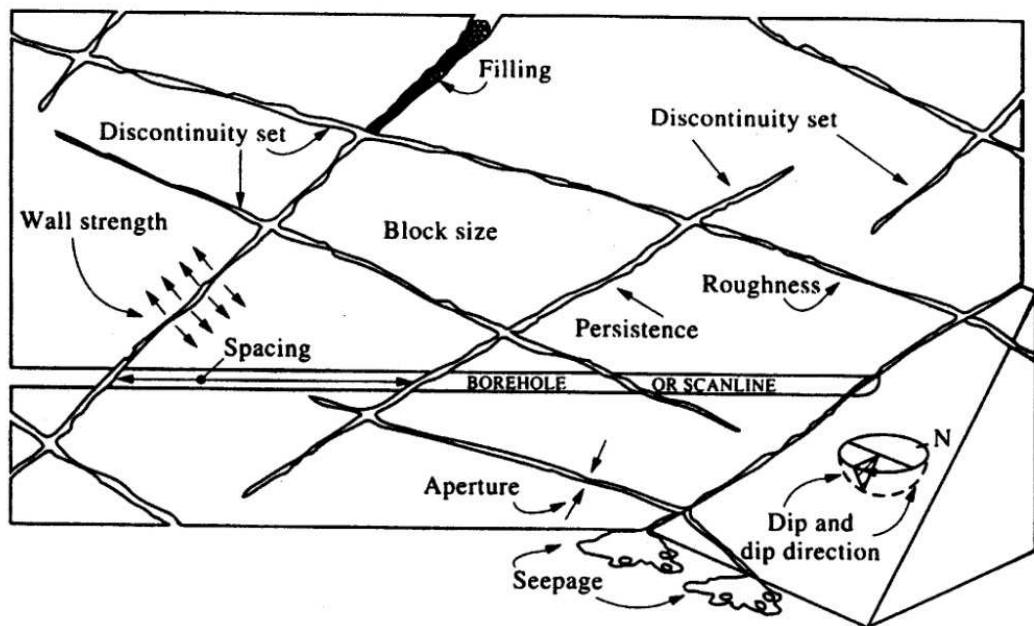


Figure 2.1: A 2-D diagram shows the primary geometrical and non-geometrical properties of discontinuities in a rock mass (Retrieved from Hudson, 1989).

2.3 MAPPING DISCONTINUITIES

Most discontinuities can be identified by mapping once the rock cut has been exposed (Piteau, 1979a; Piteau, 1979b; Piteau 1979c). Mapping discontinuities and measuring their orientations process is crucial and critical in assessing the stability of discontinuous rock slopes and rock masses as well as in mitigation and remediation techniques and blast evaluation. The discontinuity orientations are used as input to all discontinuous modeling programs and methods, including kinematic analysis methods

and limit equilibrium sliding methods (Otto et al., 2011b; Maerz et al., 2012; and Haneberg, 2008).

2.3.1 Scanline Method. Mapping discontinuities at rock slope faces is performed by using standardized methods such as scanline method using a geological compass, inclinometer, and measuring tape, photographing with a camera, and documenting by recording information on a notebook. Even though this so-called a traditional method is now still used in most of the rock engineering projects in many places over the world, the quality and quantity of the acquired data are sometimes unable to meet the requirements in some rock engineering projects.

The major drawback of traditional methods, scanline survey or cell mapping, are that it is too manual intensive operation and time consuming especially for a sound statistical analysis where a lot of measurements are required. Moreover, direct access to and reaching the rock faces physically is often difficult, dangerous, or impossible, and almost of the field measurements are carried out at the base of the rock slope within few meters of height which provide not enough nor accurate enough data that can be considered as representative samples for whole surface area of the slope (ISRM, 1978; Slob et al., 2005; and Slob et al., 2006; and Haneberg, 2008).

In addition, the way of recording and storing data cannot provide sufficient data to utilize modern information technology that can speed up the data processing and interpretation and, furthermore, can save the data in any required format for any further analysis and designation and any future use or purposes (Slob et al., 2006).

Therefore, it has been recently realized that utilizing a new technique and tool to collect in-situ geometrical rock slope data is the key point in support of slope stability

analysis with both quality and quantity and in a time fashion. Techniques such as photogrammetry (Coe, 1995), total station (Bulut & Tudes, 1996), image processing (Post et al., 2001), and the 3D terrestrial laser scanner (3D TLS) (Slob et al., 2004 & 2005; and Feng & Röshoff, 2004) which have been tested and used for mapping and extracting geometrical data of the exposed discontinuities at the slope face.

2.3.2 Light Detection And Ranging (LIDAR or LiDAR). Traditional discontinuity measurements are subjective are based mainly on the surface measurements of the exposed discontinuities, which can be biased by surface creep, dilation, and weathering. Alternatively, a LIDAR scanner can provide accurate point cloud data of the scanned slope within a few minutes, and the geometry of rock discontinuities can be extracted in an automated and objective way (Pernito, 2008). LIDARs which are sometimes called Terrestrial Laser Scanners (TLS) are geodetic instruments which become very popular for engineering and geology surveys during the last years (González-Jorge et al. 2011; and Otoo et al., 2011a).

LIDAR is so quick that comparable surveys can be conducted to an area of interest to ascertain the geometries of regional systematic joints and to compare the resulted data with those measured manually in the site of interest.

It is not difficult to carry out a 3D laser scan survey; however, it is quit challenges to convert the LIDAR data to useful information that can directly be used for the purpose of slope stability analysis or any other purpose in the rock engineering practice. Different methods or approaches have been used to handle this issue such as semi-automated approach, automated approach, and the calibration using a geological compass approach (Slob et al., 2006; Slob et al., 2005; and Maerz et al., 2011).

The idea to map discontinuities on rock mass faces using remote sensing techniques is not new, in 1976, Rengers conducted geometrical measurements for individual discontinuities using analogue terrestrial stereo-photogrammetric techniques which have been recently developed through time to be digital imaging and processing data techniques than can be used for many applications in different disciplines especially in the fields of rock engineering, rock mechanics, and landslides (Roberts and Propat, 2002; Fasching et al., 2001; Haneberg, 2005; Gaich et al., 2006; Whitworth et al., 2006; Braun, 2008; Dunning et al., 2009; Abellán et al., 2010; Sturzenegger et al., 2011; García-Sellés et al., 2011; Asahina and Taylor, 2011; and González-Jorge et al., 2011).

Slob and others (2006) have successfully used the semi-automated and automated approaches of 3D laser scanning survey to map a rock slope face composed of carboniferous meta-siltstone and slate with well-developed discontinuity sets along a secondary road in Catalonia which connects towns of Falset with Bellmunt in Baix-Camp, Spain. They found that even though the two approaches can produce high resolution data that can be used for mapping discontinuities and any other purpose in rock engineering, the full-automatic method is capable of capturing more data that are required for further statistical and/or modeling analysis.

Moreover, another one of the most recent applications of the LIDAR is in the art of forecasting of possible rock falls and rock mass slides, which are mainly controlled by the presence of discontinuities and their orientations and geometry (Abellán et al., 2010).

Alba and Scaioni (2010) have described how to extract change and rock mass deformation detection based on a LIDAR survey for the same rock face at two different times or periods. Their analysis was taking into account the multi-temporal pointcloud

geo-references and built on three main steps: (i)vegetation filtering based on near infra red imagery (NIR); (ii) detection of major changes such as loss materials; and (iii) deformation analysis and testing. Moreover, the prediction of slope failures by monitoring and understanding of ongoing even mill-metric deformation which is mainly controlled by the geometrical and orientations characteristics of discontinuities has been conducted by utilizing the LIDAR technology (Abellán et al., 2006).

However, Traditional and LIDAR measurements are limited only for the exposed discontinuities on the rock slope, which excludes detection of probable hidden discontinuities that may have a significant effect in the rock slope stability analysis. For these reasons, it is desirable to employ a geophysical tool that will be able to delineate and/or map hidden discontinuities or fractures net inside the slope.

2.3.3 Geophysical Techniques. For the past sixty years, the geophysical techniques have been increasingly applied to the exploration of natural resources, geological structures, and site investigations. This wide spectrum of applications of geophysical methods has been recently expanded to embrace geological engineering and civil engineering fields, where non-destructive techniques have proved useful role in detecting and revealing the hidden discontinuities and fractures, and generating 2-D or 3-D geologic models. Many recent studies have been conducted on mass movements combining one or more geophysical techniques to depict discontinuities and fractures within these failed slopes.

Because of the efficiency of utilizing non-destructive geophysical techniques in rock engineering, International Society for Rock Mechanics (ISRM) has suggested and described seven geophysical methods than can often be applied and utilized: seismic

refraction, shallow seismic reflection, electrical, electromagnetic, ground penetrating radar, gravity, and radiometric techniques (ISRM, 2004).

Green et al. (2006) conducted different high-resolution geophysical techniques to locate and extract geometrical features of unstable rock, in Switzerland, in order to improve the hazards assessment of the instability of a rock slope.

The stability of rock slopes is also significantly influenced by pore water pressure, which commonly infiltrates along discontinuities. The hydrogeological regime, which is controlled by the geometry of discontinuities, is generally considered one of the most critical factors affecting slope stability. In such cases, geophysical techniques are often capable of delineating the presence of groundwater in fractures and discontinuities in the rock slopes unstable slope.

Heincke and others (2010) conducted a combined 3-D geoelectric and seismic tomography study, on the large Aknes rockslide in western Norway, in order to identify shallow tension fractures and ascertain the fractures' effects on conveying seepage. They succeeded in this by comparing the geophysical results with information extracted from borehole logging and tracer tests.

On the Sandalp rock avalanche in the Canton of Glarus, Switzerland, Socco et al. (2010) conducted a study that integrated resistivity tomography, seismic P-wave tomography, and active and passive surface wave analysis geophysical methods on several profiles, deployed both on the rock avalanche deposit and on the surrounding terrain. Comparisons of the results of the geophysical investigations with the topographic benchmark have demonstrated the capability of geophysical methods to locate the

detachment surface of the rock avalanche where the contrast, the key word in geophysics, with the host properties is most striking.

2.3.3.1 Ground penetrating radar. Ground penetrating radar (GPR), which sometimes is called ground probing radar, georadar, earth sounding radar, or subsurface radar, is an effective non-invasive geophysical imaging techniques that has a wide variety applications for many different disciplines.

In terms of rock engineering, rock mechanics, and slope stability analysis art, most discontinuities can be identified by mapping once the rock cut has been exposed (Piteau, 1979a; Piteau, 1979b; Piteau 1979c). Horizontal to sub-vertical discontinuities will intersect the exposed face and can be projected back into rock mass. Vertical and near vertical discontinuities striking obliquely to the road cut will also be exposed, and can also easily be mapped. Vertical discontinuities, however, striking parallel to the road cut cannot be seen, because they do not daylight into the cut. Although these should daylight above the road cut, they are typically obscured by a layer of soil, and are not visible unless a significant effort is made to remove the soil and clean the top of the rock. As this is a costly and environmentally unfriendly undertaking, the removal of overburden above the cut is rarely attempted. Consequently, when vertical discontinuities occur parallel to rock cut, they are typically not identified, and cannot therefore be incorporated into the analysis (Maerz and Kim, 2000).

Therefore, GPR has been used to locate and map hidden fractures and discontinuities in rock and soil slopes and/or underground surface. GPR is easy to use and the results are relatively simple to interpret. GPR can be easily mounted on a vehicle, or lashed to a boom mounted on a small truck. This makes data collection fast and

efficient (Maerz and Kim, 2000). GPR is one of the least expensive non-destructive and portable geophysical methods that can be used to detect the hidden fractures and joints in a rock mass. It has been effectively used for many years ago for the purpose of mapping and detecting hidden fractures and joints in earthen materials (Mellett, 1995; Stevens et al., 1995; Jeannin et al., 2006; Theune et al., 2006; and Leucci et al., 2007).

For instance, ground penetrating radar (GPR) was successfully applied to detect and map fractures in marble quarries where GPR provided high resolutions images of about 1 and 5 cm and for depths of about 8 and 15 m using 900 and 300 MHz antennas respectively, which was helpful in the process of evolution the quality of marble which has low electrical conductivity (Grandjean and Gourry, 1996).

Maerz and Kim (2000) have conducted a field investigation in a sandstone rock formation, in Missouri, using GPR with 400 MHz antenna in the purpose of identifying the hidden vertical and/or sub-vertical discontinuities in a rock cut. The results showed the ability of the GPR to detect and depict the vertical discontinuities up to 2.5 m depth which can play a significant role in slope remediation and stabilization and loss of life reduction.

As an objective to localize main fractures and eroded areas inside ten pillars whose minimum side length of one of them is 7 m, and which presented indications of having reached stress limits, a combination of ground penetrating radar and seismic tomography imaging has been conducted in a gypsum quarry in Western Europe. The seismic method was used effectively to produce a map of velocities related to the state of the pillar's internal stress conditions, while radar data delineated the fractures locations.

The processed data of both methods showed similarities with respect to the damage zone detection (Dérobert and Abraham, 2000).

Toshioka et al. (2003) carried out GPR measurements on the vertical wall of a welded tuff rock quarry in Japan, with the objective of studying the applicability of GPR to map the distribution of fractures in the rock mass. By comparing the GPR records with the visible fractures in the face, researchers learned that electromagnetic waves were most strongly reflected by those fractures filled with water.

Porsani et al. (2006) found out that GPR is also an effective method for localizing fractures and joints and for identifying the planes of structural discontinuities (both inclined and sub-horizontal) in a granite quarry in Capão Bonito region of São Paulo State, southern Brazil, where 25, 50, and 100 MHz antennas were used.

GPR and LIDAR whose data are sometimes effectively combined and/or integrated in the analysis of slope stability in order to get more accurate and details of the geometrical properties of discontinuities for the slope stability analysis purposes.

In 2008, Torres made measurements for a rock slope stability analysis using a LIDAR in a combination with GPR on a rock exposure at a porphyry quarry at Albiano, Italy. The individual results and the integrated analysis of the geometrical information derived from LIDAR and GPR showed a reasonable degree of correlation with the results of the Scanline method, and demonstrated itself to be an attractive way of complement such information in order to reduce the degree of uncertainty regarding the geometrical characteristics of the discontinuity network of a rock mass.

Pernito (2008) conducted a slope stability analysis on a volcanic rock slope in Montemerlo, Italy, using LIDAR and GPR data; and he found that the integration

between the two methods was reliable and applicable with some limitation in interpretation of discontinuities orientations data acquired by the GPR.

2.4 SLOPE STABILITY ANALYSIS

One of the most important goals of performance slope stability analysis is to prevent or reduce or minimize the consequences of rock slope failure which may cause a lot of damage in infrastructures and buildings and loss in lives within a very short span of time (Figures 2.2 and 2.3).

A number of methods are being used for rock slope stability analysis (Hoek and Bray, 1981; and Goodman, 1989). This analysis is usually done through kinematic analysis, limit equilibrium analysis, and numerical analysis (Gurocak et al., 2008). Almost of all stability analyses of rock slopes containing discontinuities employ kinematic analysis before further other analyses in order to determine potentially unstable slopes (Aksoy and Ercanoglu, 2007).

A kinematic analysis is a good technique to only determine potential kinematic type of rock slope failure such as planar, wedge, and toppling through using stereographical, which is known sometimes as hemispherical, projection (Gurocak et al., 2008). The hemispherical projection is a method of representing and analyzing the three dimensional relations of reality on a two-dimensional diagram (Brady and Brown, 2004).

Kinematic analysis, which basically depends on stereographical projection technique, is vital for analyzing the stability of intact rocks in rock masses and must precede any subsequent analysis. Once failure mechanisms are defined, it is then possible

to design an adequate support system for loosened intact rock blocks in rock masses (Lana and Gripp, 2003).



Figure 2.2: A Catastrophic rock slide destroyed tens of houses and killed 65 persons in Al-Dhafir village in Sana'a Governorate, Yemen, in December 28th 2008 (Adopted from Petley, 2008 at: <http://www.landslideblog.org/2008/09/catastrophic-rockfalls-in-middle-east.html>).



Figure 2.3: A traffic accident happened due to a rock fall incident on a highway; Canada; (Adopted from Bloom, 2012 at <http://www.americainfra.com/article/Protecting-Roads-and-Infrastructure-from-Falling-Rocks/>).

However, kinematic analysis does neither consider forces acting on slope nor shear strengths of discontinuities of intact rocks (Gurocak et al., 2008). However, equilibrium analyses do and are generally used to estimate such forces to evaluate the factor of safety against failure (Sitar and MacLaughing, 1997).

Limit equilibrium analysis is performed if kinematic analysis shows that failure is likely (Topal, 2007). In This analysis all of the shear strength along the failure surface, the effects of pore water pressure in discontinuities, and the effects of external forces, such as seismic acceleration will be considered (Gurocak et al., 2008). This analytical method is also called as “kinetic analysis” (Kilche, 1999).

While Numerical analyses, such as finite element and distinct element, are used to verify results occurred from kinematic and/or equilibrium analyses (Gurocak et al., 2008; and Gischig et al., 2011). In this research, only kinematic analysis was used since the shear strengths of the walls of hidden discontinuities are unknown and cannot be estimated.

2.4.1 Rock Failure Types. Failures in rock cuts occur as a result of several mechanisms. Some of these mechanisms; such as raveling, undercutting, and rolling failures, are in general not conducive to predictive calculations or modeling, but rather require engineering experience and judgment to determine whether they are likely to fail or to remain stable as shown in Figure 2.4 (Maerz & Kim, 2000). In contrast, plane (planar), wedge, and toppling failures, as shown in Figure 2.5, are all conducive to predictive calculations or modeling ranging from simple limit equilibrium analysis or kinematic analysis to sophisticated numerical modeling (Hoek and Bray, 1981; Piteau, 1979d; Piteau, 1979e; Piteau, 1979f).

Franklin and Senior (1987) investigated 415 rock failures along highways in Northern Ontario, Canada; and they found out that 137 of those failures are toppling, planar, and wedge failure types with a percentage of 33% of all different types of rock failure where the proportion of toppling failures occurrence is 23%, for planar failure occurrence is 8%, and for wedge failure occurrence is 2%.

2.4.2 Kinematic Analysis for Rock Failures. “Kinematic” refers to the motion of bodies without reference to the forces that cause them to move (Goodman, 1989). Kinematic analysis, which is purely geometric, examines which types of failure are possible in a rock mass with respect to an existing or proposed rock slope (Kliche, 1999). For kinematic analysis, the lower hemispheres stereographical projection method described by Hoek and Bray (1981), by Goodman (1989), and by Wyllie and Mah (2004) is generally used.

In general practice, kinematic analysis is based on plotting all measured discontinuities planes on a stereographic projection net and evaluating the orientation (dip angle and dip direction) of particular planes (major discontinuity sets) represented as poles (normal vector to discontinuity planes) at the centers of concentration zones (Aksoy and Ercanoglu, 2007).

Furthermore, this orientation of the discontinuity planes and their intersections has to be compared with rock slope geometry (dip angle and dip direction) and, in addition to, friction angle along the discontinuity planes (Kilche, 1999; and Aksoy and Ercanoglu, 2007).



Figure 2.4: Raveling, undercutting, and rolling failures along Highway 70 road cuts, respectively, Colorado State, USA (Retrieved from Maerz & Kim, 2000).



Figure 2.5: Example of toppling, planar, and wedge rock failures respectively along highway rock cuts (Retrieved from Maerz & Kim, 2000).

2.4.2.1 Kinematic analysis for plane failure. Planar failure occurs always along a single discontinuity plane that intersects a rock slope face and so then exposed (Figure 2.6). In order for this type of rock failure to occur, the following geometrical conditions must be satisfied as illustrated in Figure 2.7 (Hoek and Bray, 1981; Goodman, 1989; Kliche, 1999; Wyllie and Mah, 2004; and Hudson and Harrison, 2007):

- The sliding discontinuity plane must daylight in the rock slope face (Figures 2.6 & 2.7).
- The strike of the sliding discontinuity plane must parallel or nearly parallel to the slope face within $\pm 20^\circ$. In other words, the dip direction of the sliding discontinuity plane (α_p) must be parallel or nearly parallel to the dip direction of the slope face (α_f) within $\pm 20^\circ$.
- The dip angle of the slope face (ψ_f) has to be greater than the dip angle of the sliding discontinuity plane (ψ_p) which has to be less than the internal friction angle of the intact rock or sliding rock block (ϕ).

In Figure 2.7, the zone between the great circle representing the dip angle of the rock slope face and the internal friction angle (friction cone) represents a critical area within which plane failure is kinematically possible (Wyllie and Mah, 2004). Therefore, whenever the dip angle of the sliding discontinuity plane is greater than the internal friction angle, the factor safety is less than 1.0 and vice versa (Kliche, 1999).

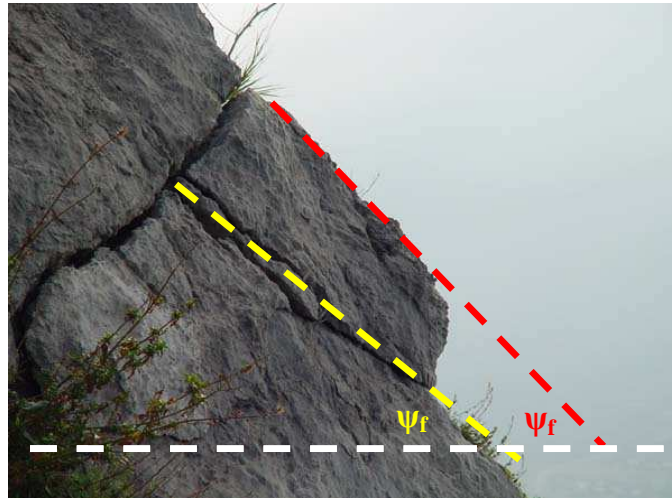


Figure 2.6: A potential plane failure on a single sliding discontinuity plane (ψ_p - dashed yellow line), Italy. Note that the dip angle of that sliding plane is less than the dip angle of the rock slope face (ψ_f - dashed red line) (Adopted from http://ookaboo.com/o/pictures/picture/14675384/Location_Lauria__ItalyLandslide_type_Sli).

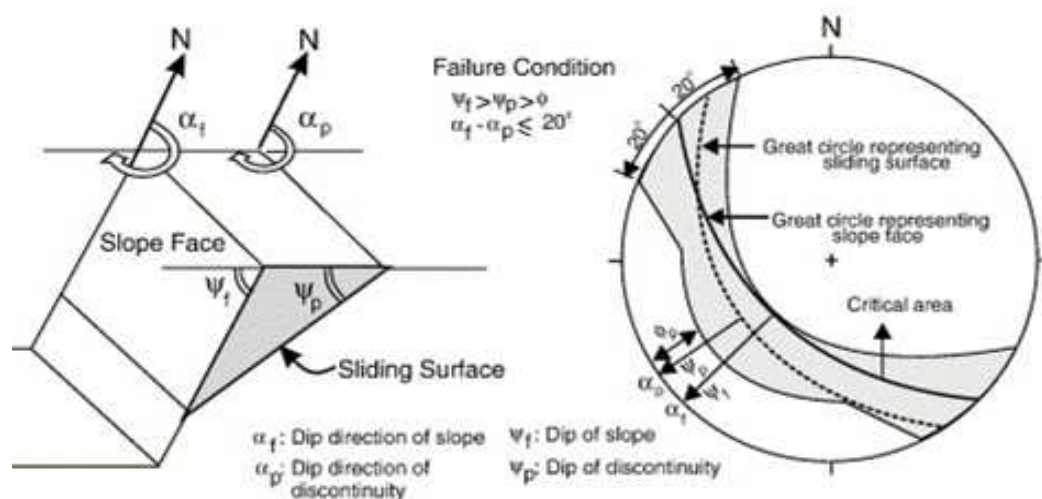


Figure 2.7: Kinematic analysis for plane failure (Retrieved from Naghadehi et al., 2011).

2.4.2.2 Kinematic analysis for toppling failure. Toppling angle occurs along a single discontinuity that must dip steeply into the rock slope face (Figure 2.8). In addition, the strike or the dip direction of the discontinuity plane must be parallel or nearly parallel within $\pm 30^\circ$ to the strike or the dip direction of the slope face as illustrated in Figure 2.9 (Hoek and Bray, 1981; Goodman, 1989; Kliche, 1999; Wyllie and Mah, 2004; and Hudson and Harrison, 2007).

Furthermore, the discontinuity plane must satisfy the following equations (Naghadehi et al., 2011):

$$- [(90^\circ - \psi_p) + \varphi \leq \psi_f]$$

$$- \alpha_p = (\alpha_f \pm 180^\circ) \pm 30^\circ$$

where,

ψ_p – the dip angle of the discontinuity plane

ψ_f – the dip angle of the rock slope

α_p – the dip direction of the discontinuity plane

α_f – the dip direction of the rock slope

As the same manner as in the plane failure, the zone between the great circle representing the dip angle of the rock slope face and the internal friction angle represents a critical zone within which toppling failure is kinematically possible (Wyllie and Mah, 2004).

Toppling failure is common in both basaltic rocks, due to columnar joints structure, and in sandstone, since sandstone beds commonly form steep slopes or cliffs where whole hillsides are underlain by those rocks which cause toppling failures (Fell et al., 2005).



Figure 2.8: A potential toppling failure at station 7 in site 2 of the study area. Notice that the potential sliding planes of some discontinuities (dashed yellow lines) are dipping steeply into the rock slope.

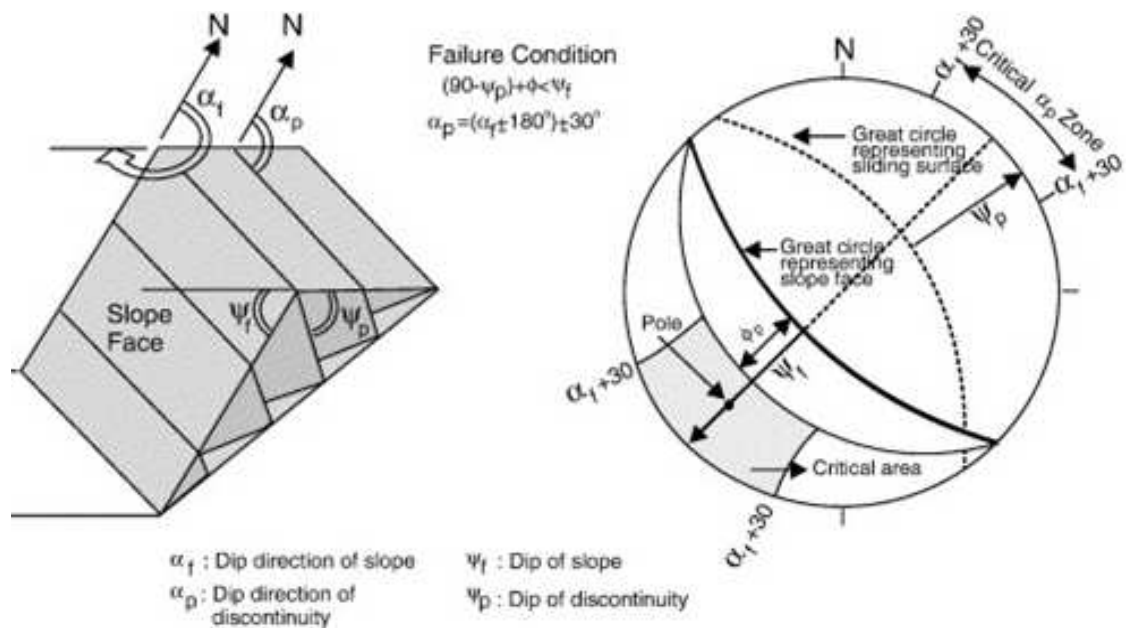


Figure 2.9: Kinematic analysis for toppling failure (Retrieved from Naghadehi et al., 2011).

2.4.2.3 Kinematic analysis for wedge failure. Wedge failure occurs when intact rocks slide along two intersecting discontinuities both of which daylight in the slope face as shown in Figure 2.10. In order for this type of rock failure to occur, the following geometrical conditions must be satisfied as illustrated in Figure 2.11 (Hoek and Bray, 1981; Goodman, 1989; Kliche, 1999; Wyllie and Mah, 2004; and Hudson and Harrison, 2007):

- The intersection of the two discontinuities must daylight in the slope face.
- The dip angle of the slope face (ψ_f) > the plunge angle of the intersection (ψ_i) > the friction angle of the two discontinuities plane (ϕ).



Figure 2.10: A wedge failure along two intersecting planes of discontinuities both of which daylight in the slope face in a limestone quarry (Adopted from <http://www.bgs.ac.uk/eqr/SlopeStability.htm>).

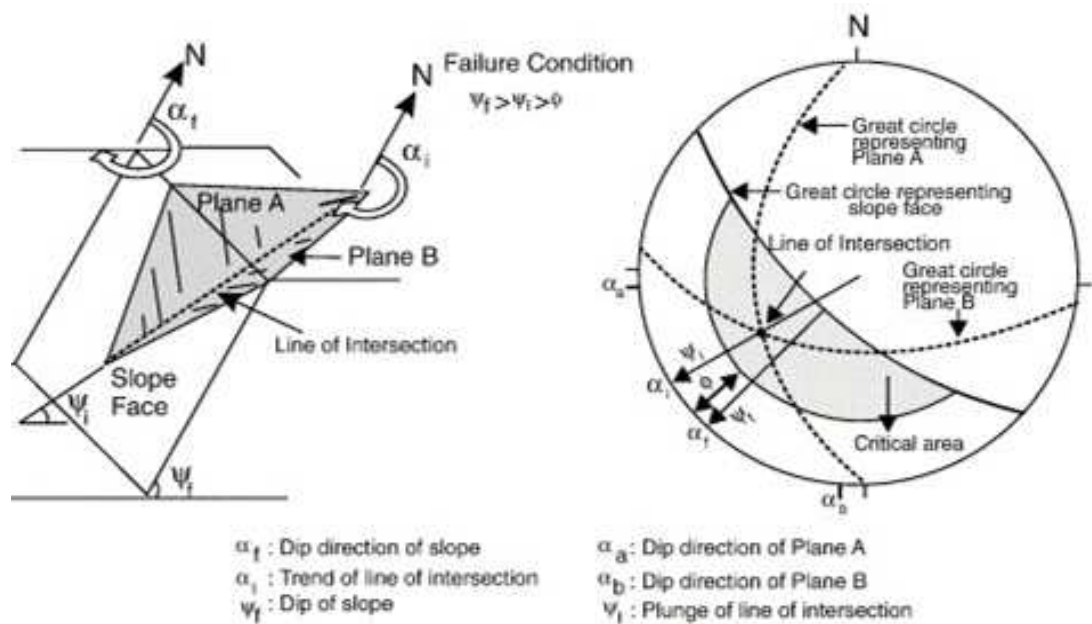


Figure 2.11: Kinematic analysis for wedge failure (Retrieved from Naghadehi et al., 2011).

2.5 STUDY AREA LOCATION

The study area of this research is a part of both of the central and the southeast parts of Missouri (Figure 2.12). Two sites were selected. Site 1 is located on 44 highway, north west edge of the City of Rolla City in Phelps County, Central MO (Figures 2.12 and 2.13); while site 2 is located on 72 highway, west of Fredericktown in Madison County, Southeast MO (Figures 2.12 and 2.14).

Site 1 is a sedimentary rock while site 2 is an igneous rock so the effectiveness of GPR in detection hidden subvertical joints in rock masses was tested in two different types of rocks. Site 1 is a sandstone rock cut which is a part of Roubidoux Sandstone Formation that is found in the Ozark region from Cabool to Gasconade City and from Salem to Doniphan in the State of Missouri. The area of exposure along the Roubidoux

Creek in Pulaski and Texas counties in Missouri are known as the “type area” for this formation (Thompson, 1991). The outcrop at this site is mainly composed of quartz-sandstone and lies between $37^{\circ} 56' 21''$ and $37^{\circ} 56' 26''$ N and $091^{\circ} 48' 23''$ and $091^{\circ} 48' 39''$ W (Figure 2.13).

Site 2 is an ignimbrite rock cut which is a part of St. Francois Mountains Volcanic Super-group which belongs to the Precambrian Era, 1.5 to 1.2 billion years old. This site is located between $37^{\circ} 33' 50''$ and $37^{\circ} 34' 20''$ N and $090^{\circ} 21' 20''$ and $090^{\circ} 22' 40''$ W (Figure 2.14). Each site was divided into stations on which the field work of this research was conducted and performed as illustrated in Figures 2.13 and 2.14.

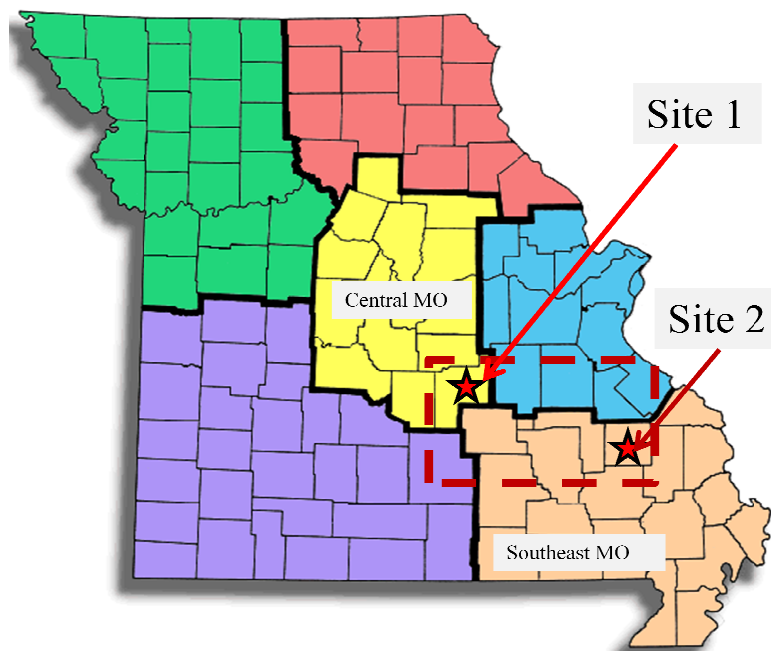


Figure 2.12: The study area (red-dashed line square) shows the locations of the two selected sites. Site 1 is in the central part of Missouri while site 2 is in the southeast part (Adopted from <http://eparc.missouri.edu/Data/RCIP/BUSECC/RE-Mo-map.htm>).

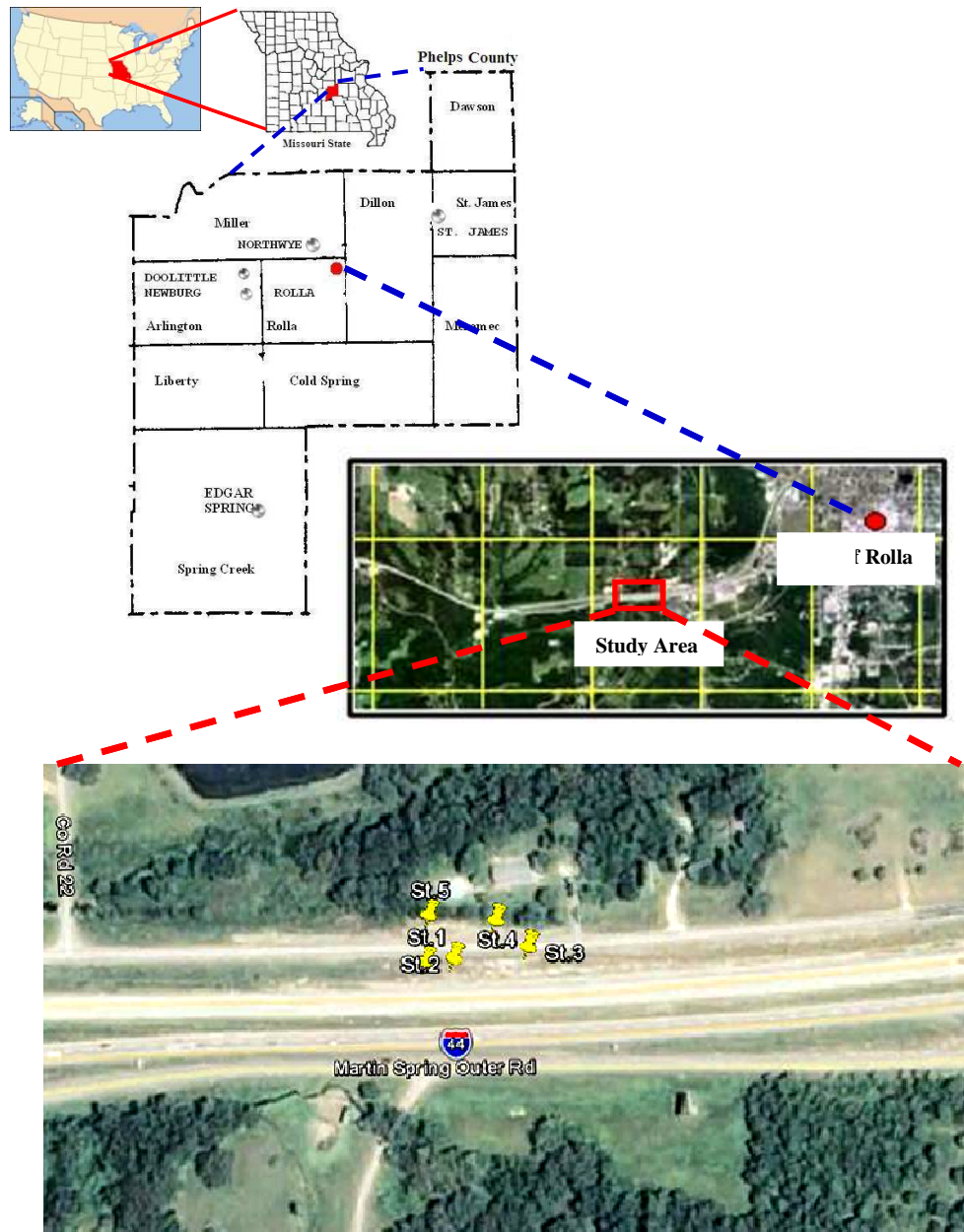


Figure 2.13: Location of site No.1 in Phelps County, MO. Site 1 was divided into five stations to conduct field work. Google Earth program was used to locate the stations of the study area (Adopted from <http://www.usgwarchives.org/maps/missouri/images/phleps.gif>; and http://en.wikipedia.org/wiki/Phelps_County,_Missouri).

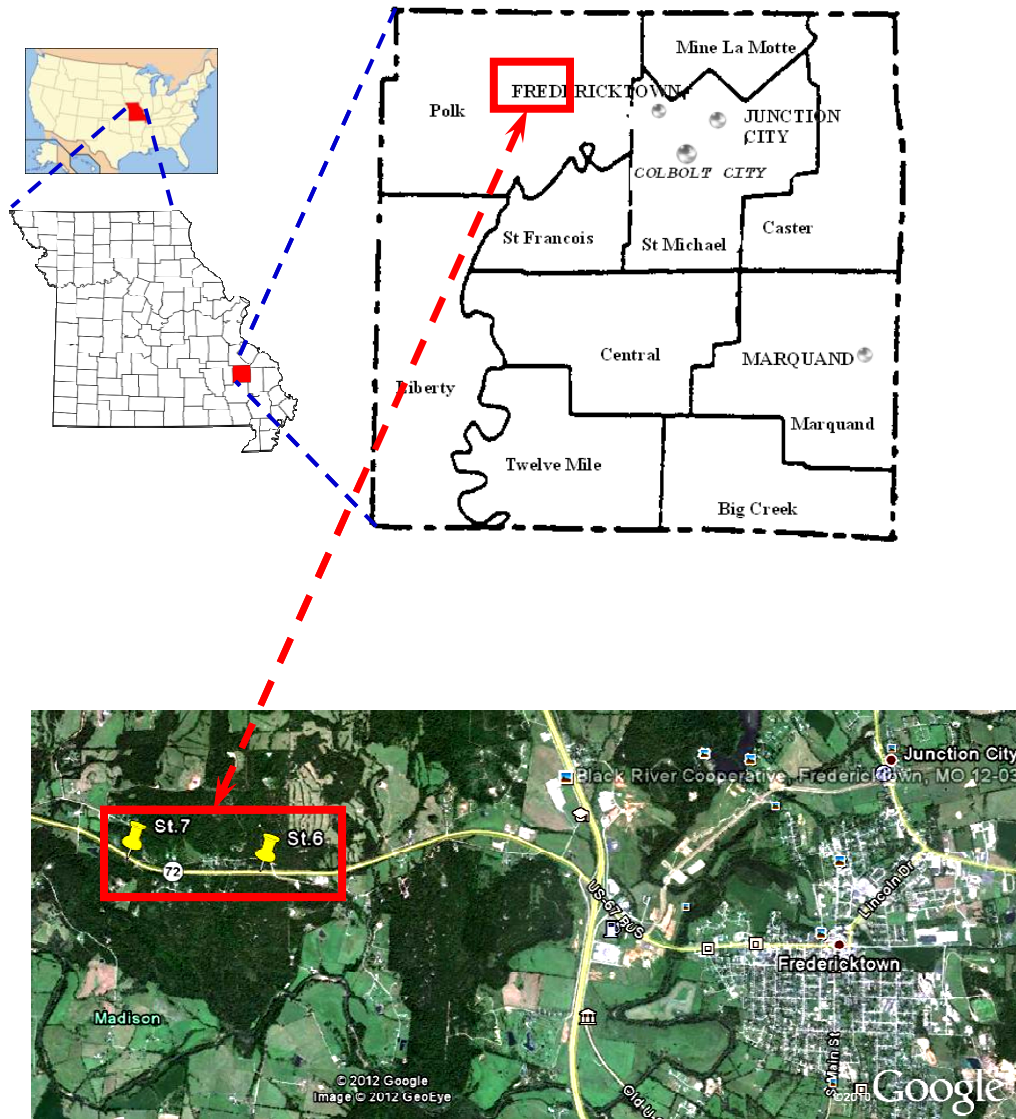


Figure 2.14: Location of site No.2 in Madison County, MO. Site 2 was divided into two stations to conduct field work. Google Earth program was used to locate the stations of the study area. (Adopted from <http://www.usgwarchives.org/maps/missouri/images/Madison.gif>; and http://en.wikipedia.org/wiki/File:Map_of_Missouri_highlighting_Madison_County.svg).

2.6 GEOLOGY OF THE STUDY AREA

Generally, site 1 is a sandstone outcrop of Roubidoux Formation whose age is Ordovician (Figure 2.15). Site 2 is an ignimbrite volcanic rock belongs to the St. Francois Mountains Volcanic Super-group whose age is Precambrian (Figure 2.16).

Roubidoux Formation consists of dolostone, sandy dolostone, sandstone, nodular and oolitic chert, and some shale. The dolostone is poorly exposed. Where observed, they are finely to coarsely crystalline, thin-to medium-bedded and are often inter-bedded with light-colored, nodular chert. Much of the chert is sandy, which distinguishes it from the chert of the Cotter Jefferson City dolomites, as well as from the most of chert in the Gasconade Dolomite. Even though infrequently exposed, well cuttings indicate this dolostone dominates the formation.

In Rolla Quadrangle area, two sandstone intervals often characterize the surface expression of the formation. A layer of sandstone, 15- to 20-feet thick, occurs at or near the base, and a thicker layer of sandstone, 20 to 25-feet-thick, occurs in the upper part of the formation. In the northeastern portion of the quadrangle, the subsurface Roubidoux contains two similar thick sandstone intervals as seen in water well residue logs.

The sandstone constituents are dominantly angular to sub-angular quartz. The sands contain diagnostic heavy minerals. The top of both the upper and lower sandstone intervals contain sand-sized and large fragments of tri-politic chert. Some of the dolostone layers are also sandy.

The Roubidoux weathers to a distinctive brick-red, sandy soil containing considerable chert. The residue in the lower part of the formation contains mud-cracked sandstones, often with well-preserved, chertified crack fillings, pebble molds in chert, and

“honeycombed” chert. Cryptozoal chert is associated with the dolostone between the two thicker sandstone intervals. The algal structures are about one-foot-wide, smaller than those in the Gasconade Dolomite. Stromatolitic structures appear to be present also, but are not clearly evident because of dolomitization. Mollusks and large gastropod, which is a marker in the Roubidoux to the south, have not been found here.

The thickness of the formation varies from about 100 feet in the west and southwest portion of the quadrangle to 140 feet in the central and south-central part of the quadrangle. Generally, the contact with the Gasconade is usually not exposed.

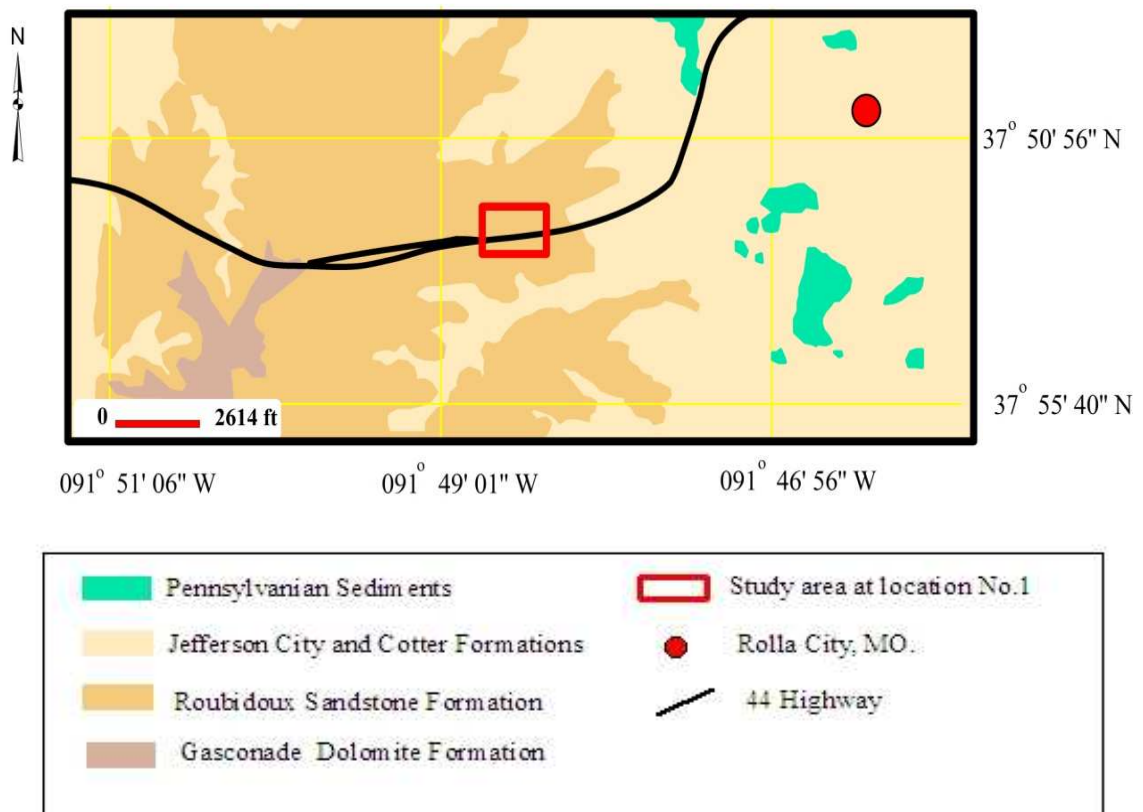


Figure 2.15: The geology of the study area at site 1.

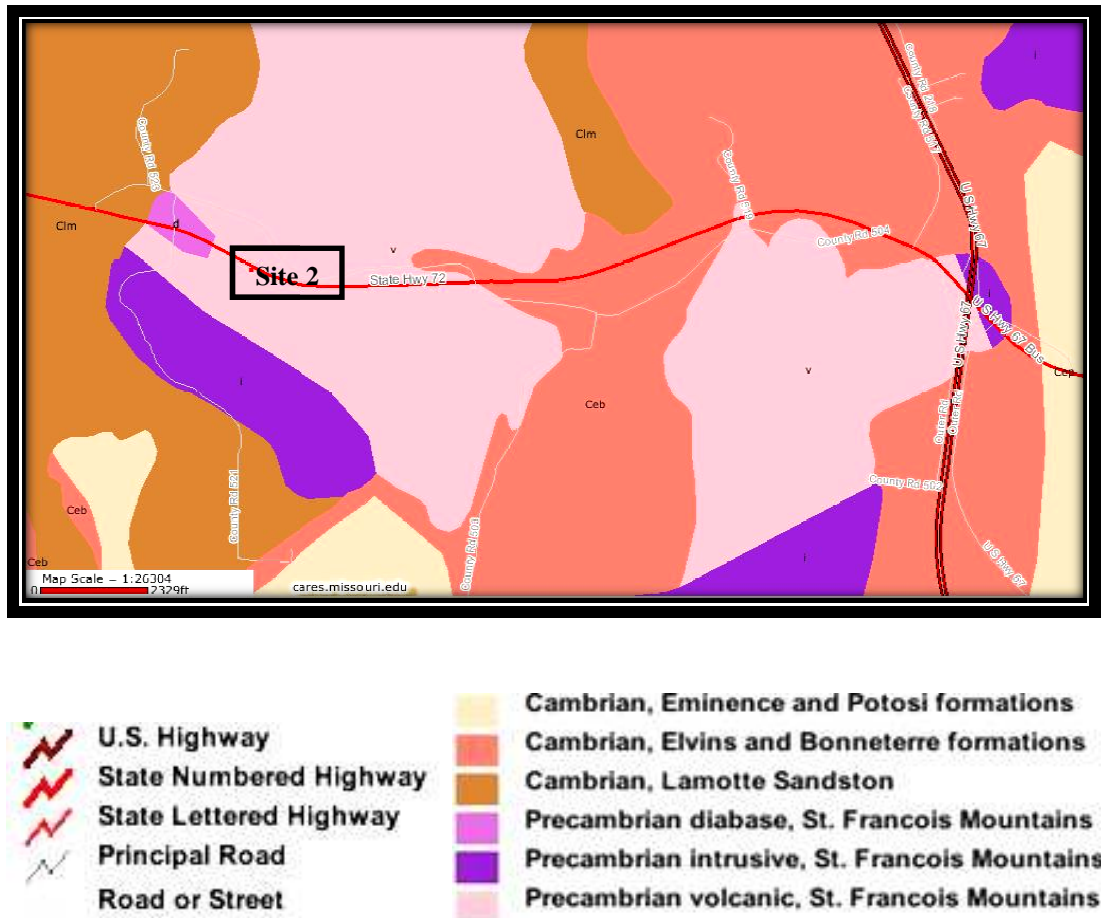


Figure 2.16: The geology of the study area at site 2.

Roubidoux Sandstone Formation overlies Gasconade Dolomite Formation with uneven contact surface of disconformity (Spreng and Proctor, 1993) and is overlaid by Cotter –Jefferson City Dolomite.

The Roubidoux Formation is separated from the Gasconade by its higher content of quartz sand, including numerous sandstone beds especially in the upper half, and generally thinner bedding. The quartz sand content also serves to distinguish the Roubidoux from the overlying Jefferson City Dolomite. Partly because of the increased

permeability due to the sandstones and partly due to the thin- to medium-bedded nature of its carbonate beds, the Roubidoux weathers back rapidly and the resulting slopes are characterized by loose blocks of sandstone.

Above those formations, sandstones and conglomeratic sandstones are draped over and are the most common rock exposures of Pennsylvanian Sediments (P). Thickest accumulations of these sediments occur in the eastern to northeastern part of the study area, where karst fills are steeply dipping.

The geology of site 2 is a part of the geology of the St. Francois Mountains of southeast Missouri (Figure 2.16). Approximately 1.4 billion years ago, southeast Missouri was a landscape dominated by volcanic calderas, some of which were up to 15 miles in diameter. Large calderas such as these generally erupt rhyolite and ignimbrite, a volcanic rock that is very high in silica, a compound comprised of the elements silicon and oxygen. The higher the silica content in magma, the more viscous, or thick, will be the lava. Viscous magmas tend to hold more volcanic gas and therefore erupt explosively. Rhyolite calderas produce the most violent eruptions of any type of volcano on earth (Department of Natural Resources-MO, 2008).

3. BACKGROUND AND THEORY OF GROUND PENETRATING RADAR (GPR)

3.1 OVERVIEW

Geophysical methods respond to the physical properties of the subsurface media and can be classified into two distinct types: i) passive methods which detect variations within the natural fields associated with the Earth, such as the gravitational and magnetic fields; and ii) active geophysical methods such as GPR method and seismic methods which means the earth's response to generated signals. The earth's responses (reflected, refracted, transmitted, and/or scattered signals) are measured using appropriate detectors whose output can be displayed and interpreted (Reynolds, 1997). The reflection method is most often used for geological structure applications (Kovin, 2010); and it is of most concern in this research work.

The term 'ground penetrating radar (GPR)', 'ground-probing radar', 'subsurface radar', 'surface-penetrating radar (SPR)', or 'georadar' refer to a range of electromagnetic techniques designed primarily to localize objects or interfaces or discontinuities buried beneath the ground surface or located within a visually opaque structure (Daniels, 2004).

GPR has become enormously popular and specifically within the engineering community since the mid of the 1980s; however, GPR has been used for geological investigations since the 1960s, especially in connection with the development of radar echo-sounding of polar ice sheets (Reynolds, 1997).

GPR is an active geophysical method for commonly non-destructive subsurface imaging and based on the propagation of electromagnetic waves in the subsurface

(Reynolds, 2003; Daniels, 2004; Conyers, 2004; Otto and Sass, 2006; and Sass, 2007). The first use of electromagnetic waves for locating remote buried objects is attributed to Hülsmeyer in a German patent in 1904; however, the first published paper of such investigation was by Leimbach and Löwy in 1910 (Reynolds, 1997).

GPR product, which is a radiogram image, is not only an image of the subsurface but is the recorded response of the subsurface materials to the propagation of electromagnetic (EM) energy in the microwaves range and across a relatively narrow range of radio waves with frequencies of, typically, 10 MHz and over 1.5 GHz (Takahashi, 2004; Booth et al., 2009; and Cassidy, 2009a). Therefore, the understanding for underground propagation of electromagnetic waves' mechanism and theory, whose history spans for more than two centuries, and how their interactions with subsurface materials is a crucial step in using and applying the GPR technique for subsurface investigation and discontinuities detection (Annan, 2001; and Cassidy, 2009a); thus a brief theoretical background about GPR is herein presented.

3.2 THEORY OF ELECTROMAGNETIC ENERGY

Electromagnetic field theory is a discipline concerned with the study of charges, at rest and motion, which produce currents and electric-magnetic fields which follow paths similar to sine curves, as illustrated in Figure 3.1, which shows the relationship between these fluctuating electric and magnetic fields, the wavelength (λ), the maximum amplitude (A_0), the intensity of the waves which is related to its amplitude squared, and the propagation direction of the electromagnetic waves (Balanis, 1989).

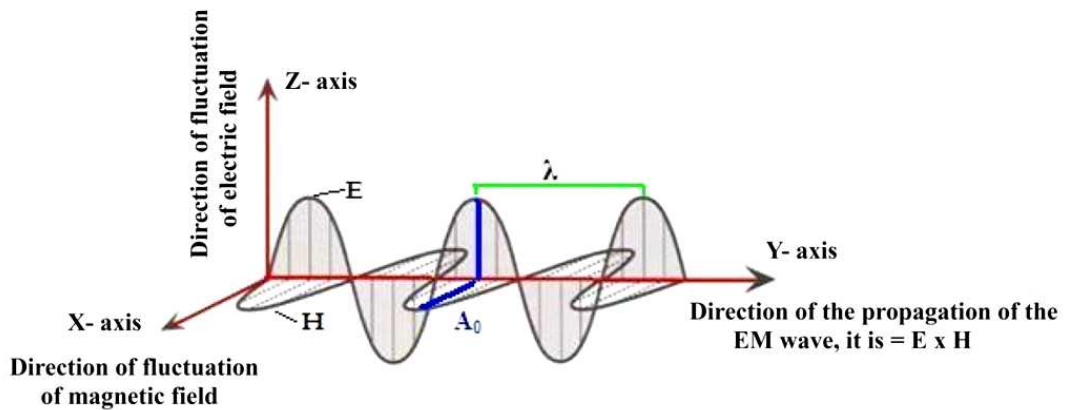


Figure 3.1: The main components of the electromagnetic fields (EM) and the direction of the propagation of the EM waves along only Y-axis for the electric field (E) and the magnetic field (H) (Adopted from Kovin, 2010).

Wavelength is defined as the distance between consecutive corresponding points of the same phase, such as crests, troughs, or zero crossings while the frequency (f) of electromagnetic waves can be defined as a number of cyclical waves per time unit. In other words, it is the number of waves that pass a given point per second. Therefore, the period is the reciprocal of frequency. The wavelength and frequency can be related to the speed of the EM waves on equations:

$$f = 1/t \quad (3.1)$$

$$c = \lambda f \quad (3.2)$$

f = frequency in hertz unit (Hz) which is 1/second (s)

t = time in second (s)

c = the speed of light (in vacuum, $299,792,458 \text{ ms}^{-1} \approx 0.3 \text{ m/ns}$)

λ = EM wavelength in meter unit (m)

The study of electromagnetic fields requires enough understanding for its both theoretical and applied concepts. The theoretical concepts are described by a set of basic laws formulated primarily through experiments conducted during the nineteenth century by many scientists such as Faraday, Gauss, Ampere, Coulomb, Volta, and Lenz. These theoretical concepts were then combined into a consistent set of vector equations by Maxwell and then are widely acclaimed Maxwell's Equations; while the applied concepts of electromagnetic are formulated by applying the theoretical concepts on the design and operation of practical systems (Balanis, 1989).

3.2.1 Maxwell's Equations. Electric and magnetic fields are generally vector quantities which have both magnitude and direction. The relations and variations of these fields are governed by Maxwell's equations (Balanis, 1989). These equations state the basic principles of radio waves propagation in a medium and describe the interaction between electric and magnetic fields and the relationship between the charge and current density (Griffiths, 1999). EM fields and relationships are expressed as follows (Annan, 2009; and Cassidy, 2009a):

Faraday's Law of Induction

$$\nabla \times E = - \frac{\partial B}{\partial t} \quad (3.3)$$

Maxwell's modified circuit Law

$$\nabla \times H = - \frac{\partial D}{\partial t} + J \quad (3.4)$$

Gauss' theorem in electrostatics

$$\nabla \cdot D = \rho \quad (3.5)$$

Gauss' theorem in magneto-statics

$$\nabla \cdot B = 0 \quad (3.6)$$

where

E – electric field intensity or strength vector (in volts per meter, V/m)

B – magnetic flux density vector (in Tesla, T, or Wb/m^2 or *Tesla*)

H – magnetic field intensity or density (in Amperes per meter, A/m)

J – electric current density vector (in Amperes per meter squared, A/m^2)

D – electric induction or electric flux density which is called sometimes the electric displacement (in coulombs per meter squared, C/m^2)

ρ – electric charge density (in coulombs per meter cubed, C/m^3)

∇ - del vector operator

\times - vector cross product

\cdot - Vector dot product

3.2.2 Constitutive Equations. Constitutive relationships are the means of describing a material's response to electric-magnetic fields (Annan, 2009). Four constitutive equations describe the response of materials to the applied electromagnetic field:

$$J = \sigma E \quad (3.7)$$

$$D = \epsilon E \quad (3.8)$$

$$B = \mu H \quad (3.9)$$

$$M = \chi H \quad (3.10)$$

where

σ - electrical conductivity of the material (in Siemens per meter, S/m)

ϵ - dielectric permittivity of the material (in Farads per meter, F/m)

μ -magnetic permeability of the material (in Henrys per meter, H/m)

χ - magnetic susceptibility

M - magnetization

Four quantities, namely electrical conductivity, dielectric permittivity, magnetic permeability and magnetic susceptibility describe the properties of a material; however, only the first three mentioned properties or relations, equations (3.7) – (3.9), are the most important for GPR applications (Annan, 2001; Annan, 2009; Cassidy, 2009a; and Kovic, 2010).

In general, Maxwell's EM field equations [Equations (3.3) – (3.6)] mathematically describe the physics of EM, while constitutive relations [Equations (3.7) – (3.10)] quantify material properties. Combining the two provides the foundations for quantitatively describing the spatially and temporally varying coupled electric and magnetic fields and their interdependence and thus GPR signals (Annan, 2009; Cassidy, 2009a; Kovic, 2010). These vector equations are valid for heterogeneous, isotropic, linear and stationary media (Balanis, 1989).

3.3 ELECTROMAGNETIC PROPERTIES OF EARTH MATERIALS

The subject of electromagnetic properties of materials is a wide-ranging topic. Comprehensive background can be found in Santamarina et al. (2001). In this context a nutshell and common related basic issues will be discussed. In most GPR applications, variations in dielectric permittivity (ϵ) and electrical conductivity (σ) are most important properties or factors while variations in magnetic permeability (μ) are seldom of concern

(Annan, 2009) since that in most circumstances, the magnetic effect of materials has little effect on the propagating of GPR waves and their magnetic permeability is often simplified to the free-space value of 1.26×10^{-6} H/m (Cassidy, 2009a). Accordingly, the value of relative magnetic permeability (μ_r) of non-magnetic earth materials, rocks, soils and many other materials, is 1 (Reynolds, 1997); where

$$\mu_r = \mu / \mu_0 \quad (3.11)$$

μ - absolute magnetic permeability of a material

μ_0 – the magnetic permeability of free space (air)

Earth subsurface materials are often described as dielectric materials. The term of ‘dielectric’ describes a class of non-conducting materials that can accommodate a propagating EM field; however in reality, all subsurface materials possess some form of free charges and thus show some degree of EM attenuation. In extreme cases, a material that contains a high degree of free charges is effectively considered a conductor where the majority of the EM energy will be lost in the conduction process as heat; therefore, GPR is ineffective in higher-conductivity environments such as saline environments and areas that have high clay contents (Cassidy, 2009a). Accordingly, the electromagnetic properties of earth materials are related to their chemical composition and water content both of which control and govern the speed and the degree of the attenuation of EM waves propagation in earth materials (Reynolds, 1997).

Each earth material has specific electrical properties. The most three electrical properties of an earth material are dielectric permittivity (ϵ), electrical conductivity (σ), and magnetic permeability (μ) which are generally not constant (Dezelic, 2004; and Annan, 2009). These electrical properties depend on the strength, direction, and

frequency of the EM fields in addition to the spatial homogeneity of the material. For GPR applications, the values of these properties are assumed independent of the parameters of existing fields (Annan, 2001).

Rocks, soils, and many other earth materials are non-magnetic but are electrically conductive and dielectric. Dielectric conductivity (σ) can be defined as the ability of a material to pass free electrical charges under the influence of an applied electric field. In contrast, dielectric permittivity (ϵ) can be described as the ability of a material to restrict the flow of free electrical charges under the influence of an applied electric field (Cassidy, 2009a). When the absolute of dielectric permittivity value (ϵ) compared to the dielectric permittivity value of the free space or air (ϵ_0), the relative dielectric permittivity (ϵ_r) or what is known in many published texts as a dielectric constant (k) is resulted.

$$\epsilon_r = k = \epsilon / \epsilon_0 \quad (3.12)$$

The dielectric permittivity of free space (or permittivity constant) is given as 8.8542×10^{-12} F/m and differs negligibly from the permittivity of air (Dezelic, 2004; and Cassidy, 2009a). Table 3.1 lists the relative dielectric permittivity (dielectric constant, k) of some common subsurface materials and their typical range under natural conditions.

The relative dielectric permittivity defines the index of refraction of the medium, and controls the speed of the electromagnetic waves in that medium. By means of using the relative dielectric permittivity value of an earthen material, the velocity of electromagnetic waves, GPR waves, can be calculated as follows:

$$V = c / (\epsilon_r)^{1/2} \quad (3.13)$$

where

V - the velocity of propagated electromagnetic waves in the material.

c – the speed of light.

ϵ_r - relative dielectric permittivity of the material (non-dimensional value).

Table 3.1: Typical values of relative dielectric permittivity for some common earth materials (Retrieved from Cassidy, 2009a).

Material	Relative dielectric permittivity (ϵ_r) or dielectric constant (k)
Air	1
Clay – dry	2 – 20
Clay – wet	15 – 40
Concrete – dry	4 -10
Concrete – wet	10 – 20
Freshwater	78 – 88
Freshwater ice	3
Seawater	81 – 88
Seawater ice	4 – 8
Permafrost	2 – 8
Granite – dry	5 – 8
Granite – fractured and wet	5 – 15
Limestone – dry	4 – 8
Limestone – wet	6 – 15
Sandstone – dry	4 – 7
Sandstone – wet	5 -15
Shale – saturated	6 – 9
Sand – dry	3 – 6
Sand – wet	10 – 30
Sand – coastal, dry	5 – 10
Soil – sandy, dry	4 – 6
Soil – sandy, wet	15 – 30
Soil – loamy, dry	4 – 6
Soil – loamy, wet	10 – 20
Soil – clayey, dry	4 – 6
Soil – clayey, wet	10 – 15
Soil – average	16

3.4 FUNDAMENTALS OF GPR TECHNOLOGY

GPR is typically used to investigate and detect subsurface targets or objects such as discontinuities whose electrical properties differ from those of surrounding environment. Parameters of either reflections from subsurface interfaces or transmitted electromagnetic waves are employed to study the dielectric properties of the subsurface features. Some physical properties of subsurface target(s) such as its nature and components (discontinuity, in-filled-discontinuity, buried metal, rock, soil, etc), electrical conductivity, magnetic permeability, and more specific relative dielectric permittivity in addition to the type and the frequency of the used antenna have to be taken into consideration for a better understanding GPR data.

3.4.1 GPR System Components. The SIR-GPR instrument, which was used in this work, consists of three basic components: a transmitter and a receiver which are combined as an antenna unit, and a control GPR system unit (Figures 3.2, 3.3, and 3.4).

The antennae unit is the most important element of GPR instruments (Koppenjan, 2009; and Kovin, 2010). It is basically used to emit and receive electrical energy to and from hidden targets such as discontinuities in the rock masses.

In general, two types of antennae are commonly used: monostatic antenna and bistatic antenna. A monostatic GPR antenna is a single dipole for emitting (transmitting) and receiving the EM signals, which means that the same antenna works as a transmitter and receiver at the same time. However in some other circumstances, GPR instruments that have both transmitting and receiving antennae housed or shielded within the same instrument and are normally considered monostatic because they are coincident and cannot be separated (Cardimona, 2002). This later type of monostatic was used in this

research. In contrast, a bistatic antenna is that one which employs separate dipoles for emitting and receiving EM signals, a separate transmitting antenna and a separate receiving antenna (Figure 3.3).

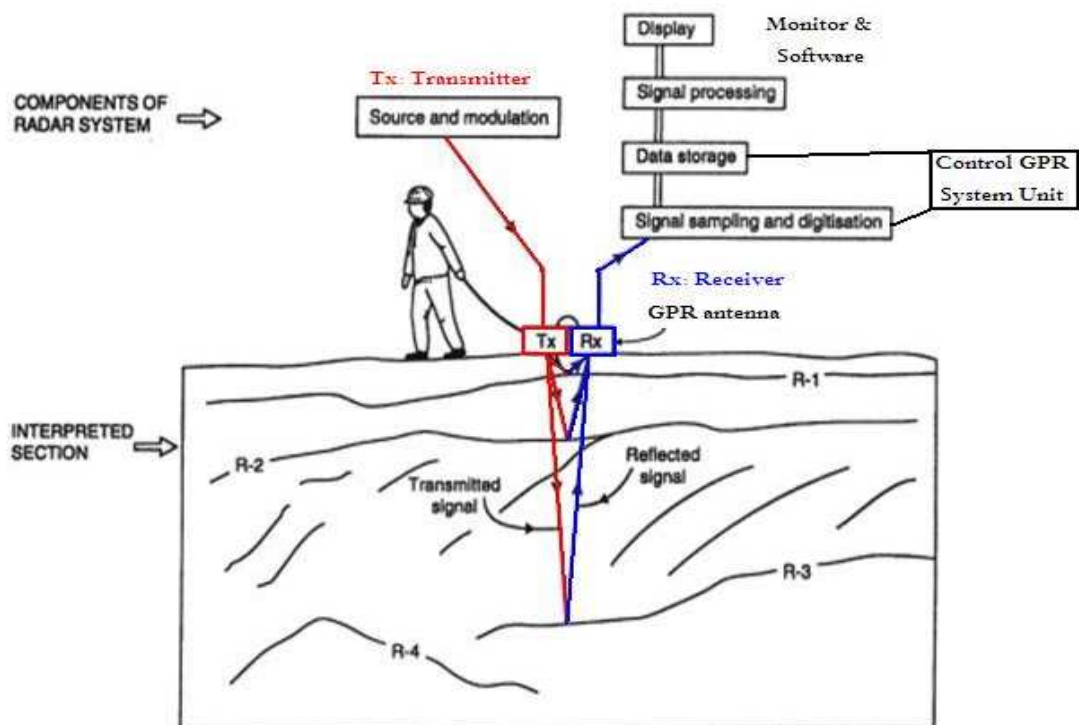


Figure 3.2: A simple diagram shows the basic components of GPR system (Adopted from Reynolds, 1997).

GPR antennae operate in megahertz (MHz) frequencies range (10 MHz – 2500 MHz). The resolution of the acquired GPR data and the penetration depth of GPR waves are mainly controlled by the frequency of the used antenna. Signals of high-frequency antenna produce high resolution data that reflects more details about the target but have a limited depth of penetration while, in contrast, low-frequency signals propagate deeper

but produce low resolution data (Beres and Haeni, 1991; Kovic and Anderson, 2005, 2006, and 2010; Otto and Sass, 2006).

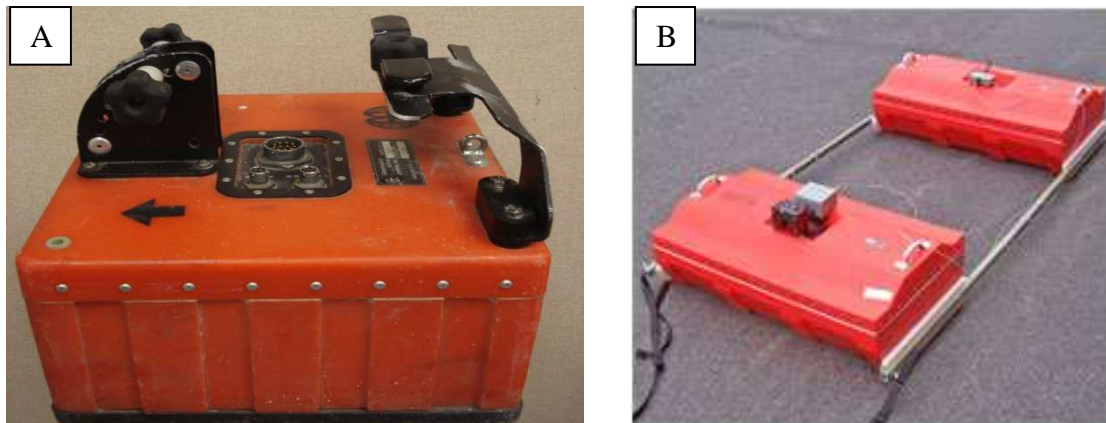


Figure 3.3: (A) Shielded 400 MHz monostatic GPR antenna, which was used in this research, and (B) a bistatic GPR antenna.

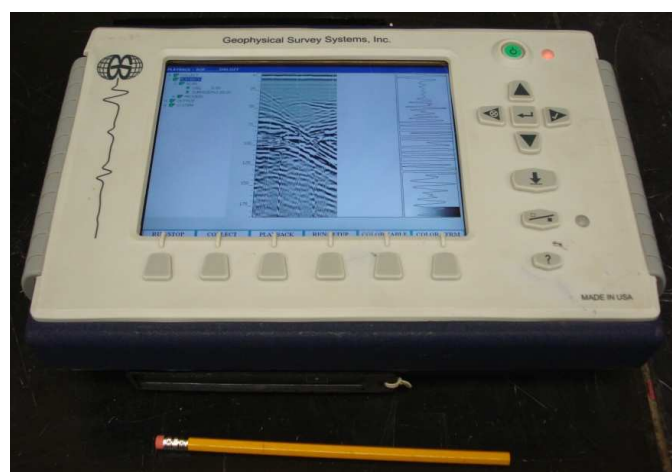


Figure 3.4: The GPR – GSSI control unit which was used in this research. This equipment is manufactured by Geophysical Survey Systems, Inc. (GSSI).

GPR survey methods use the reflection of short impulses of electromagnetic energy spanning a range of frequencies from about 50% below to 50% above some specified central frequency (Milson, 2003). Therefore, a typical 400 MHz antenna, which was used in this research, has a significant content of frequencies as low as 200 MHz and as high as 600 MHz. The characteristics of the antenna determine the center frequency of the EM wave and the associated bandwidth is determined by the pulse width. Accordingly, the antenna of 400 MHz has a center frequency 400 MHz and bandwidth equals approximately to the impulse GPR center frequency (Milson, 2003; and Koppenjan, 2009).

The control unit of the GPR system controls all the parameters of radiated signals, timing, amplifier and filter setting, and digitization rate (Kovin, 2010). In this unit as shown in Figure 3.4, the electrical energy is converted into electromagnetic energy which is, then, transmitted through the antenna to the subsurface or into the rock slope wall. Any subsurface interface, e.g. discontinuities, will cause some of this transmitted EM energy to be reflected back to the control GPR system unit where this reflected EM energy will be converted again to an electric energy that will be displayed in the monitor unit (Lang, 1996). With an aid of professional software such as RADAN software, a computer can be used later on for GPR data visualization, data storage, editing, processing, and printing hardcopies.

3.4.2 Principals of GPR Operating. Dezelic (2004) summarized the basic principles of GPR operating to four main points as follows:

- i. GPR waves pass through the earth materials.
- ii. Each material has specific electrical properties.

- iii. EM energy propagates away from the GPR source along an expanding wavefront.
- iv. Variation in electrical properties of subsurface materials causes GPR wave reflection.

When GPR operates in time domain, it means transmitting a time-pulse of EM energy that propagates into the ground subsurface. The propagation of EM is described as an expanding spherical wavefront propagating away from the source. The wavefront is defined as a surface of constant phases of transient signal at certain time after excitation while the ray along which the EM waves travels is defined as a conceptual perpendicular line to the wavefront and along. Therefore, the EM wave-field can be generally described as an infinite number of travelling rays in all directions as illustrated in Figure 3.5 (Anderson, 2010).

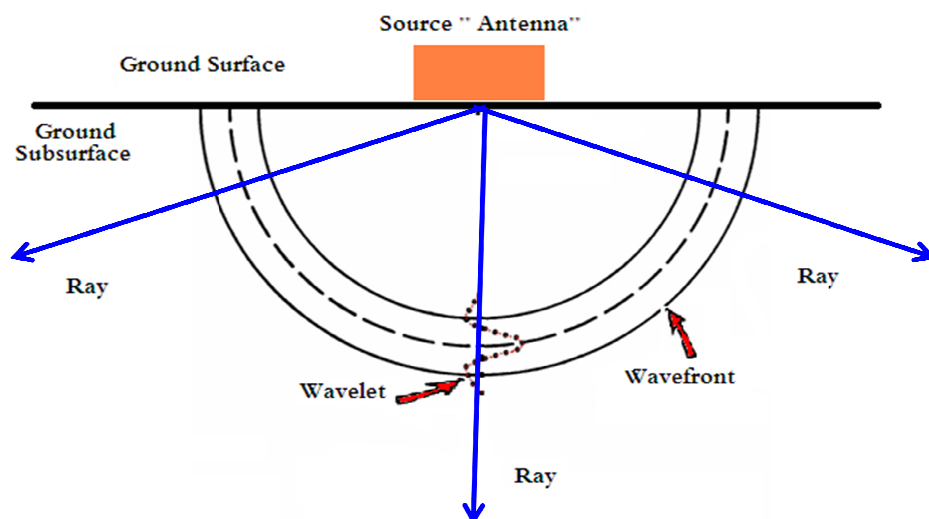


Figure 3.5: The concept of electromagnetic energy propagation as a wavefront related to the EM rays from a local source or GPR antenna (Adopted from Anderson, 2010).

In homogeneous medium, wavefront surfaces are symmetrical relatively to the point source position. In contrast, in a heterogeneous medium, the wavefront surfaces become asymmetric relatively to spatial changes in velocity of EM waves propagation (Kovin, 2010).

When EM wave encounters a boundary or interface such as a discontinuity plane or void, across which there is an abrupt change in dielectric constant between two different media or materials, the electromagnetic energy is partially reflected from and transmitted through bounded media, and thus, Snell's Law can be applied as illustrated in Figure 3.6.

Snell's Law of reflection states that:

$$\sin \theta_i = \sin \theta_r \quad (3.14)$$

where

θ_i - angle of EM ray incidence

θ_r – angle of EM ray reflection

In terms of EM velocity as illustrated in Figure, the Snell's Law can be written as:

$$\sin \theta_i / V_1 = \sin \theta_t / V_2 \quad (3.15)$$

where

V_1 – the velocity of EM in medium 1

V_2 – the velocity of EM in medium 2

θ_t – angle of EM ray's angle of refraction or transmission (Kleyn, 1983; and Anderson, 2010)

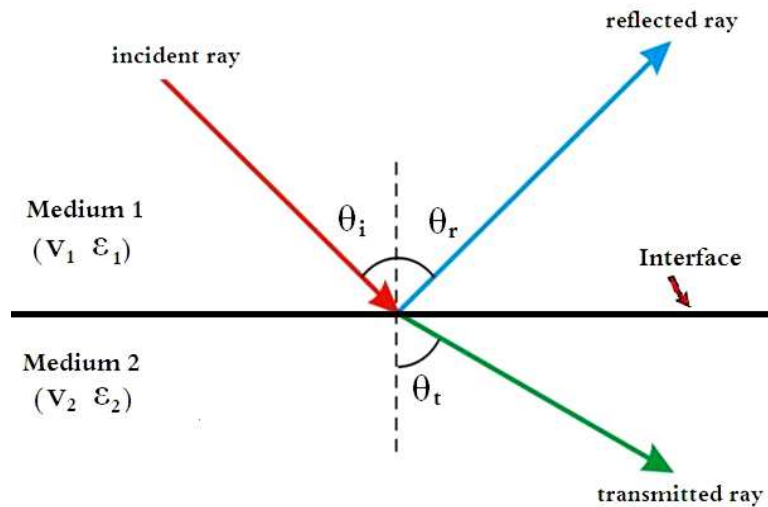


Figure 3.6: The reflection and refraction or transmission of electromagnetic waves at a planar interface of two different materials.

For calculation purposes, it is normally to be assumed that the GPR pulses are vertically or perpendicularly incident in order to do migration process and to compute the true depths to targets as will be explained later in this chapter. This assumption is strongly applicable for monostatic GPR radar especially for that type which has a single dipole for emitting and receiving EM pulses Figure 3.7. The amplitude of the reflected GPR waves from subsurface targets is mainly influenced by the degree of contrasts in dielectric constant, electrical conductivity, and magnetic permeability (Gregoire, 2001). The amount of the EM energy reflected from an interface between two subsurface different media increases as the difference or the contrast between the values of dielectric permittivity of those two media increases (Conyers, 1997). The reflected EM rays are recorded on the GPR antenna receiver and plotted as a trace in a function of time which is associated with the depth and survey position (Dezelic, 2004).

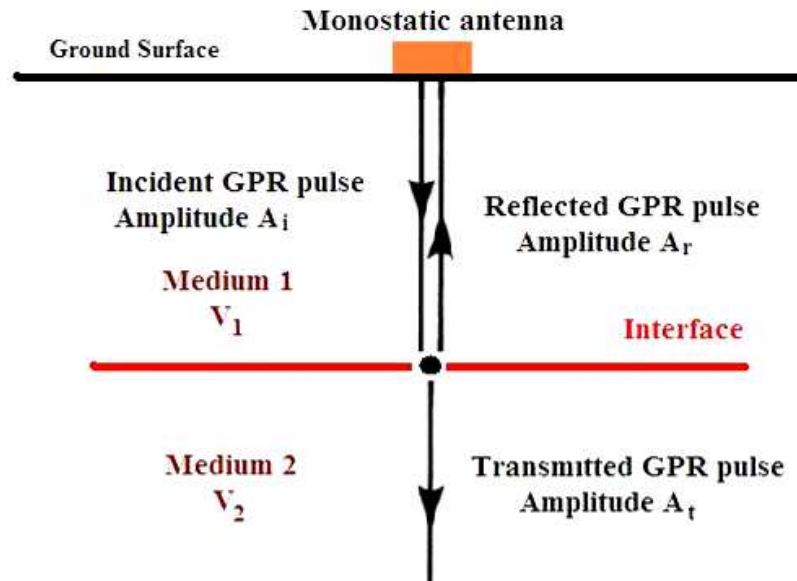


Figure 3.7: Normal incident, reflected, and transmitted GPR pulse related to their amplitudes through two different subsurface media using monostatic antenna.

Consequently for normal GPR pulses incidents and particularly for monostatic GPR antennae pulses, the reflection strength R of the interface of two different media can be calculated as follows (Pernito, 2008):

$$R = \frac{\sqrt{\epsilon_1} - \sqrt{\epsilon_2}}{\sqrt{\epsilon_1} + \sqrt{\epsilon_2}} \quad (3.16)$$

Where

ϵ_1 – the dielectric permittivity of medium 1

ϵ_2 – the dielectric permittivity of medium 2

It is necessary to operate the GPR effectively; therefore, the following requirements should be successfully met:

- i. Efficient coupling of EM energy into the ground.

- ii. Adequate penetrating for the EM radiation through the subsurface ground having regarded to target depth, in other words an adequate depth and spatial resolution of the target.
- iii. Obtaining a sufficiently large reflected or scattered signal from dielectric discontinuities or other targets for detection at or above the ground surface.
- iv. Having an adequate bandwidth in regard going the desired resolution and noise level (Daniels, 2004).

Researches and experiments have shown that for most earth materials within 100 m depth or less, the attenuation of EM waves rises with increasing frequency and that at a given frequency wet materials exhibit a higher loss, more attenuation, than dry ones (Daniels, 2004).

3.4.3 Estimation of Target Depth. GPR is a time-scaled system that functions by transmitting electromagnetic energy as waves through subsurface material (Sucre et al., 2011). Once the EM energy contact an interface plane such discontinuity plane whose electrical properties differ from those electrical properties of surrounding subsurface earth materials, a portion of this energy is reflected back to the GPR system at the ground surface.

To convert the amount of time for the GPR signals which travel through the subsurface material until reaching the discontinuity plane and return back to GPR system on the surface into a depth scale, calculating the velocity of GPR signals is essentially required (Anderson, 2010; and Sucre et al., 2011).

Several methods are available to determine the velocity of GPR signals, and then to estimate target depth. These methods usually include use of calibration over a target of

known depth, measurement of dielectric permittivity in laboratory, and common mid-point calibration (Goodman et al., 2009; Sucre et al., 2011). However, the first method, which was used in this research and will be explained further in Ch.5, is considered to be the most direct and accurate method to estimate the velocity of GPR pulses (Conyers and Goodman, 1997; Conyers, 2004; and Sucre et al., 2011).

Generally as shown in Figure 3.8, the method of calibration over a target of known depth involves measuring the two-way travel time (2WTT) to a known depth of a discontinuity plane reflector which appears on GPR data record, and then calculating the velocity of GPR signals by using the equation no.:

$$V = 2d/t \quad (3.17) \text{ (Morey, 1974)}$$

Then, depth to any discontinuity within that material is can be estimated where $d = (V * t)/2$, or when the relative dielectric permittivity is known, the depth will be:

$$d = (0.15 * t) / (\epsilon)^{1/2} \quad (3.18)$$

where

d = True perpendicular depth vector which is measured horizontally in the direction of Y-axis from any specific point located on the plane of the rock slope face to the plane of the detected hidden subvertical joint. This perpendicular depth vector also is measured vertically when it is related to the ground surface or any other horizontal plane that parallels to the ground surface. This depth is common known in geophysical and GPR references as the vertical depth regardless if the GPR survey is carried out on the ground surface, a wall of building, a cliff, or on a rock slope face.

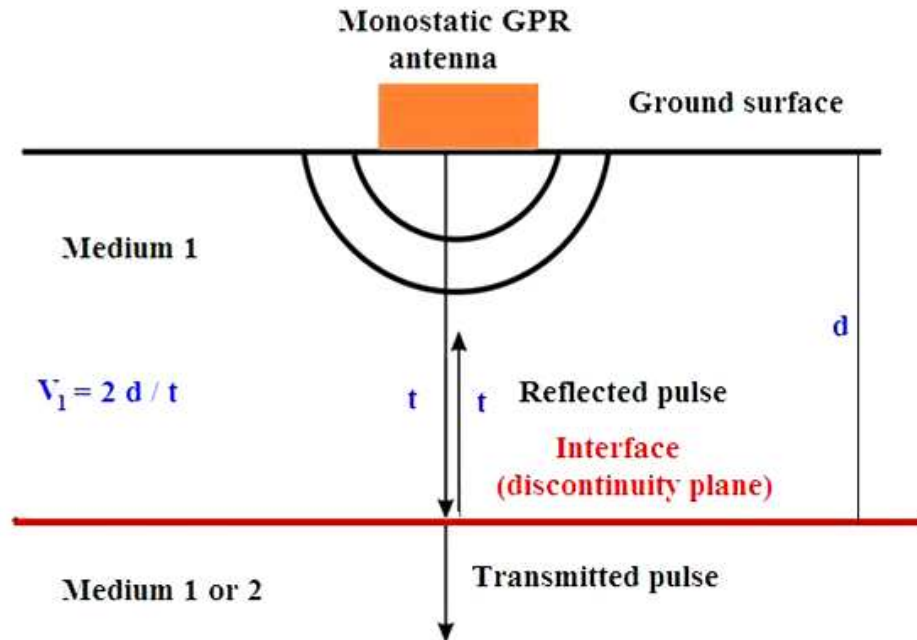


Figure 3.8: The concept of estimation the GPR velocity and then target depth based on the two way travel time of GPR pulses through a subsurface medium to known depth discontinuity plane.

3.5 GPR PULSE RESOLUTION

The trade-off between resolution of GPR pulses and depth of penetration is one of the principal problems of utilizing GPR system since the higher resolution which is accompanied by high EM frequency is the lower depth of penetration for EM waves. On other word, resolution is lower for lower frequency GPR pulses or antennae.

Two main types of resolution are known: vertical (radial, depth, longitudinal, or range) resolution and horizontal (lateral, angular, or sideways displacement) resolution as illustrated in Figure 3.9 (Annan, 2009).

3.5.1 Vertical GPR Resolution. Vertical resolution (R_v) is defined as the minimum distance between two reflectors to be distinguished on the GPR record; so it defines the minimal separation between the two reflectors oriented perpendicular to the direction of wave propagation (Annan, 2001; and Kavin, 2010). Simplistically, vertical resolution is a function of frequency and so it depends on the frequency and propagation velocity of GPR waves (Otto and Sass, 2006; and Sass, 2007).

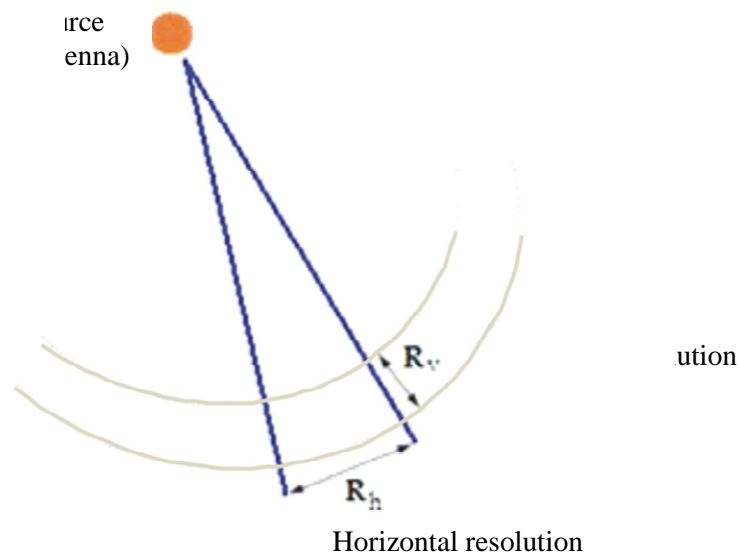


Figure 3.9: Vertical and horizontal GPR resolution (Adopted from Anna, 2011).

Each GPR antenna is designed to operate over a range of frequencies (bandwidth) where the peak power occurs at the center frequency of the antenna (Reynolds, 1997). Hence, a 400 MHz antenna has a center of frequency of 400 MHz, and accordingly, it has a pulse period of $1/(400 \text{ MHz})$ which equals 2.5 ns (nanosecond) where $1 \text{ Hz} = 1/\text{s}$. The

equivalent length (in meters) of the pulse is the product of the pulse period and the velocity of the EM waves for the appropriate material (Reynolds, 2003).

For instance, if a 400 MHz GPR antenna is used for an earth material (dry sandstone) through which GPR pulses velocity is 0.106 m/ns, the 400 MHz antenna has pulse period equals 2.5 ns and thus the pulse wave length is the product of 0.106 m/ns \times 2.5 ns which is 0.265 m which is for site 1. However, for site 2 where the measured GPR velocity (V) is 0.074 m/ns, the pulse wave length of the utilized 400 MHz antenna is 0.185 m.

The minimum vertical resolution and thus minimum resolvable thickness of a layer is theoretically considered as one-quarter (1/4) of the wavelength (λ) (Reynolds, 1997; and Annan, 2001; Otto and Sass, 2006).

$$R_v = \lambda/4 \quad (3.19)$$

As a result, the minimum resolved aperture of any detected hidden joint in site 1 is about 6 cm while it is about 4 cm in site 2.

3.5.2 Horizontal GPR Resolution. As shown in Figure 3.10, when GPR waves propagate, they expand to form a cone shape which called “footprint” or “Fresnel Zone” whose radius defines the horizontal resolution (R_h) (Dezelic, 2003). The farther the target from the GPR source, the larger both of the wave-field (footprint) and the first Fresnel zone, the lower will be the horizontal resolution in discriminating between adjacent targets (Cardimona, 2002; and Reynolds, 1997). The first Fresnel Zone describes the minimum area in which target (an aperture of discontinuity) with smaller dimensions will not be imaged (Reynolds, 1997). Consequently, if the distance between two targets is

less than the size of first Fresnel Zone, these two targets will not be distinguishable horizontally (Kovin, 2010).

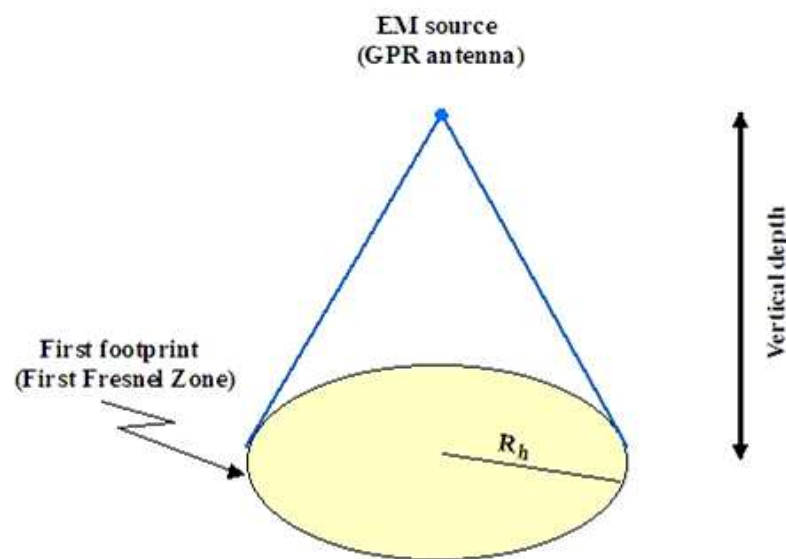


Figure 3.10: The GPR horizontal resolution in terms of Fresnel Zone. The target cross-sectional area is equivalent to the area of the first Fresnel Zone (Adopted from Reynolds, 1997; and Dezelic, 2004).

3.6 GPR DATA ACQUISITION MODES (GPR FIELD SURVEY MTHODS)

Generally for data acquisition, there are two types of GPR systems which are used impulse GPR and continuous-wave (CW) GPR. The main difference between the two types of GPR systems is the way that each one of them operates and acquires data. Impulse GPR system, which was used in this research, acquires data in the time domain where a shot pulse of energy is transmitted and the reflected waves are received as a function of time and indicate the energy scattered from subsurface objects.

The continuous-wave GPR system acquires data in the frequency domain and transmits continuously (transmitter always on) which involves transmitting of continuous signal over a fixed bandwidth. The reflected energy is recorded as a function of frequency and indicates the energy scattered from subsurface (Koppenjan, 2009).

In terms of GPR field survey methods (GPR survey profiling modes), there are four common methods of deployment of GPR systems are used in field (Sheriff and Geldart, 1995; and Reynolds, 2003):

- i. Continuous common offset profiling (GPR reflection Profiling);
- ii. Wide-angle reflection and refraction (WARR) profiling (Common source profiling);
- iii. Common midpoint profiling (CMP); and
- iv. Trans-illumination profiling (GPR tomography profiling).

Each of these survey profiling has particular GPR instruments and specific methodology of data processing and interpretation for certain buried targets and environmental settings. Herein is a brief description for each one of those different GPR field survey methods.

3.6.1 Continuous Common Offset Profiling (GPR Reflection Profiling). This method is the most often used in the practice of GPR survey because it provides for the acquisition of a very small horizontal sampling with good resolution, but with a very large data collection, in relatively short time and requires minimum personnel effort (Cardimona, 2002; and Kovic, 2010). In this method, the GPR data are acquired by moving continuously a monostatic antenna or by moving continuously and simultaneously the transmitter and the receiver of the bistatic antenna. The transmitter

and the receiver in bistatic antennae are kept a fixed distance apart so the antennae separation is held constant for common offset profiling, fixed offset, along a GPR survey line over the ground surface as illustrated in Figures 3.10 and 3.11 (Cardimona , 2002; Reynolds, 1997; and Kovin, 2010). This method of surveying is analogous to continuous seismic reflection methods (Beres and Haeni, 1991; and Reynolds, 1997).

Interpretation of the data of this method requires providing GPR waves velocity information from other sources such as WARR method or CMP method, or it can be retrieved from the analysis of diffraction hyperbolas if available (Reynolds, 1997; and Kovin, 2010). The continuous common offset configurations for both monostatic and bistatic GPR antennae types are shown in Figures 3.11 and 3.12 respectively.

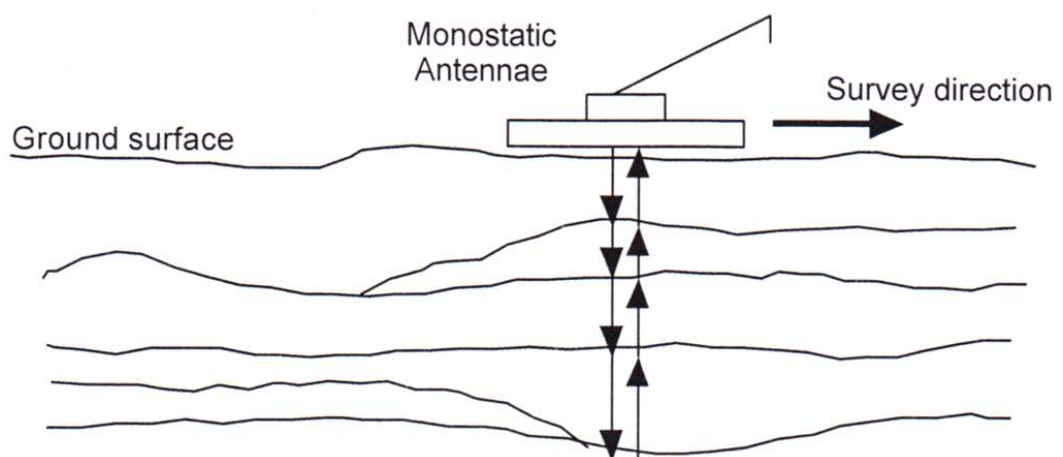


Figure 3.11: A shielded monostatic GPR antenna is towed along a survey line on a study area of interest, and the data is interpreted to be normal incidence reflection signals (Adopted from Cardimona, 2002).

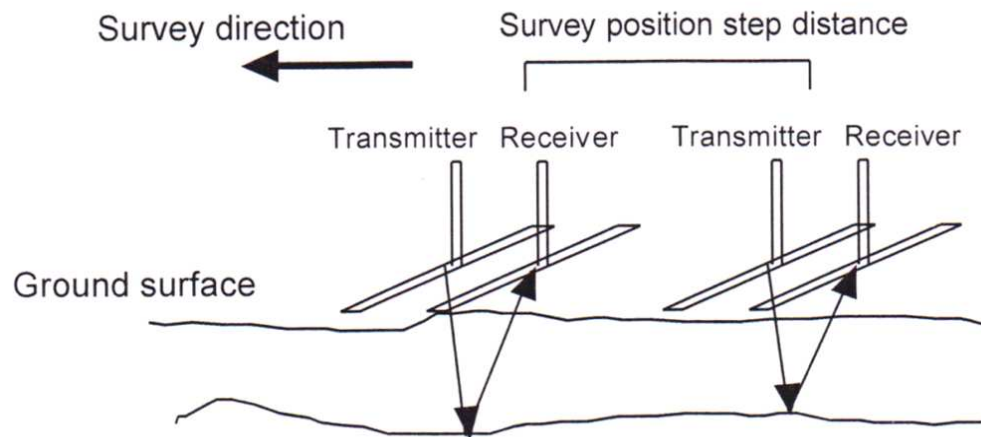


Figure 3.12: A bistatic GPR antenna which consists of two separate transmitter and receiver antennae. The two antennae placed at fixed offset distance along survey line on the study area of interest, and the data is interpreted to be near-normal incidence reflection signals (Adopted from Cardimona, 2002).

3.6.2 Wide-Angle Reflection and Refraction (WARR) Profiling (Common Source Profiling). Only bistatic GPR antennae can be used in this method where the transmitter antenna is kept at a fixed location or position while the receiver antenna is towed away at uniform increasing offsets.

Figure 3.13 illustrates how this method is conducted and why is called wide-angle refraction and refraction survey profiling where the reflection angle of EM waves from any specific subsurface interfaces will increase as long as the receiver antenna is towed away from the transmitter antenna. This method of GPR surveying is generally used to determine the velocity and is also known as a step mode data collecting because each GPR data trace is recorded after stopping at each observation station.

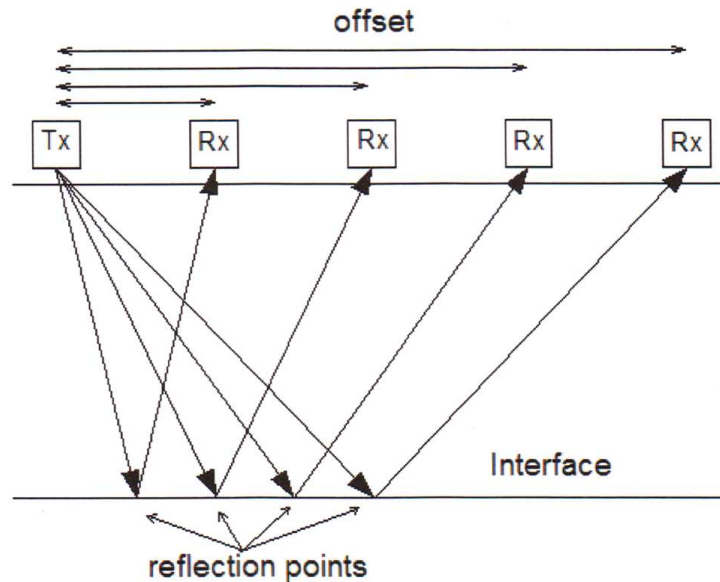


Figure 3.13: WARR method or common source survey profiling method using only bistatic GPR antenna where the transmitter antenna (Tx) is fixed while the receiver antenna (Rx) is towed away so the offset distance increases (Adopted from Kavin, 2010).

The location of a WARR survey line should to be over an area where the principal reflectors are planar and either horizontal or dipping only at very small angles. It also requires assuming that the properties of the subsurface materials are uniform and that the reflector characteristics are the same along the GPR survey line. However, this assumption may not be true in all cases of investigations which may produce erroneous results. Accordingly, to avoid making such assumption and results, the common midpoint profiling (CMP), which will be explained next, is a good alternative and preferable deployment for the same analysis (Reynolds, 1997).

3.6.3 Common Midpoint Profiling (CMP). In this method of GPR surveying (Figure 3.14), a bistatic GPR antenna is most often used in which both the transmitter and receiver antennae are progressively moved away from each other, collecting data at each new offset distant but the midpoint between the two antennae stays at a fixed location, and thus, a real consistency at depth is not a requirement. This method is also related to step mode as WARR mode but more accurate and preferred to use (Cardimona, 2002; Reynolds, 2003, and Kovin, 2010).

The resultant GPR data (radiogram image) can be used to determine the electromagnetic waves velocity. The change in travel time (move-out of antennae) as a function of increasing offset between the transmitter and the receiver antennae is directly related to the electromagnetic waves velocity of the subsurface (Cardimona, 2002). In some cases, the CMP method can be used to get continuous velocity or high resolution data about the subsurface but will be time consuming (Kovin , 2010).

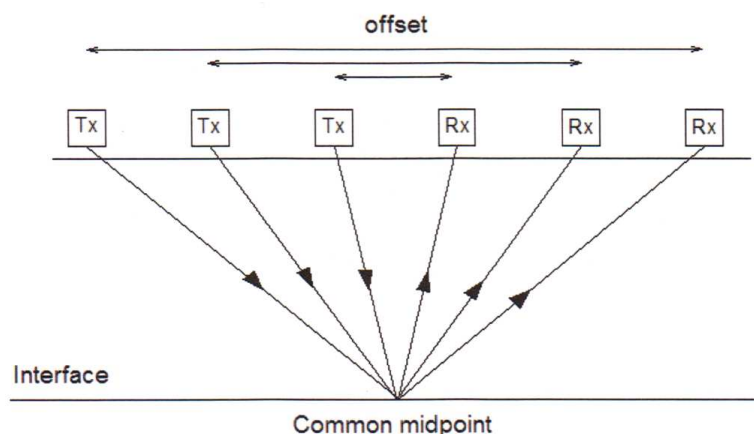


Figure 3.14: Common Midpoint GPR survey method using a bistatic antenna. The transmitter (Tx) and the receiver antennae are moved away to keep the same position of reflection point (Adopted from Kovin, 2010).

It is obvious that this method of GPR survey profiling cannot be done using a monostatic GPR antenna. However, pulling a monostatic antenna over a known subsurface target can estimate GPR waves velocity either by simple calculation using equation 3.17 ($V = 2d/t$) or by measuring the move-out of a diffracted arrival from the target which, in fact, yields a monostatic mode of a common midpoint profiling as depicted in Figure 3.15 (Cardimona, 2002).

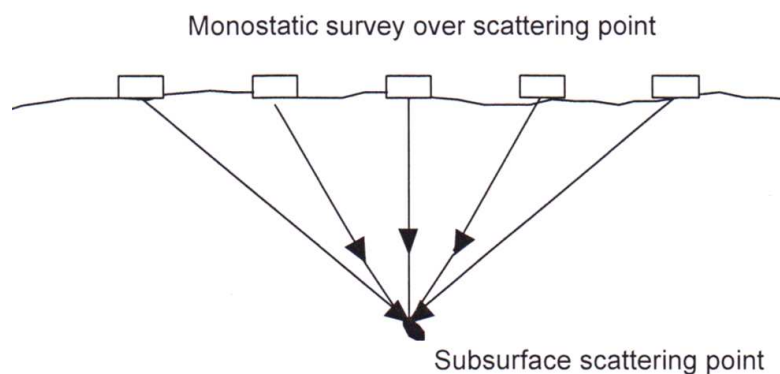


Figure 3.15: Common midpoint GPR profiling using a monostatic antenna over a point in-homogeneity in subsurface (Adopted from Cardimona, 2002).

3.6.4 Trans-illumination Profiling (GPR Tomography Profiling). This method is commonly used when the access to the target is limited and/or the depth of the GPR signals penetration is not enough to depict and image that target, i.e. in underground mines. In this method, the transmitter and receiver are on opposite sides of the medium under investigation (Reynolds, 1997). For instance, the GPR antennae can be placed in two separated boreholes, and the GPR signals are then propagated from the transmitter

through the underground medium to the receiver. Both transmitted and scattered electromagnetic waves are recorded, analyzed, and then interpreted (Figure 3.16).

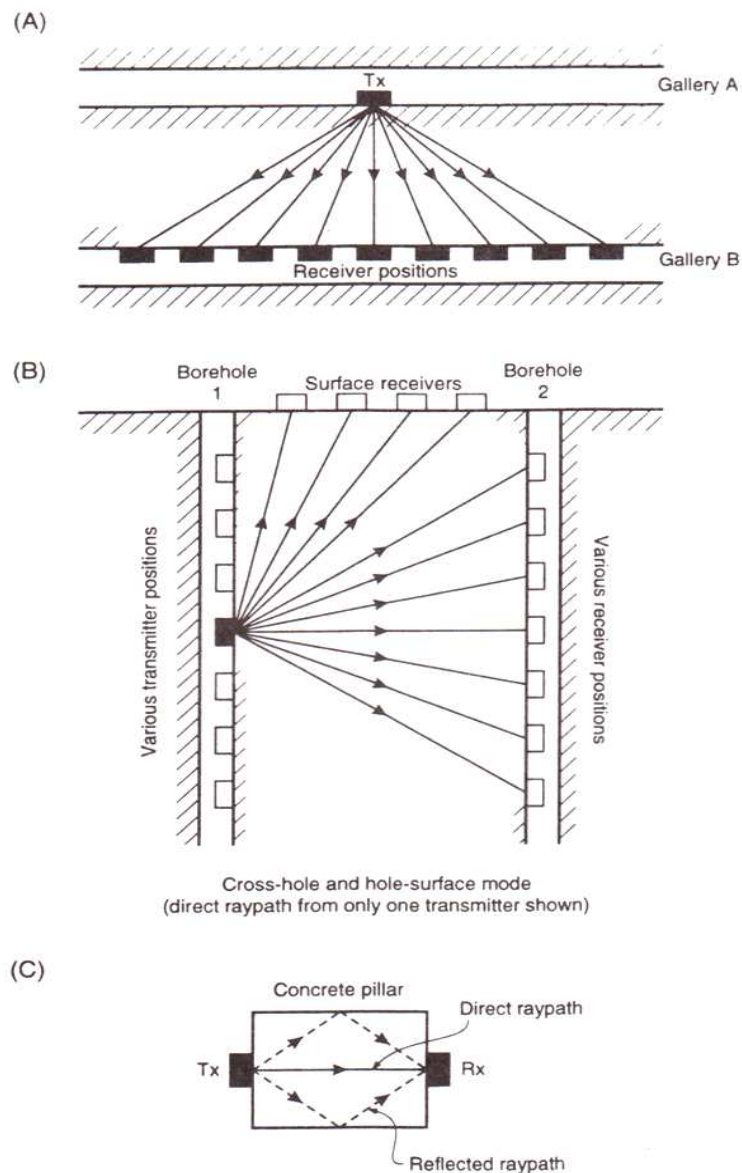


Figure 3.16: Trans-illumination and cross-hole GPR method of data acquisition: (A) between galleries in a mine, (B) between boreholes or hole-surface, and (C) through a concrete pillar. In all cases the distance between the transmitter and receiver is known (Adopted from Reynolds, 1997 & 2003).

Despite using boreholes; this method is still considered a non-destructive geophysical method particularly when high frequencies antennae whose sizes are small (e.g. 900 MHz or 1500 MHz antennae) are used (Reynolds, 1997).

Basically, both monostatic and bistatic antennae can be used in either discrete acquisition mode (impulse GPR system) or in continuous acquisition mode (Continuous waves GPR system); however, in terms of data quality and time matter, monostatic antenna is more capable and effective in a continuous survey mode; while, in contrast, bistatic antenna is more capable and effective in a discrete acquisition mode (Reynolds, 1997; and Cardimona, 2002).

3.7 GPR DATA PROCESSING, ANALYSIS, AND INTERPRETATION

GPR data are recorded digitally and need extensive processing which can be done either in the field or the office. There are many different GPR processing and analysis techniques (Cassidy, 2009a).

However, the core point is how much the quality of acquired GPR data is well since if the collected data are poor of quality to start with, no amount of data processing will rescue it – hence the adage “rubbish in, rubbish out”. In general, it is strongly recommended to start with the simplest processing options first and stop when there is nothing else to gain from the process phase (Cassidy, 2009a).

GPR system is often described in terms of processes involving amplification (gains) and attenuation (losses) measured in decibels (dB). The gain, in dB, in the system equals to $10 * \log_{10} (J/I)$ where I is the power input to the system while J is the output power from the system. Accordingly, a 10 dB gain in the GPR system corresponds to a

tenfold, and a 20 dB gain to a hundredfold, increase in signal power while negative values indicate losses (Milson, 2003).

The main purpose of GPR data processing is to make the interpretation easier which is basically achieved by improving the raw-data quality. Many users can interpret directly from the monitor display of the GPR system units, the screen. However, the dynamic range of the information produced on the screen is about 10-20 dB, whilst the dynamic range of a GPR system is at least 60 dB. This means that only a small component of the available information is presented on the screen (Cassidy, 2009a).

Consequently, the goal of GPR data processing, advanced signal processing, is to extract more information that can help to characterize the nature and the physical and geometrical properties of the target rather than just to help the user to see something in a the screen or the radargram.

The degree of GPR data processing are determined by many factors such as: 1) the budget available; 2) the quality of required and acquired data; 3) the available software; 4) the available time; 4) the experience of the operator; 5) the structural details and the physical and geometrical characteristics of the target (Cassidy, 2009a & 2009b; and Reynolds, 1997). A RADANTM (Radar Data Analyzer) software package, which is produced by Geophysical Survey Systems Inc. (GSSI), was mainly and effectively used for GPR data processing in this research.

3.7.1 Filtering. After position correction (zero or time-offset correction) step for acquired GPR data, it is common, as a first step in GPR data processing technique, to filter the data. The main goal of GPR data filter technique is to focus the radiogram image and so improve the visual quality of the data (Cassidy, 2011b). For many

applications, this is sufficient to locate the subsurface features. It is usually possible to set both high-pass and low-pass filters (de-wow filtering method) to remove instrumentation noise from the data, and thus to sharpen the signal waveform at the time of survey (Reynolds, 1997; Annan, 2009; and Christie et al., 2011).

Furthermore, it is advisable to keep the filter setting as broadband as possible to avoid or minimize the potential of excluding any valuable data. It is far cheaper to filter broadband data after the field work has been completed than to realize that the data quality has been compromised by the use of filter settings which are too harsh, thereby necessitating a repeat of the field work (Reynolds, 1997).

3.7.2 Deconvolution. The purpose of deconvolution is normally to maximize bandwidth and reduce GPR pulse dispersion to ultimately maximize resolution. However, this process has limited benefits because of the normal GPR pulses. The higher GPR frequencies tend to be more rapidly attenuated resulting in lower resolution with increasing depth (Annan, 2009).

3.7.3 Time Gain. GPR signals are very rapidly attenuated as they propagate into the ground. Signals from greater depths are very small when compared to signals from shallower depths. Simultaneous display of these signals requires conditioning before visual display. Equalizing amplitudes by applying a time-dependent gain function compensates for the rapid fall off in radar signals from deeper depths. Such time-varying amplification is referred to time gain and range gain when manipulating GPR data (Annan, 2009). A low-attenuation environment may permit exploration to depths of tens of meters; while in high-attenuation environment, penetration depth can be less than 1 m (Annan, 2009).

3.7.4 Migration. As with deconvolution, migration can be seen as an inverse processing step which attempts to correct the geometry of the subsurface in the GPR image (radiogram image) with respect to the survey geometry (Cardimona, 2002).

As depicted in Figure 3.17-A, when a GPR monostatic antenna is towed horizontally on a rock slope face which can be treated as a plane; the GPR antenna emits EM pulses which are normal incident at point A on the rock slope face. On other words, these pulses are perpendicular to the plane of the rock slope face but not necessary to be normal or perpendicular to the plane of any detected hidden joint.

Since the strike of a joint can be defined as the bearing of the intersection of the plane of the joint and a horizontal line, so the pulses of the GPR can be imagined as a horizontal plane penetrates the slope materials and goes through the plane of the detected joint resulting in an intersection line which can be considered as “the strike line” of this joint. This strike line will be recorded as a linear feature (reflector, interface, or even) on the GPR radiogram as shown in Figure 3.17 B.

However, when the GPR pulses travel through the medium of the slope material at point A, they will reflect back from point A' at the plane of the hidden subvertical joint to the GPR antenna which will record this reflection at point B as illustrated in Figure 3.18.

This results a linear feature or “the strike line” of the hidden subvertical joint with an apparent declination angle (α) less than the true declination angle of the strike line of the detected joint (β) which requires a correction for its geometry (migration) for accurate GPR data interpretation purposes. The declination angle here can be defined as the angle

between the strike direction, not the bearing, of the detected the detected hidden joint and a horizontal line as illustrated in Figures 3.17-B and 3.18.

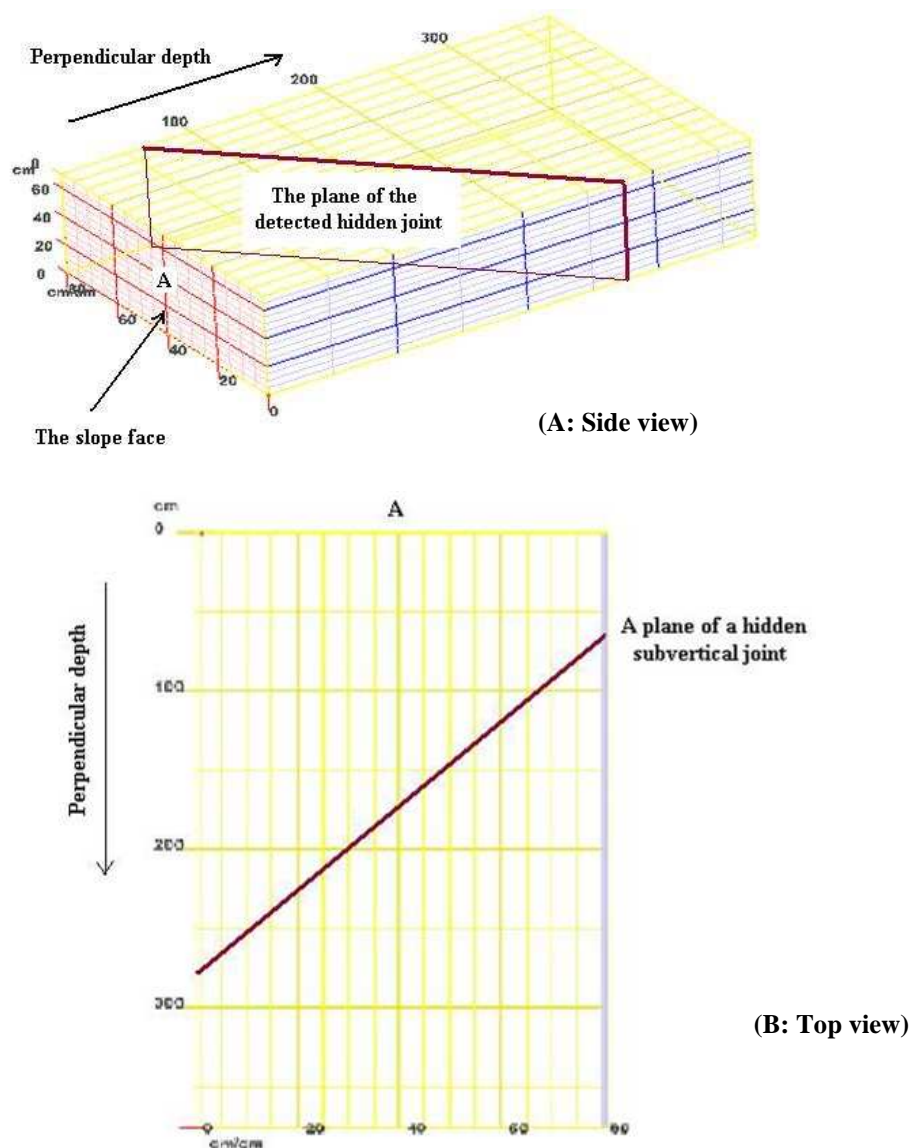


Figure 3.17: (A) GPR pulses of a horizontal survey line can be treated as a perpendicular plane to the rock slope face. (B) The intersection between the plane of the penetrating GPR pulses and the plane of detected hidden joint results in a linear feature can be considered as the strike line of that detected hidden joint.

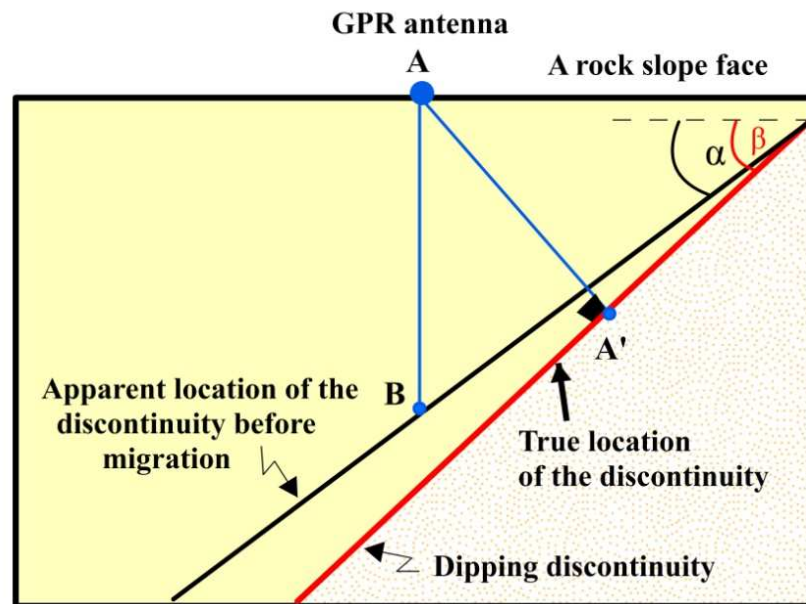
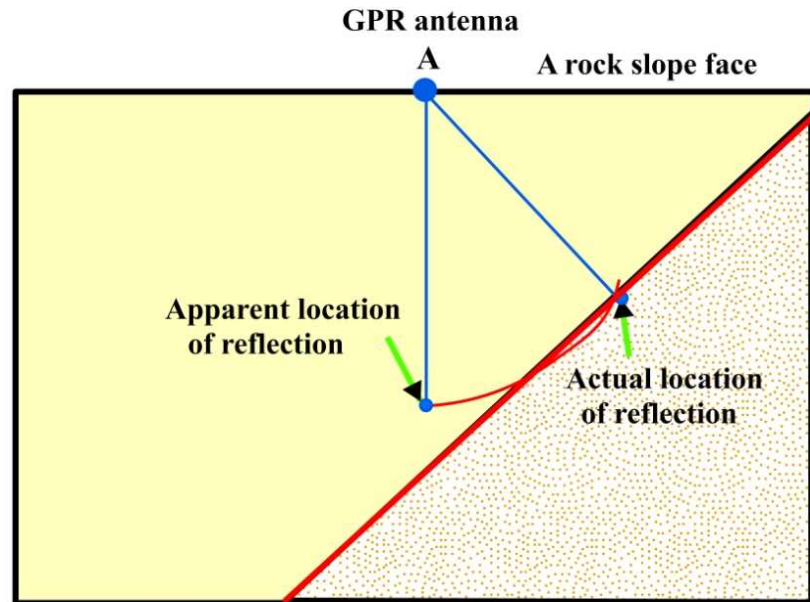


Figure 3.18: A top view of the linear feature “the strike direction line” of a subvertical hidden joint shows the apparent location and the true location of that joint. β is the true declination angle of the strike direction line while α is its apparent declination angle.

Simply, migration is a spatial deconvolution whose main purposes are to place a given subsurface target in its correct geometrical position on the GPR data record (radiogram image) (Reynolds, 1997; Daniel, 2004; Annan, 2009; and Cassidy, 2009b).

When the GPR velocity and relative dielectric permittivity for the rock slope material are measured, the two-way travel times can be translated to depths, and then migration can be done (Reynolds, 1997; Stark, 2008).

As mentioned before that when a horizontal GPR survey is carried out on a rock slope face, GPR pulses will be considered perpendicular to the plane of the rock slope and so travel horizontally through the rock slope face as illustrated in Figure 3.17 A.

For a dipping discontinuity, migration process results in the dip angle of slopping discontinuity being corrected to a steeper angle (Cassidy, 2009a and 2009b). The same concept can be used that migration process results in the declination angle of the strike line being corrected to a steeper angle. The manual migration, which was used in this research, for GPR data are explained in many geophysical references (Kleyn, 1983; Jenyon & Fitch, 1985; Lines & Newrick, 2004; Conyers, 2004; and Stark, 2008).

Figure 3.19 illustrates the main concepts to make a manual migration for a detected subvertical hidden joint plane. Consider a monostatic GPR antenna pulse at shot point A on rock slope face. A subvertical joint plane has a true dip angle (θ) while its strike makes a true declination angle (β) with an imaginary horizontal line that parallels to the plane of the rock slope face.

The GPR electromagnetic pulse incident normally with an angle 90° at point A' on the dipping discontinuity plane and then reflects back to the receiver in the GPR system on the slope face to be plotted at point B. this results with an apparent location for

the strike line with an a declination angel (α) and so an apparent perpendicular depth z ($z = AB$) less than the true perpendicular depth (d) from point A to point C. This results a linear feature of the strike of the dipping discontinuity plane is imaged by the GPR system with an apparent location (green line) as illustrated in Figure 3.19.

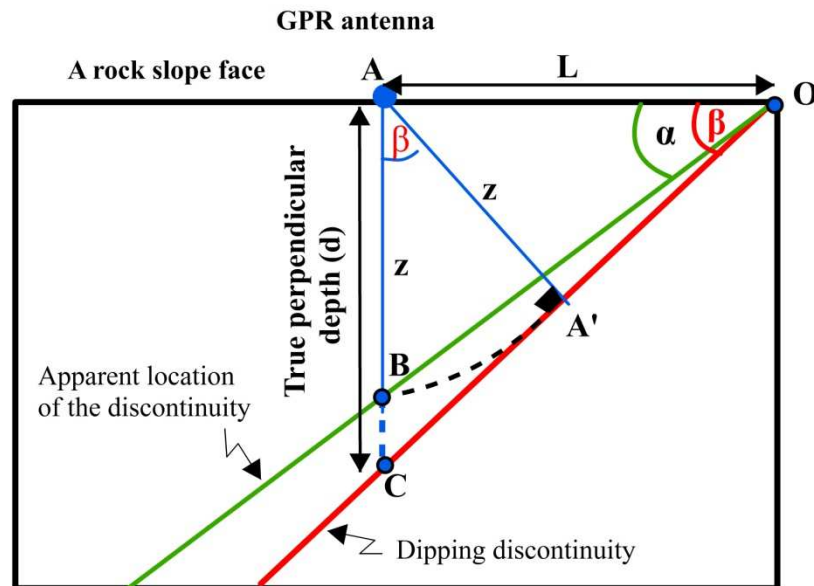


Figure 3.19: Top view illustrates the concepts of manual migration for the strike line of a dipping discontinuity. The apparent location of the strike line (green line) has a declination angle (α) less than the true declination angle (β) of the true location of the strike direction line (red line).

Since GPR electromagnetic energy propagation is treated as a wavefront as illustrated in Figure 3.5 and explained in section 3.4.2, the line $A'B$ is the arc of a circle which is centered at point A on the surface where the monostatic antenna is positioned,

and, therefore, $z = AB = AA'$, where z is the apparent perpendicular depth. Based on the trigonometric relations that can be concluded from Figure 3.19, the following mathematical relationships can be listed:

$$\text{From triangle O-A-B:} \quad \tan \alpha = z/L \quad (3.20)$$

$$\begin{aligned} \text{From triangle A-A'-C} \quad \cos \beta &= z/d \\ d &= z / \cos \beta \end{aligned} \quad (3.21)$$

$$\text{From triangle O-A-C} \quad \tan \beta = d/L \quad (3.22)$$

By substitute d from eq. 3.21:

$$\begin{aligned} \tan \beta &= (z / \cos \beta) / L \\ \tan \beta &= z / (L * \cos \beta) \end{aligned} \quad (3.23)$$

By substituting eq. 3.20 in eq. 3.23:

$$\begin{aligned} \tan \beta &= \tan \alpha / \cos \beta \quad (3.24) \\ \tan \beta * \cos \beta &= \tan \alpha \\ (\sin \beta / \cos \beta) * \cos \beta &= \tan \alpha \\ \sin \beta &= \tan \alpha \quad (3.25) \end{aligned}$$

Equation 3.25 is the key step for manual migration in this research. The difference between the true declination angle and the apparent declination angle is small for small angles but becomes significant when a true declination angle discontinuity is 25° and more as listed in Table 3.2.

Once the declination angles are measured and calculated, the true perpendicular depth from any specific point on the rock slope face to any detected hidden joint can be estimated using equation 3.21 as shown in the appendix. Based on that, manual migration

process was done for all detected hidden subvertical joints in the study area as will be explained in chapter 5.

Table 3.2: The apparent declination angle (ϕ) and the true declination angle (β) of the detected hidden subvertical joint which is shown as a linear event or interface in radiogram images.

Apparent declination angle (α) in degree	True declination angle (β) in degree
4.98°	5°
9.85°	10°
14.51°	15°
18.88°	20°
22.91°	25°
26.57°	30°
32.73°	40°
35.26°	45°
37.45°	50°
40.89°	60°
42.19°	65°
43.22°	70°
44.00°	75°
44.56°	80°
44.89°	85°
45.00°	90°

After correcting the geometry of the detected hidden subvertical joints, measuring their orientations step comes using the LIDAR data based on the equation of the plane can be conducted. The planes of the detected hidden joints have been individually related to the plane of the rock slope face whose orientations (dip angle and dip direction) were

measured by LIDAR. However, the local coordinates of LIDAR data have to be calibrated first to convert the Cartesian coordinates into geographical coordinates had as will be explained in the following two chapters.

4. BACKGROUND AND PRINCIPLES OF LIGHT DETECTION AND RANGING SYSTEM (LIDAR)

4.1 OVERVIEW

Light Detection And Ranging (LIDAR or LiDAR) Laser scanning systems use lasers to make measurements from a tripod or other stationary mount, a mobile surface vehicle, or aircraft (Dot.CA, 2011). LIDARs which are sometimes called Terrestrial Laser Scanners (TLS) are geodetic instruments which become very popular for engineering and geology surveys during the last years (González-Jorge et al., 2011; and Otoo et al., 2011a). The term LIDAR, which will be referred here in this research, is referred in some other references as terrestrial laser scanner (TLS), the in-situ 3D-laser scanner (3D TLS), terrestrial LIDAR, ground-based laser scanner, or ground-based LIDAR.

LIDAR enables rock slope faces to be remotely scanned, digitally captured, from a fixed location at distances ranging from tens to hundreds of meters (Slob et al., 2005; Turner et al., 2006; and García-Sellés et al., 2011). LIDAR is usually accompanied with specialist software programs to process its data and has a field work of view up to 360° horizontally and vertically varies from 80° to 270° based on the LIDAR scanner system used.

A number of LIDAR scanners are available on the market from different manufactures such as Leica and Riegl which are commonly used in North America (Turner et al., 2006). The underlying principles of the different types of LIDAR scanners

are essentially the same, but the quality of the resultant data set “point cloud” may vary among manufactures and models (Slob and Hack, 2004).

4.2 LIDAR SCANNER COMPONENTS

LIDAR scanner consists normally of a range “distance” measurement system and a mechanical laser beam deflection system (Feng and Röshoff, 2004; and Fröhlich and Mettenleiter, 2004). The laser deflection system points a laser pulse into the direction to be measured; the laser pulse is emitted and then reflected back from the surface of a rock cut of an interest to the LIDAR scanner to be detected. The accuracy of range measurement depends mainly on the intensity the reflectivity of the rock cut surface. The intensity of reflectivity depends mainly on the angle of laser beam incidence and the physical properties of the surface (Fröhlich and Mettenleiter, 2004).

4.2.1 Point Cloud Produced by LIDAR. LIDAR simply transmits a laser pulse to a rock cut surface of interest which reflects back the signal to the instrument, and by the same way, this process continuous until finishing scanning the rock cut surface. This scan can acquire automatically millions of points in a short time with a high accuracy in the order of 3-5 mm. The closer the points are together the higher the resolution and thus the more the image resembles a photograph as shown in Figure 4.1.

The accuracy of a single point depends primarily on the accuracy of the distance of measurement “range measurement”. Depending on different types of LIDAR scanners which are available on the market, i.e. Leica or Reigl, and different methods (such as time-of-flight or phase methods), achievable accuracies of range measurements vary from sub-millimeters to centimeters. In addition, the color, the texture, and the degree of

roughness of the surface of the scanned rock cut effect on the degree of the reflection which affects on the accuracy of the range measurement (Koch and Kaehler, 2009).

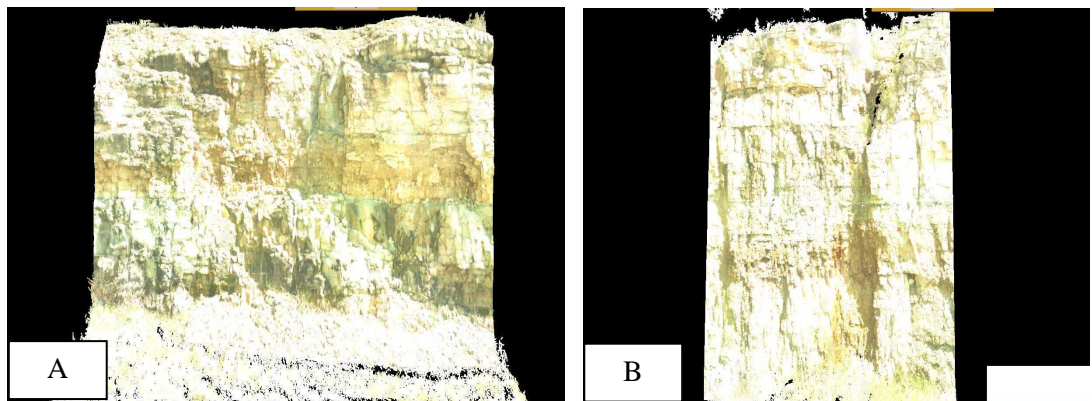


Figure 4.1: The more scanned points are the more resolution and more details. (A) A scanned rock cut which has 9.5 million points while (B) is the same rock cut but with less details, 8.2 million points.

The resultant points are identified by local xyz coordinates related to the scanner position by measuring the horizontal and vertical angles and the distance between the center of the scanner and the rock cut point (Koch and Kaehler, 2009). These xyz coordinates and their associated intensity of reflectivity from the surface are known as a “Point cloud” (Otoo et al., 2012). By measuring the geographical coordinates using a compass at the field for at least one point or location at the rock slope face for each scan, the local coordinates of the LIDAR data set “Point cloud” can be transformed into a geographical coordinates system which allows to locate any part of or discontinuity on the rock slope face in real 3D space.

From point cloud, detailed information about the geometry of the rock cut can be extracted remotely with no need for physical contact-measurements as illustrated in Figure 4.2 (Slob et al., 2002; and Slob et al., 2005). The point cloud is usually post-processed to create a three-dimensional (3D) model of the rock cut which is difficult to be obtained using traditional engineering survey instrumentations such as total station “electronic theodolite” (González-Jorge et al., 2011).

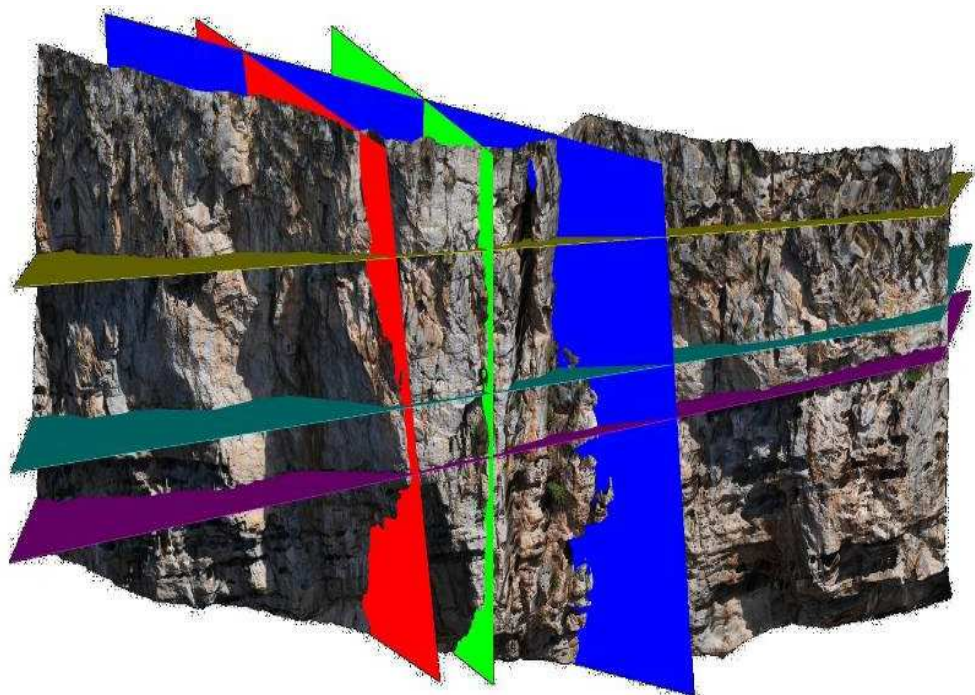


Figure 4.2: The orientation of rock mass discontinuities can be extracted from LIDAR points cloud (Adopted from <http://www.rockfalldefence.com>).

Moreover, the point cloud can be used to generate 3D orientations on Stereonet (Slob et al., 2005; and Kemeny et al., 2006); Generally, this point cloud produced by the laser scanner is searched for a region of co-planar points, and using any three non-linear points selected by cursor of a computer mouse from this region can determine the orientation of this plane solving the classic 3 point problem (Otoo et al., 2011a; and Duan et al., 2011).

Furthermore, The point cloud can provide information about the intensity of the reflected laser pulse from the rock cut surface, which can be used for other purposes and detecting different surface properties (Bornaz et al., 2003) such as roughness of rock mass discontinuities (Rahman et al., 2006).

4.3 CLASSIFICATION OF LIDAR SCANNERS

LIDAR Scanners can be classified either based on the distance measurement principle (i.e. triangulation, phase or pulse) or based on the technical specifications achieved. First of all, there is no one universal laser scanner for all conceivable applications. Some scanners are suitable for indoor use and medium ranges (up to 100 m), other scanners are better for outdoor use with long ranges (up to some 1000 m) and there are also scanners for close range applications (up to some meters) with a high precision (Fröhlich and Mettenleiter, 2004). The most common classification of LIDAR scanners is based on the principle of the distance measurement system. Accordingly, LIDAR scanners can be classified into time-of-flight or “pulsed” scanners, phase-based scanners, and triangulation-based scanners.

A time-of-flight LIDAR scanner, which is also known as “pulsed LIDAR scanner”, is most common used in civil engineering and large projects that covers large areas because of its longer effective maximum range (typically 125 – 1000 m) and data collection rate of 50,000 points/second, or more (Dot.CA, 2011). The advantage of long ranges implies reasonable accuracy (Fröhlich and Mettenleiter, 2004). The accuracy of this kind of scanners is less compared to the others. This type of scanner was used in this research.

A phase-based LIDAR scanner has a shorter maximum effective range which is restricted to one hundred meter (typically 25 – 75 m) compared to a time-of flight scanner (50000 points per second), but has much higher data collection rate compared to the time-of-flight scanner (Fröhlich and Mettenleiter, 2004; and (Dot.CA, 2011). Accuracy of the measured distances within some millimeters are possible (Fröhlich and Mettenleiter, 2004). Both of time-of-flight and phase-based LIDAR scanners can be used for different applications in civil engineering, geology, archaeology, and other applications; however, the first type is more commonly used because of the distances range that has.

A triangulation-based LIDAR scanner is a scanner which can be used for distance ranges up to few meters with high accuracy down to some microns of a meter. However, this type has limited applications and is more commonly used in industrial applications (Fröhlich and Mettenleiter, 2004). Based on the type of the used LIDAR scanner and the accuracy (resolution) or the point cloud density, time for a single scan can therefore varies from few minutes to few hours.

4.4 TECHNIQUES OF LIDAR SURVEY

In terms of scanning rock exposures, the distance measurement system using LIDAR scanners can be correlated to both the distance range and the resulting accuracy of the LIDAR scanner system. Accordingly, two common different techniques for range measurements or survey can be used with laser scanners. These two techniques are: time-of-flight, which was used in during LIDAR field work in this research, and phase techniques.

The time-of-flight method is commonly used for geodetic surveying or for measuring large civil engineering structures (Slob and Hack, 2004). The LIDAR scanner using this technique has a laser diode that sends a laser pulse to the surface of a target such as a rock cut (Slob and Hack, 2004; and García-Sellés et al., 2011). The laser pulse moves through a rapidly changing elevation and azimuth angle of a mirror inside the instrument. The pulse is diffusely reflected back from the surface of the target to the receiver in the LIDAR instrument (Slob and Hack, 2004). The time that the laser pulse takes to travel from the LIDAR diode to the surface of the target and returning back to the receiver of the instrument is measured precisely related to the distance from the LIDAR instrument location to the target and the speed of light ($c \approx 3 \text{ m/ns}$) (Slob and Hack, 2004; Nasrallah et al., 2004; González-Jorge et al., 2011; and García-Sellés et al., 2011). This distance can be determined by multiplying the velocity of light (c) by the half of the time-of-flight between the transmission and the reception of the laser pulse (Figure 4.3).

However, this type of survey is limited in measurement speed because a second measurement (pulsed laser) cannot start until sufficient time has passed to guarantee that a measurable reflection will not return from the first pulse (English et al., 2005).

A phase-based modulates the emitted laser light into multiple phases and compares the phase shifts of the returned laser energy. The scanner uses phase-shift algorithms to determine the distance based on the unique properties of each individual phase as shown in Figure 4.3 (Dot.CA, 2011).

Usually several scans can be obtained from different points of view to ensure that the whole entire rock cut will be covered and scanned, and the resultant point clouds are subsequently aligned and merged. The alignment and merging tasks are based on the identification of overlap zones of these scans. This process is typically assisted by algorithms implemented on commercial software. The merged point cloud can be relatively or absolutely positioned using GPS techniques (García-Sellés et al., 2011).

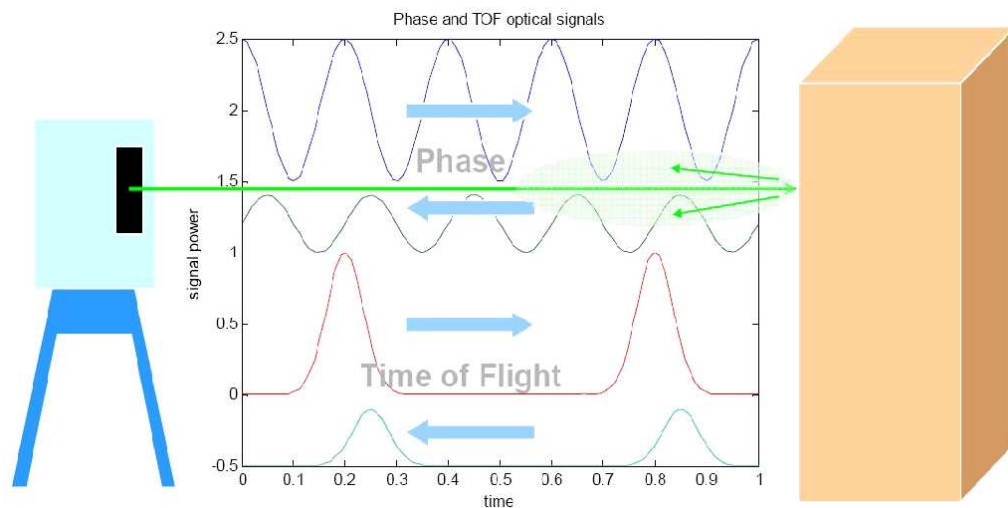


Figure 4.3: The principles of range measurement in the phase-based survey and time-of-flight survey using LIDAR scanners (Adopted from <http://ahmct.ucdavis.edu/pdf/UCD-ARR-08-06-30-06.pdf>).

4.5 ADVANTAGES AND LIMITATIONS OF USING LIDAR

4.5.1 Advantage of LIDAR. The advantage of employing such technology for geodetic purposes with high resolution survey is based on the capability of performing both large scale and small scale analyses and to rapidly obtain information on inaccessible rock exposures (Gigli and Casagli, 2011). Stuezenegger and Stead (2009) have listed some other advantages which are:

- The survey is not restricted to the base of an outcrop thereby providing more representative statistical samples.
- The ability to survey inaccessible steep and high rock slope faces.
- The survey can be undertaken remotely which reduce risks and hazards, in terms of traffic accidents and or rock falls, for workers in terms.
- The ability to build databases for surveyed rock slope face which can be used and updated anytime.
- The reduction of bias resulting from operator compared to manual and traditional methods used for measuring rock slope face and its discontinuities geometry. Furthermore, LIDAR allows discontinuities orientation measurements when conventional compass clinometers readings are affected by magnetic ore bodies.

4.5.2 Limitations of LIDAR. LIDAR measurements are only for exposed discontinuities and not for linear features such as the traces resulting from the intersection between a discontinuity plane and a rock slope face. In addition, the incident angle of laser beam and the distance to the target may affect on the accuracy of resultant point

clouds. Some common limitations are outlined by Sturzeneger and others (2007 and 2009). These limitations are occlusion, vertical and horizontal orientations bias, and truncation (Figure 4.4).

- Occlusion occurs when parts of a rock slope face cannot be scanned or sampled because it is obscured by protruding features (Sturzenegger et al., 2009). The effects of occlusion is that parts of the rock slope are prevented from being scanned and characterized where important information about the rock slope maybe needed (Pernito, 2008).
- Truncation occurs when the exposure of discontinuity, particularly the linear trace, is less than the available resolution of the used LIDAR (Pernito, 2008).
- Orientation bias occurs when the scanner beam is parallel or nearly parallel to the orientation of the discontinuity, which may reduce the accuracy of the slope stability analysis. (Pernito, 2008).
- Furthermore, Edward and Dare (2005) pointed out that atmosphere can affect on the resolution of point cloud as well as on the degree of the reflectivity from the surface of targets.
- It is always preferred to take perpendicular or nearly perpendicular scan to produce good quality of resolution of point cloud; otherwise, the resolution will be decreased (Sturzeneger et al., 2011). This condition cannot be applied in all environments of work since some highways do not have spacious shoulders or even shoulders which make playing this condition not possible and/or risky.

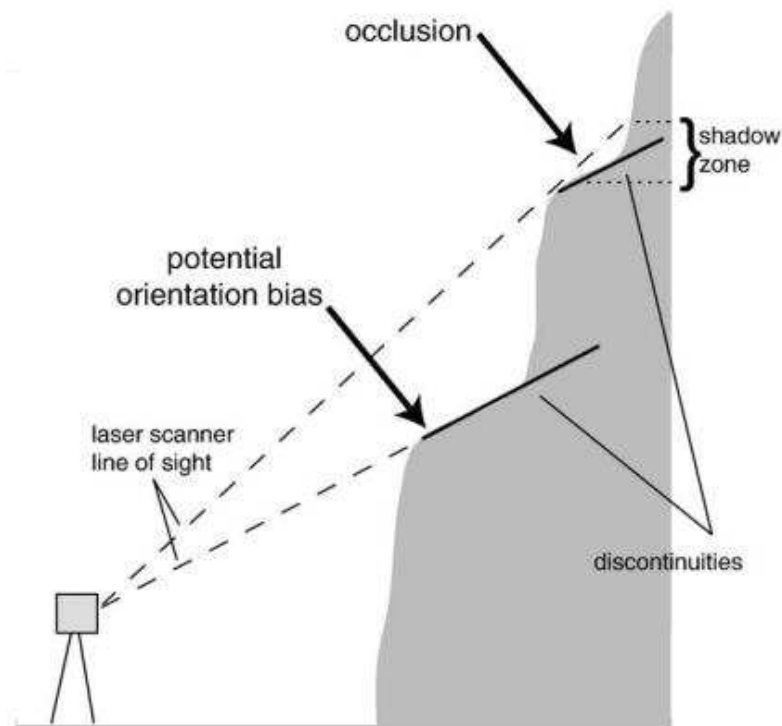


Figure 4.4: shows that when the scanner beams directed in the same direction of the extension of the discontinuity this may cause orientations bias. Also when the beam of the scanner is directed upwards at an angle steeper than a discontinuity, occlusion results in a shadow zone (Adopted from Sturzenegger et al., 2007).

4.6 SPECIFICATIONS OF LEICA AND RIEGL LIDAR SCANNERS

The specifications differ from a manufacture to another and from a model to another which play a significant role in terms of accuracy of resultant point clouds and the time will be taken to achieve the scan process for the rock slope face.

Leica and Riegl LIDAR scanners are more common used in North America (Turner et al., 2006). Moreover, they are most advanced instruments which use pulses technology, using the time of flight method, on the market for the moment (Fröhlich and

Mettenleiter, 2004).The specifications of Leica HDS3000 “ScanStation 2” LIDAR scanner, which was used in this research as shown in Figure 4.5, are listed in Table 4.1. It consists of the hardware and accompanied software program (Cyclone) as shown in Figure 4.6. The hardware components include the scanner unit, and a connected laptop to run, operate, and drive the scanner unit in order to scan the target of interest (rock cut exposures) and to record and store the data on range, angles, and intensity of reflection for each reflected and detected laser pulse via a network connection. While the installed Cyclone program is used for data set processing either in the field or in an office.



Figure 4.5: A back view for the Leica-ScanStation2 which was in this research.

Cyclone is able to connect both time-of-flight and phase-based scanners data. The point clouds can be superimposed with color data from standard CCD cameras; and therefore, it is a kind universal software tool (Fröhlich and Mettenleiter, 2004).

The system of Riegl (Figure 4.7) is pulsed system (time-of-flight scanner) with accuracy in centimeters (Fröhlich and Mettenleiter, 2004). Table 4.2 lists the specifications of the model LMS-Z390i terrestrial LIDAR of Riegl system.

Table 4.1: A summary of Leica HDS3000 LIDAR scanner (Modified after Otoo et al., 2012).

Laser scanning type ($\mu\phi$)		Pulsed
Color		Green
Range		300 m at 90%; 134 at 18% albedo
Scan rate		Up to 50,000 points/seconds maximum instantaneous rate
Scan resolution	Spot size	From 0 – 50 m: 4 mm (FWHH-based); 6 mm (Gaussian – based)
	Selectability	Independently, fully selectable Vertical and horizontal point-to-point measurement spacing
	Point spacing	Fully selectable horizontal and vertical < 1 mm minimum spacing, through full range; single point dwell capacity
	Maximum sample density	< 1 mm
Field of view (FOV)	Horizontal (deg.)	Up to 360
	Vertical (deg.)	Up to 270
	Aim/Sighting	Optical sighting using QuickScan button
	Scanning optics	Single mirror, panoramic, front and upper window design
	Digital Imaging	Low, Medium, High Automatically spatially rectified
Camera		Integrated high-resolution digital camera
Scanner Dimensions (mm)		265 x 370 x 510 without handle and table stand
Weight		18.5 kg
Power supply		36 V, AC or DC

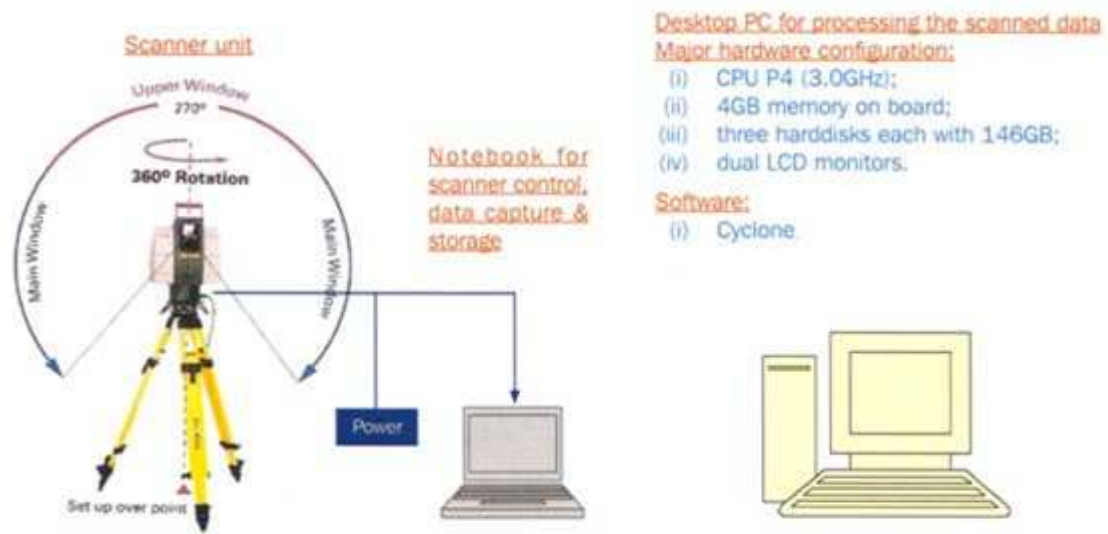


Figure 4.6: Field view of Leica HDS3000 LIDAR scanner system, which was used in this research, with associated software programs (Cyclone6 was used in this research) for LIDAR data set processing (Adopted from Chow, 2007).



Figure 4.7: Riegl LMS-Z390i scanner (Adopted from <http://www.geographica.hr>).

Table 4.2: Specifications of Riegl LMS-Z390i terrestrial laser scanner according to manufacture datasheet (Modified from Riegl webpage: <http://www.riegl.com>).

Range Finder Performance		Maximum measurement range (m)	up to 400
		Minimum measurement range (m)	1
		Accuracy (mm)	6
		Repeatability (mm)	4 (single shot); 2 (averaged)
		Measurement rate (pts/s)	11,000 at low scanning range (oscillating mirror) 8,000 at high scanning rate (rotating mirror)
		Laser wavelength	Near infrared
		Beam divergence (mrad)	0.3
Scanner Performance	vertical (line) scan	Scan angle range (deg.)	0 - 80
		Scan speed	1 scan/sec to 20 scan/sec at 80 deg.
		Angular Step-width (deg.) (between consecutive laser shots)	0.002 – 0.2
		Angle measurement resolution (deg.)	0.001
	horizontal (frame) scan	Scan angle range (deg.)	0 - 360
		Scan speed	0.01/sec to 15/sec
		Angular Step-width (deg.) (between consecutive scan lines)	0.002 – 0.75
		Angle measurement resolution (deg.)	0.001
Power supply input voltage		12 – 28 V DC	
The dimensions of the device		463 mm x 210 mm (length x diameter)	
Weight		approx. 15 kg	

LIDAR scanners can scan millions of points at the rock slope face within a short time and in the order of the accuracy of 3 to 5 mm. Each point can be identified by a set of local (X, Y, Z) coordinates that have to be transferred and converted to geographical or spherical coordinates. That is basically can be done once the LIDAR measurements are calibrated requiring taking at least one measurement of a subvertical planar structure that is in the scanned image.

Accordingly, the geometry of the planes of the detected hidden subvertical joints using GPR can be related to the geometry of the plane of the rock slope face which was scanned by LIDAR. This can be conducted basically based on the equation of the plane which requires at least three points to be identified and measured geometrically as will be explained in Chapter 5, the next chapter.

5. METHODOLOGY

5.1 OVERVIEW

Since the main goal of this research is to develop an approach to measure the geometrical orientations of hidden subvertical joints in rock slopes using GPR data and LIDAR measurements in combination, the study area was divided into two different sites which are commonly rock cuts along highways and have almost subvertical cuts. The first site (Site No.1) is Rubidoux Sandstone outcrop on highway 44 northwest Rolla City in Phelps County, and the second site (Site No.2) is on highway 72 west Fredericktown in Madison County. Each site represents an individual case and has its own geology and topography.

A reconnaissance field visit was first made to determine geology and structure of each site individually, in addition to, to evaluate the ease of accessibility to that site. Then, a literature review and some relevant information, maps, and satellite images were collected for the study area as well as for each site.

Each site was divided into different stations where each station could be treated as an individual rock slope face. All those stations have almost quasi-smooth rock faces whose dip angles are subvertical to vertical. Field work was conducted on each station (Figures 5.1 and 5.2). Site No.1 was divided into five stations while site No. 2 was divided into two stations as shown in Figures 5.1 and 5.2.

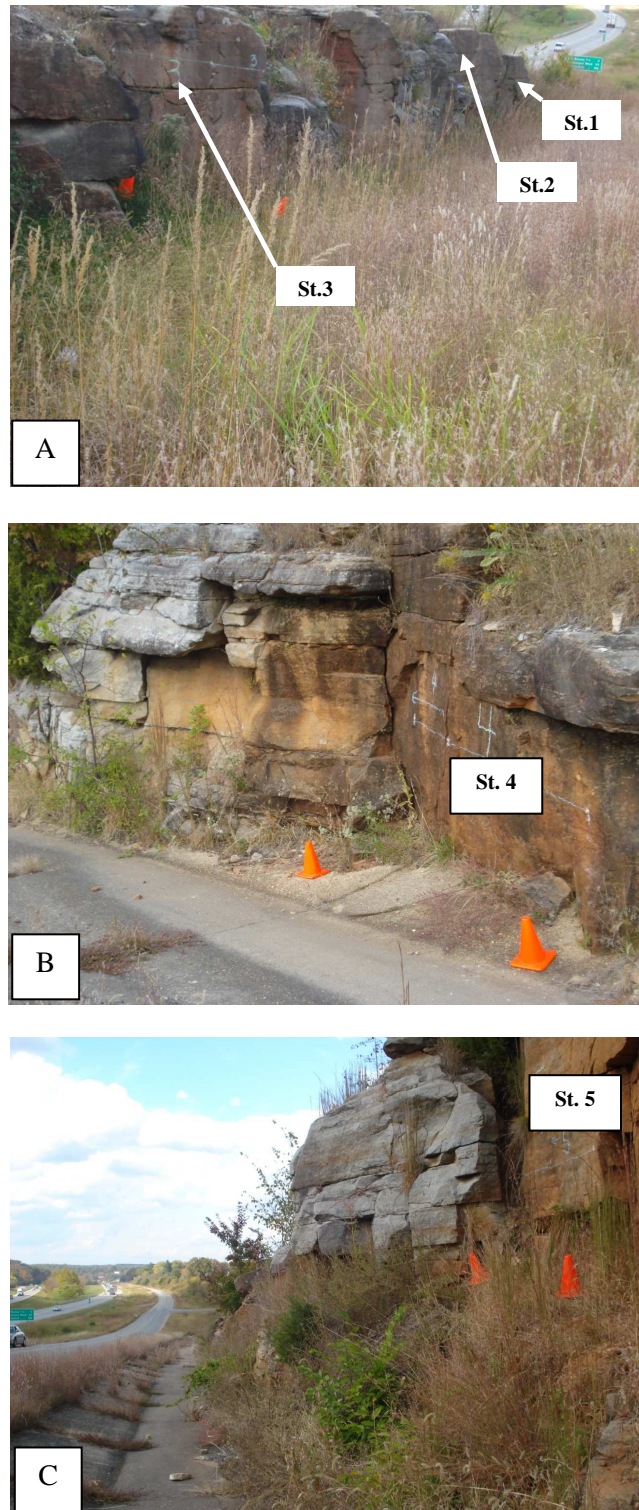


Figure 5.1: (A) a side of Site No.1 where is divided into three stations (St.1, St.2, and St.3); (B) and (C) show the other side of Site No.1 where St.4 and St.5 are located.

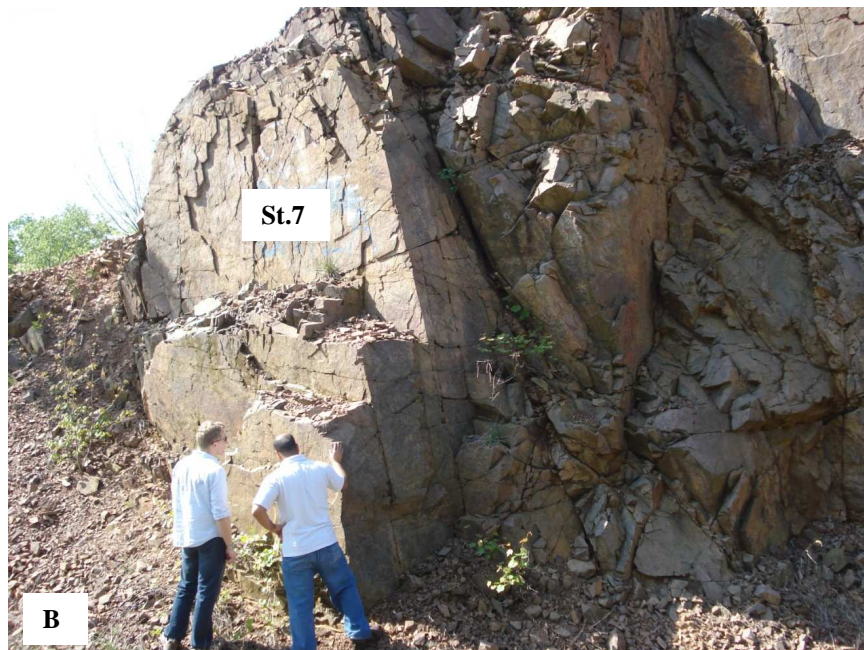


Figure 5.2: (A) Station 6 (St.6) and (B) St. 7 in site 2, Madison County-MO.

It is important to define the meaning of the term “subvertical joint or discontinuity”. In terms of geology and structural geology, it is known that any 2-D structure or plane whose dip angle is 90° or zero is known as a vertical or horizontal plane, respectively. However, any plane that has a dip angle in the range between zero and 90 degree can be considered as a sub-horizontal, subvertical plane or oblique plane with no specific definition in literatures for them. However, in this research, it has been proposed the following classification for discontinuity planes, based on the dip angle value (θ):

- i. Horizontal plane if $\theta = \text{Zero } (0^\circ)$
- ii. Sub-horizontal plane if $0^\circ < \theta < 30^\circ$
- iii. Oblique plane if $30^\circ \leq \theta \leq 60^\circ$
- iv. Sub-vertical plane if $60^\circ < \theta < 90^\circ$
- v. Vertical plane if $\theta = 90^\circ$

Hence, the most concern in this study is to detect and depict any hidden discontinuity whose dip angle is more than 60° and striking parallel to sub-parallel to a rock slope face (Figure 5.3).

5.2 FIELD SURVEY

The field work was conducted at each station by utilizing three main different methods which are: i) scanline survey; ii) ground penetrating radar (GPR) survey; and iii) LIDAR survey.

5.2.1 Scanline Method. In this traditional method, the discontinuity geometrical information is collected along a measured-length line at a rock slope face. The

information sometimes includes joint wall roughness (JR) but always includes orientation of discontinuities, strike and dip directions and dip angles. In our research, only orientation, which is measured by a geological compass and inclinometer, for both discontinuities and rock slope cuts or faces were taken and recorded on a notebook to achieve the goals and objectives of this research.

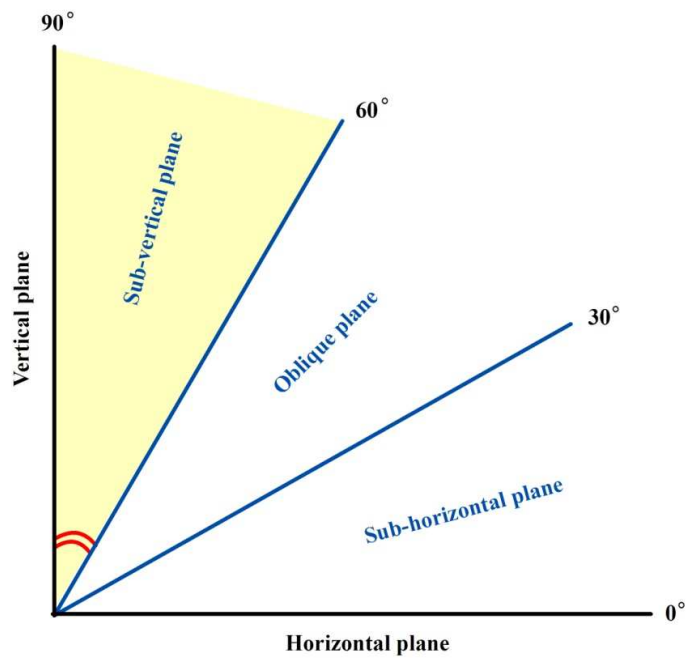


Figure 5.3: Proposed classification for planes based on dipping angle (θ). The shaded yellow area shows the planes of interest in this research.

The exposed surface area of each rock slope face or station of the study area, in almost of cases, is not more than 25 m^2 , the use of a measurement tape for scanline method will not give enough data for sound slope stability analysis; since the scanline

will intersect with a very few number of exposed joints on the rock slope face leading to underestimation of rock slope stability analysis as illustrated in Figure 5.4. Therefore, all exposed joints which can be measured manually on the rock slope face at each station were measured and recorded to get enough data and more details (Table 5.1). All the scanline method results are listed in appendix A.



Figure 5.4: Shows the location (blue circle) of where the tape measurement should be for scanline survey at St.1. Notice that the scanline did not intersect with more than three joints on the rock face which push us to measure manually the orientation of all accessible joints without relying on the scanline itself.

Table 5.1: Manual measurements results for the measured exposed discontinuities at station 1 (St.1).

Joint No.	Strike Direction	Dip Direction	Dip angle (θ)
1	190	280	90
2	215	305	9
3	280	10	1
4	294	24	4
5	307	37	2
6	184	274	79
7	177	267	66
8	28	118	26
9	26	116	35
10	29	119	23
11	303	33	3
12	185	275	90
13	170	260	64

5.2.2 Ground Penetrating Radar Field Measurements. Ground penetrating radar (GPR) is a non-destructive and non-invasive geophysical method for rapid and high resolution imaging of subsurface objects or targets (Takahashi, 2004). Ground penetrating radar can be used for mapping hidden discontinuities in rock masses and for wide variety of other applications in such as transportation and infrastructures investigations, military, mining, civil engineering, geology, and archeology.

Typically GPR uses the transmission of electromagnetic (EM) waves within the range of radio waves for detecting subsurface or hidden and/or buried targets such as discontinuities, geological structures such as folds, strata sequences, utilities, tombs, ancient graves, and landmines and to estimate earth materials thickness such as soils (Reynolds, 1997; Goodman et al., 2009; Maerz and Kim, 2000; Kovin and Anderson, 2005; Capineri et al., 2008; Yarovoy, 2009; and Sucre et al., 2011).

The operating frequency of GPR is higher than several mega hertz (MHz). GPR instruments can be used on the ground surface or in boreholes. Only a surface GPR system was used in this research. The GPR system which was effectively used on the ground surface, in terms of resolution and penetration of depths, was SIR-3000 (Subsurface Interface Radar) model manufactured by Geophysical Survey Systems, Inc. (GSSI) with a monostatic 400 MHz frequency shielded antenna (Figure 5.5).

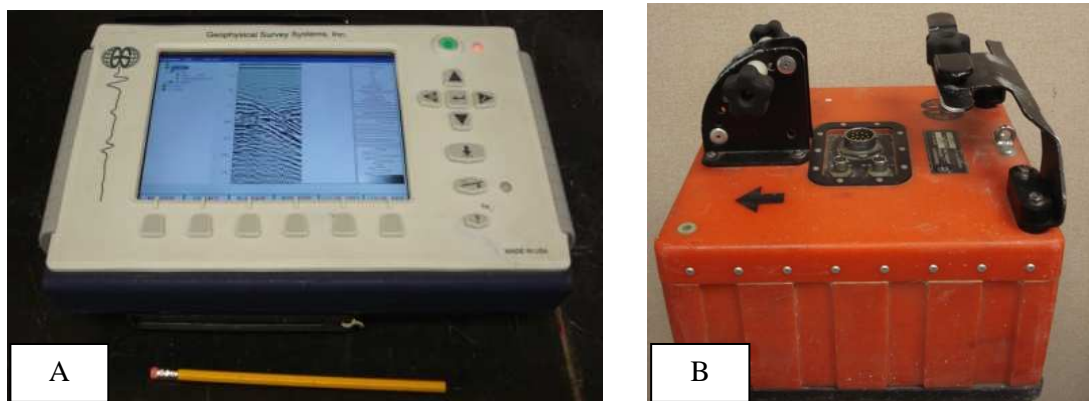


Figure 5.5: The used SIR 3000-GPR system (A), and the used 400 MHz shielded monostatic antenna (B).

Moreover, the use of 1500 MHz antenna was ineffective due to the limitation of depth of penetration even though the resolution was high but within less than 1 m depth which is not enough for the purpose of sound slope stability analysis. Furthermore, the 270 MHz antenna, in addition to its low resolution compared to the resolution of 400 MHz antenna, is heavy that causes difficulties carrying and towing it by hand on the rock

slope cuts, acquiring good quality GPR data, which may produce huge bias in data quality and survey consistency (Figures 5.6 and 5.7).

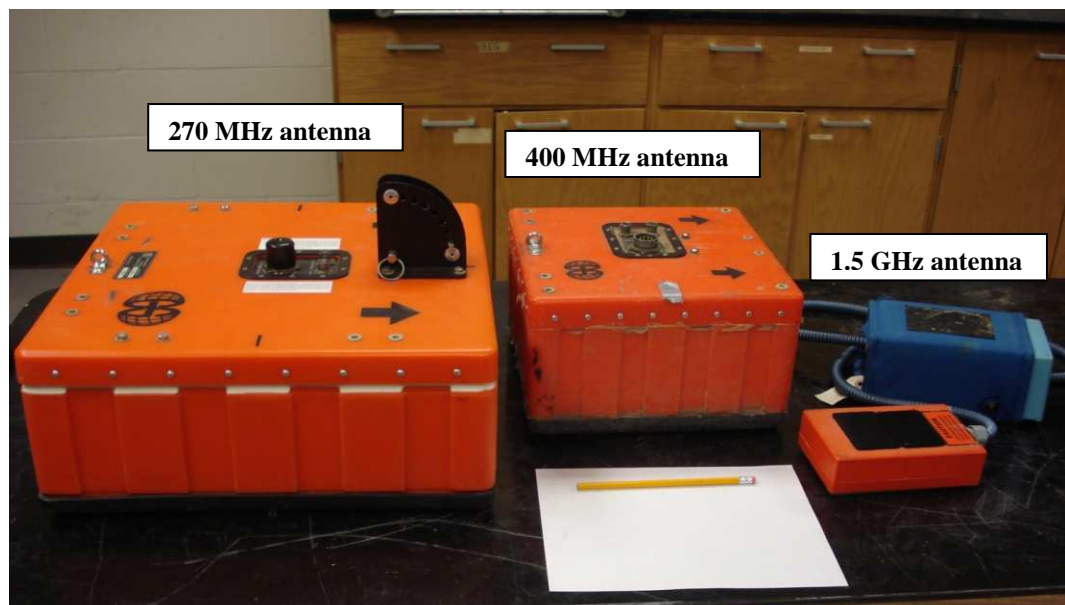


Figure 5.6: Monostatic antennae 270 MHz, 400 MHz, and 1500 MHz respectively. With increasing the frequency, the resolution of data increases but the penetration of depth decreases and as well as the size of the antenna.

5.2.2.1 Estimation of GPR pulse velocities. Two large rock samples were collected from site 1 and site 2 of the study area to measure the velocity of GPR pulses that travel through each type of these rock samples. The rock samples were trimmed into rectangular blocks using a large diameter diamond-saw blade at the Rock Mechanics and Explosive Research Center in Missouri University of Science (Figures 5.8 and 5.9).

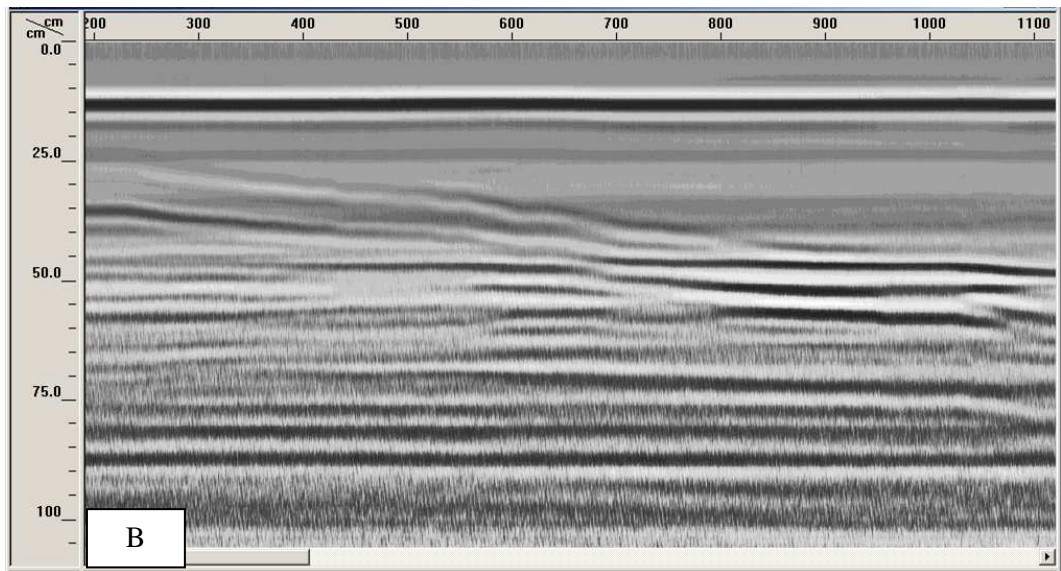
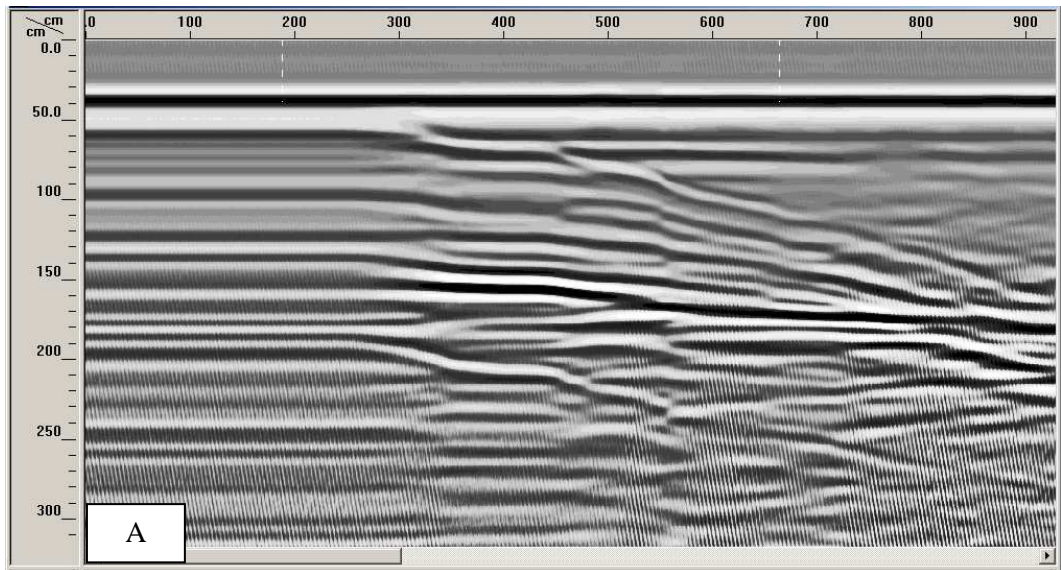


Figure 5.7: Raw time-domain GPR data acquired using 400 MHz antenna (A) and 1500 MHz antenna (B) at St.1. The higher frequency antenna (1500 MHz) has the higher resolution but lower penetration depth.



Figure 5.8: The sandstone sample from Phelps County-MO and the trimmed two blocks of the sample in order to conduct a lab measurement for the velocity of the GPR pulses that travel through this type of sedimentary rock. The thickness of the top block is 10.60 cm.



Figure 5.9: The ignimbrite rock sample from Madison County-MO and the trimmed two blocks of the sample in order to conduct a lab measurement for the velocity of the GPR pulses that travel through this type of igneous rock. The Thickness of the top block is 7.40 cm.

These samples became wet after sawing them, however the sandstone sample was significantly wet and so it was dried by putting it in an oven under a temperature of 100 C° for about 20 hours. The sandstone sample was then put under room temperature for couple of hours before starting the lab test. The ignimbrite rock sample of site 2 was dried under room temperature for two days.

Two consecutive laboratory experiments utilizing 1500 MHz GPR monostatic antenna were conducted on the two blocks of each type rocks, sandstone and ignimbrite rock samples. The two rock blocks were positioned on top each other with a separation between them acts as a discontinuity plane. The purpose is to estimate the most accurate GPR velocity and then relative dielectric permittivity values of each type of these rocks in dry conditions, so an indication about the dielectric permittivity value can be concluded when attenuation occurs due to such clay filling materials and/or water presence. When GPR velocity is estimated, true perpendicular depths to detected subvertical discontinuities can be then determined.

To simulate natural conditions, the two blocks of each type of rock, sandstone and ignimbrite, were positioned on top of each other creating two layers with a separation was 1.80 cm and 0.70 cm between the two blocks of sandstone and ignimbrite samples respectively. This separation can be treated as an interface of discontinuity plane through which the velocity of the GPR pulses will have an abrupt change (Figures 5.10 and 5.11).

The 1500 MHz GSSI-GPR monostatic antenna was used in time domain mode and moved over the surface of the top block of each type of the rock samples in order to detect the artificial discontinuity plane. All tests were repeated more than once to assure

repeatability of data and results, and the obtained results were identical for each rock sample.



Figure 5.10: The two blocks of sandstone rock sample were positioned on top of each other to create an artificial joint with a filled-air aperture of 1.8 cm wide.



Figure 5.11: The two blocks of ignimbrite rock sample were positioned on top of each other to create an artificial joint with a filled-air aperture of 0.8 cm wide.

The lab measurements results show that the GPR pulse velocity through the dry sandstone sample of Rubidoux outcrop was 0.106 m/ns while the velocity was 0.704 m/ns for dry ignimbrite of Ironton County. Moreover, the measured relative dielectric permittivity of sandstone sample was 6 which matched the used one in the field work; while the measured relative dielectric permittivity of ignimbrite sample was 16 which did not match the used one in the field work. Accordingly, the relative dielectric permittivity of ignimbrite sample was adjusted in GPR data set before estimation the perpendicular (vertical) depth. The following sections show how the velocity was calculated for the sandstone and ignimbrite dry rock samples respectively.

5.2.2.1.1 Estimation of GPR pulse velocity through sandstone sample of site

1. The GPR system was set up on time mode and with appropriate parameters as listed in Table 5.2. The 1500 MHz GSSI-GPR monostatic antenna was used in time domain mode and moved over the surface of the top block of the sandstone sample. The thickness of the top block was 10.5 cm, which means the true perpendicular (vertical) depth (d) to the created discontinuity plane is 10.5 cm (Figure 5.12). The GPR data record image (radiogram image) is shown in Figure 5.13. When the vertical axis (Y-axis) was set in a depth mode in the monitor of the GPR system, the radiogram image showed that the perpendicular (vertical) depth to the discontinuity was 10.6 cm which means that the accuracy and the precision of this work are good.

From the results shown in Figures 5.12 and 5.13, the model (Figure 5.14) was created to demonstrate the steps of calculation the velocity of the GPR pulses that transmitted through the sandstone rock sample.

Table 5.2: The parameters which were entered into the GPR system of the 1500 GHz monostatic antenna to estimate the velocity of the GPR pulses in sandstone sample collected from Roubidoux Outcrop, Rolla-MO.

Parameter	Value	Parameter	Value	Parameter	Value
sample	512	range	13 ns	rate	100
Bits	16	Dielectric	8	Sample/unit	2 scan/cm



Figure 5.12: The thickness of the top block is 10.50 cm which means the true perpendicular (vertical) depth to the created discontinuity is 10.50 cm. The separation between the two blocks was 1.80 cm.

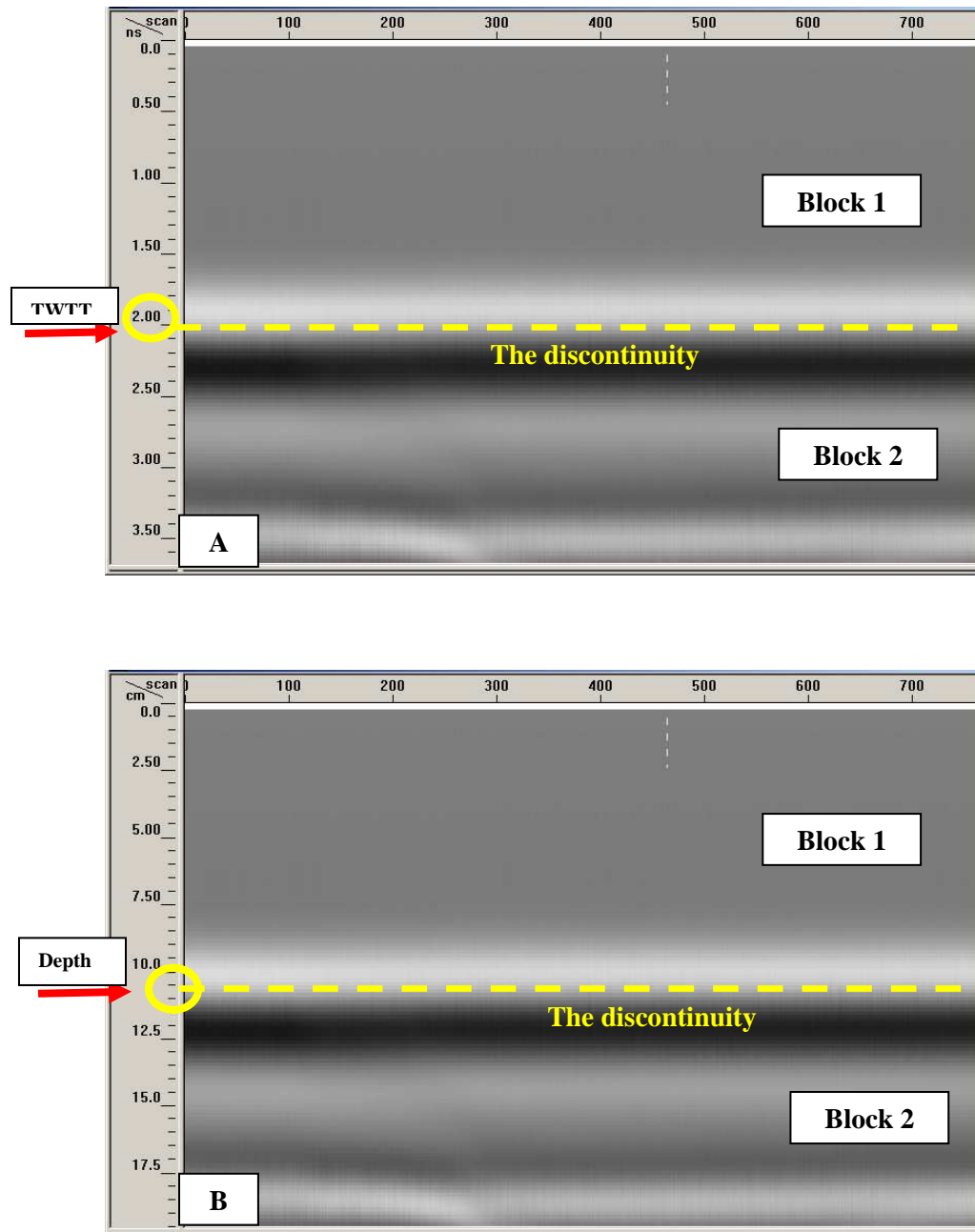


Figure 5.13: The radiogram image shows the two way travel time (TWTT) from the surface of top block (block 1) to the discontinuity plane location (dashed line). The TWTT was 2ns as shown in image A; while the perpendicular (vertical) depth to the discontinuity was 10.50 cm as shown in image B. The zero correction and display gain process were applied to the radiogram images to enhance the resolution and the clarity of the images.

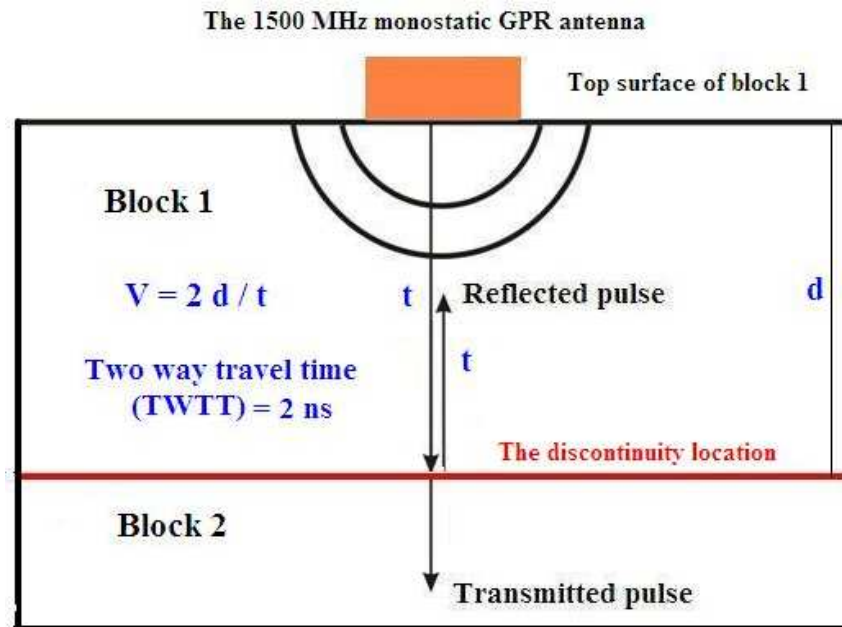


Figure 5.14: The geometry of the used two blocks to measure the GPR pulses velocity in the laboratory of geophysics in Missouri University of Science and Technology.

From the previous two radiogram images in Figure 5.13,

- The two way travel time = 2 ns = t
- The perpendicular (vertical) depth = 10.60cm = 0.106m

By using equation 3.17 ($V = 2d / t$),

$$V = (2 * 0.106 \text{ m}) / 2 \text{ ns} = 0.106 \text{ m/ns}$$

Now, the relative dielectric permittivity of the sandstone sample can be estimated using the following equation:

$$V = c / (\epsilon)^{1/2} \quad (5.1)$$

where, c is the speed of light in meters per nanosecond, which is 0.3 m/ns; and thus the relative dielectric permittivity of the sandstone (ϵ) is 8.

This result matches the used relative dielectric permittivity for Rubidoux sandstone during the field work of acquiring GPR data.

Now, the two way travel time (TWTT), the GPR pulses velocity, and the relative dielectric permittivity were measured and estimated in the laboratory, the perpendicular (vertical) depth can be estimated to any detected discontinuity in GPR data record as follows:

$$d = (0.15 * t) / (\epsilon)^{1/2} \quad (5.2)$$

By substitute the values of t and ϵ in the equation (5.2),

$$d = \{0.15 * 2\} / (\epsilon)^{1/2}$$

$$d = 0.3 \text{ ns} / (8)^{1/2} = 0.106 \text{ m}$$

0.106 m = 10.60 cm which is the same as the one was measured previously in the lab. Consequently the selected dielectric value ($\epsilon = 8$) or less will be suitable and significant for GPR acquiring data and processing data for the Rubidoux Sandstone outcrop located on 44 highway south west Rolla City.

Some studies show that even though the attenuation of GPR pulses will increase when apertures of discontinuities are filled with water or even with clay materials, the reflection of the pulses will increase from these surfaces because of increase the difference between relative dielectric permittivity between these discontinuities and surrounding environments (Hack, 2000).

5.2.2.1.2 Estimation of GPR pulses velocity through ignimbrite sample of site

2. The GPR system was set up on time mode and with appropriate parameters as listed in Table 5.3. The 1500 MHz GSSI-GPR monostatic antenna was towed over the surface of the top block of the ignimbrite rock sample.

Table 5.3: The parameters which were entered into the GPR system of the used 1500 GHz monostatic antenna to estimate the velocity of the GPR pulses in ignimbrite rock sample collected from Madison County-MO.

Parameter	Value	Parameter	Value	Parameter	Value
sample	512	range	10 ns	rate	100
Bits	16	Dielectric	6	Sample/unit	2 scan/cm

The thickness of the top block was 7.40 cm, which means the true perpendicular (vertical) depth (d) to the created discontinuity plane has to be 7.40 cm. However, the radiogram image shows that this depth is about 12.20 cm which is not correct as illustrated in Figure 5.15.

Hence, after estimation the velocity of the GPR pulses through the ignimbrite sample, its relative dielectric permittivity has to be adjusted before measuring the perpendicular depth to the created discontinuity or even for any other detected discontinuity in site 2.

First, the two way travel time of GPR pulses (TWTT) to the created discontinuity was estimated from the radiogram as shown in Figure 5.16. Then the velocity can be estimated. After that value of the dielectric permittivity value has to be adjusted before estimation the true perpendicular (vertical) depth.

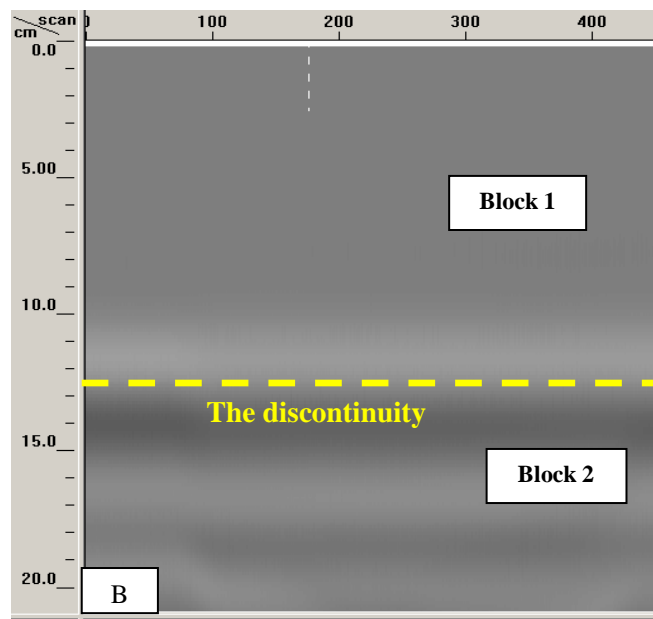


Figure 5.15: (A) The true perpendicular depth (d) from the surface of the top block to the created discontinuity or separation, which is 7.40 cm. (B) The apparent perpendicular depth (z) from the surface of the top block to the created discontinuity or separation, which was 12.20 cm, in radiogram before correcting the used relative dielectric permittivity of the ignimbrite rock. The zero correction and display gain process were applied to the radiogram images to enhance the resolution and clarity of the images.

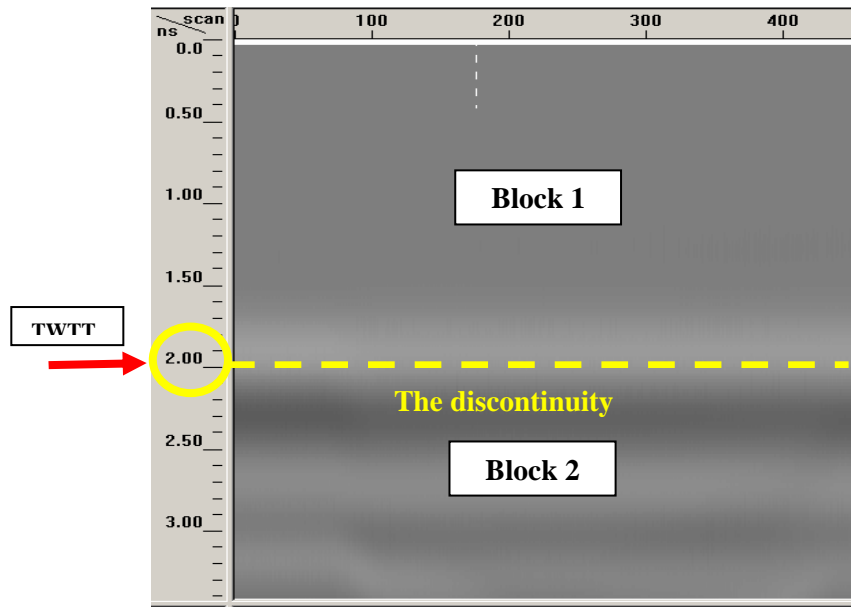


Figure 5.16: The two travel time of GPR pulses from the surface of the top ignimbrite block to the created discontinuity is 2 ns. The zero correction and display gain process were applied to enhance the resolution and clarity of the radiogram images.

To estimate the velocity first, from the above radiogram image,

- The two way travel time = 2 ns = t.
- The measured perpendicular depth to the created fracture = 0.074 m.

By using equation 3.17 ($V = 2d / t$), $V = (2 * 0.074 \text{ m}) / 2 \text{ ns} = 0.074 \text{ m/ns}$.

Now, the relative dielectric permittivity of the ignimbrite sample can be estimated using the following equation:

$$V = c / (\epsilon)^{1/2} \quad (5.1)$$

where, c is the speed of light in meters per nanosecond, which is 0.3 m/ns; and thus: $\epsilon = 16$. As a result, the used relative dielectric permittivity for the ignimbrite rock sample ($\epsilon = 6$) during the field work of acquiring GPR data has to be adjusted to the new resulting value ($\epsilon = 16$).

Finally, the true perpendicular depth (d) to the created discontinuity between the two blocks of the ignimbrite rock sample was estimated using the radiogram image as illustrated in Figure 5.17. The value of the relative dielectric permittivity of GPR profiles acquired in site 2, ignimbrite of St. Francois Volcanic Super-group, has to be adjusted to be 16 each time during estimating the apparent and true perpendicular depths, z and d respectively, to the detected hidden joints.

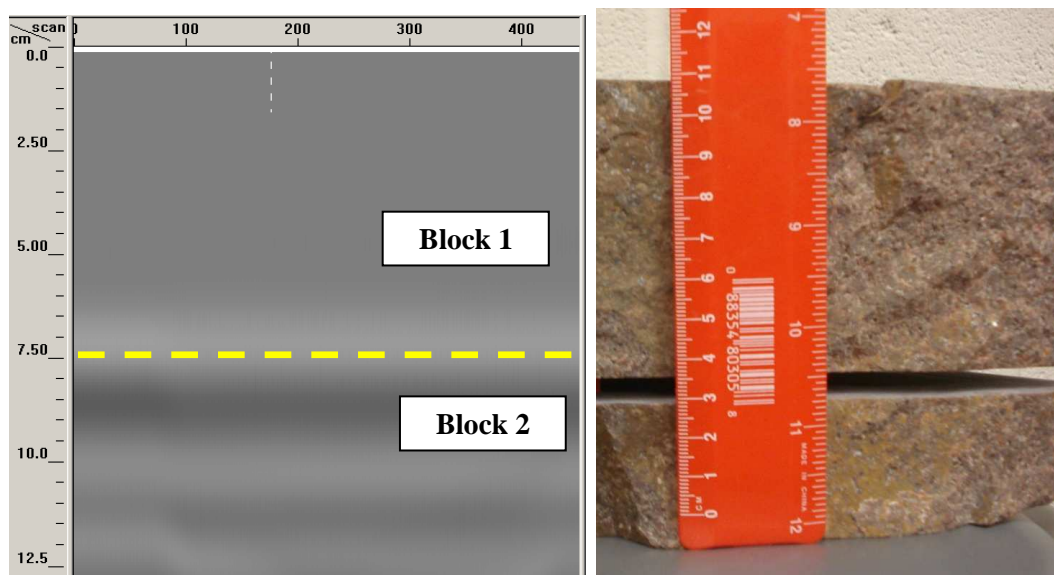


Figure 5.17: The radiogram image shows true perpendicular depth to the created discontinuity after adjusting the relative dielectric permittivity of ignimbrite in GPR data set. The resulting perpendicular depth from the radiogram ($d = 7.50$ cm) is almost the same as the measured perpendicular (vertical) depth in the lab ($d \approx 7.50$ cm). The zero correction and display gain process were applied to enhance the resolution and clarity of the radiogram images.

5.2.2.2 Modes of GPR survey. GPR systems usually operate and acquire data either in time-domain system (impulse GPR system) or in frequency-domain system (continuous waves GPR system) using generally a common offset survey method for monostatic GPR-antenna system. The GPR data survey can be done either using distance mode or time mode in which the horizontal distance will be normalized before processing the acquired GPR data (Figure 5.18).

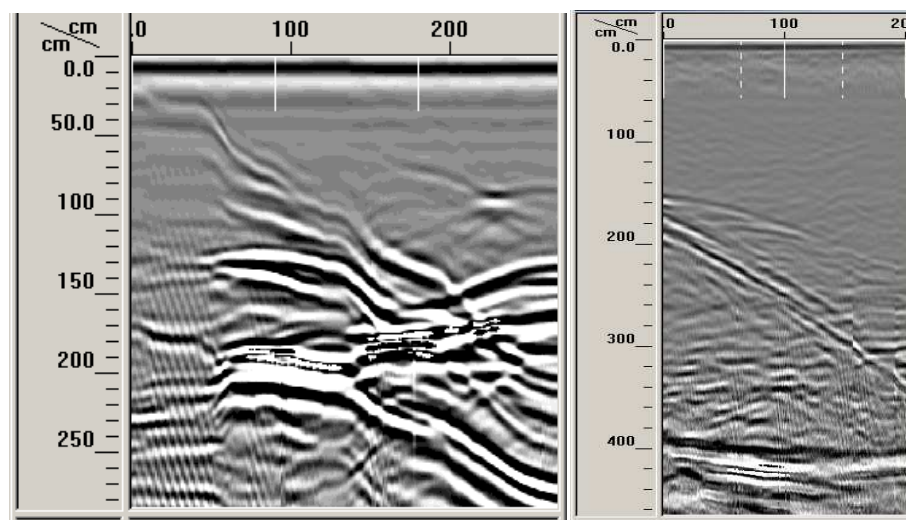


Figure 5.18: The produced radiograms from GPR data acquired using 400 MHz antenna in time-mode (left image) and distance-mode (right image) surveys at Station.3 (St.3). In time mode (left image), the data will be acquired regardless the antenna is towed or not which results in exaggerated horizontal distance that will have to be normalized before any further GPR data processing steps.

When it comes to creating 3-D images for detected hidden subvertical joints or any other targets, distance-mode survey will be required rather than time-mode survey. Normally, the GPR antenna is attached to a wheel which is fixed on a GPR cart and is

connected by a cable to the GPR system which has to be set up on distance mode. However, since our GPR field work is conducted on rock slope faces and cuts to detect subvertical to vertical discontinuities in the study area, so using that cart is not possible and even not effective especially with using 400 MHz shielded monostatic antenna.

To overcome this problem, a wheel was attached appropriately to the 400 MHz antenna and tested many times, after conducting a distance calibration for the GPR system, to ensure its capability and effectiveness in measuring distances during acquiring the GPR data in the field (Figure 5.19).

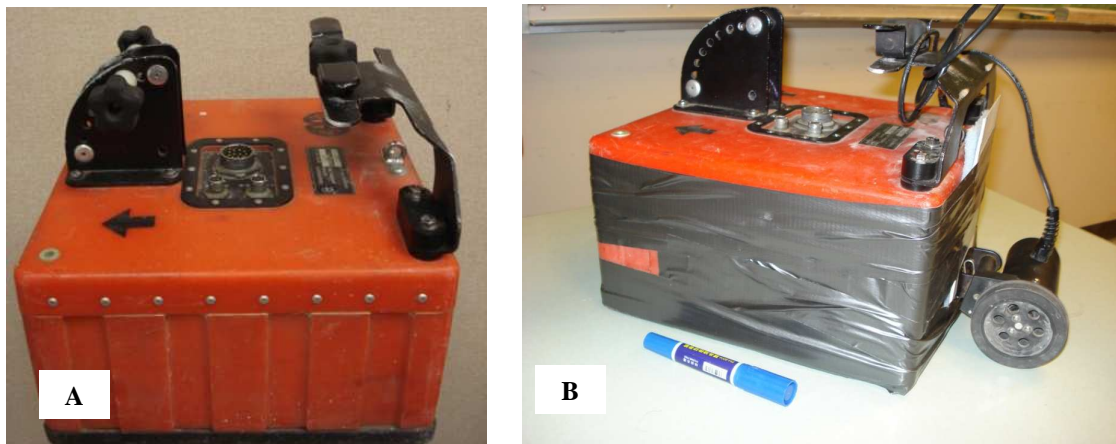


Figure 5.19: A 400 MHz antenna with no attached wheel (A), and with an attached wheel (B) to be used in a distance mode survey.

5.2.2.2.1 GPR distance mode survey. The GPR data were acquired using a 400 MHz shielded monostatic GPR antenna manufactured by the Geophysical Survey System, Inc. (GSSI). A wheel was attached to the antenna as illustrated in a previous

section, and the distance mode was used during data acquisition. Five to ten horizontal GPR survey lines with length ranging from 1.40 m to 3.00 m and intervals ranging from 10 cm to 20 cm were done at each station, rock slope face, in order to create 3-D images for each rock slope face visualizing the geometry of each detected hidden subvertical joints as will be explained later in this chapter in migration section.

On each rock slope face, three slight independent marks were etched onto the surface by using a hammer. These three marks are coplanar but not colinear. These three points will be used in this context as the three index points. On pictures and images in this research, the index point 1 was distinguished by drawing a small blue circle, while the index points 2 and 3 were distinguished by drawing small red and orange circles respectively (Figures 5.20 and 5.21).

These three index point represent fixed points on the rock slope faces from which the apparent and the true perpendicular depths to the detected hidden subvertical joints have been measured by using GPR data record images (radiogram images). Creating tick mark on the GPR data record was done on each one of the index points at each station (rock slope face) of the study area (Figure 5.21)

Two of the GPR survey lines passed through the three index points on the surface of each rock slope face in the study area. However, to distinguish these two GPR survey lines from the other lines, they were drawn on photos as dashed lines contained the three circles which represented the three index points (Figure 5.22), and these two GPR survey profiles will be known as “the two index GPR survey profiles” in the context from now and on.

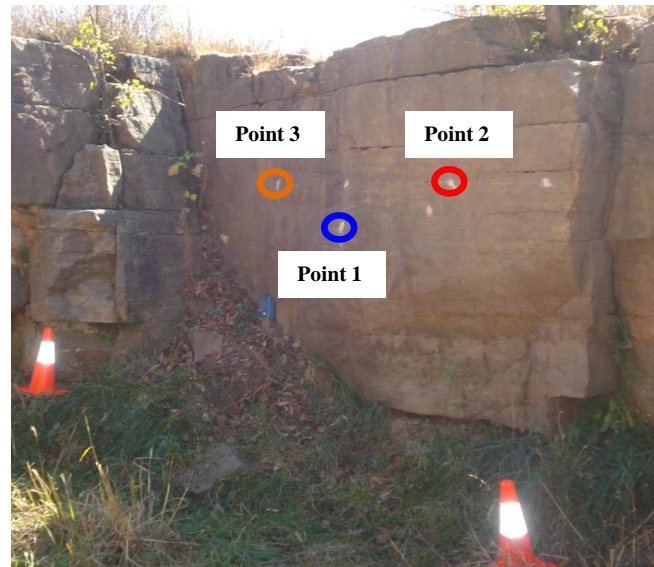


Figure 5.20: Creating three different locations on each rock slope face (rock slope face of station no.1) by using a hammer to create the three index points as reference to measure perpendicular depths from the surface of the rock face to detected hidden discontinuities.

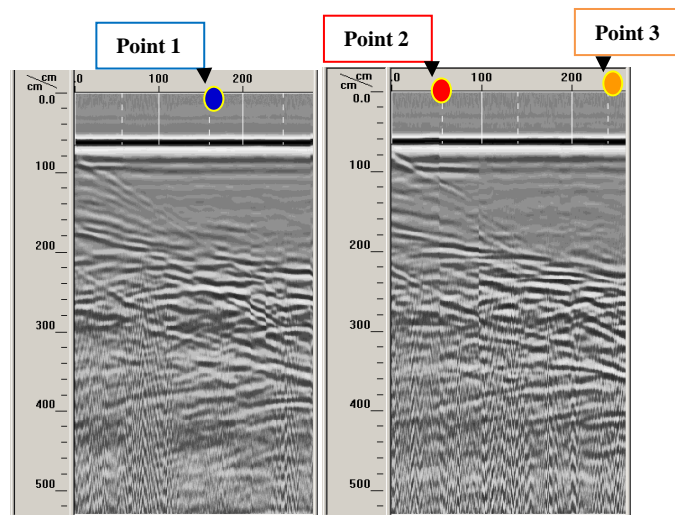


Figure 5.21: Identifying the three index points locations by colors on the radiogram images. The small blue circle represents index point.1, while the small red and the orange circles represent the index points 2 and 3 respectively.

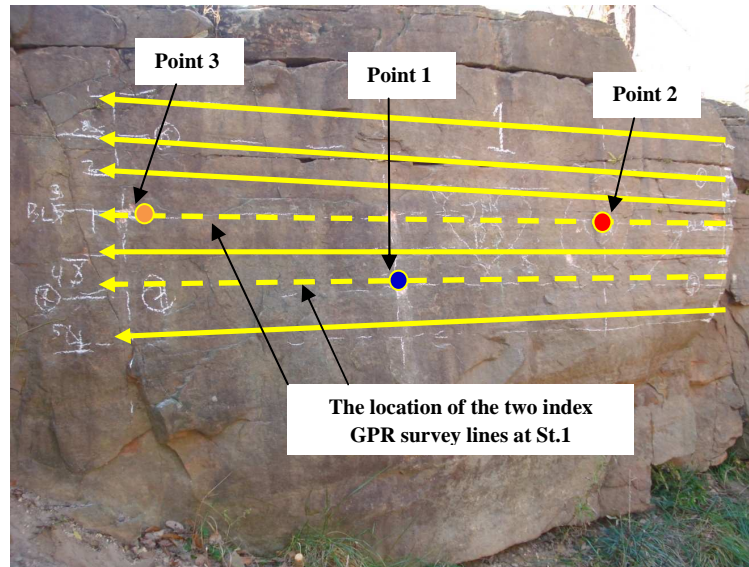


Figure 5.22: The location of the GPR survey lines including the two index lines (dashed lines) at St.1. The colored circles are the locations of the three index points. The small blue circle represents the index point.1, while the small red and the orange circles represent the index points 2 and 3 respectively.

These two index GPR survey lines are very important since they passed through the three index points at each station. The perpendicular depth from the rock slope face surface to any detected hidden subvertical discontinuity will be estimated from these points using the radiogram images.

Furthermore, the true geometry or orientation (dip direction and dip angle) of these joints will be determined based on the Cartesian and spherical coordinates of these three index points using LIDAR technology and the equation of the 3-point as will be explained later in this chapter. Always, in this research, the index point 2 and the index point 3 are located on the same index GPR survey line while the index point 1 is located

on a separate GPR survey line. Moreover, the first GPR survey line is located at the bottom of the area of survey close to the base of the rock slope face; in contrast, the last GPR survey line is located at the top of the rock slope face (Figure 5.23).

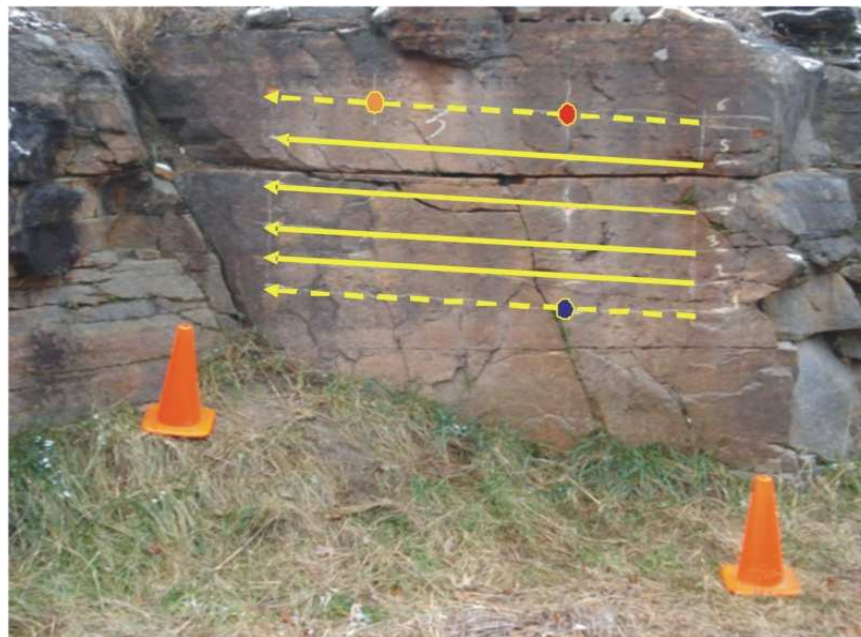


Figure 5.23: The locations of the two index GPR survey line (the two dashed lines) at station 3, which passed through the three index points.

The location and the number of the GPR survey lines for each station were controlled by the accessibility to the station, the dimensions of station (the rock slope face), the degree of smoothness of the rock slope face, and the height of the team of the personnel including the author for this research who were acquiring the field data; so the location and the length of the survey lines vary from one station to another within the

same site of the study area. For instance, station 2 seems has small area as shown in Figure 5.24, but in reality its height is much more than the height of the author.

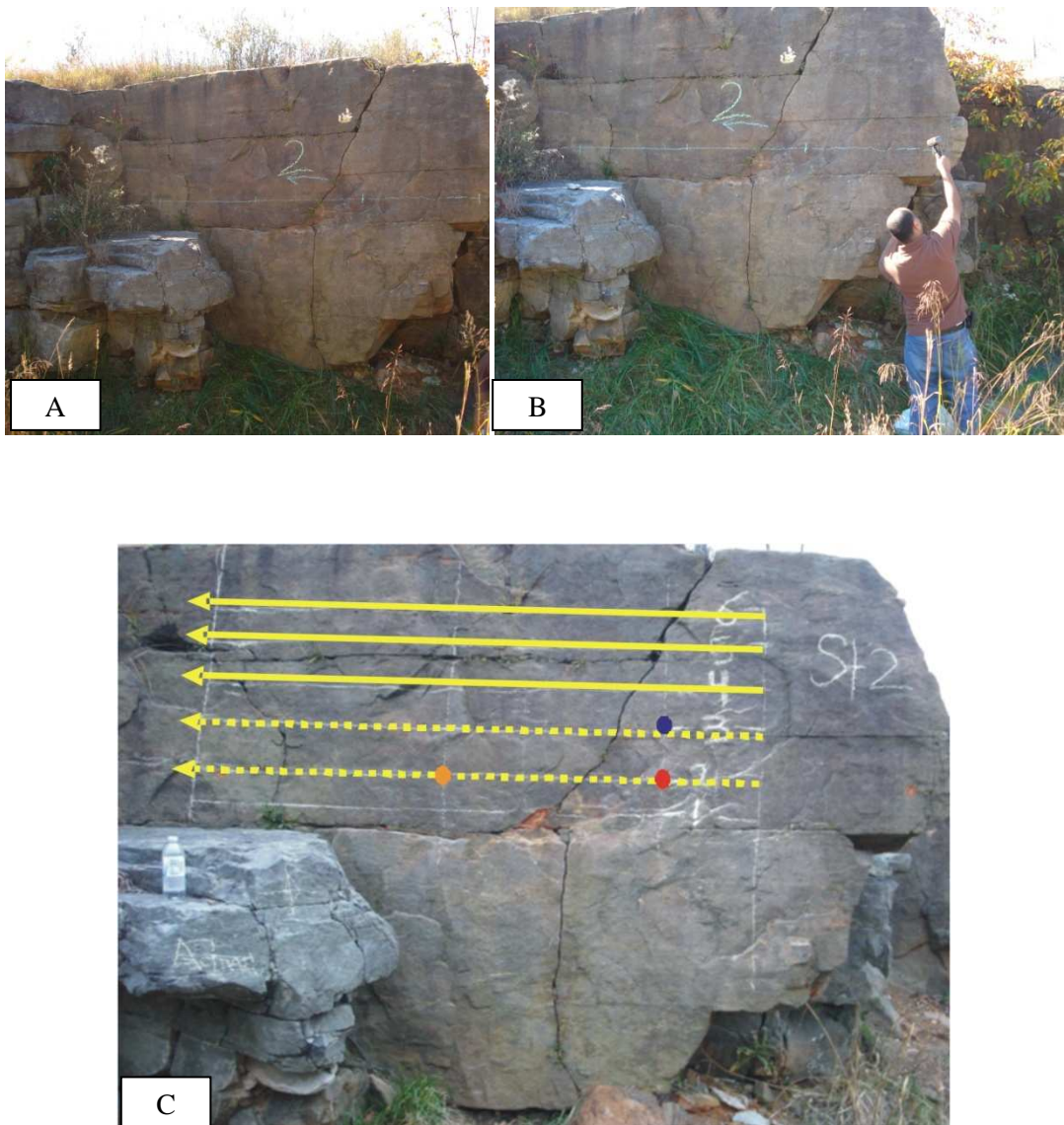


Figure 5.24: The location of the GPR survey lines vary from one station to another based on the extensions and the surface condition of the rock cut. (A) Shows St.2 as it seems small but (B) shows its real dimensions while (C) shows the locations of the GPR survey lines at this station.

In the purpose, first, of creating a smooth surface on which the 400 MHz GPR monostatic antenna will be moved on each GPR survey line in this study area, a wooden panel whose dimensions are 310 cm length, 32 cm width, and 2.5 cm thickness was used as a try to create a smooth surface at station 1 (Figure 5.25).



Figure 5.25: A wooden panel was used as a try to create a smooth surface on which the GPR antenna was towed at St.1 (left image), while the right image shows the process of drawing using chalk the location of the GPR survey lines on the rock slope face.

Even though this try was very time consuming and needed five persons to acquire the GPR data, the resultant data showed multiple reflection, which may cause misinterpretation, due to using this panel. However, this multiple reflection was absent when we towed the antenna directly to the surface of the rock cut (Figure 5.26). Hence, all the field work of acquiring the GPR data was done then with no using a wooden panel in the study area.

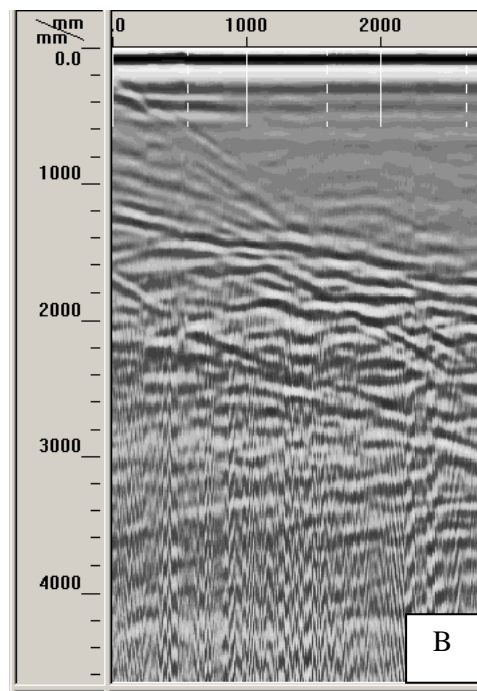
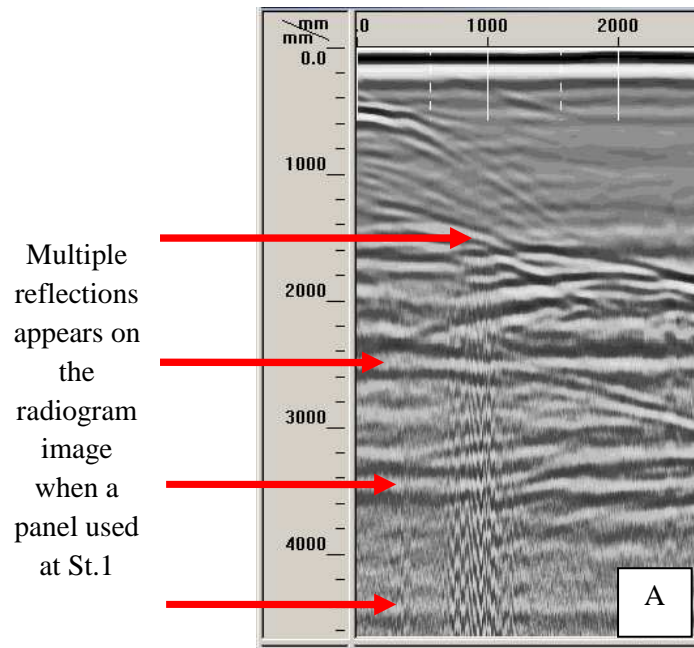


Figure 5.26: The multiple reflections resulted from using a panel during acquiring GPR data at St.1 (A), and a good radiogram image (B) when acquiring the data with no using the wooden panel.

5.2.2.3 GPR data processing. GPR data processing is required to remove noise and enhance the visualization of the radiogram image by increasing the resolution. Zero correction, filtering, auto-gain, color table, displaying gain, de-convolution, and migration techniques have been done using RADAN software as steps of processing for all the acquiring GPR data. However, migration process was done manually instead of using the software. Since migration is the most important part of GPR processing for this research to get the correct geometry of the detected hidden discontinuities, it will be described in the following section.

5.2.2.3.1 Migration. The word migration in geophysical prospecting means the word move. Migration is a technique that moves dipping reflectors (interfaces) to their true subsurface positions and collapses hyperbolic diffractions (GSSI, 2007). It is commonly the final step in the processing armory of the GPR user. It is generally used for improving GPR data resolution and developing more spatially realistic images of the subsurface (Cassidy, 2009b).

Migration is simply a mathematical process which is used to reconstruct and relocate a dipping discontinuity plane to its true position and thus its true geometry. Migration can be done utilizing either specialist software such as RADAN or manually as described in section 3.7.4 in Chapter 3. RADAN software offers two methods to migrate GPR data: Hyperbola (diffraction) migration method and Kirchoff migration method which is more accurate. Even though GPR data migration can be used successfully in relatively homogenous environments such as pavements and glacial environments, it tends, unfortunately, to be less successful for complex and heterogeneous sites (Cassidy,

2009b). Therefore, manual migration to avoid uncertainty may result from variability in inherent properties of hidden joints.

Several parallel horizontal GPR survey lines were carried out at each rock cut face as illustrated in Figure 5.27. Hence, the pulses of the GPR of each survey line can be imagined as a horizontal plane penetrating the slope and go through the plane of the detected joint resulting in an intersection line which can be considered as “the strike line” of this joint as illustrated in Figure 3.17 B. This strike line will be recorded as a linear feature (reflector, interface, or even) on the GPR radiogram as shown in Figure 5.28.

Manual migration was done for all detected hidden subvertical joints in the study area using GPR radiogram images and based on the equation 3.25:

$$\sin \beta = \tan \alpha$$

where

β - the true declination angle of the strike line of the detected hidden subvertical joint.

α - the apparent declination angle of the strike line of the detected hidden subvertical joint.

Then the next step was to estimate the true perpendicular depths from the three index points located on the surface of the rock cut to the plane of each detected hidden joint. It is very important to keep in mind again that this depth is only perpendicular to the plane of the rock slope face, and thus, to each of the two index GPR survey lines separately.

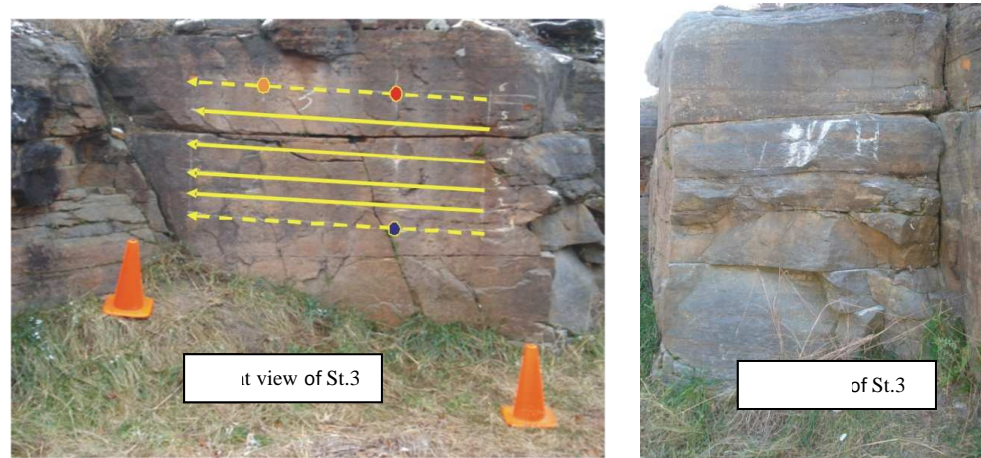


Figure 5.27: Parallel horizontal GPR survey lines (dashed lines are the two index lines) which are parallel to the strike direction of the plane of the rock face of station 3. The left image shows a linear trace of only one joint (joint no.1) which was detected in radiogram image as shown in Figure 5.28.

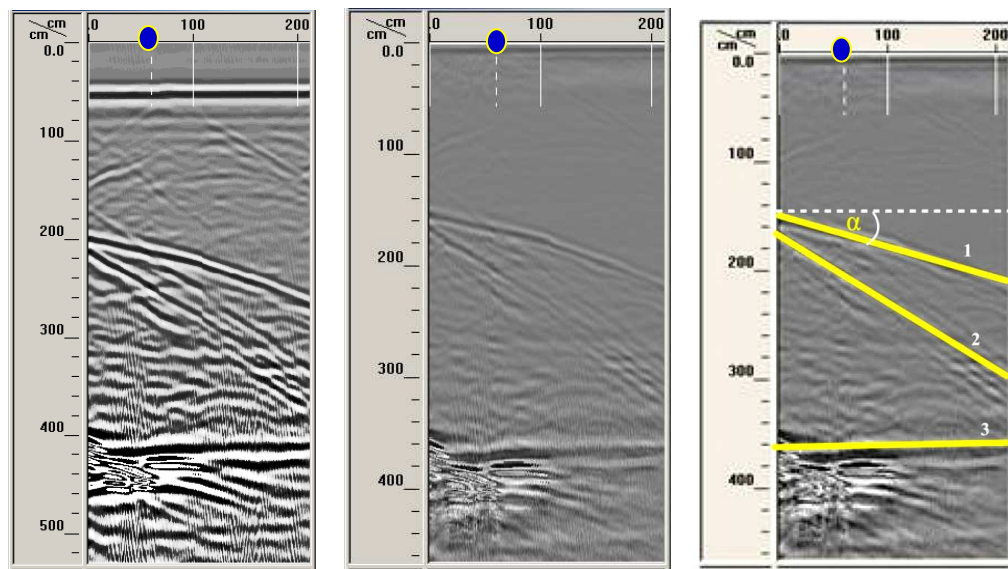




Figure 5.28: The radiogram of profile 1 at St.1. Raw radiogram (A), processed radiogram (B), and the detected hidden subvertical joints (yellow lines) (C). The strike of joint No.1 has an apparent declination angle (α) is 17° and so a true declination angle (β) is 17.80° .

The true perpendicular depths (d) can be estimated using equation 3.21 ($d = z / \cos \beta$). However, the apparent perpendicular depth (z) has to be estimated first from the radiogram using appropriate software (RADAN) as shown in Figure 5.28. This apparent perpendicular depth is estimated from the processed radiogram but before migration process as shown in Figure 5.28. The resultant declination angles and the perpendicular depths are listed in the appendix.

To explain how manual migration was done using our new equation (5.1), For instance as at station 3, the hidden subvertical joint No. 1 whose trace was depicted in radiogram image (Figure 5.28) has an apparent declination angle ($\alpha = 17^\circ$); and thus by applying the equation 5.1 ($\sin \beta = \tan \alpha$), it has a true declination angle ($\beta = 17.80^\circ$) as listed in Table 5.4.

Table 5.4: The values of the apparent and true perpendicular depths of the detected hidden subvertical joint No.1 at St.3.

Joint No.	Apparent perpendicular depths (z) from point 1 on the rock slope face of St.3, in cm.	Apparent (α) and true (β) declination angle of the strike		True perpendicular depths (d) from index point 1 on the rock slope face of St.3, in cm
	Point 1 	α	β	Point 1 
1	165	17°	17.8°	167

The most important point for this research is to estimate the apparent and true perpendicular depths, z and d respectively, from the locations of the three index points, on which GPR tick marks were taken at the rock slope face of each station of the study area, to the detected hidden subvertical joints separately (Table 5.4).

Three fixed slight marks were created at each station during the field work, so these marks represent the location of both the tick marks of GPR data records and the three index point which will be used for LIDAR data analysis as will be explained later in this chapter. The apparent perpendicular depths (z) can be easily estimated from the 2-D radiogram image and/or the created 3D radiogram image (Figures 5.28 and 5.29 and Table 5.3) and as well as the true perpendicular depths (d) can be estimated (Table 5.3).

Therefore, a true 3-D geometry of the detected joints can be created as shown in Figure 5.29. Those inferred orientations of the detected hidden subvertical joints were extrapolated at one end of their planes to be located appropriately behind the rock slope faces as shown in the Figure 5.29.

These 3D geometrical images provide accurate information about the extension of the linear traces of some detected hidden joints. This extension can be transferred to strike direction which needs to be estimated in addition to the dip direction and dip angle. These 3D GPR images of the planes of the detected hidden joints can be related to the plane of the rock slope face measured by LIDAR. Then, based on the combination between the GPR data and the LIDAR data, the geometry of the detected hidden subvertical joints can be estimated using the concept of the equation of plane as will be explained in the next section.

5.2.3 LIDAR Field Measurements. LIDAR or Terrestrial LIDAR (Light Detection And Ranging) scanner is a new technology that can provide detailed information about the geometry and discontinuities orientations of rock slope faces with no need for physical contact-measurements (Hack & Turner, 2002; and Slob et al., 2005).

LIDAR scanner is known in some references as the 3-D TLS (the 3-dimensions Terrestrial Laser Scanner).

In LIDAR scanner, a point is analogous to the pixel on which digital cameras work and many points make up which is called a point-cloud. The 3D TLS transmits a green laser pulse to the object of interest which reflects the laser signal back to the instrument.

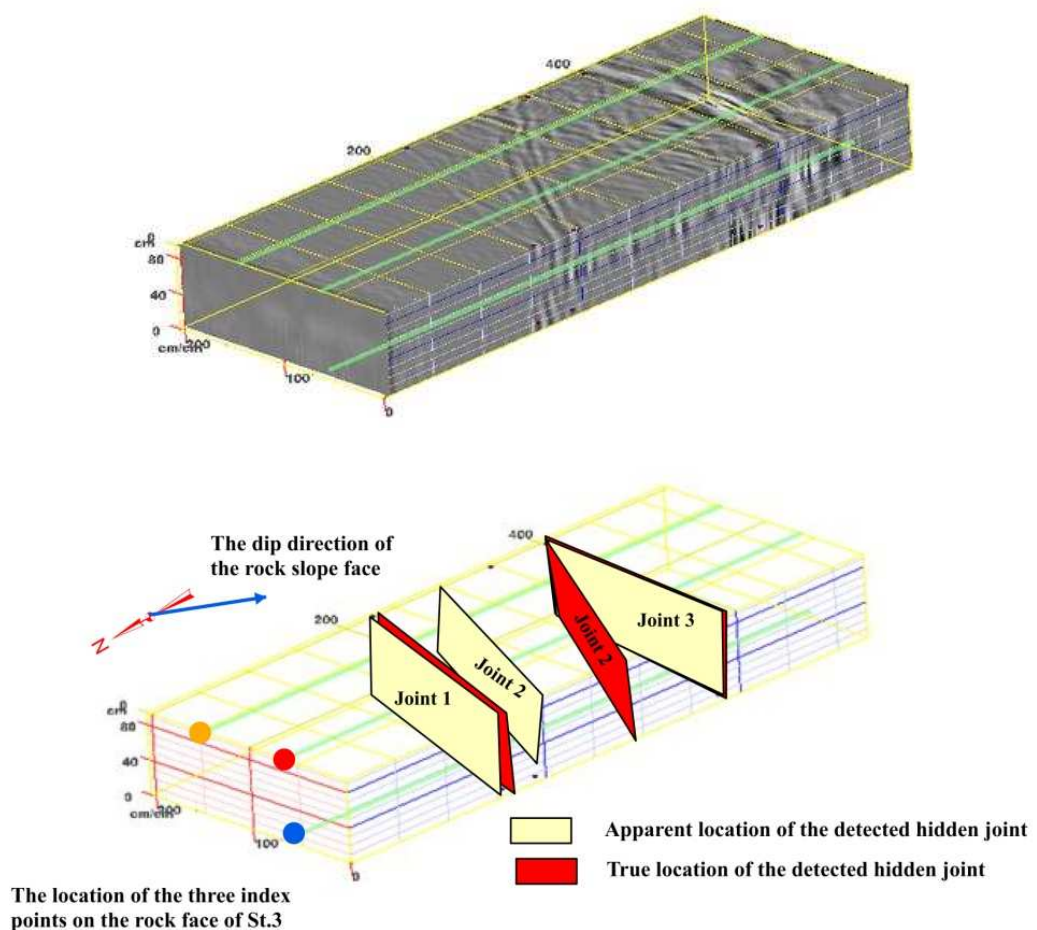


Figure 5.29: The created 3D image of St. 3 using RADAN software (above) and the 3D-image for the detected hidden subvertical joints with apparent and true strike directions.

The horizontal distance between the instrument and the object is measured using the time of flight or a phase comparison between the outgoing and the returning signal. Each point is then identified with three coordinates X, Y, Z, while a color is associated with the level of reflectivity from the surface.

LIDAR scans were taken using a Leica ScanStation II scanner (Figure 5.30). ScanStation-II scanner is a tripod-mounted system which deploys front and top windows with an oscillating mirror design to cover the full field-of-view of 360° horizontally and 270° vertically. In addition, it has a detection range of 90 m at 90% of reflectivity. Moreover, it can scan 50,000 points per second with a high accuracy in the order of 3-5 mm. A connected laptop collects recorded data on range, angles, and degree of reflectivity of returning laser signals. The scanning system also collects simultaneous photographs from a digital camera which is suited inside the system itself.



Figure 5.30: A Leica ScanStation II (LIDAR scanner) which was used in this study.

The grass, shrubs, and small plants were removed manually from some of the rock slope faces in order to create a clear and clean view for using the LIDAR scanner (Figure 5.31). The LIDAR scanner was used at all stations separately. Each station has its own point-cloud data.



Figure 5.31: Station 1 before (A) and after (B), respectively, removing the grass to create a clean view for using the LIDAR. Notice that the locations of the three index.

5.2.3.1 Calibration and geometry of rock slope face measurements using LIDAR. The LIDAR point cloud is defined by a set of (X, Y, Z) coordinates where z is the vertical coordinate and which is inherently correct and always is vertical assuming that the LIDAR is correctly level. Since LIDAR's coordinates, X, Y, and Z coordinates, do not typically match a global geographic coordinates, a single calibration measurements is required for LIDAR measurements, and which can be simply conducted using a Brunton compass (Maerz et al., 2012).

A reference object has to be identified and selected at each station (rock slope face). This reference object can be any part of the station itself, such as a vertical joint plane, or any other subvertical-planar object whose geometry can be measured using the compass. The last one was chosen and used in this study since it has smooth surfaces and fixed geometry and which can be used at all station of the study area (Figure 5.32).

The dip direction and dip angles were measured using the compass for both the reference object and the rock slope face at each station. The measurements were recorded in a field notebook (Table 5.5). Then a scan for each station including the reference object was conducted by the LIDAR to create a point cloud image for that station (Figure 5.32).

Later in the office, using the Cyclone⁶ program, Cyclone-SCAN is the software interface for operating the Leica ScanStation, HDS6100, and HDS3000, open the LIDAR viewer for that station which was scanned, e.g. station 1. Pick three individual points on, first, the surface of the reference object using the mouse cursor. These points should spread out as far as possible on the same surface of the reference object, and care must be taken that the three points are not co-linear or close to be collinear.

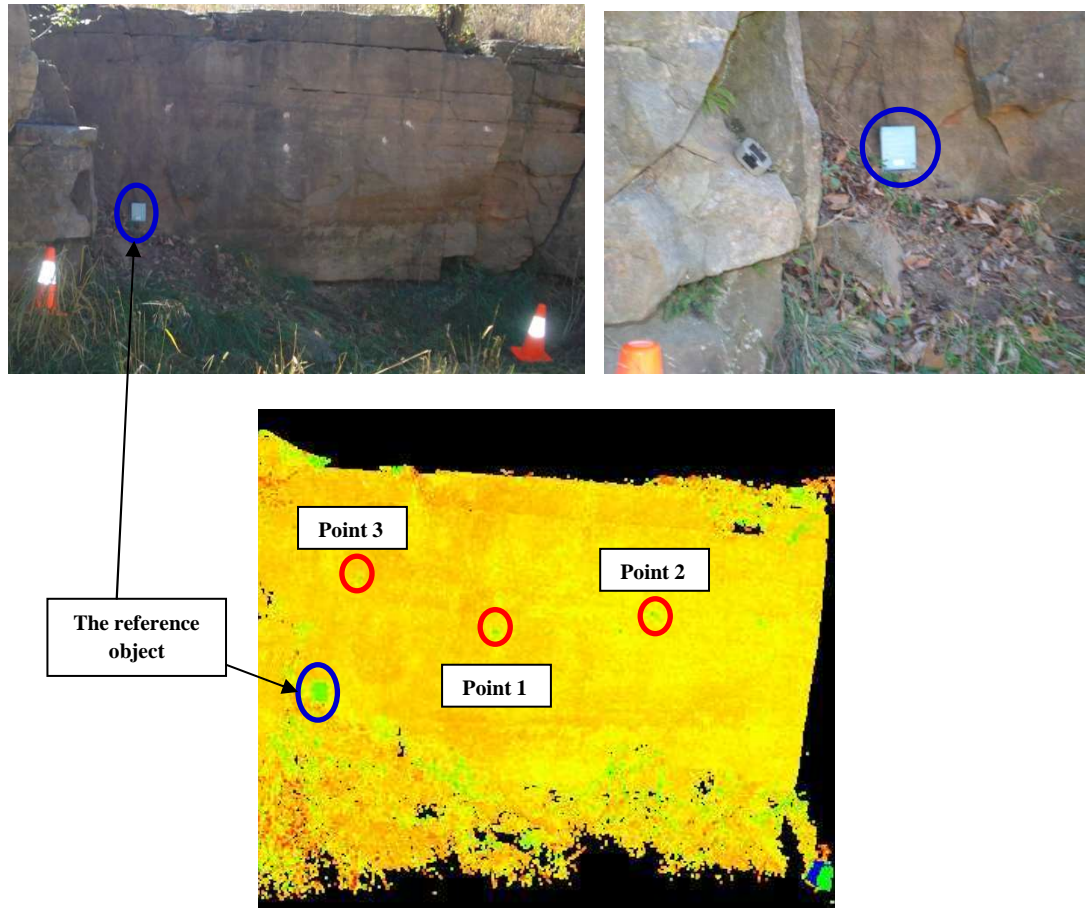


Figure 5.32: The location of both the reference object (the blue circle) and the three index points (red circles) at St. 1. The below image is a point cloud image using LIDAR.

Table 5.5: The field measurements using a Brunton compass for both the reference object and the rock slope face at station 1.




Field Measurements at St.1			
Dip direction (D.D.) and dip angle (θ)			
The reference object		The rock slope face	
D.D.	θ	D.D.	θ
025°	87°	025°	84°

Some LIDAR viewer will allow the coordinates of the data points to be exported; however in our case, the coordinates of these three selected points were recorded manually (Table 5.6). Do the same steps for the rock slope face, e.g. St.1, however, the selected three points have to be the three index points which were marked on the rock slope face (as shown in Figure 5.32), then record the coordinates of the rock slope face manually (Table 5.7.).

Table 5.6: The coordinates of the three points of the reference object at station 1 at site 1 using Cyclone 6 program.

3-point coordinates of the reference object			
Point	X	Y	Z
1	5340.39	16836.05	- 818.78
2	5413.34	16797.72	- 865.40
3	5361.48	16814.03	- 924.44

Table 5.7: The coordinates of the three index points of the rock slope face at station 1 using Cyclone 6 program.

The three index point coordinates at the rock slope face of St.1			
Point	X	Y	Z
1 	6458.09	16235.77	-324.57
2 	7422.82	15878.50	-122.79
3 	5639.71	16751.02	-003.56

5.2.3.1.1 Three point equation and the conversion to spherical coordinates.

The standard equation of a plane in a space is defined as:

$$AX + BY + CZ + D = \text{zero}$$

Where (A, B, C) is a vector normal to the plane. The equation of the plane through 3 different points (X₁, Y₁, Z₁), (X₂, Y₂, Z₂), and (X₃, Y₃, Z₃) is given by the following determinants:

$$A = \begin{vmatrix} 1 & Y_1 & Z_1 \\ 1 & Y_2 & Z_2 \\ 1 & Y_3 & Z_3 \end{vmatrix} \quad B = \begin{vmatrix} X_1 & 1 & Z_1 \\ X_2 & 1 & Z_2 \\ X_3 & 1 & Z_3 \end{vmatrix} \quad C = \begin{vmatrix} X_1 & Y_1 & 1 \\ X_2 & Y_2 & 1 \\ X_3 & Y_3 & 1 \end{vmatrix} \quad D = - \begin{vmatrix} X_1 & Y_1 & Z_1 \\ X_2 & Y_2 & Z_2 \\ X_3 & Y_3 & Z_3 \end{vmatrix}$$

Expanding the above matrixes gives:

$$A = Y_1 (Z_2 - Z_3) + Y_2 (Z_3 - Z_1) + Y_3 (Z_1 - Z_2)$$

$$B = Z_1 (X_2 - X_3) + Z_2 (X_3 - X_1) + Z_3 (X_1 - X_2)$$

$$C = X_1 (Y_2 - Y_3) + X_2 (Y_3 - Y_1) + X_3 (Y_1 - Y_2)$$

$$-D = X_1 (Y_2 Z_3 - Y_3 Z_2) + X_2 (Y_3 Z_1 - Y_1 Z_3) + X_3 (Y_1 Z_2 - Y_2 Z_1)$$

Note that if the three points are co-linear then the normal vector (A, B, C) will be (0, 0, 0), so the three selected points on a surface of the reference object or on the rock slope face have to be nor collinear not closely co-linear. Then, (A, B, C) is converted to a unit normal vector as follows:

$$(X, Y, Z) = (A, B, C) / \text{sqrt} (A^2 + B^2 + C^2)$$

Accordingly, Cartesian coordinates (X, Y, Z) are converted to spherical coordinates (r, θ , ϕ) as illustrated in Figure 5.33. One should be aware that the convention of naming the two angles (θ , ϕ) is sometimes reversed in some reference literatures which may cause kind of confusion. Since the concern is with normal unit on the unit hemisphere, r will always be equal to 1, and so will not be calculated (Maerz et al., 2012).

The values of θ , which is the dip angle, and ϕ (in radians) are calculated:

$$\cos \theta = Z/r, \text{ where } r = 1$$

$$\tan \phi = Y/X, \text{ where if } X = \text{zero, } \tan \phi \text{ is undefined.}$$

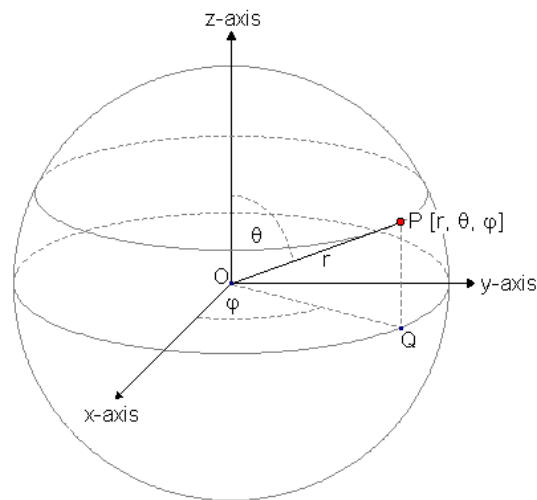


Figure 5.33: Cartesian coordinates are related to spherical coordinates (Adopted from http://www.vias.org/comp_geometry/math_coord_sphere.htm).

The geographic coordinates system requires a value between 0 and 360° (in radian: 0 and 2π), therefore, the transformation is as follows (Maerz et al., 2012):

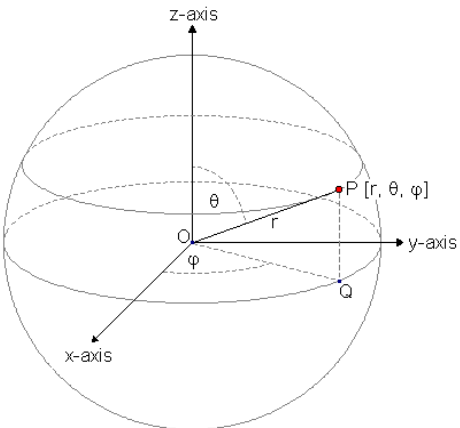
- i. If in quadrant 1 ($X > 0, Y < 0$), $\varphi \rightarrow 90^\circ - \varphi$
- ii. If in quadrant 2 ($X < 0, Y < 0$), $\varphi \rightarrow 180^\circ - \varphi$
- iii. If in quadrant 3 ($X < 0, Y > 0$), $\varphi \rightarrow 270^\circ - \varphi$
- iv. If in quadrant 4 ($X > 0, Y > 0$), $\varphi \rightarrow 360^\circ - \varphi$

The φ angle is then rotated from local coordinates system obtained from LIDAR to a global coordinates system referred to y axis as the North direction. All these mathematical steps are strongly recommended to be calculated using Excel Microsoft program. Then, on the excel sheet, the measurements obtaining from LIDAR for the reference object can be calibrated by a comparison with those ones taken by the compass in the field. This comparison is for the measured geometry of the reference object by the compass and the LIDAR (Table 5.8).

Once that is done, the Cartesian coordinates of the rock slope face measured by LIDAR (Table 5.7) will be entered into the excel sheet with no more need to make any more calibration for any taken measurements at that particular station where the measurements of the reference object were already calibrated (Table 5.9). In other words, each station will need one calibration only for the attitude of the reference object at that station. The reference object could be any planar part of the rock slope face or any other selected object which has a planar surface.

Table 5.8: The coordinate values and the geometry of the reference object for LIDAR measurements calibration at the rock slope face of St.1.

3-point coordinates of the reference object				Dip direction (D.D.) and dip angle (θ) measurements			
				Field		LIDAR	
Point	X	Y	Z	D.D.	θ	D.D.	θ
1	5340.39	16836.05	- 818.78	025°	87°	025°	84°
2	5413.34	16797.72	- 865.40				
3	5361.48	16814.03	- 924.44				



$\theta = 84^\circ$ (by LIDAR)

$\phi = 66^\circ$

The correction of the dip direction rotation = 179° clockwise.

Table 5.9: Geometrical measurements of the rock slope face at St.1 after the calibration process for LIDAR measurements.

The three index point coordinates at the rock slope face				Geometry of the rock slope face			
Point	X	Y	Z	Field		LIDAR	
				D.D.	θ	D.D.	θ
1	6458.09	16235.77	-324.57	028°	73°	026°	69°
2	7422.82	15878.50	-122.79				
3	5639.71	16751.02	-003.56				

5.2.3.1.2 The geometry of the detected hidden subvertical joints using

LIDAR. As illustrated in Figure 5.34, the rock slope face of St.1 was treated as a plane whose dip angle and dip direction 69° and 026° respectively (Table 5.9). The true perpendicular depth (d) from each index point on the rock slope face to each detected hidden joint is different and which was measured from both 2-D and 3-D GPR data image and listed in Table 5.10 (see the appendix). On other words, each detected joint has three corresponding points to those the three index points. Those three points are defined in this research as the three corresponding index points.

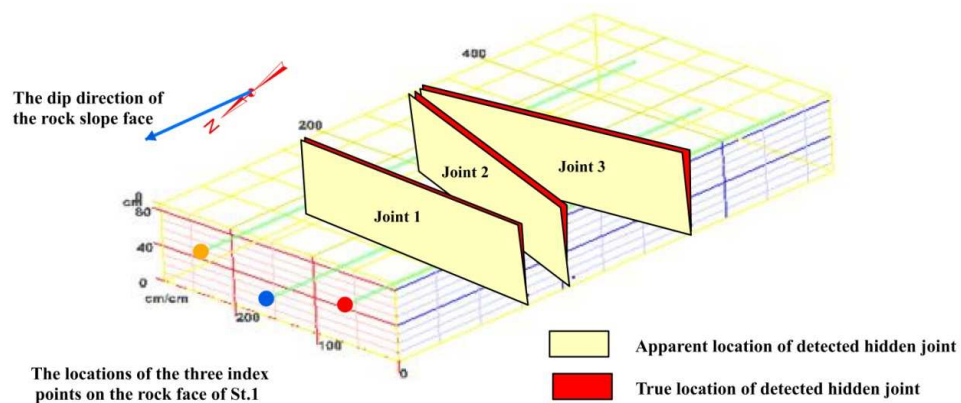








Figure 5.34: The 3D image of St.1 showing the apparent and true geometry of the detected hidden subvertical joints.

Table 5.10: The apparent and true perpendicular depths from the three index point on the rock slope face of St.1 to the detected hidden subvertical joints.

Joint No.	Apparent perpendicular depths (z) from the 3-points on the rock face of St.1, in cm.			Apparent (α) and true (β) Declination angle of the strike		True perpendicular depths (d) from the 3-points on the rock slope face of St.1, in cm		
	Point 1 	Point 2 	Point 3 	α	β	Point 1 	Point 2 	Point 3 
1	148	133	170	11°	11.2°	149	135	171
2	261	234	282	16°	16.7°	262	237	284
3	325	344	314	10°	10.2°	327	345	315

The depth direction, which is perpendicular to the strike direction, at each station was treated as a vector and so resolved to two components X' and Y'' components. As illustrated in Figure 5.35, the depth direction vector of St.1 was resolved to:

$$Y' = Y - d \cos 26^\circ; \text{ and}$$

$$X' = X - d \cos 64^\circ$$

Then the coordinates for each detected joint can be calculated, and then by using the 3-point equation which was calibrated for the LIDAR measurements, the geometry can be determined for each detected hidden joint. Verification field measurements for some those detected joints was conducted using a Brunton Compass, and the results showed good correlation (Table 5.11). All the field data and calculation results are listed in the Appendix.

Generally, the geometrical results showed good agreement between those measured GPR and LIDAR in a combination and those measured using a geological compass as will be discussed in the next Chapter.

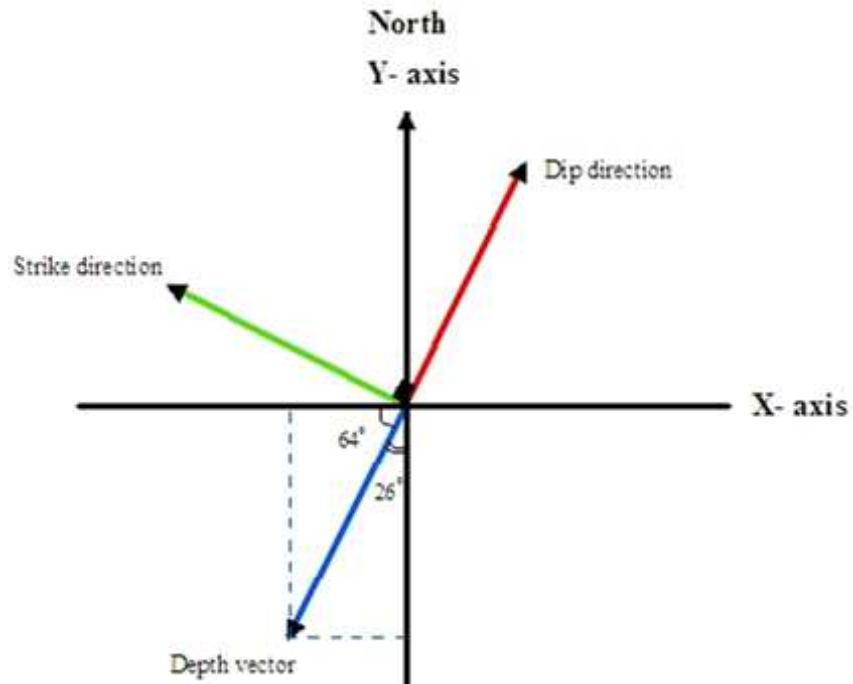


Figure 5.35: The depth vector at St.1 was resolved to: $Y' = Y - d \cos 26^\circ$; and $X' = X - d \cos 64^\circ$.

Table 5.11: Geometrical measurements using LIDAR for the detected hidden subvertical joints at St.1.

		Geometrical measurements of the detected hidden subvertical joints						
Joint No.	Point No.	The 3-corrospoding index points coordinates			LIDAR		Filed verification	
		X'	Y'	Z'	D.D.	θ	D.D.	θ
1	1	6392.77	16101.85	-324.57	025°	69°	025°	NA
	2	7363.64	15757.16	-122.79				
	3	5564.74	16597.33	-003.56				
2	1	6343.23	16000.28	-324.57	024°	68°	027°	72°
	2	7318.92	15665.48	-122.79				
	3	5515.20	16495.76	-003.56				
3	1	6314.73	15941.86	-324.57	027°	69°	026°	71°
	2	7271.57	15568.41	-122.79				
	3	5501.61	16467.90	-003.56				

Now, the orientations of the detected hidden subvertical joints have been measured. Then, a stereonet Lambert lower hemisphere projection using OpenStereo software created by Grohmann and Campanha (IGc-USP) was conducted to plot all the measured geometry of both exposed and hidden joints of each station separately. In general, the stereonet projection helps to build an image about the joints and joint sets distribution, and thus, to evaluate and converted this distribution to data can be integrated into slope stability analysis. However, in our research, the main point of using the stereonet projection was to plot the distribution of the measured joints, both exposed and hidden subvertical joints, to see if the measured hidden joints can make a difference a difference in terms of poles distribution (Figure 5.36).

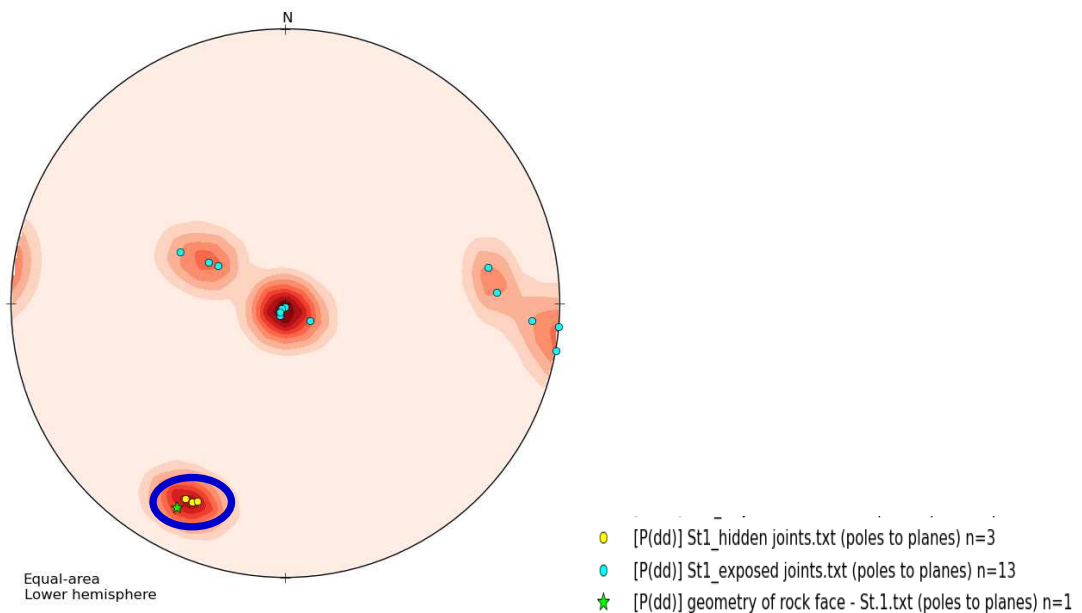


Figure 5.36: Equal area projection shows that the three detected hidden subvertical joints in station 1 represent an individual joint set (blue circle).

6. RESULTS AND DISCUSSION

6.1 OVERVIEW

In terms of rock type and locations, two different sites were selected to represent the study area of this research. Site 1 is a sedimentary rock type (sandstone) which is located on the 44 highway in Phelps County, MO (Figure 2.12). Site 2 is an igneous rock (ignimbrite) located on the 72 highway in Madison County, MO (Figure 2.13). It is necessary to mention that all of station 1, 2, and 3 are located on one side of site 1 while stations 4 and 5 on the other side; however all of them are close for each other (Figure 2.12). Moreover, station 6 and station 7 are on opposite sides at site 2 with a distance between them about 0.60 mile (Figure 2.13).

A reconnaissance field visits were done for both sites to build a general view about the structural geology and the geometry of both the two sites. Based on these visits, each site was divided into different station, each station represent an individual rock slope, on which field work was performed and carried out utilizing the following methods:

- Manual measurements using a Brunton compass for the geometry for both the station and the exposed joints. The results of this method will be presented in this Chapter.
- A 400 MHz GPR monostatic antenna was used to detect both hidden subvertical and vertical joints at each station. The results are presented in the appendix.

- LIDAR technique using ScanStation2 to scan each rock slope face (station) in the purpose to measure the orientation of the detected hidden subvertical and vertical joints related to the geometry of the rock slope face of that station. The results are presented in the appendix while the procedures of how estimate the orientation of the detected hidden joints were explained in Chapter 5 – Methodology.

GPR data processing using RADAN software was done for all acquired data at each station. All the GPR raw data and the final processed data are in the Appendix. The velocity of GPR pulses travelling through sandstone and ignimbrite of site 1 and site 2 respectively was estimated in the lab. The velocity was 0.106 m/ns and 0.074 m/ns for sandstone and ignimbrite samples respectively.

Field verification for some detected hidden joints was done at all stations except station 4 and 5 in site 1. Moreover, kinematic analysis was conducted for both exposed joints and detected hidden joints for each station.

6.2 RESULTS OF THE STATIONS OF SITE 1

6.2.1 Station 1. The rock slope face of this station is relative smooth across which the 400 MHz GPR monostatic antenna was towed easily (Figure 6.1). Usually, rock slope faces have irregular and/or undulated surfaces which cause a minor variation in the value of the measured dip angle of the slope using a geological compass from one part to another part on the same rock face. However, the LIDAR scan can overcome this problem and give more reasonable and reliable measurements because it treats the whole

face as one plane using the 3-point equation which cannot be done using manual measurement methods (Table 6.1).

This valuable advantage of using LIDAR has been recognized during the work on this research. In spite of that difference between the measured geometry of the rock slope face using the LIDAR and that one using a geological compass, this difference was within $\pm 4^\circ$ for dip direction and within $\pm 2^\circ$ for dip angle which can be due to human and/or device errors (Table 6.1).



Figure 6.1: Front view and side view of the rock slope of the station 1 at site 1.

Table 6.1: The dip direction (D.D.) and the dip angle (θ) of the rock slope face of station 1 resulting from the manual method and the LIDAR technique.

Geometrical measurements of St.1			
Field		LIDAR	
D.D.	θ	D.D.	θ
028°	73°	026°	69°

The manual measurements using a Brunton compass for exposed joints on this station are listed on Table 6.2. Three joint set were identified using Lambert stereonet projection as shown in Figure 6.2.

Table 6.2: The manual geometrical measurements for dip direction (D.D.) and dip angle (θ) of the measured exposed discontinuities at the rock slope of St.1.

Joint No.	D.D.	θ	Joint No.	D.D.	θ
1	280°	90°	8	118°	26°
2	305°	09°	9	116°	35°
3	010°	01°	10	119°	23°
4	024°	04°	11	033°	03°
5	037°	02°	12	275°	90°
6	274°	79°	13	260°	64°
7	267°	66°			

The GPR technique was significantly able to identify three hidden subvertical joints at perpendicular depth from the rock slope face between 149 cm and 320 cm as illustrated in Figure 6.3 and in the appendix (Figures 3 & 4). As shown in Figure 6.1, the exposed side of this station is very limited in width, so it was not possible to track any linear trace of any one of those detected hidden joints. However, field verification measurements were done by investigating some discontinuities, whose planes extend inside and semi-parallel to the rock slope face of St.1, in the surrounding rock blocks as shown in Figure 6.3.

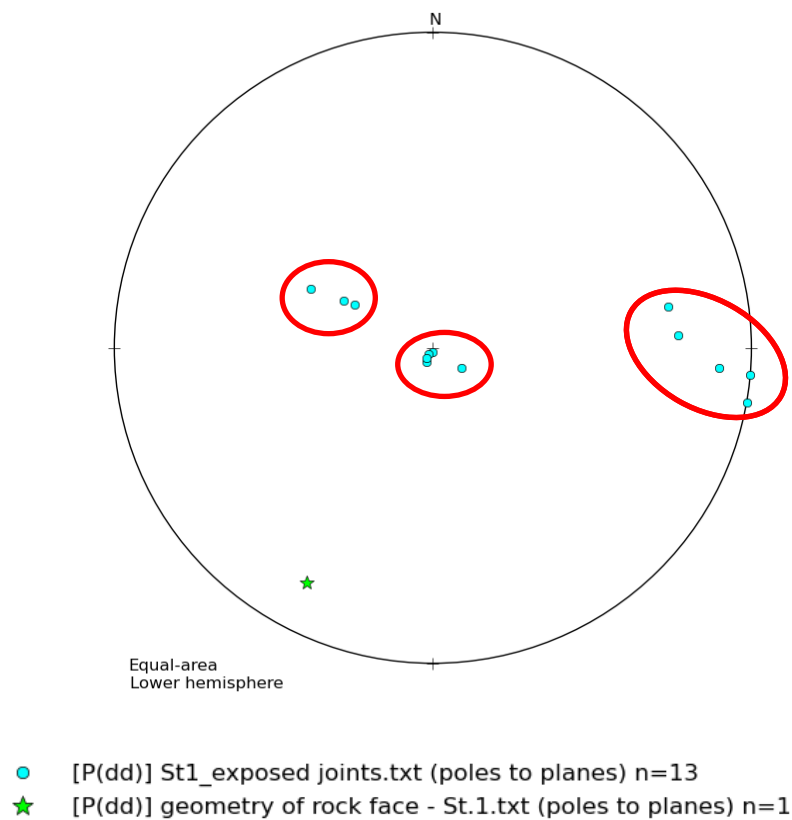


Figure 6.2: Projections of vectors normal to exposed joints and rock face planes (poles) on a unit lower hemisphere- Lambert stereonet at St.1. The poles of these exposed joints can be clustered into three sets.

The orientations for those hidden joints are determined using the LIDAR technique and the three point equation as listed in Table 6.3. Field verification measurements were possible for some of those hidden joints (Table 6.3).

When the orientations of those hidden joints were plotted on the equal-area stereonet projection, they produced a new joint set which can be added to those joint sets of the measured exposed joints. Based on the density contouring of the normal vectors (poles) of the detected hidden subvertical joints set, the joint representing the detected

hidden joints set has a dip direction of 025° and a dip angle of 69° as shown in Figure 6.4.

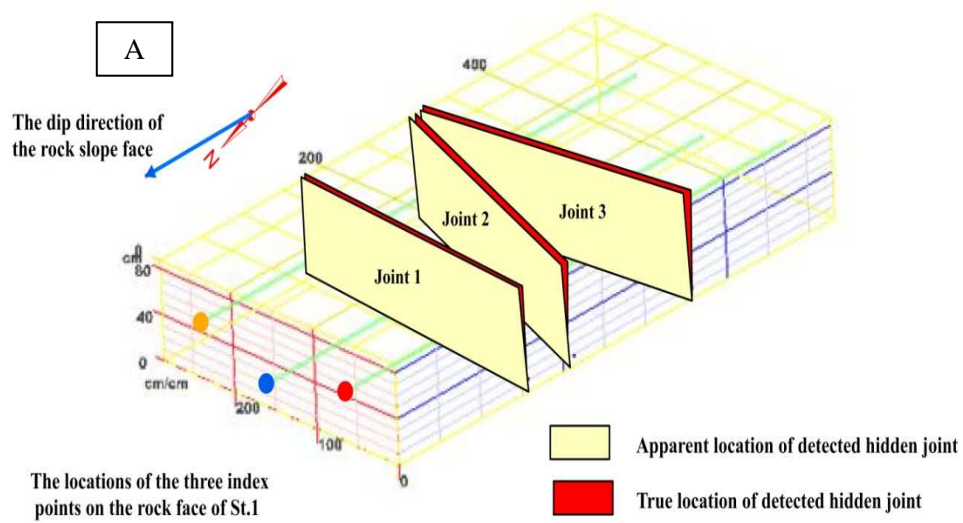


Figure 6.3: (A) True 3D GPR image for St.1 showing the location of the detected hidden subvertical joint. (B) Field verification was done by investigation some discontinuities whose planes extend parallel inside St.1, in the surrounding rock blocks.

Table 6.3: Some field verification measurements for the detected hidden subvertical joints at station 1.

Hidden Joint No.	LIDAR		Field verification	
	D.D.	θ	D.D.	θ
1	025°	69°	025°	NA
2	024°	68°	027°	72°
3	027°	69°	026°	71°

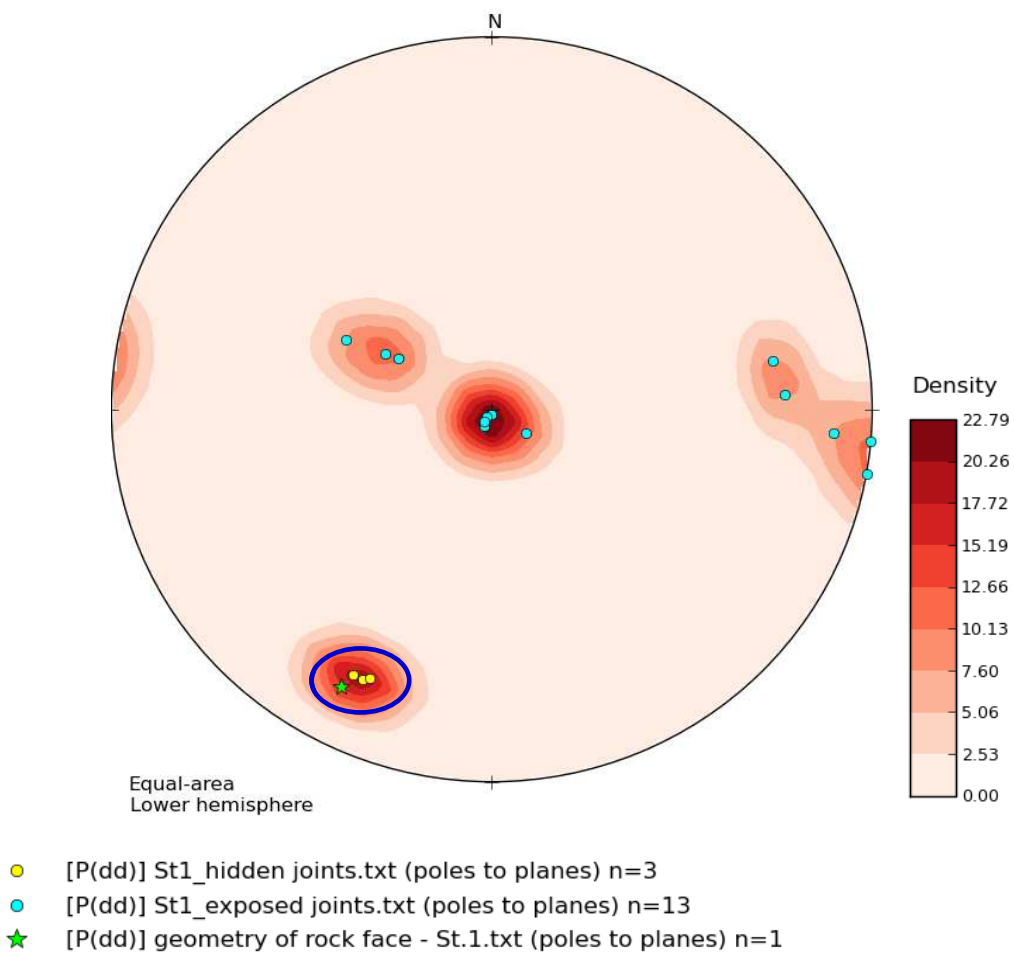


Figure 6.4: The poles of the three detected hidden joints at station 1 can be represented as a separate joint set (blue circle).

6.2.2 Station 2. Station 2 (St.2) is located next to St. 1; and it has almost the same strike and dip direction as St.1 (Figure 6.5). This station has a subvertical rock slope face whose dip direction is 020° using LIDAR (Table 6.4). The difference between the measured geometry of the rock slope face using the LIDAR and that one using a geological compass was $\pm 5^{\circ}$ for dip direction and $\pm 4^{\circ}$ for dip angle (Table 6.4).

Only few discontinuities are exposed on the rock face which may cause underestimation for slope stability analysis. The manual measurements using A Brunton compass for the measured exposed joints on this station are listed on Table 6.5. Three joint sets can be identified using Lambert stereonet projection as shown in Figure 6.6.



Figure 6.5: A front view of the rock slope of St.2 in site 1.

Table 6.4: The geometrical measurements for the rock slope face of St.2.

Geometrical measurements of St.2			
Field		LIDAR	
D.D.	θ	D.D.	θ
022°	85°	027°	81°

Table 6.5: Manual measurements for dip direction (D.D.) and dip angle (θ) of exposed discontinuities at St.2.

Joint	D.D.	θ
1	295°	89°
2	108°	55°
3	028°	04°
4	025°	03°
5	029°	01°
6	030°	02°
7	115°	72°
8	285°	90°
9	283°	88°

GPR technique was significantly able to identify two hidden subvertical joints at perpendicular depth from the rock slope face between about 200 cm and about 360 cm as illustrated Figure 6.7 as well as in the appendix (Figures 9 & 10). The orientations for those hidden joints are determined using the LIDAR technique by apply the three point equation as listed in Table 6.6.

Since these two detected joints have linear traces that appear on the side of the rock slope face at 200 cm and 270 cm for detected hidden joint 1 and joint 2 respectively (Figure 6.7), the field verification measurements were possible for those hidden joints (Table 6.6).

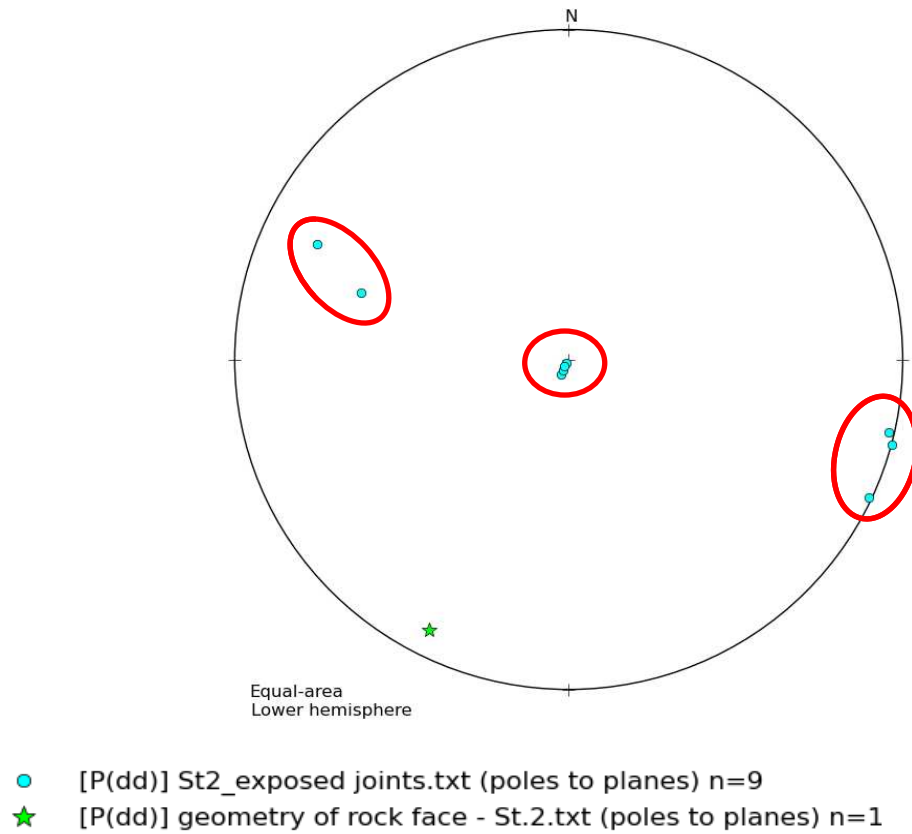


Figure 6.6: The Lambert stereonet projections of the normal vectors (the poles) of the measured exposed joints as well as the rock slope face of the station (St.2). The poles of these exposed joints can be clustered into three sets (red circles).

Table 6.6: The orientations of the two detected hidden joints measured by LIDAR at St.2 in addition to the field verification measurements.

Hidden Joint No.	LIDAR		Field verification	
	D.D.	θ	D.D.	θ
1	029°	78°	035°	85°
2	035°	82°	030°	83°

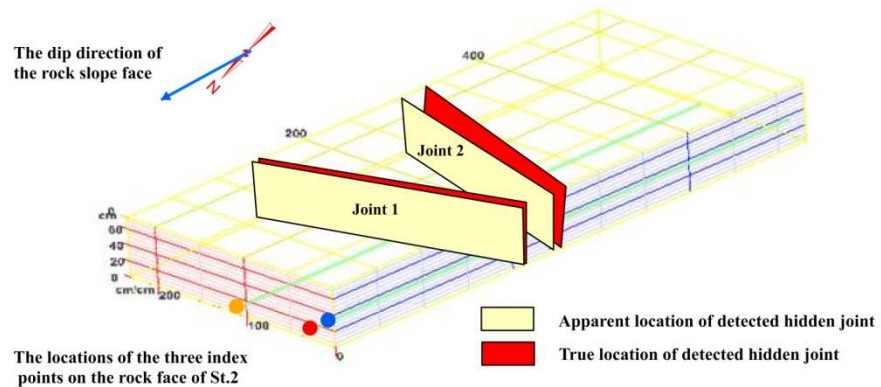


Figure 6.7: The position of the linear traces of the two detected hidden joints exposed on the side of the slope verifies the accuracy of the resulting true 3D GPR image of station 2. Note that the true perpendicular depths (d) of these two hidden joints in the 3D image were verified by field measurements.

The true perpendicular depths measured by GPR as illustrated in Figure 6.7 and showed in the appendix (Figures 9 & 10) match accurately those perpendicular depths as well as the orientations measured in the field. This give a strong indication about the accuracy and the reliability of using our new approach in detecting, mapping, and measuring the geometry of hidden subvertical joints in rock masses.

Based on the contouring of the poles concentration of the detected hidden subvertical joints set, the detected hidden joints can be clustered as a joint set whose dip direction and dip angle are 031° and 81° respectively as shown in Figure 6.8.

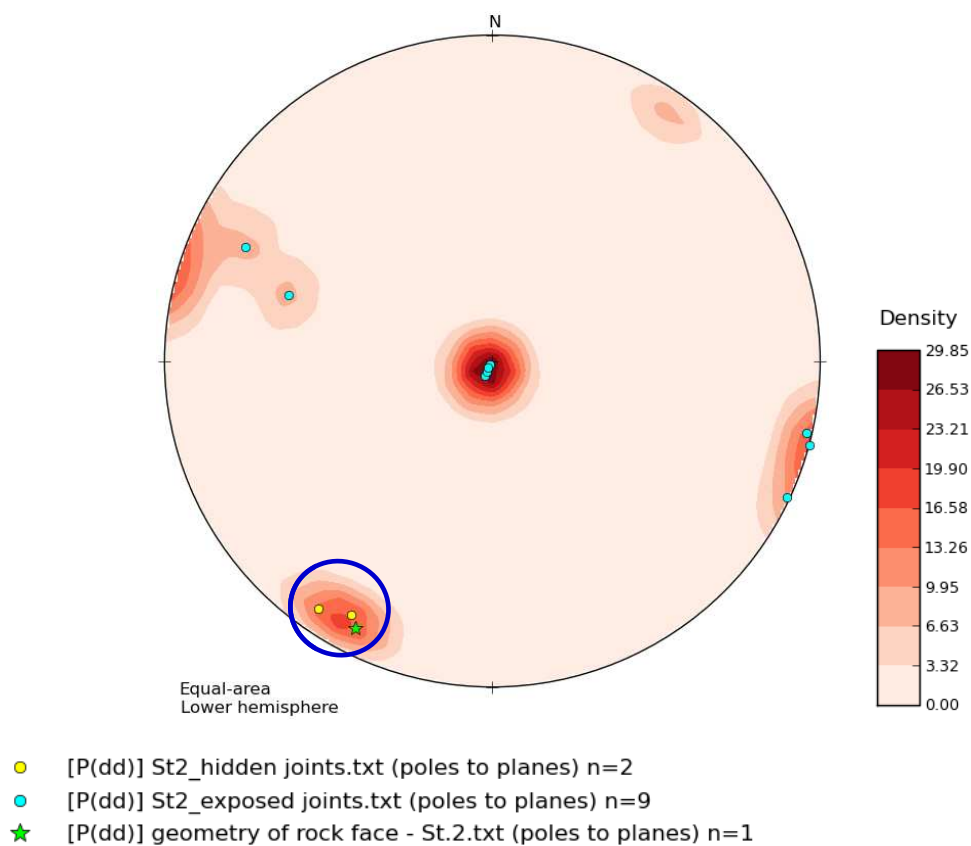


Figure 6.8: The poles of the two detected hidden joints at station 2 can be represented as a separate joint set (blue circle).

6.2.3 Station 3. Even though the rock slope face of this station is adjacent to both stations 1 and 2; it has a significant different dip direction which dips steeply into the face with a direction of 199° using LIDAR (Figure 6.9 and Table 6.7). The difference between the measured geometry of the rock slope face using the LIDAR and that one using a geological compass was $\pm 3^\circ$ for dip direction and $\pm 2^\circ$ for dip angle (Table 6.7).

As at station 2, only few discontinuities are exposed on the rock face of St.3. The manual measurements using A Brunton compass for exposed joints on this station are listed on Table 6.8. Six joint sets can be identified based on the stereonet projection shown in Figure 6.10.



Figure 6.9.: A front view of the rock slope of St.3 in site 1.

Table 6.7: The geometrical measurements for the rock slope face of St.3.

Geometry of the rock slope face of St.3			
Field		LIDAR	
D.D.	θ	D.D.	θ
202°	87°	199°	85°

Table 6.8: Manual measurements for dip direction (D.D.) and dip angle (θ) of exposed discontinuities at St.3.

Joint No.	D. D.	θ	Joint No.	D. D.	θ
1	025°	03°	9	290°	45°
2	283°	73°	10	280°	52°
3	280°	78°	11	272°	81°
4	025°	01°	12	332°	68°
5	050°	89°	13	336°	71°
6	019°	02°	14	272°	63°
7	017°	02°	15	311°	88°
8	119°	83°	16	309°	86°

GPR identified significantly three hidden subvertical joints at perpendicular depth from the rock slope face between about 160 cm and about 400 cm as illustrated in Figure 6.11 and also in the appendix (Figures 15 & 16). The orientations for those hidden joints are determined using the LIDAR technique and the three point equation as listed in Table 6.9. Only one of those detected joints has a linear trace appear on the side of the rock slope face as shown in Figure 6.11 , so the field verification measurements was possible only for this detected hidden joint, joint no.1 (Table 6.9). Based on the contouring of the poles concentration of the detected hidden subvertical joints set, this joints set has a dip direction of 197° and a dip angle of 88° as shown in Figure 6.12.

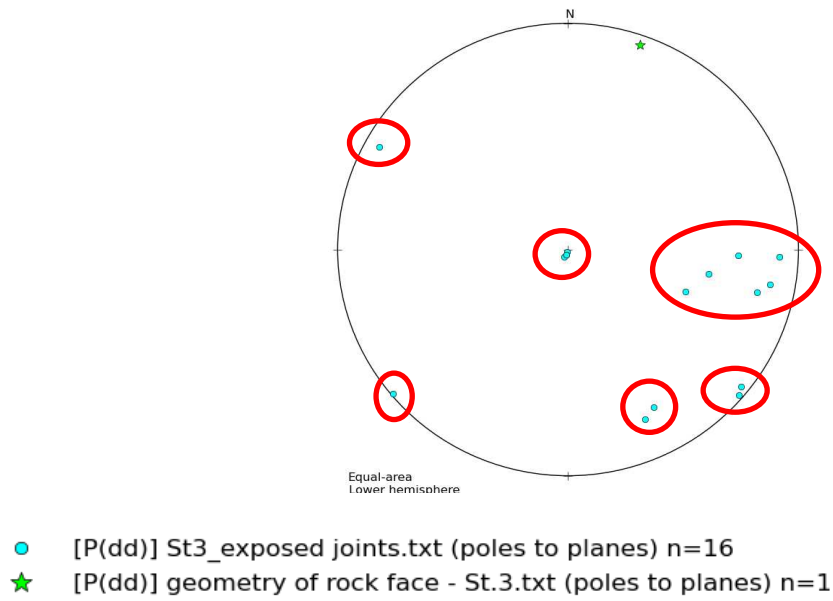


Figure 6.10: The poles of the measured exposed joints at St.3 can be clustered into six joint sets (red circles).

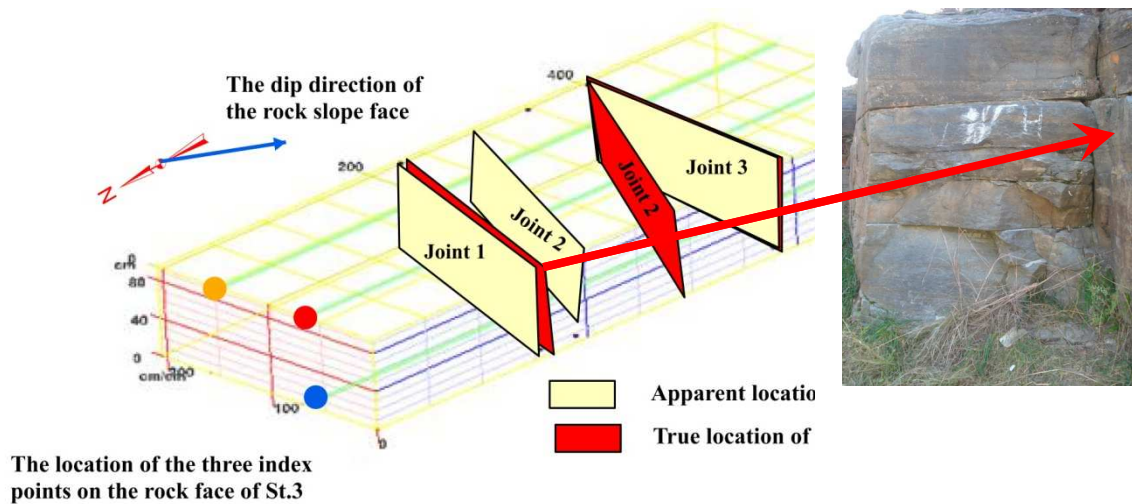


Figure 6.11: True 3D GPR image of station 2. Note that the true perpendicular depth (d) to the linear trace of the detected hidden joint (joint 1) in the 3D image was verified by field measurements.

Table 6.9: The orientations of the three detected hidden joints measured by LIDAR at St.3 in addition to the field verification measurements.

Hidden Joint No.	LIDAR		Field verification	
	D.D.	θ	D.D.	θ
1	197°	86°	194°	89°
2	193°	88°	NA	NA
3	199°	89°	NA	NA

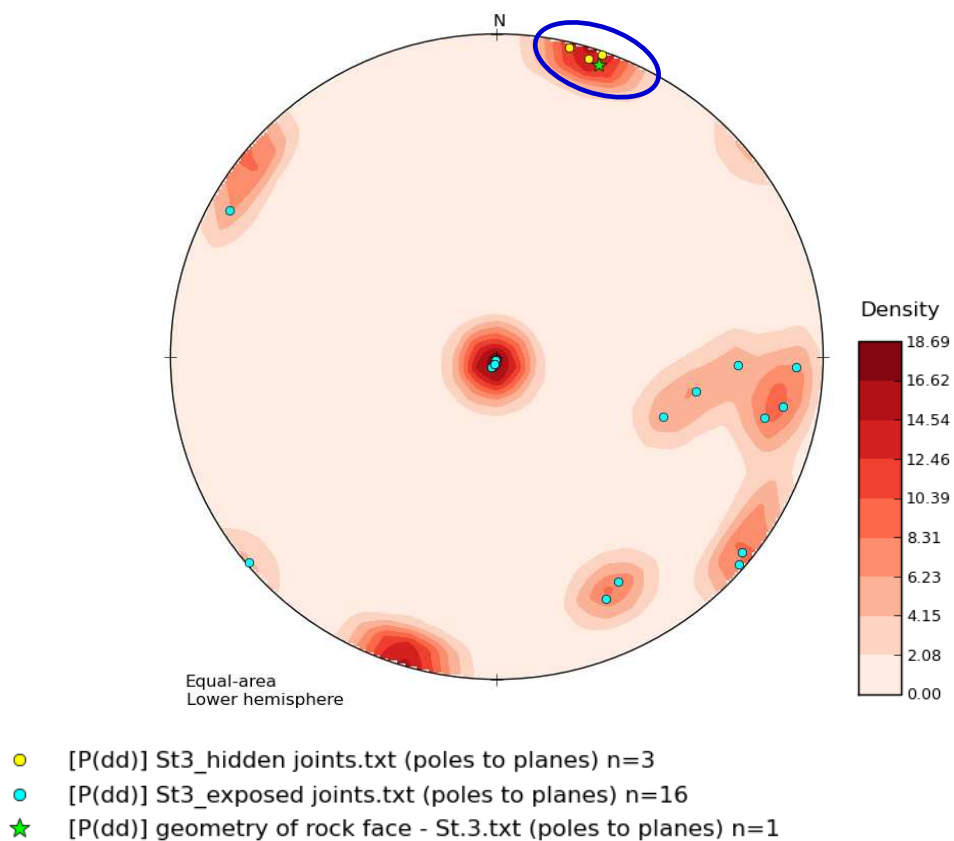


Figure 6.12: The poles of the two detected hidden joints can be represented as a separate joint set (blue circle) at station 3.

6.2.4 Station 4. The dip direction and dip angle of the rock slope face of this station is 202° and 90° respectively measured by LIDAR (Figure 6.13). The difference between the measured geometry of the rock slope face using the LIDAR and that one using a geological compass was $\pm 7^\circ$ for dip direction and $\pm 3^\circ$ for dip angle (Table 6.10).

A few discontinuities are exposed on the rock face of this station. The orientations of these discontinuities were measured using a Brunton compass as listed on Table 6.11. Based on the stereonet projection for those discontinuities, five joint sets can be identified as shown in Figure 6.14.



Figure 6.13: A front view of the rock slope of St.4 in site 1.

Table 6.10: The geometrical measurements for the rock slope face of St.4.

Geometrical measurements of St.2			
Field		LIDAR	
D.D.	θ	D.D.	θ
195°	87°	202°	90°

Table 6.11: Manual measurements for dip direction (D.D.) and dip angle (θ) of exposed discontinuities at St.4.

Joint No.	D. D.	θ	Joint No.	D.D.	θ
1	207°	03°	6	284°	72°
2	135°	87°	7	112°	78°
3	210°	15°	8	102°	85°
4	204°	01°	9	207°	01°
5	128°	49°	10	209°	02°

Only one hidden subvertical joint was identified at depth about 355 cm by GPR instrument as illustrated in Figure 6.15 and as well as in the appendix (Figures 21 & 22).

The orientation of this hidden joint was estimated by LIDAR using the 3-point equation. Its dip direction and dip angle was 021° and 89° respectively Table 6.12. Based on the density contouring on the stereonet for both exposed discontinuities and that hidden joint, a new joint set was identified representing that detected hidden subvertical joint as illustrated on Figure 6.16.

Unfortunately, field verification measurements were not possible for this joint since this joint is located deeply at depth about 3.55 m from the rock face of station 4 as illustrated in Figure 6.15 and in the appendix (Figures 21 & 22).

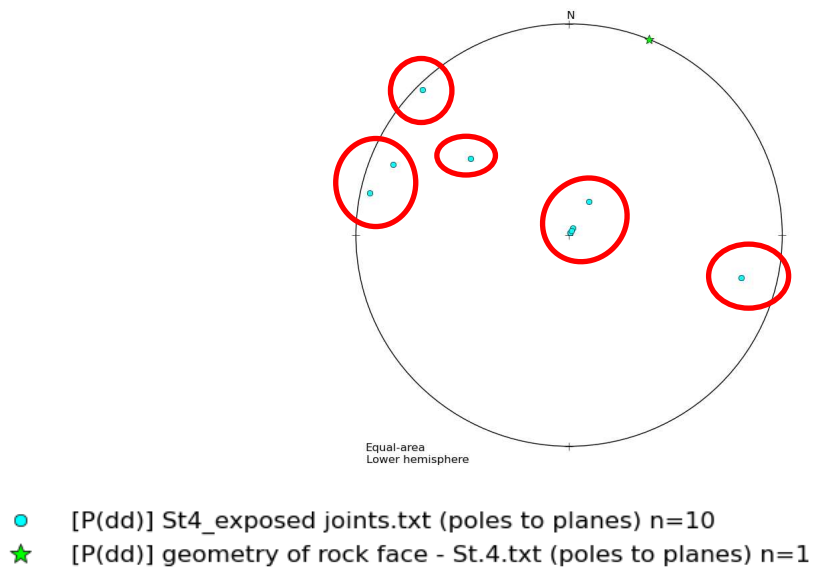


Figure 6.14: The Lambert stereonet projections of the normal vectors (the poles) of the measured exposed joints of St. 4 can be clustered into five joint sets (red circles).

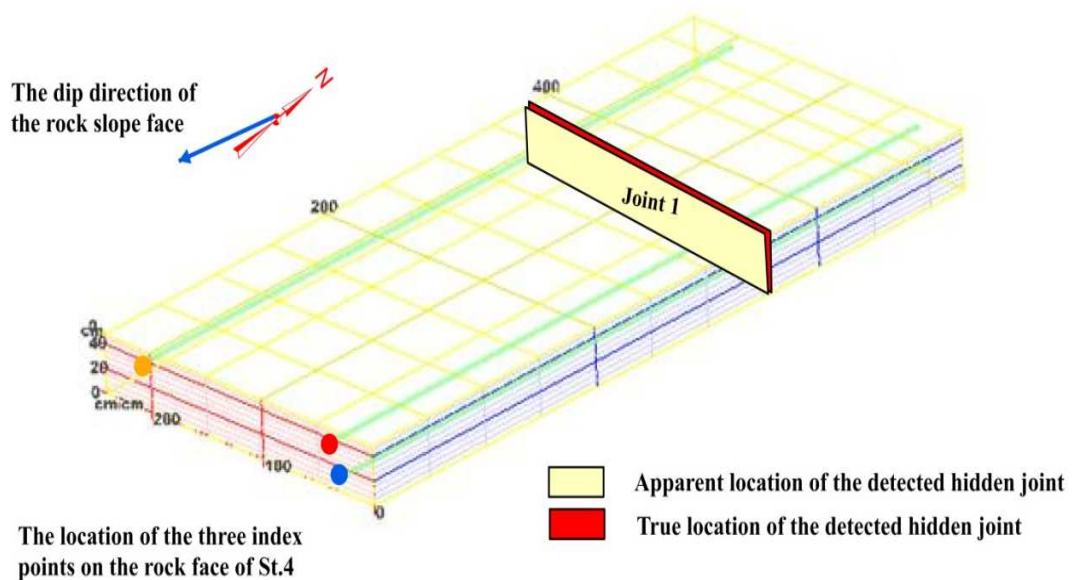


Figure 6.15: True 3D GPR image for St.4 showing the location of the detected hidden subvertical joint. Field verification was not possible for this station.

Table 6.12: The orientations of only the one detected hidden subvertical joint measured by LIDAR at station 4.

Hidden Joint No.	LIDAR		Field verification	
	D.D.	θ	D.D.	θ
1	021°	89°	NA	NA

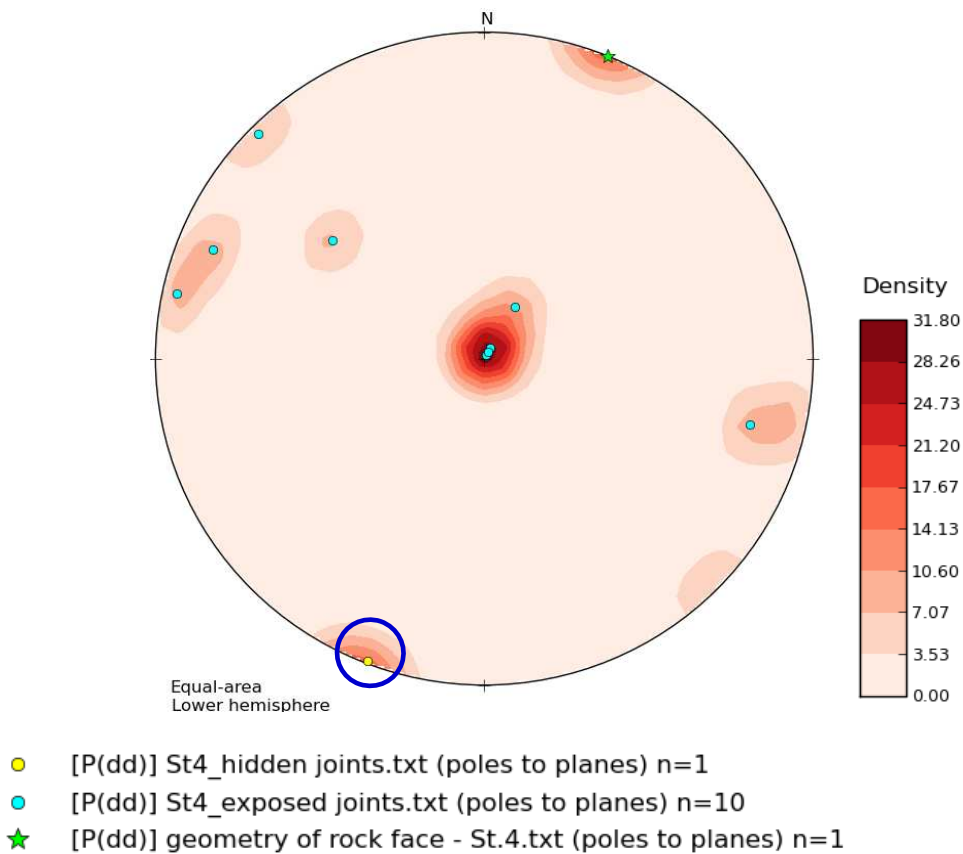


Figure 6.16: The detected hidden subvertical joint at St.4 can be represented as a separate joint set (blue circle).

6.2.5 Station 5. Station 5 (St.5) is located next to west of station 4. It has a subvertical rock slope face whose dip angle is 87° (Figure 6.17). The dip direction of this station seems toward the south-west however by using LIDAR, which can treat the whole of the scanned rock slope face or a part of interest of it as a plane, the dip direction is north-east. This advantage of using LIDAR is strongly beneficial in terms of slope stability analysis when relate detected hidden joints to the plane of the rock slope face.

The difference between the measured geometry of the rock slope face using the LIDAR and that one using a geological compass was $\pm 5^\circ$ for dip direction and $\pm 1^\circ$ for dip angle (Table 6.13).



Figure 6.17: A front view of the rock slope of St.5 in site 1.

Table 6.13: The geometrical measurements for the rock slope face of St.5.

Geometrical measurements of St.5			
Field		LIDAR	
D.D.	θ	D.D.	θ
010°	88°	015°	87°

The manual measurements for the orientations of the measured exposed discontinuities at this station are listed in Table 6.14. Four joint sets can be identified as shown in the stereonet projection in Figure 6.18.

The GPR technique was significantly able to identify four hidden subvertical joints at perpendicular depth from the rock slope face between about 180 cm and about 340 cm as illustrated in Figure 6.19 and as well as in the appendix (Figures 27 & 28). The orientations for those hidden joints are determined using the LIDAR technique and the three point equation as listed in Table 6.15.

Table 6.14: Manual measurements for dip direction (D.D.) and dip angle (θ) of the measured exposed discontinuities at St.5.

Joint No.	D. D.	θ	Joint No.	D. D.	θ
1	184°	02°	9	203°	87°
2	187°	01°	10	209°	05°
3	082°	71°	11	251°	89°
4	097°	03°	12	207°	90°
5	088°	87°	13	206°	89°
6	189°	02°	14	207°	00°
7	205°	03°	15	304°	59°
8	206°	03°	16	308°	57°

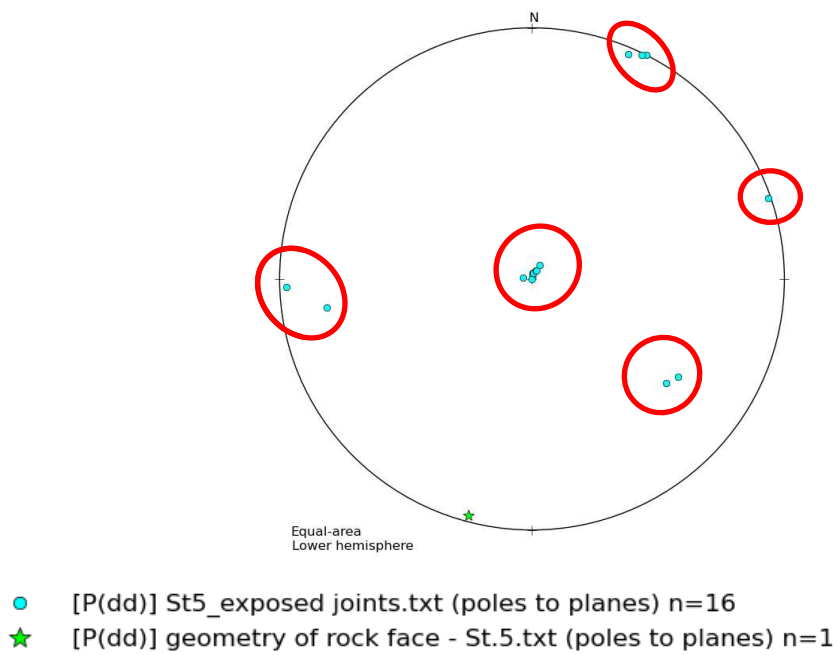


Figure 6.18: The Lambert stereonet projections of the normal vectors (the poles) of the measured exposed joints St.5 can be clustered into four joint sets (red circles).

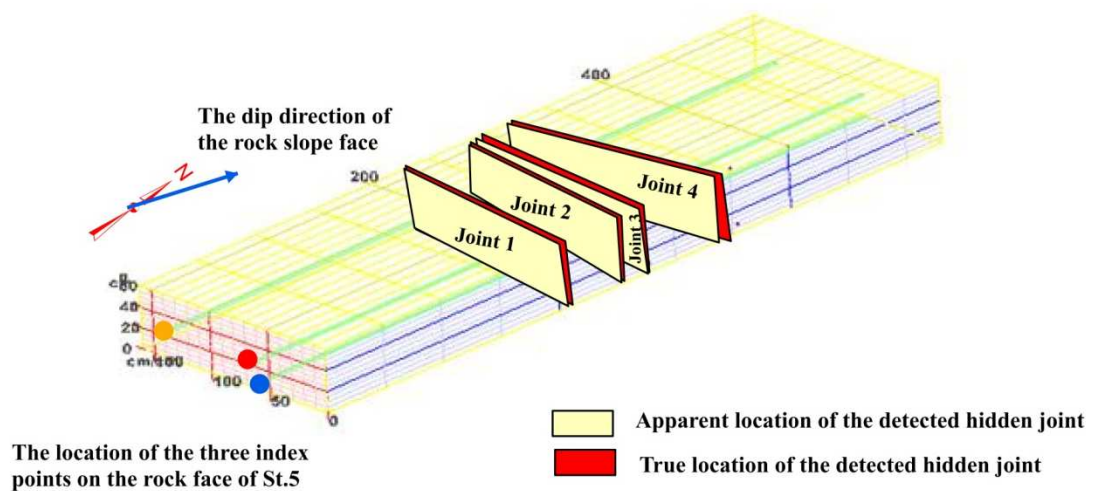


Figure 6.19: True 3D GPR image for St.5 showing the location of the detected hidden subvertical joint. Field verification was not possible in this station.

Table 6.15: The orientations of the four detected hidden joints measured by LIDAR at St.5 in addition to the field verification measurements.

Hidden Joint No.	LIDAR		Field verification	
	D.D.	θ	D.D.	θ
1	015°	88°	NA	NA
2	014°	89°	NA	NA
3	016°	88°	NA	NA
4	015°	82°	NA	NA

Based on the concentration contouring of the poles of both detected hidden joints and exposed joints, the hidden joints can be considered as an additional set which is parallel to joint set 4 but with an opposite dip direction (Figure 6.20). This joint set has a dip direction of 015° and dip angle of 87°.

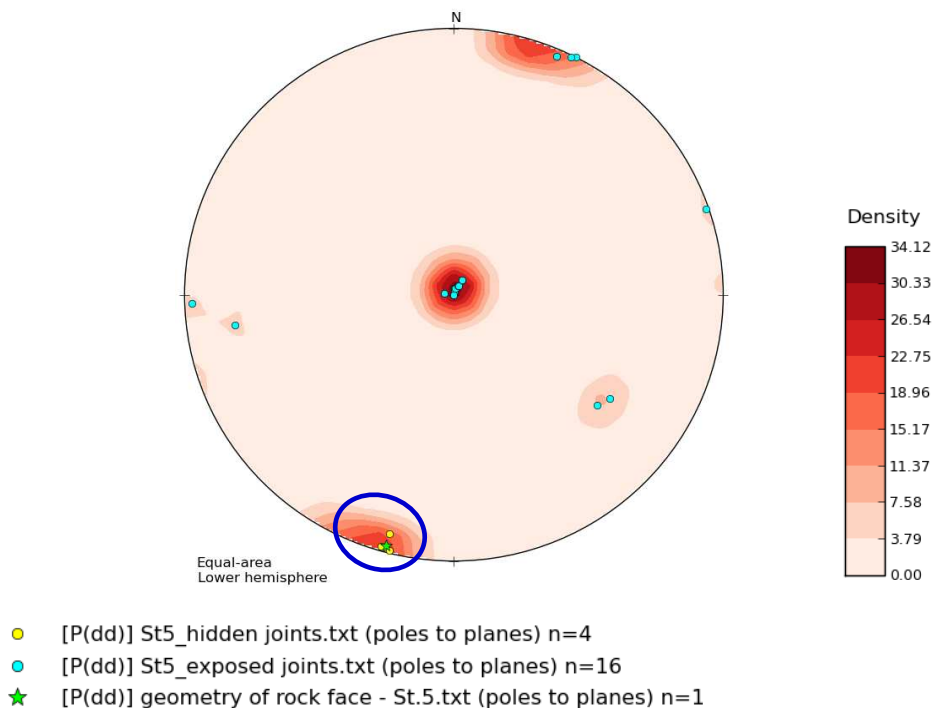


Figure 6.20: The normal vectors (the poles) of the four detected hidden subvertical joints at station 5 can be represented as a separate joint set (blue circle).

6.3 RESULTS OF THE STATIONS OF SITE 2

6.3.1 Station 6. This is the first selected station on the 72 highway in site 2, Madison County. This station numbered as station 6 based on the total number of the selected stations in both site1 and site 2 in the study area. This station has a subvertical rock slope as shown in Figure 6.21. The measured dip direction and dip angle using LIDAR of this rock slope station are 159° and 89° respectively. The difference between the measured geometry of the rock slope face using the LIDAR and that one using a geological compass was $1 \pm^\circ$ only for dip angle (Table 6.16).



Figure 6.21: A front view of the rock slope of St.2 in site 2 (Madison County).

Table 6.16: The geometrical measurements for the rock slope face of St.6.

Geometrical measurements of St.6			
Field		LIDAR	
D.D.	θ	D.D.	θ
159°	88°	159°	89°

The orientations of the measured exposed joints on the rock slope face of this station are listed in Table 6.17. The normal vectors (the poles) of these measured joints can be clustered into four sets as shown in Figure 6.22.

Table 6.17: Manual measurements for dip direction and dip angle of exposed discontinuities at St.6.

Joint No.	D.D.	θ	Joint No.	D.D.	θ
1	068°	84°	8	066°	84°
2	065°	90°	9	075°	90°
3	250°	78°	10	069°	70°
4	250°	36°	11	235°	75°
5	256°	35°	12	235°	58°
6	250°	35°	13	145°	20°
7	063°	75°			

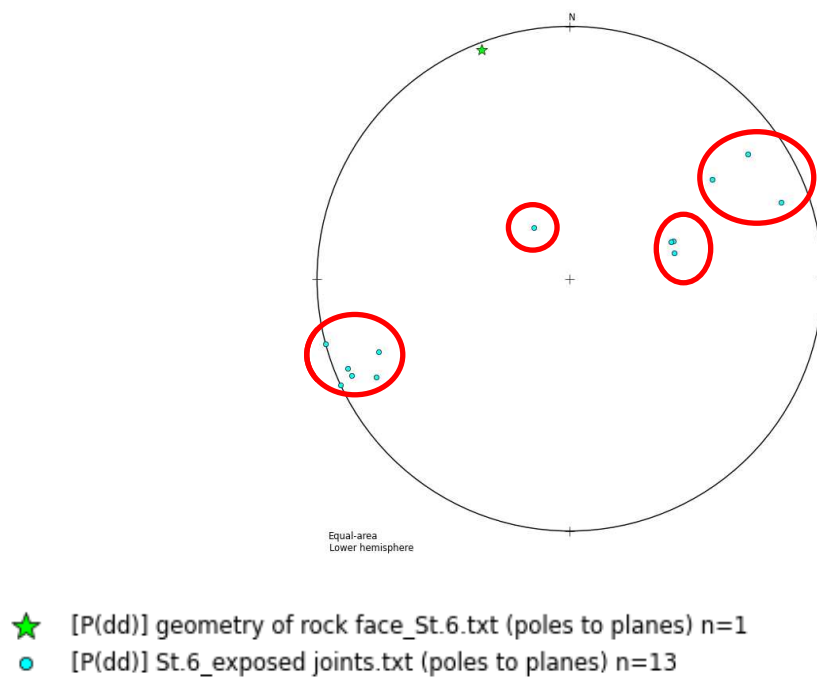


Figure 6.22: The Lambert stereonet projections of the normal vectors (the poles) of the measured exposed joints of St.6 can be clustered into four joint sets (red circles).

GPR technique was significantly able to identify six hidden subvertical joints at perpendicular depth from the rock slope face between about 30 cm and about 300 cm as illustrated in Figure 6.23 and in the appendix (Figures 32 & 33).

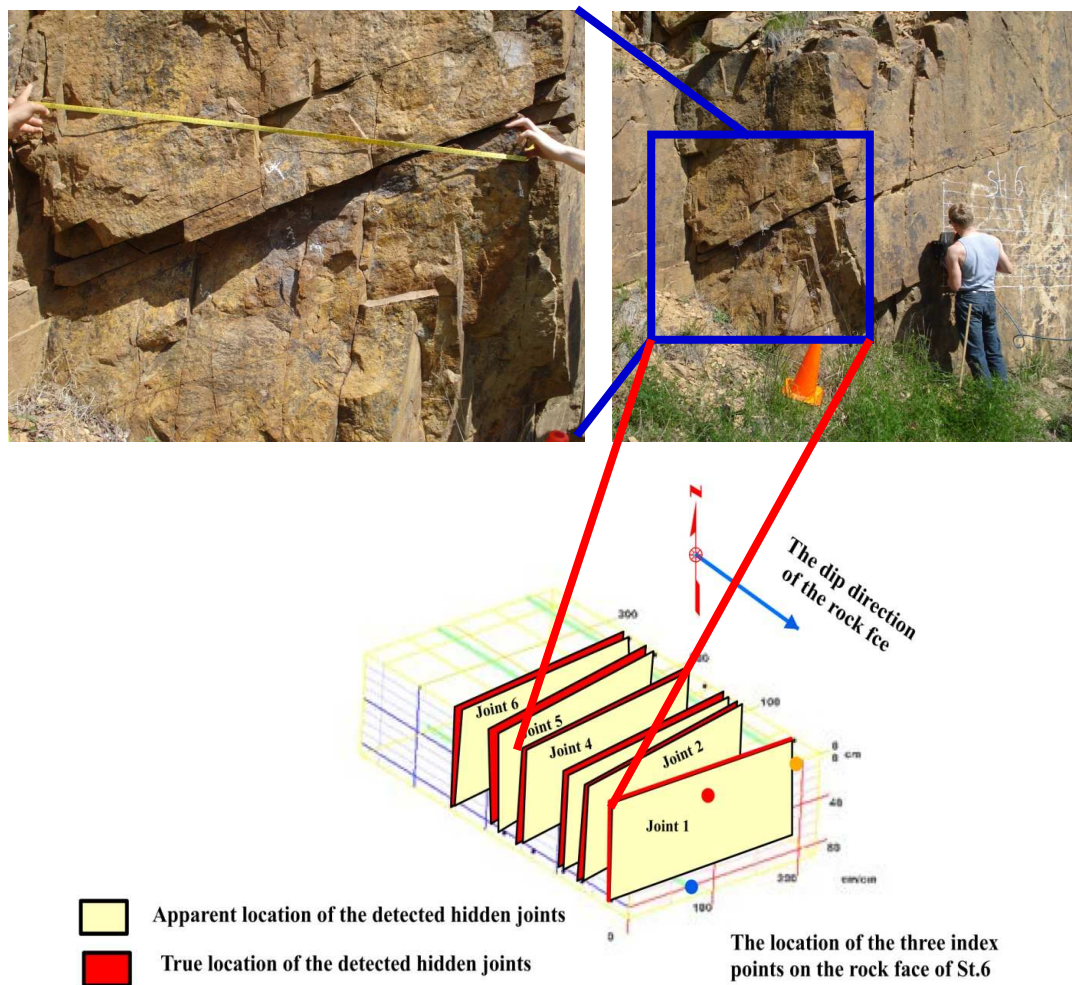


Figure 6.23: The position of the linear traces of only four of the six detected hidden joints are exposed on the side of the slope verifies the accuracy of the resulting true 3D GPR image of station 2. Note that the true perpendicular depths (d) of these four hidden joints in the 3D image match those in the field. Joint 4 dips steeply into the slope face as indicated from the LIDAR measurements.

The orientations for those hidden joints are determined using the LIDAR technique (Table 6.18). Only four of these six detected joints have linear traces appear on the side of the rock slope face as shown in Figure 6.23; so the field verification measurements were possible for those four detected hidden subvertical joints (Table 6.18).

Based on the concentration zones of the normal vectors (the poles) of the detected hidden subvertical joints set, these hidden joints can be clustered into two joint sets. The first joint set has a dip direction of 158° and a dip angle of 90° ; while the second set , which is only one joint, has a dip direction of 336° and dip angle of 90° as illustrated in Figure 6.24.

Table 6.18: The orientations of the six detected hidden subvertical joints measured by LIDAR at St.6 in addition to some field verification measurements.

Hidden Joint No.	LIDAR		Field verification	
	D.D.	θ	D.D.	θ
1	159°	89°	155°	90°
2	158°	90°	153°	85°
3	158°	89°	152°	88°
4	338°	90°	336°	90°
5	158°	90°	NA	NA
6	158°	90°	NA	NA

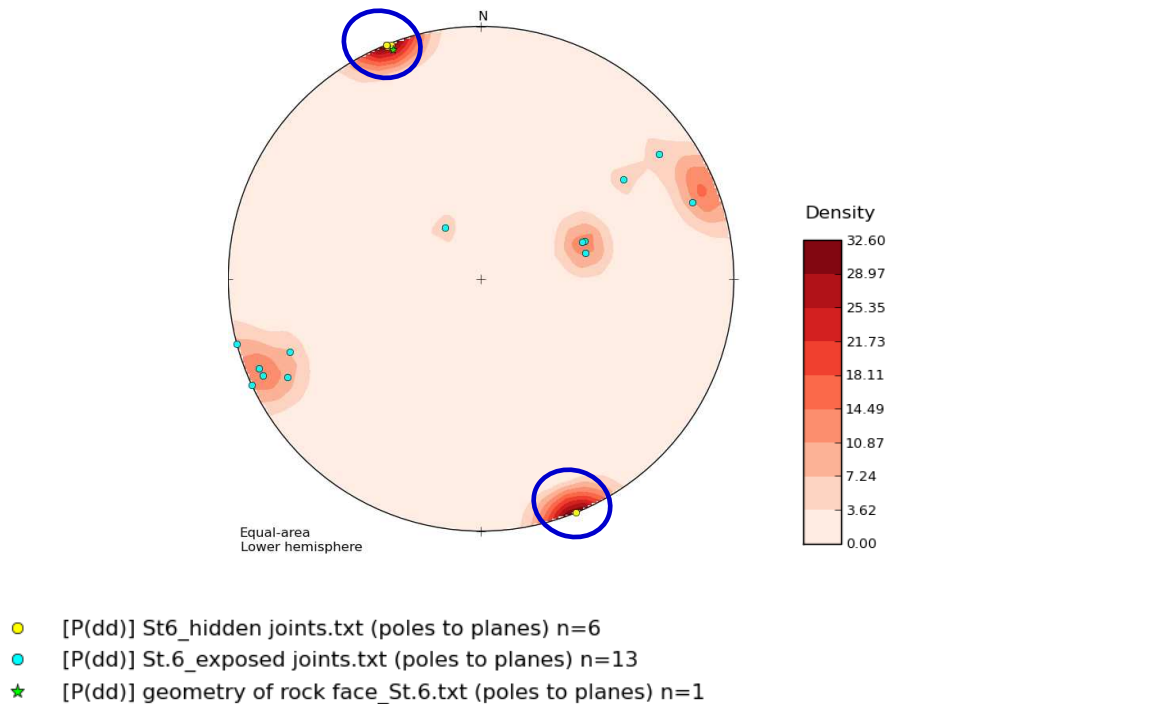


Figure 6.24: The two sets of the poles (blue circles) represented the six detected hidden subvertical joints at station 6.

6.3.2 Station 7. This station is located about 0.6 mile to the west of station 6 in Madison County. The rock mass of this station is more fractured compared to station 6 (Figure 6.25). From the field investigation for this station, some discontinuities dip steeply into the rock slope face which may cause toppling failure (Figure 26) .

The geometry of the rock slope face of this station is listed in Table 6.19. The orientations of the measured exposed discontinuities using a Brunton compass are listed in Table 6.20. The normal vectors (the poles) of these joints can be clustered into three sets as shown in Figure 6.27.



Figure 6.25: A front view of the rock slope of St.7 in site 2 (Madison County).



Figure 6.26: A side view of St.7 in site 2 is showing some discontinuities dipping steeply into the slope face which may cause toppling failure in the future (Madison County).

Table 6.19: The geometry of the rock slope face of St.7.

Geometrical measurements of St.7			
Field		LIDAR	
D.D.	θ	D.D.	θ
65°	90°	65°	89°

Table 6.20: Manual measurements for dip direction (D.D.) and dip angle (θ) of the measured exposed discontinuities at St.7.

Joint No.	D.D.	θ
1	330°	52°
2	330°	08°
3	335°	01°
4	329°	43°
5	334°	48°
6	330°	90°
7	145°	20°

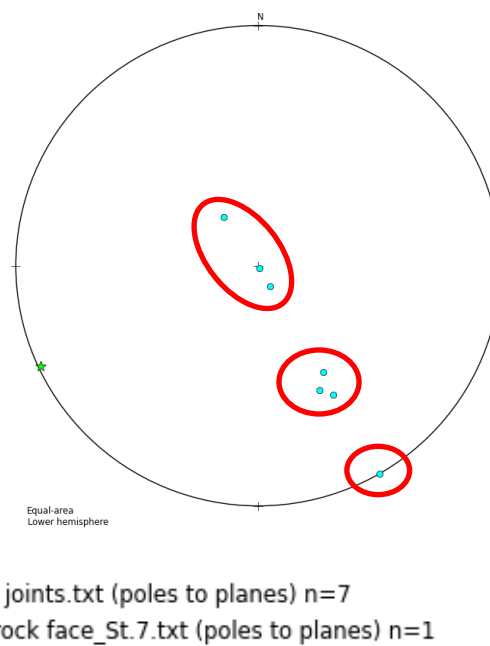


Figure 6.27: The Lambert stereonet projections of the normal vectors (the poles) of the measured exposed joints of St.7 can be clustered into three joint sets (red circles).

Three hidden subvertical joints were detected in this station by GPR instrument. These joints were depicted at depth ranges between 55 cm and 150 cm as illustrated in Figure 6.28 and as well as in the appendix (Figures 38 & 39).

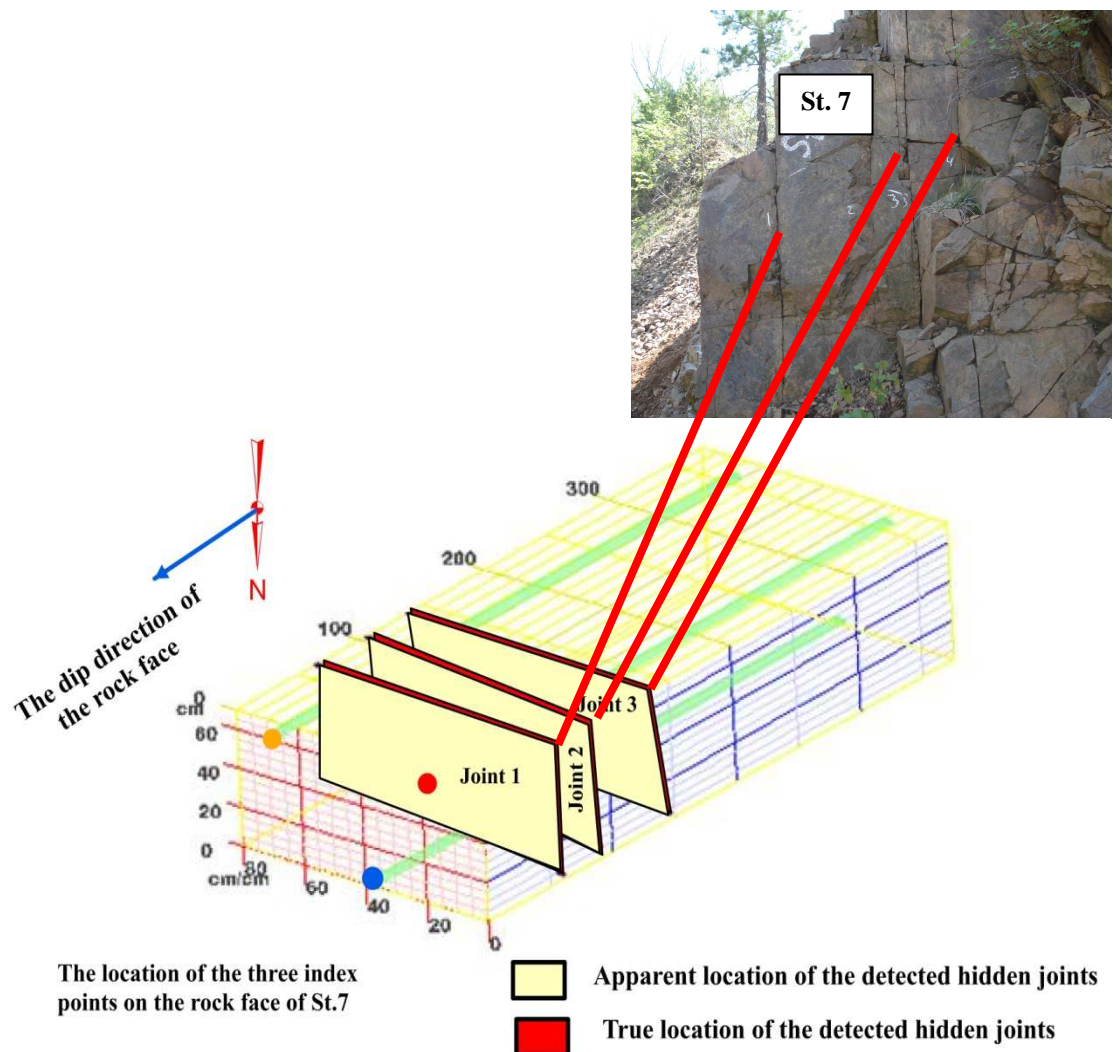


Figure 6.28: The position of the linear traces of the three detected hidden subvertical joints are exposed on the side of the slope which verifies the accuracy of the resulting true 3D GPR image of station 2. Note that the true perpendicular depths (d) of these three detected hidden subvertical joints in the 3D image match almost those in the field.

The orientations for these three detected hidden subvertical joints are determined using both the LIDAR technique and the three point equation as listed in Table 6.21. All these detected hidden joints have linear traces appear on the side of the rock slope face as shown in Figure 6.28; so the field verification measurements were possible for their geometry (Table 6.21). Based on the concentration contouring of the poles of the detected hidden subvertical joints set, these joints can be clustered as an individual joint set whose dip direction and dip angle are 65° and 89° respectively as shown in Figure 6.29.

Table 6.21: The orientations of the three detected hidden joints measured by LIDAR and the field verification measurements at St.7.

Hidden Joint No.	LIDAR		Field verification	
	D.D.	θ	D.D.	θ
1	065°	89°	069°	87°
2	066°	89°	069°	88°
3	065°	90°	070°	88°

Even though this station, which is an ignimbrite rock, has many subvertical joints whose linear traces appear on the side of its rock slope, only three hidden subvertical joints could be detected significantly and resolved by GPR technique and only within a depth of about 2 m (Figure 36.0A). In contrast, station 6, which is also an ignimbrite rock and close from station 7, many discontinuities were detected and resolved within about 3.5 m using the GPR technique (Figure 6.30 B).

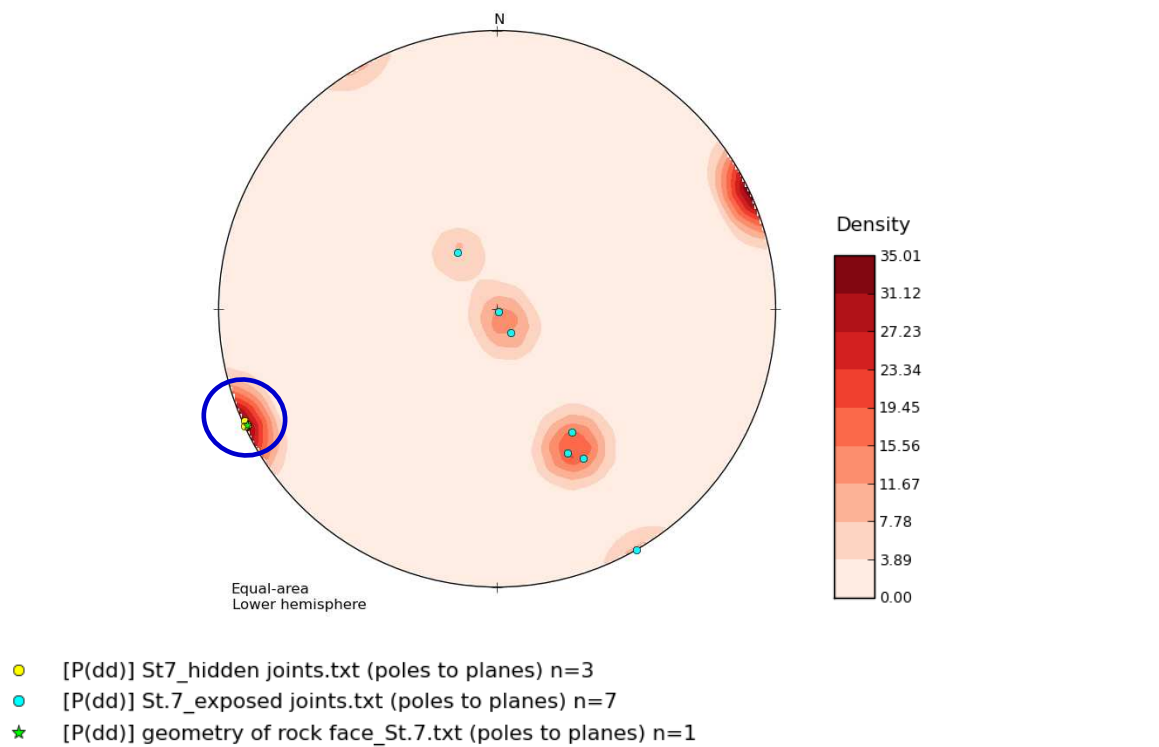


Figure 6.29: The normal vectors (the poles) to the three detected hidden subvertical joints at station 7 can be a separate joint set (blue circle).

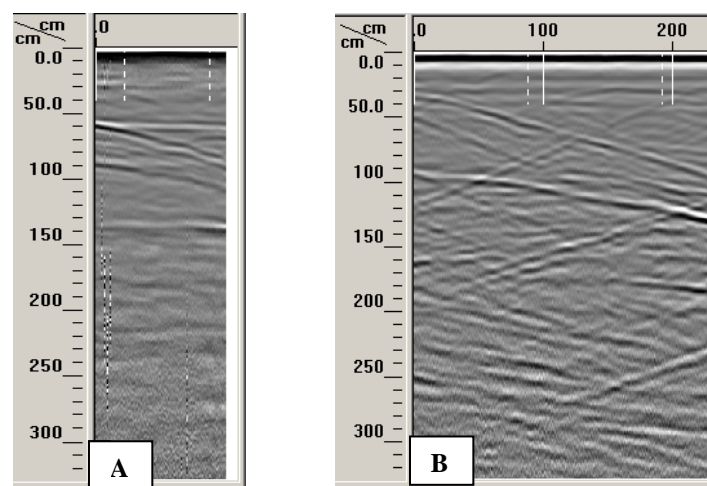


Figure 6.30: In terms of resolution and so the number of detected hidden joints, the penetration depth of the GPR pulses was less in station 7 (A) than in station 6 (B).

This can be mainly referred to the attenuation of GPR pulses that encountered more in station 7 than in station 6 as illustrated in Figure 6.30. This attenuation can be due to the following reasons:

- The mineral composition and, therefore, the chemical composition of station 6 differ from the mineral and chemical composition of station 7 (ignimbrite igneous rock).
- The rock slope of station 7 is more fractured than that one of the station 6. These fractures in St.7 could be filled with clay materials which caused attenuation for GPR pulses.

6.4 DISCUSSION

Many studies show that LIDAR is a promising remote sensing techniques for collecting geometrical information of discontinuities in a rock mass with high accuracy (Slob et al., 2004; Feng and Röshoff , 2004; Slob et al., 2005; Sturzenegger et al., 2007; Pernito, 2008; Torres, 2008; Sturzenegger et al., 2009; and Sturzenegger et al., 2011).

The geometrical orientations resulting from field verification for some of the detected hidden joints are very close to those measured by LIDAR. The comparison between the field verification and LIDAR measurements shows that the difference is generally within $\pm 3^\circ$ for dip angles and ± 5 for dip directions. This difference is likely to be caused by the fact that a geological compass can be affected by local magnetism and human errors; in addition to that the LIDAR treat discontinuities as perfect planes, which are mathematically preferable, while they are no perfectly planar in reality. All the stereonet projection results show that all the detected hidden joints represented additional joint sets in all stations of the study area.

Comparison between those joints that have linear traces and measured on the rock slope and those mapped using GPR and measured using LIDAR have shown reasonable correlation (Grandjean and Gourry, 1996; Porsani et al., 2006; Pernito, 2008; and Torres, 2008). However, the measured linear traces of joints using a compass may have less correlation, in some circumstances, with those mapped and measured using GPR and/or LIDAR. In terms of strike direction, Torres (2008) and Pernito (2008) have shown that the extension of linear traces of some joints measured using a compass may differ from those measurements that are resultant from GPR and/or LUDAR. This explains why the difference between the measured dip directions using a compass and those using LIDAR can take place in some measurements and reach up to 6° .

However, the difference between the measured dip angles using a compass and those using LIDAR was no more than 4° . This difference in dip angle measurements could be referred to the fact that LIDAR has been taken the measurement for the joint as a plane. This plane is measured as it is a smooth with no undulation which may differ from reality where the plane of a joint has not the same dip angle on each point on its plane. This point seems as a weakness of using LIDAR but is a strength at the same time, since LIDAR measure the whole plane of the joint which can be related precisely to the plane of the rock slope face and thus predict the mode of rock failures.

The results show that the number of the detected hidden subvertical joints using GPR technique was as a maximum six joints which are in station 6 at site 2. The extension of all the planes of the detected hidden joints were enough big, so the three corresponding index points could be plotted on their planes. Accordingly, there are some

other small joints were detected by GPR but not included in this study due to their limit extension constrain (see the radiograms images in the Appendix).

Based on the minimum vertical resolution (Annan, 2001; Cardimona, 2002; Annan, 2009; and Cassidy, 2009 a & b), the minimum resolved aperture of any detected hidden joint in site 1 is about 6 cm while it is about 4 cm in site 2. However, Kovic (2010) utilized a 400 MHz GPR antenna to detect fractures and joints in pillars of a mine. Based on finite-difference time-domain (FDTD), he found out that when a 400 MHz GPR antenna is used, one millimeter opening aperture of a fracture can be detected. Consequently, his findings explain why some hidden subvertical joints whose apertures are less than the value of the minimum vertical resolution were detected and mapped using the 400 MHz GPR antenna in our study area (Figures 6.23 and 6.28).

In general, the strength of the GPR pulses reflection from a rock discontinuity depends mainly on the aperture of the discontinuity and the infilling materials both which control the reflection coefficient (Grégoire, 2001). This will give a distinctive linear interface, reflector, or event, with a high amplitude compared to background reflection, in the radiogram image.

As a result, this distinctive reflection signature can be used as criteria in objectively delineating the discontinuities in rock masses (Pernito, 2008). The amount of reflected GPR pulses increase as the difference between relative dielectric permittivities increase. Open discontinuities which are filled with water and/or clay are clearly visible in GPR radiogram than those discontinuities which are closed or with no filling material (Tpsioaka, 2003; Pernito, 2008; and Torres, 2008).

This situation can be seen clearly in radiograms of station 2 which were acquired after a slight rainy night. The reflection is stronger compared to the surrounding stations in site 1; however, the penetration of depth with appropriate resolution was less in addition to the background noise was more which caused to some extent a difficult to identify the hidden joints..

The trade-off between resolution of GPR pulses and depth of penetration is one of the principal problems of utilizing GPR system since the higher resolution which is accompanied by high EM frequency is the lower depth of penetration for EM waves (Annan, 2001; Cardimona, 2002; Annan, 2009; and Cassidy, 2009 a & b). On other word, resolution is lower for lower frequency GPR pulses or antennae.

Both of resolution and penetration of depth of GPR pulses depend on the electrical properties of the rock slope and the infilling materials. The relative dielectric permittivity of ignimbrite rock cuts in site 2 is higher than that one of sandstone rock cuts in site. Accordingly, the penetration of depth using the same GPR antenna (400 MHz) was less in site 2 than in site 1. The probable occurrence of infilling-clay materials in apertures can cause also a significant a significant attenuation for GPR penetration.

Another common limitation of using GPR technology is the GPR data processing and interpretation which is still subjective and depends mainly on the interpreter's skills and experience to interpret radiograms. However, field verifications, especially for exposed linear traces, can help to avoid or minimize this effect.

Another limitation maybe added is that the area of rock mass which is highly fractured may cause more diffraction in GPR data as well as attenuation for GPR pulses. The effective of penetration of depth within which some hidden subvertical joints could

be detected in station 7 was less than 160 cm while this depth was to about 300 cm in station 6 although both stations are ignimbrite rock cuts but station 7 is more fractured than station 6.

7. CONCLUSIONS AND RECOMMENDATIONS

7.1 OVERVIEW

The main objective of this research is to measure the geometrical orientations of the detected hidden subvertical joints which are parallel or semi-parallel to rock slope faces. GPR was significantly able to detect and map those joints in types of volcanic and sedimentary rock masses. In addition, LIDAR was able to estimate accurately the orientation of the detected hidden subvertical joints. More detailed conclusions are listed below.

Many studies have showed the ability of GPR in detecting and mapping hidden joints and fractures in rock masses as mentioned in the literature review section. However, very few of these studies focused on extracting the geometry of the hidden discontinuities in rock masses. Seol and others (2001) developed a method to find the strike direction from three different acquisition modes for the same survey in a granitic rock mass.

Pernito (2008) used a 500 monostatic GPR antenna in a continuous mode (time mode) carrying out both of two long horizontal and several vertical GPR survey lines to map and measure the extension of the exposed linear traces of discontinuities so can be integrated into rock slope stability analysis. He used the automated LIDAR method developed by Slob and others (2002) to extract the geometry of the exposed facets.

His study was primary to delineate the subsurface characteristics of rock mass discontinuities. Particularly, to detect discontinuities that may not detected by LIDAR, and to verify the continuation of discontinuity planes that are detected by the same

method. He found out that the extension of the linear traces of joints can be measured more accurately using GPR and LIDAR in a combination compared to the resultant measurements using only a geological compass. Accordingly, the strike directions of those linear traces were measured more accurately rather than using a scanline method. However as a result, his proposed approach was able to detect only exposed joints, linear traces.

Torres used the same approach but he was able to build a 3D discontinuity network and extract the geometry of hidden discontinuities within limited depths and with uncertainties in measurements due to the subjective occur in GPR data processing and interpretation.

The previous studies only measured the orientations of the linear traces and/or the hidden joints planes based on the sampling of the nearest neighborhood measured by LIDAR which may cause bias when it comes to the extension and the persistence of hidden joints which should be treated as planes.

In this study, the rock cut was treated as whole plane upon which the planes of the detected subvertical hidden joints were related. Some field measurements have been done and verified the resultant geometrical measurement for those joints whose linear features can be detected on the rock slope surface. The depth of GPR penetration was not significantly affected by the approach itself but is affected by the relative dielectric permittivity of the rock cut materials as well as the frequency of the used antenna.

7.2 GPR AS A TOOL FOR DISCONTINUITY MAPPING

In general, GPR is a powerful tool for detecting and mapping hidden discontinuities especially those which are subvertical and parallel to semi-parallel to rock slope face. Moreover, many other points have been concluded through the stages of the work in this research. These conclusions can be pointed out as following:

- GPR-pulse system is preferred to be used in a distance-mode to locate those joints in rock masses.
- A 400 MHz monostatic GPR antenna is an appropriate antenna in terms of depth and resolution to detect hidden subvertical joints in rock masses. It was able to detect and map significantly such joints within 2 m depth with high resolution.
- The only obvious problem with utilizing a 400 MHz monostatic antenna is that the presence of a shadow zone within the few centimeters 20 cm of depth which may be needed to be considered in mining industry not in rock slope stability. This zone can cause missing detecting some joints within 20 cm of depth. To overcome this problem, a 1500 MHz antenna is recommended to be used to map only the potential subvertical joints occurring within that depth of zone.
- Some GPR data processing techniques are necessary to enhance the resolution and visualization of radiograms, the GPR images. Zero correction, high and low pass filtering, display gain, auto-gain, and deconvolution are generally required for GPR data processing to detect accurately hidden discontinuities in rock masses.

- Migration is highly recommended to be used to locate correctly the position of the detected joints, and therefore, to measure their orientations.
- Using two parallel GPR survey lines can be enough for acquiring data which can be used with a combination of LIDAR data to estimate the geometry of the detected hidden joints. However, creating 3D radiograms are recommended to track precisely and accurately the geometrical extension of the detected hidden joints.

The type of the investigated rock plays a significant role in terms of determination the velocity of the GPR pulses. The more attenuation for GPR pulses is the less velocity GPR pulses have. The ignimbrite rock cuts at site 2, volcanic rocks, show more attenuation for GPR pulses compared to the sandstone rock cuts at site 1.

Consequently, determination the velocity of GPR and, therefore, the relative dielectric permittivity of the investigated intact rocks is highly required to verify or modify the used entered parameters in GPR system by operator. For instance, the relative dielectric permittivity of ignimbrite at site 2 which was entered in the GPR system during acquiring the field data was 6. This value led to incorrect depths values that would affect on the migration process and results; however, the lab test for the GPR velocity for site 2 showed that the relative dielectric permittivity is 16. As a result, the perpendicular depths were estimated accurately and as well as the orientations of the detected joints.

7.3 LIDAR AS A TOOL TO ESTIMATE THE ORIENTATIONS OF THE HIDDEN SUBVERTICAL JOINTS

It is well established that discontinuities measurements obtained from traditional methods can be affected by orientation bias (Terzaghi, 1965); Terzaghi (1965)

demonstrated the sampling bias that result from using scanline method (linear survey) or outcrop (planar) survey of discontinuities with preferred orientations, particularly with those discontinuities which are roughly parallel to an exposed rock cut face. This bias may lead to underrepresented of joint survey to be limited to that exposure. Accordingly, Terzaghi (1965) proposed a trigonometric factor correction for linear and planar sampling of discontinuities to compensate for that bias. This factor was developed by Mauldon and Mauldon (1997). Wang and Mauldon (2006) found out that using Terzaghi's correction factor may be difficult, especially when the linear or planar sampling is roughly parallel to the existing discontinuities.

However, this bias in linear or planar sampling is limited only when the discontinuity surfaces "facets" are measured using LIDAR (Sturzenegger et al., 2009; Sturzenegger et al., 2011). In addition, in our research, a geological compass with no measuring tape was used to measure the orientations of the exposed joints, while the rock cut (slope) faces were measured using LIDAR, which may diminish or delete the effect of that bias.

The investigation results show how easily, quickly, and accurately rock slope face can be measured using LIDAR technique, avoiding manual measurements that are dangerous in some cases. In addition, LIDAR technique can give accessibility to measure the geometry of rock slope faces at locations that cannot be reached by human.

One new advantages of using LIDAR can be added which is that LIDAR can treat a rock slope face as a plane to which detected hidden subvertical joints can be related. Accordingly, using the three point equation to measure the geometry of the detected hidden joints in a rock slope will be possible and more reliable.

7.4 RECOMMENDATION FOR FUTURE WORK

The main disadvantage of this research approach, using a GPR and LIDAR in a combination, is that it needs a physical contact with rock slopes when carrying out GPR survey, which may jeopardize workers' life. Besides, it is time consuming when utilizing GPR instrument which requires at least two to three personnel to perform GPR field work. Moreover, GPR data processing is subjective and depends on the experience of the operator.

Generally, this approach can be used to detect and measure the orientations of joints and fractures in rock masses, tunnels, roofs and pillars of mines, open pits and quarries. However, the desirable depth of investigation will control selecting the type of suitable GPR antenna and thus the application field. High frequency antennae, such as 1.5 or 1.6 GHz, can be utilized significantly to detect small fractures within shallow depths may not exceed three feet. In addition, 900 MHz antenna could be the best choice in terms of resolution and depth of penetration. This antenna can detect small aperture-joints or fractures in rock masses, mine roofs and pillars within depths of a few feet more than the detected depth using 1.5 GHz antenna.

Both of these antennae are portable and easy to be used to significantly detect and map hidden non-horizontal joints in ceilings and walls of mines, rock cuts, and more particularly in quarries where quality and quantity of blasted materials are more concern. It is often conducting blasting in quarry industry; hence, the approach of this research may help to locate highly fractured areas where no need for more detonations materials and so decrease the cost of blasting process. Furthermore, it could locate the more sound

areas where more detonation materials would be needed to extract the required quantity and quality of aggregate.

In contrast, the 400 MHz GPR antenna is more recommended to be used to detect and map joints and fractures in rock cuts than 1.5 and 1.6 GHz whose penetration depth may not exceed than 3 feet. However, the 400 MHz GPR antenna could be difficult to be used to map joints in roofs and ceils due to its weight and dimension constrains.

Since this approach is build on using the GPR distance mode, it may help to determine the best location for installing rock bolts and/or anchors and, therefore, increase the degree of certainty of rock mass or mine roofs or pillars stabilization method. Furthermore, it may be used to extract some other properties of discontinuities such as persistence and spacing which are needed to evaluate quarry materials and ornamental extracted rocks from open pits. Furthermore, it can be sued for uneven and/or curved rock mass surfaces.

Although it is recommended to use this method for further studies in terms of detection and mapping hidden discontinuities especially the ones are parallel and semi-parallel to rock slope faces, it would be recommended to develop this approach to conduct kinematic analysis for those detected joints within the first two meters of depth where may rock failures can be induced by different factors and then take place.

This approach is not recommended to be used for highly fractured or weathered rock cuts where high concerns during slope analysis will be normally taken into consideration. However, the rock cuts and roofs and/or pillars of mines which show a minor distribution for exposed joints on their surfaces may have many hidden joints are

needed to be detected and integrated into slope analysis to avoid underestimation of stability.

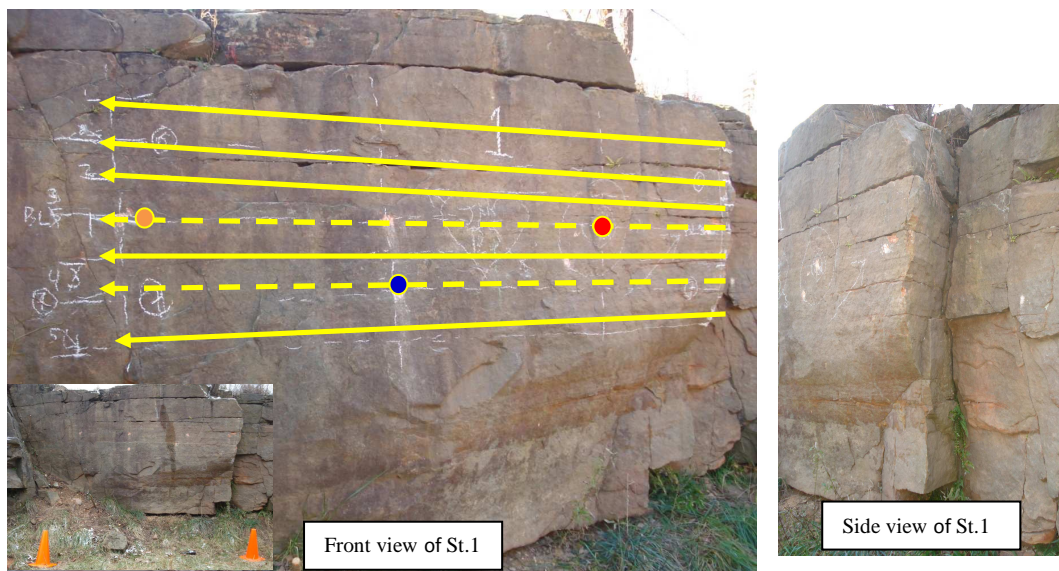
In spite of the uncertainty which is still valid for those detected hidden joints for which field verification was not possible, this method is a straight and understandable method. Besides, the error that may resulting from using automatic algorithm in LIDAR can be negligible in this proposed approach since no need for such algorithm to extract geometrical information about the facets and linear traces of exposed joints.

APPENDIX

HIDDEN JOINT ORIENTATION

MEASUREMENTS

SITE 1_STATION 1



The geometry of the GPR survey lines at St. 1

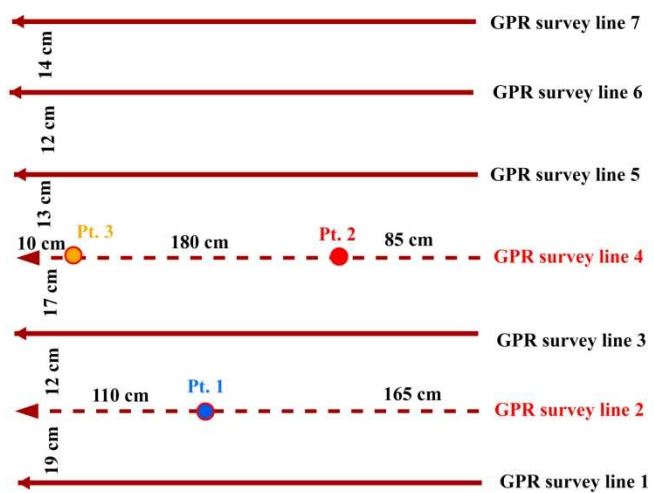


Figure 1: The location of the GPR survey lines (dashed lines are the two index lines) at St.1 and their geometry. The colored circles are the locations of the three index points.

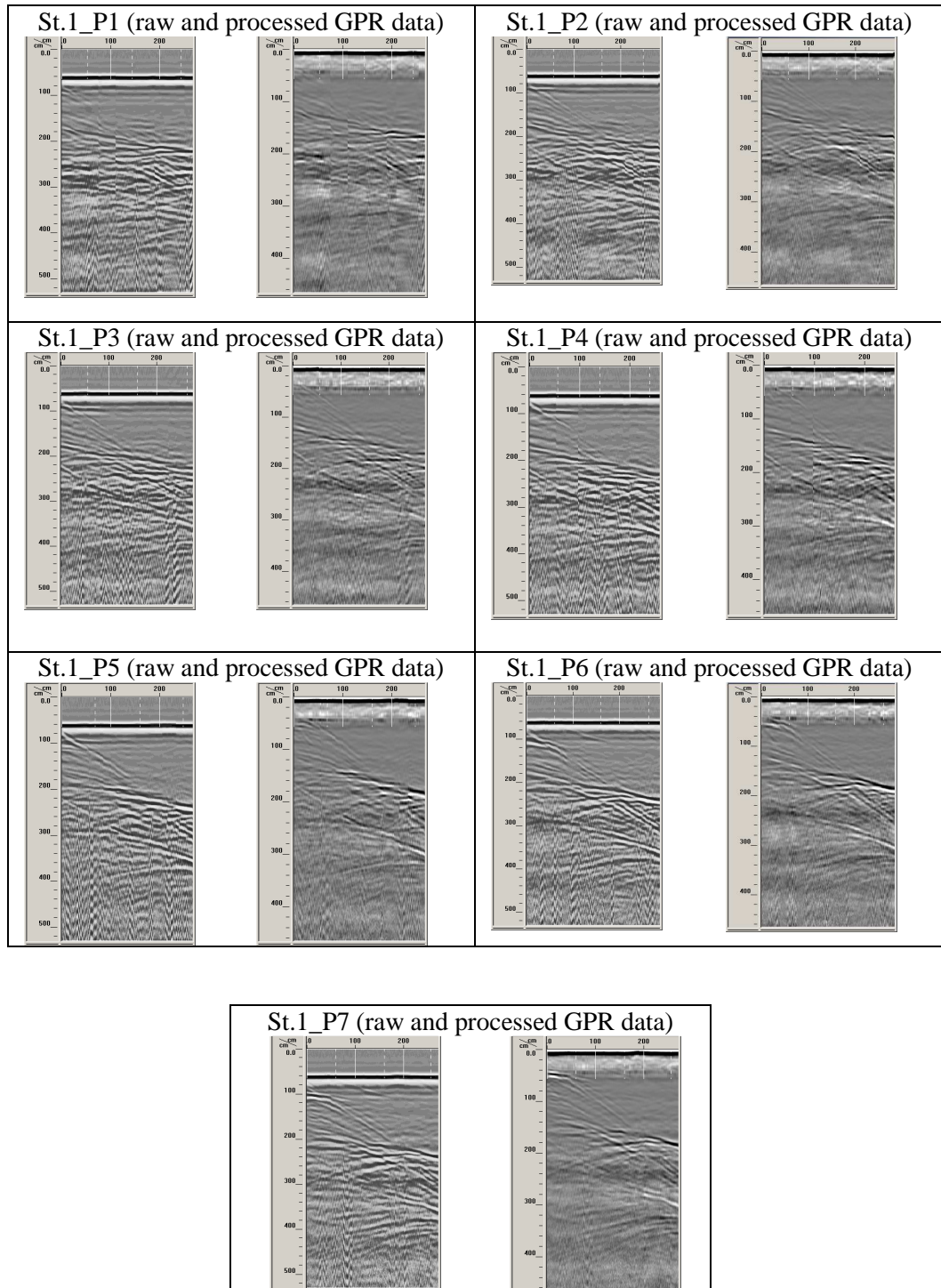


Figure 2: Radiograms images (GPR profiles) show the acquired raw and processed GPR data at station 1.

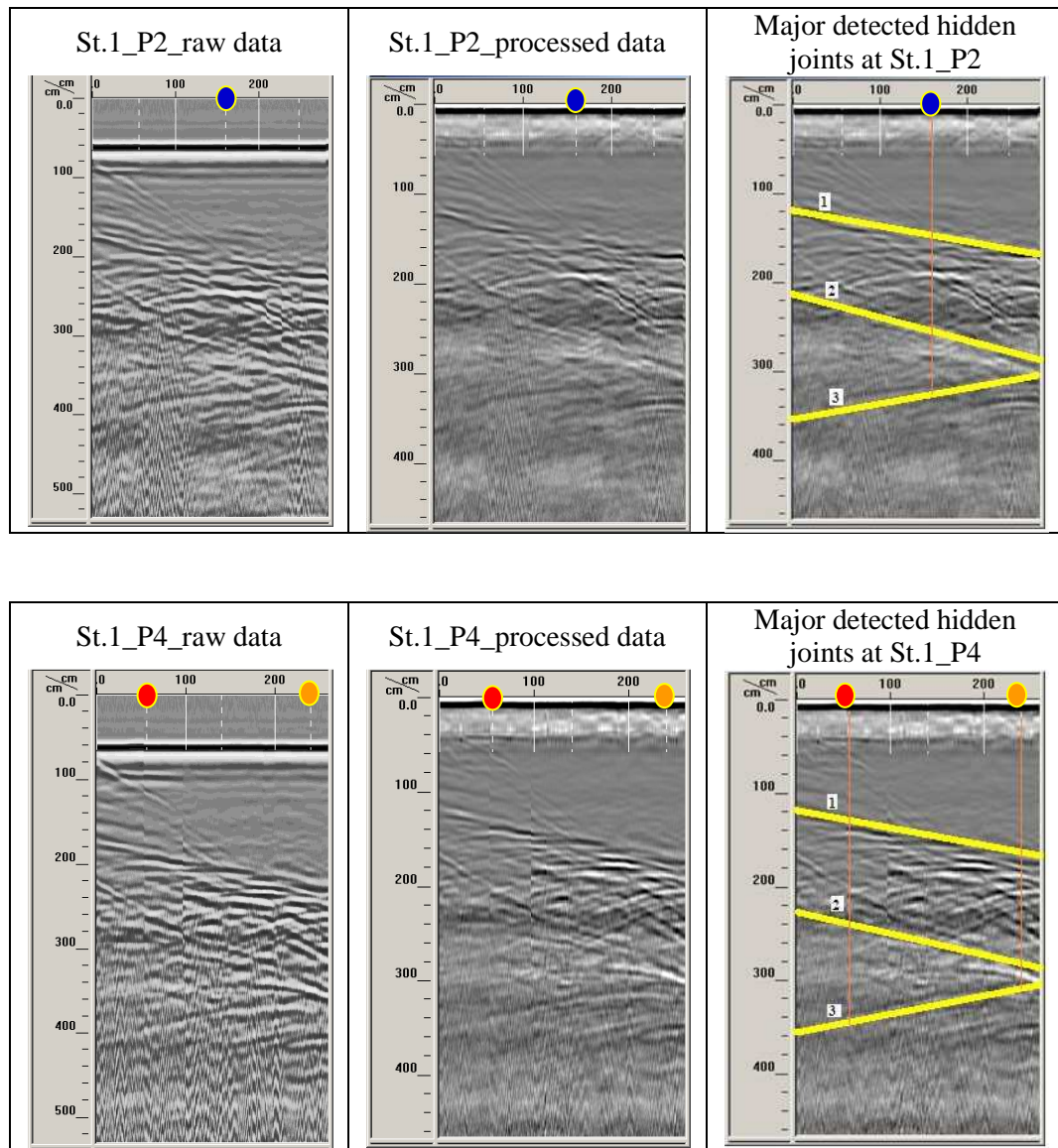


Figure 3: The apparent perpendicular depths (z) to the detected hidden subvertical joints in St.1 after GPR data processing for the two index lines.

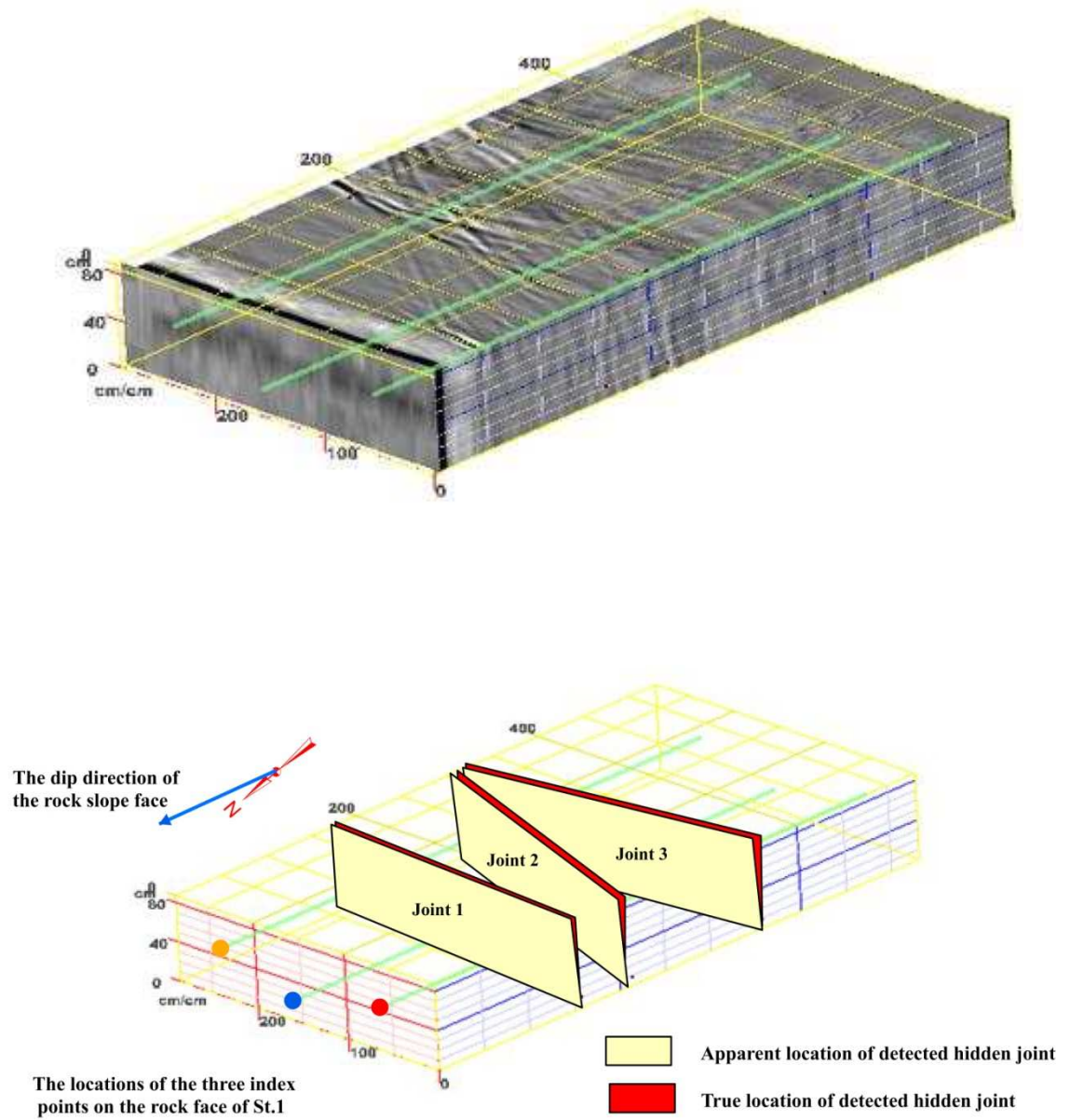


Figure 4: The created 3D image of Station 1 using RADAN software (above image) and the 3D-image for the detected hidden subvertical joints with apparent and true strike directions (blow image).

Table 1: The apparent and true perpendicular depths from the rock slope face to the detected hidden subvertical joints at St.1.







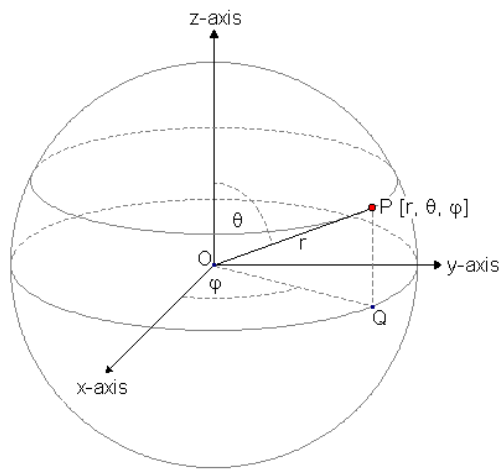
Joint No.	Apparent perpendicular depths (z) from the 3-points on the rock face of St.1, in cm.			Apparent (α) and true (β) declination angles of the strike		True perpendicular depths (d) from the 3-points on the rock slope face of St.1, in cm		
	Point 1 	Point 2 	Point 3 	α	β	Point 1 	Point 2 	Point 3 
1	148	133	170	11°	11.2°	151	136	173
2	261	234	282	16°	16.7°	272	244	294
3	325	344	314	10°	10.2°	330	350	319




Table 2: The coordinate values and geometry of the reference object for LIDAR measurements calibration at the rock slope face of St.1.

3-point coordinates of the reference object				Dip direction (D.D.) and dip angle (θ) measurements			
				Field		LIDAR	
Point	X	Y	Z	D.D.	θ	D.D.	θ
1	5340.39	16836.05	- 818.78	025°	87°	025°	84°
2	5413.34	16797.72	- 865.40				
3	5361.48	16814.03	- 924.44				



$\theta = 84^\circ$
 $\phi = 66^\circ$
 The correction of the dip direction rotation = 179° clockwise.

Table 3: Geometrical measurements of the rock slope face at St.1 after the calibration process for LIDAR measurements.

The three index point coordinates at the rock slope face				Geometry of the rock slope face			
Point	X	Y	Z	Field		LIDAR	
				D.D.	θ	D.D.	θ
1 	6458.09	16235.77	-324.57	028°	73°	026°	069°
2 	7422.82	15878.50	-122.79				
3 	5639.71	16751.02	-003.56				

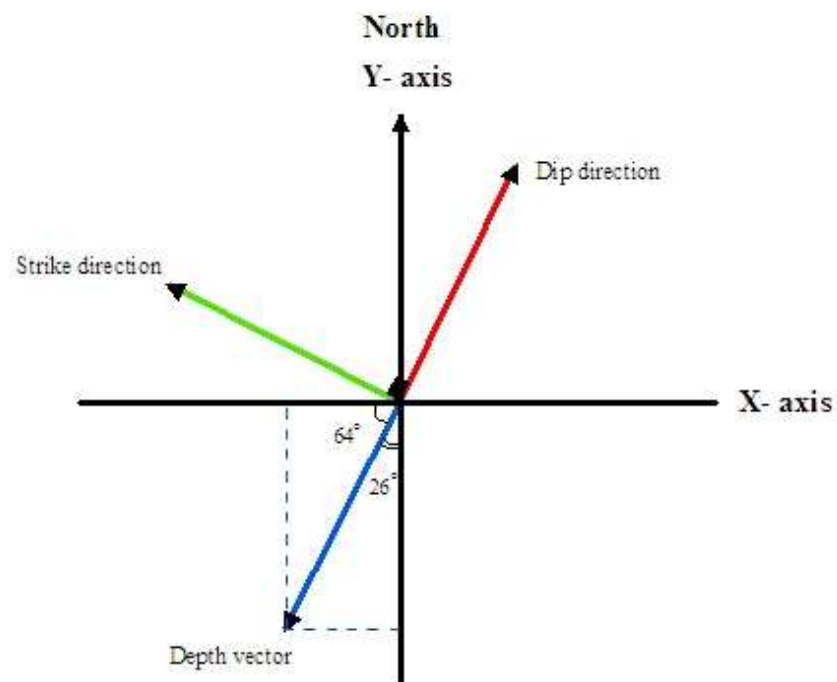


Figure 5: Resolved depth vector at St.1 to Y' and X' ; $Y' = Y - d \cos 26^\circ$; and $X' = X - d \cos 64^\circ$

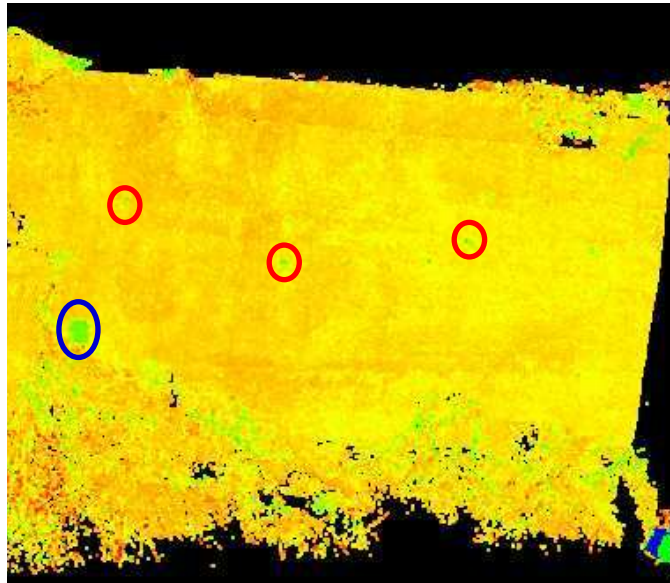
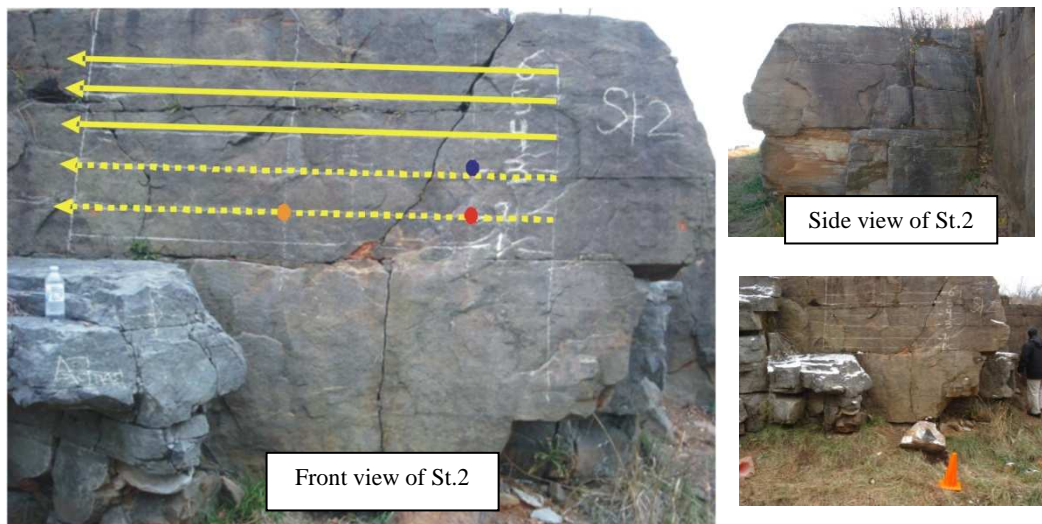


Figure 6: Point cloud image showing the location of the reference object (the blue circle) and the location of the three index points (the red circles) on the rock slope face of St.1.

Table A4: LIDAR geometrical measurements for the detected hidden subvertical joints in St.1 based on the true perpendicular depth vector components analysis and by using the 3-point equation.

		Geometrical measurements of the detected hidden subvertical joints						
Joint No.	Point No.	The 3-corresponding index points coordinates			LIDAR		Field verification	
		X'	Y'	Z'	D.D.	θ	D.D.	θ
1	1	6391.89	16100.05	-324.57	025°	69°	025°	NA
	2	7363.20	15756.26	-122.79				
	3	5563.87	16595.53	-003.56				
2	1	6338.85	15991.30	-324.57	024°	68°	027°	72°
	2	7315.85	15659.19	-122.79				
	3	5510.82	16486.77	-003.56				
3	1	6313.42	15939.17	-324.57	027°	69°	026°	71°
	2	7269.38	15563.92	-122.79				
	3	5499.86	16464.30	-003.56				

SITE 1_STATION 2



The geometry of the GPR survey lines at St.2

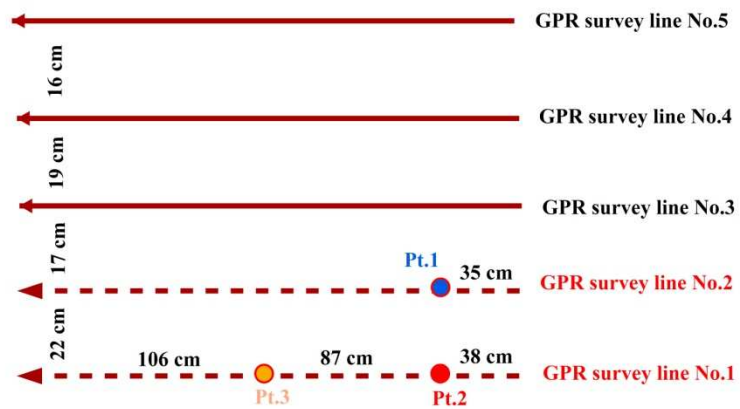


Figure 7: The location of the GPR survey lines (dashed lines are the two index lines) at St.2 and their geometry. The colored circles are the locations of the three index points.

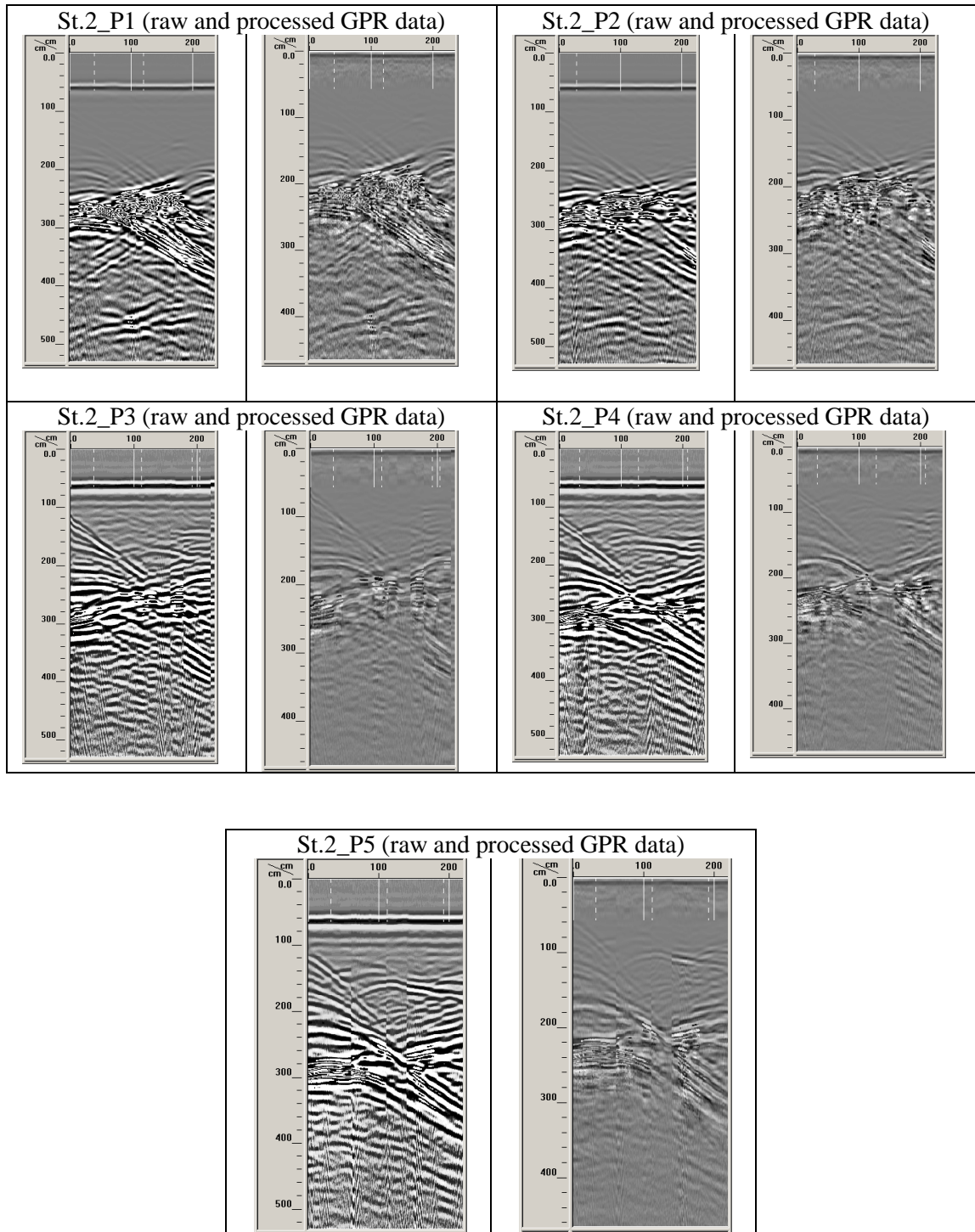


Figure 8: Radiogram images (GPR profiles) show the acquired raw and processed GPR data at St. 2.

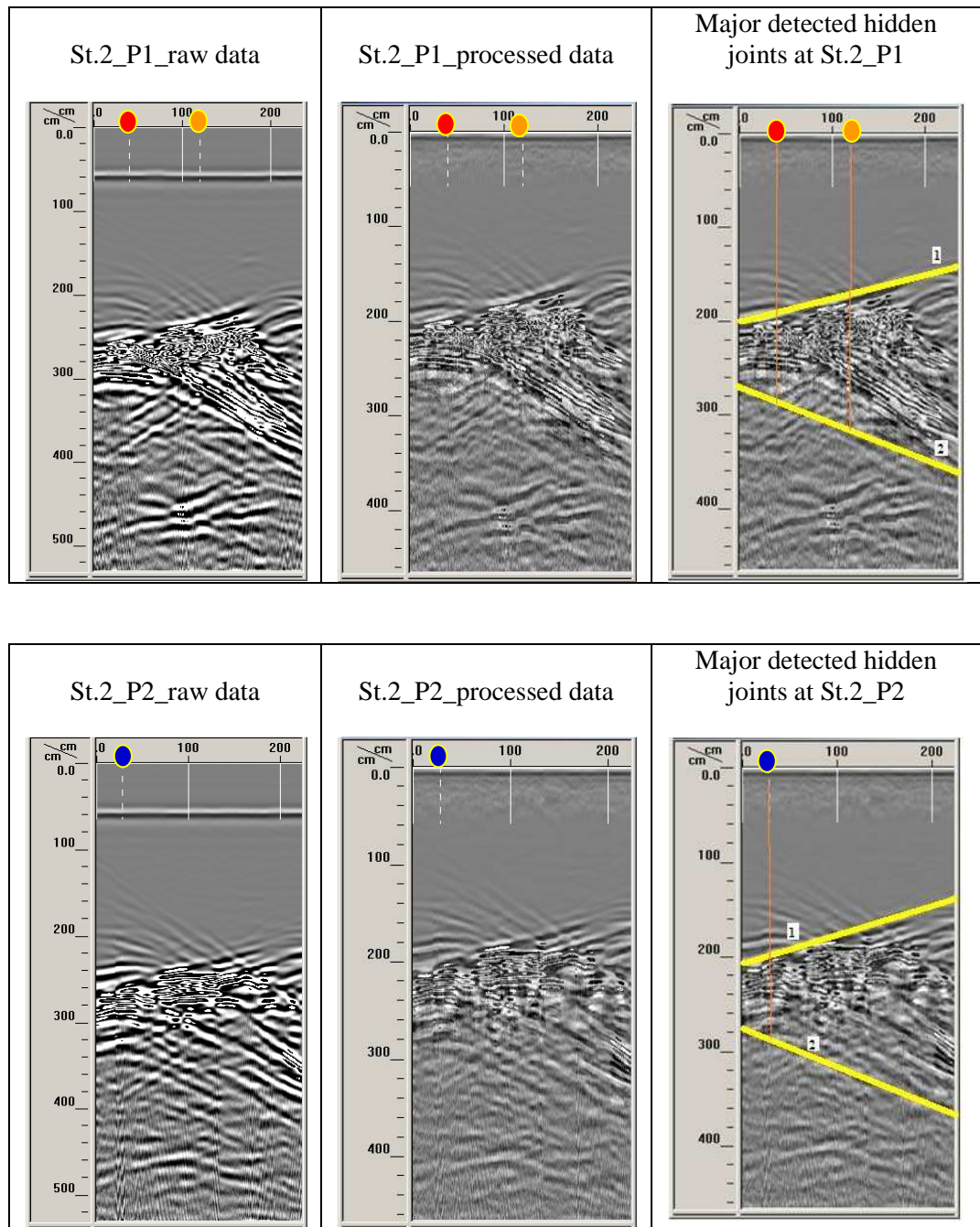


Figure 9: The apparent perpendicular depth (z) to the detected hidden subvertical joints in St.2 after GPR data processing for the two index lines.

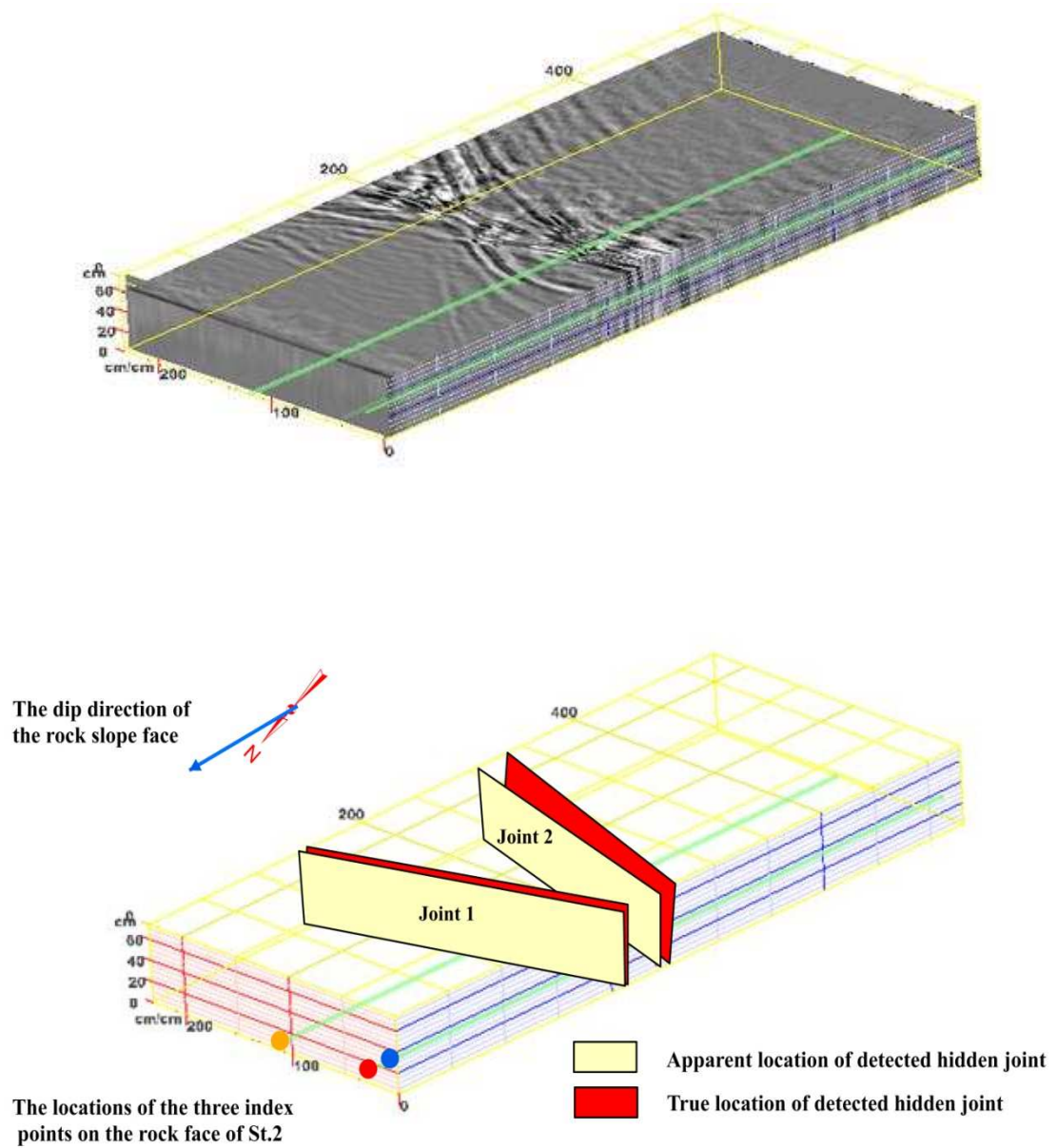


Figure10: The created 3D image of St. 2 using RADAN software (above image) and the 3D-image for the detected hidden subvertical joints with apparent and true strike directions (blow image).

Table 5: The apparent and true perpendicular depths from the rock slope face to the detected hidden subvertical joints at St. 2.







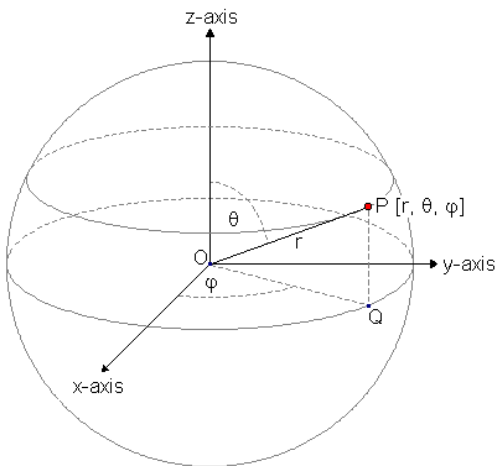
Joint No.	Apparent perpendicular depths (z) from the 3-points on the rock slope face of St.2, in cm.			Apparent (α) and true (β) declination angles of the strike		True perpendicular depths (d) from the 3-points on the rock slope face of St.2, in cm		
	Point 1 	Point 2 	Point 3 	α	β	Point 1 	Point 2 	Point 3 
1	188	198	177	16°	16.7°	196	207	185
2	287	285	318	22°	23.8°	314	311	348




Table 6: The coordinate values and geometry of the reference object for LIDAR measurements calibration at the rock slope face of St. 2.

3-points coordinates of the reference object				Dip direction (D.D.) and angle (θ) measurements			
				Field		LIDAR	
Point	X	Y	Z	D.D.	θ	D.D.	θ
1	5340.39	16836.05	- 818.78	025°	87°	025°	84°
2	5413.34	16797.72	- 865.40				
3	5361.48	16814.03	- 924.44				



$\theta = 84^\circ$
 $\phi = 66^\circ$
 The correction of the dip direction rotation = 179° clockwise.

Table 7: Geometrical measurements of the rock face at St.2 after the calibration for LIDAR.

The three index points coordinates at the rock slope face				Geometry of the rock slope face			
				In field		By LIDAR	
Point	X	Y	Z	D.D.	θ	D.D.	θ
1 	2991.82	15447.26	464.68	022°	85°	027°	81°
2 	2979.83	15417.44	260.11				
3 	2194.30	15803.41	248.70				

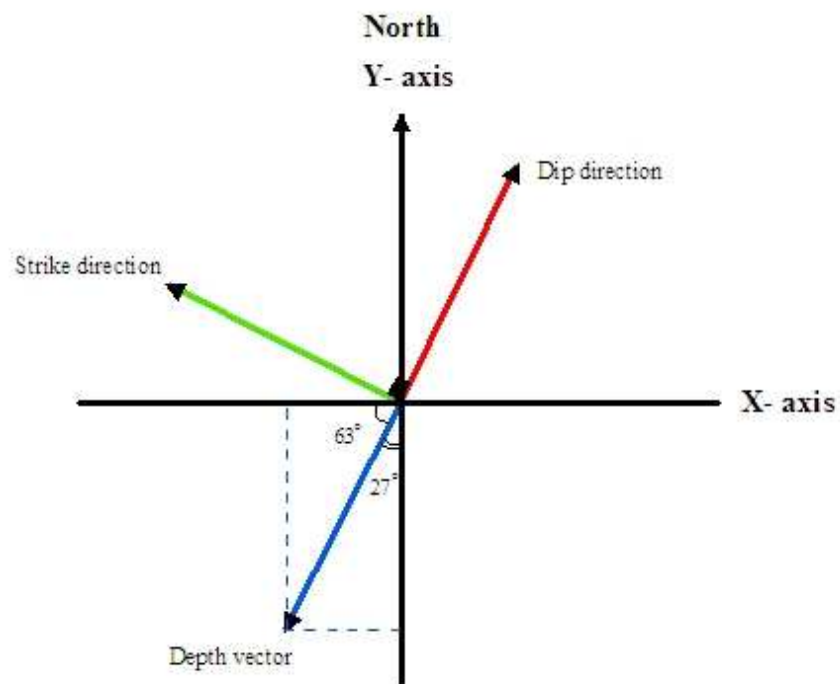


Figure 11: Resolved depth vector at St.2 to Y' and X' ; $Y' = Y - d \cos 27^\circ$; and $X' = X - d \cos 63^\circ$

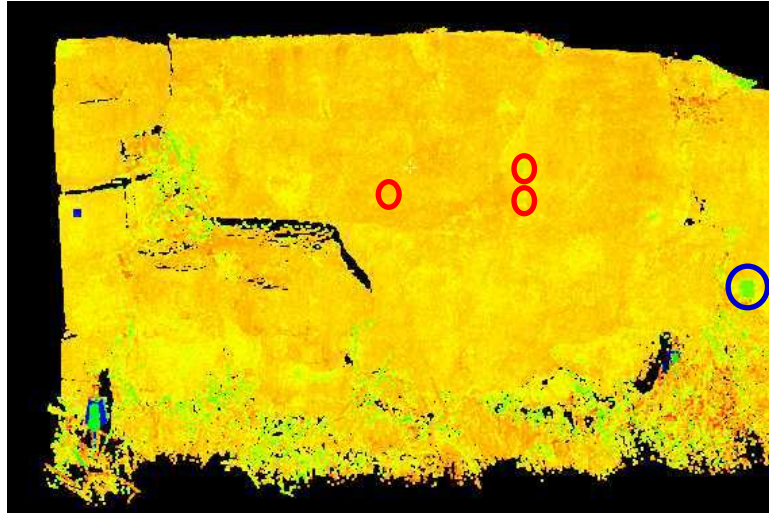
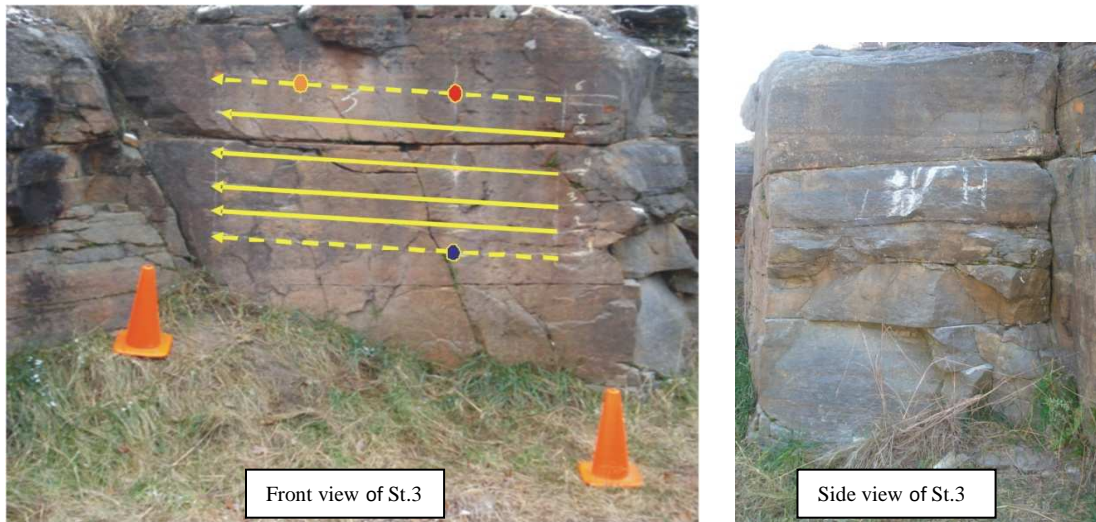


Figure 12: Point cloud image showing the location of the reference object (the blue circle) and the location of the three index points (the red circles) on the rock slope face of St.2.

Table A8: LIDAR geometrical measurements for the detected hidden subvertical joints in St.2 based on the true perpendicular depth vector components analysis and by using the 3-point equation.

Geometrical measurements of the detected hidden subvertical joints								
Joint No.	Point No.	The 3-corrospoding index points coordinates			LIDAR		Field verification	
		X'	Y'	Z'	D.D.	θ	D.D.	θ
1	1	2903.42	15272.62	464.68	029°	78°	035°	85°
	2	2886.47	15233.00	260.11				
	3	2110.87	15638.58	248.70				
2	1	2850.21	15167.49	464.68	035°	82°	030°	83°
	2	2839.57	15140.34	260.11				
	3	2307.35	15493.34	248.70				

SITE 1_STATION 3



The geometry of the GPR survey lines at St.3

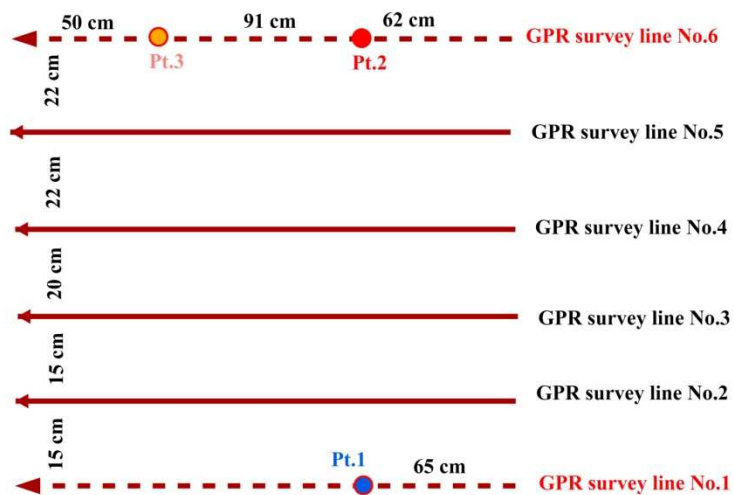


Figure 13: The location of the GPR survey lines (dashed lines are the two index lines) at St.3 and their geometry. The colored circles are the locations of the three index points.

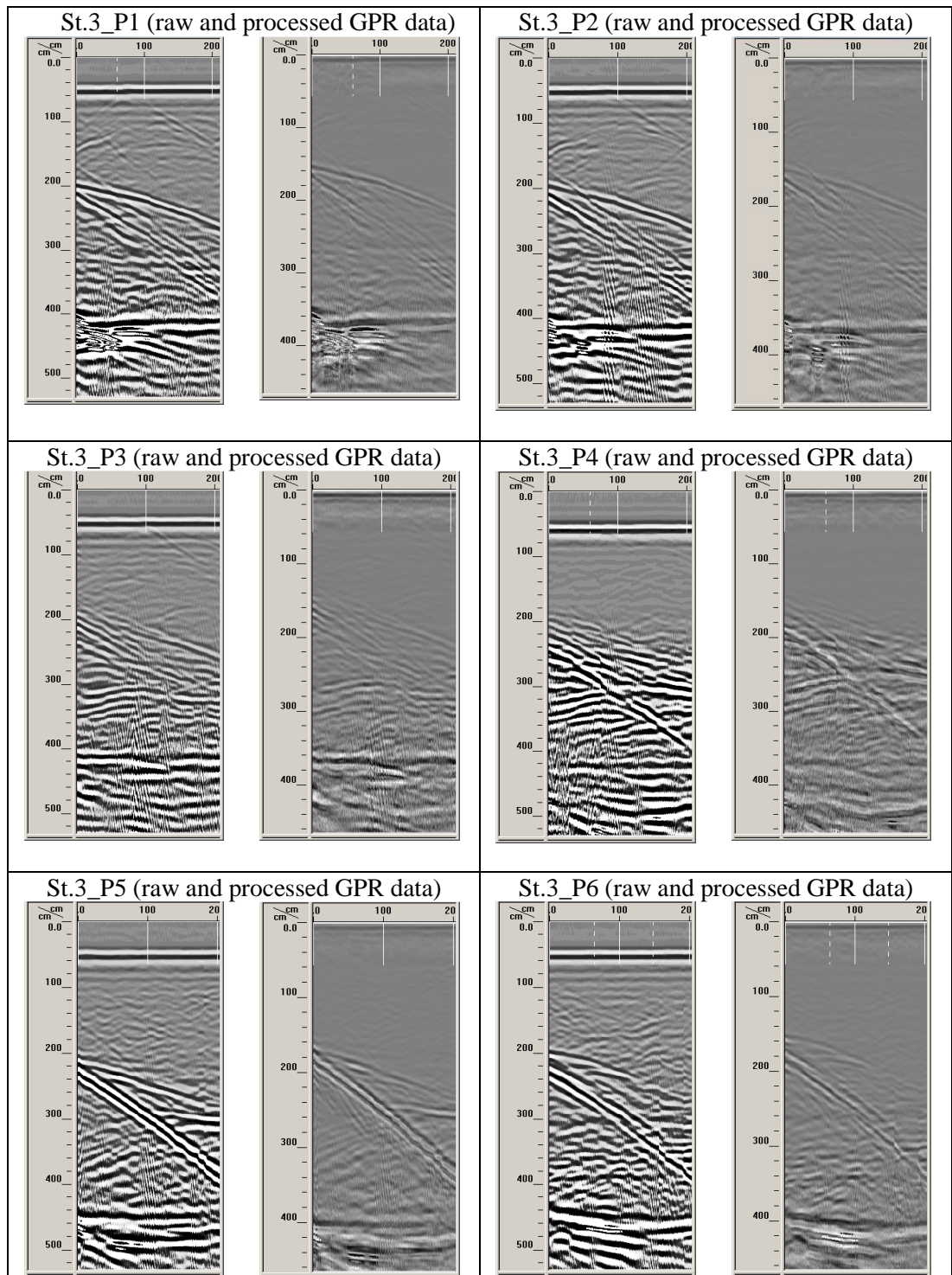


Figure 14: Radiogram images (GPR profiles) show the acquired raw and processed GPR data at St. 3.

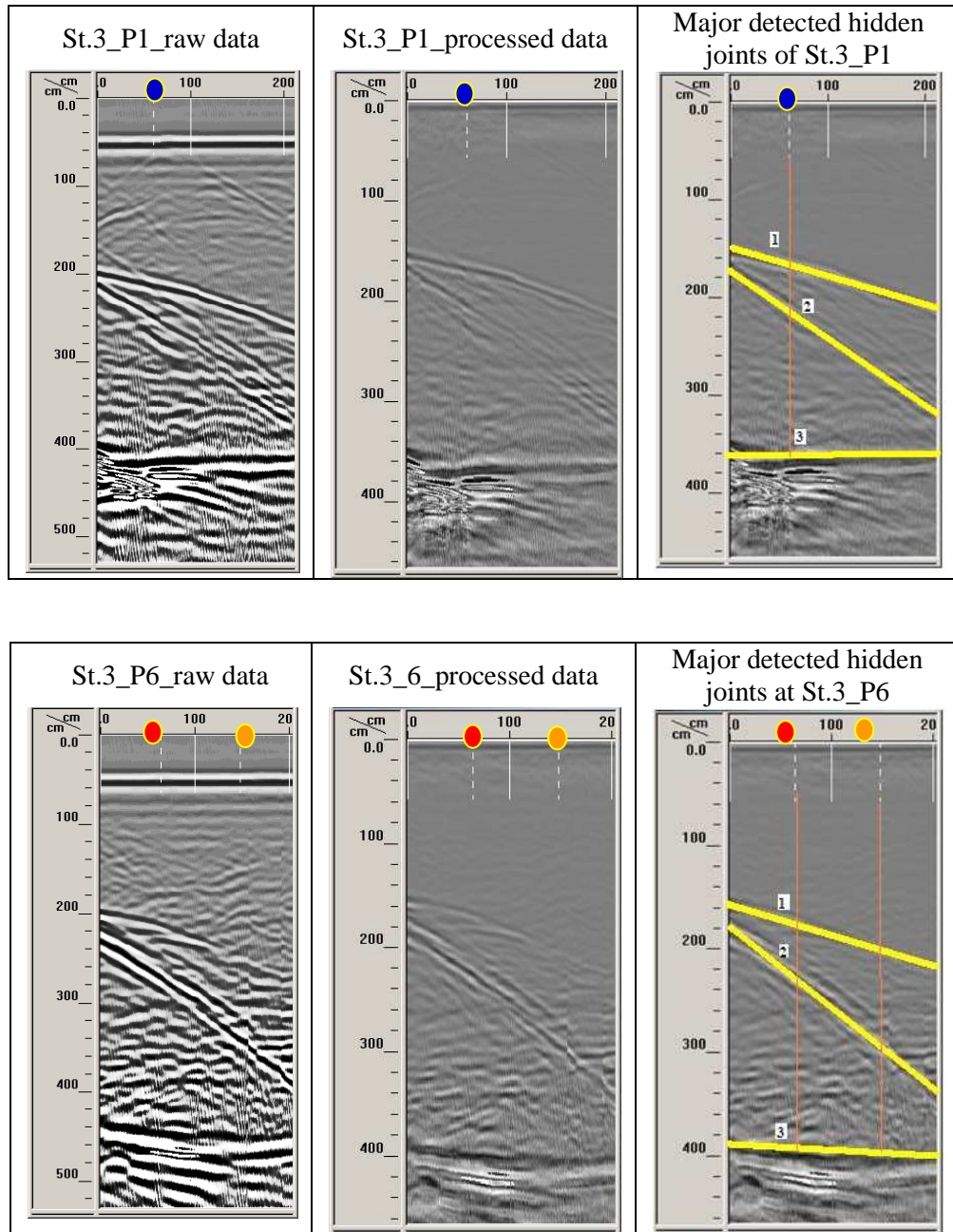


Figure 15: The apparent perpendicular depths (z) to the detected hidden subvertical joints in St.3 after GPR data processing for the two index lines.

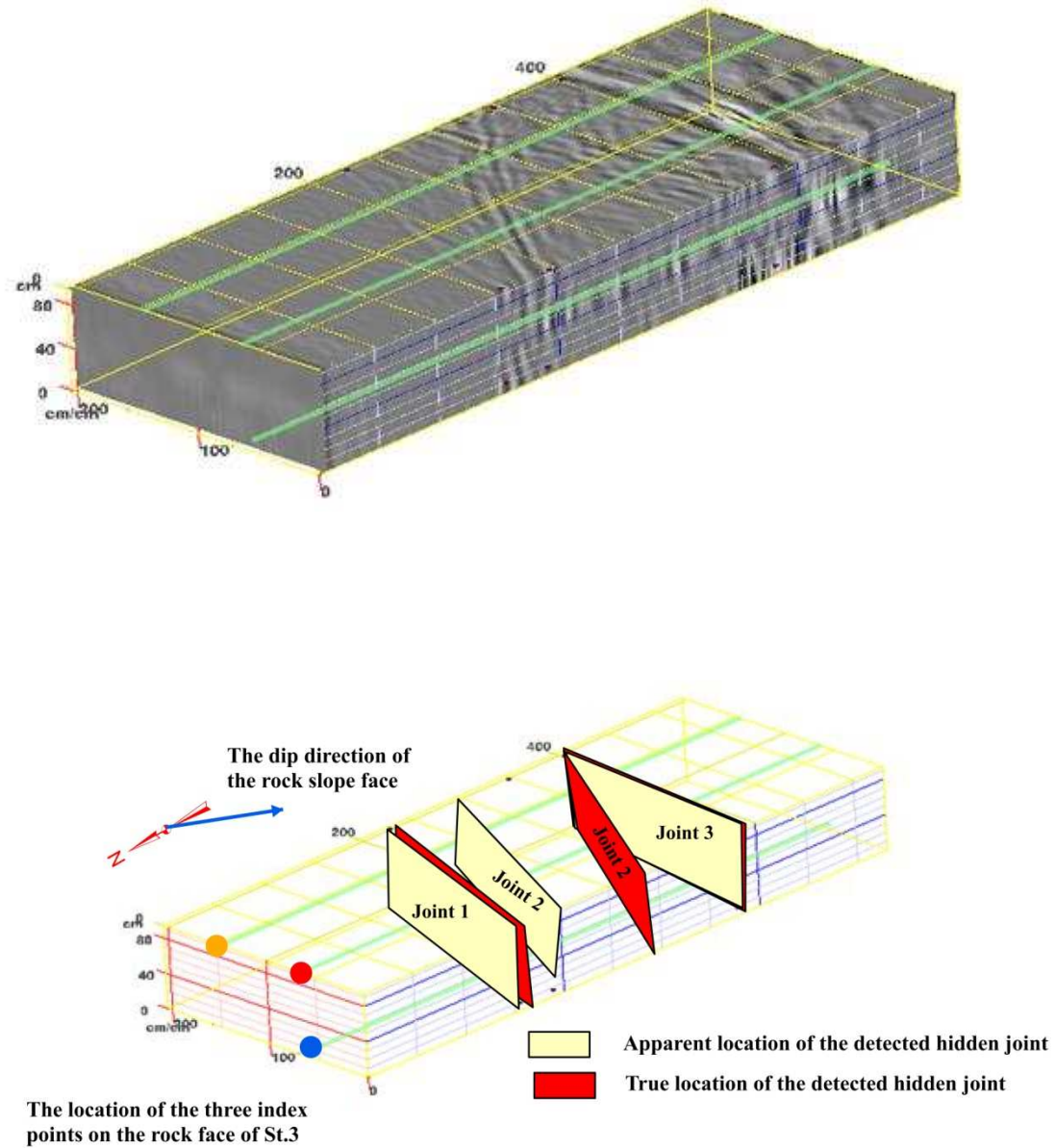


Figure 16: The created 3D image of St. 3 using RADAN software (above image) and the 3D-image for the detected hidden subvertical joints with apparent and true strike directions (blow image).

Table 9: The apparent and true perpendicular depths from the rock slope face to the detected hidden subvertical joints at St.3.







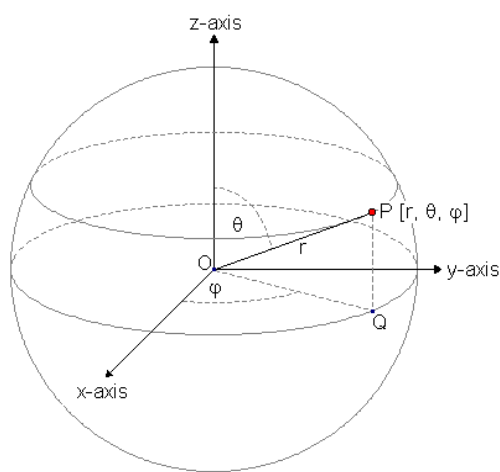
Joint No.	Apparent perpendicular depths (z) from the 3-points on the rock slope face of St.3, in cm.			Apparent (α) and true (β) declination angles of the strike		True perpendicular depths (d) from the 3-points on the rock slope face of St.3, in cm		
	Point 1 	Point 2 	Point 3 	α	β	Point 1 	Point 2 	Point 3 
1	165	172	206	17°	17.8°	173	181	216
2	208	223	290	35°	44.4°	291	312	406
3	364	396	404	03°	03°	364	396	404

Table 10: The coordinate values and geometry of the reference object for LIDAR measurements calibration at the rock slope face of St.3.

3-points coordinates of the reference object				Dip direction (D.D.) and dip angle (θ) measurements			
				Field		LIDAR	
Point	X	Y	Z	D.D.	θ	D.D.	θ
1	7625.47	15958.21	-596.57	030°	90°	030°	90°
2	7585.06	15985.46	-632.00				
3	7610.34	15969.23	-692.15				



$\theta = 90^\circ$
 $\phi = 56^\circ$
 The correction of the dip direction rotation = 4° clockwise.

Table 11: Geometrical measurements of the rock face at St. 3 after the calibration for LIDAR.

The three index point coordinates at The rock slope face				Geometry of the rock slope face			
Point	X	Y	Z	Field		LIDAR	
				D.D.	θ	D.D.	θ
1	8966.93	15322.53	-936.98	202°	87°	199°	85°
2	8977.10	15359.48	-486.48				
3	8170.74	15708.86	-394.12				

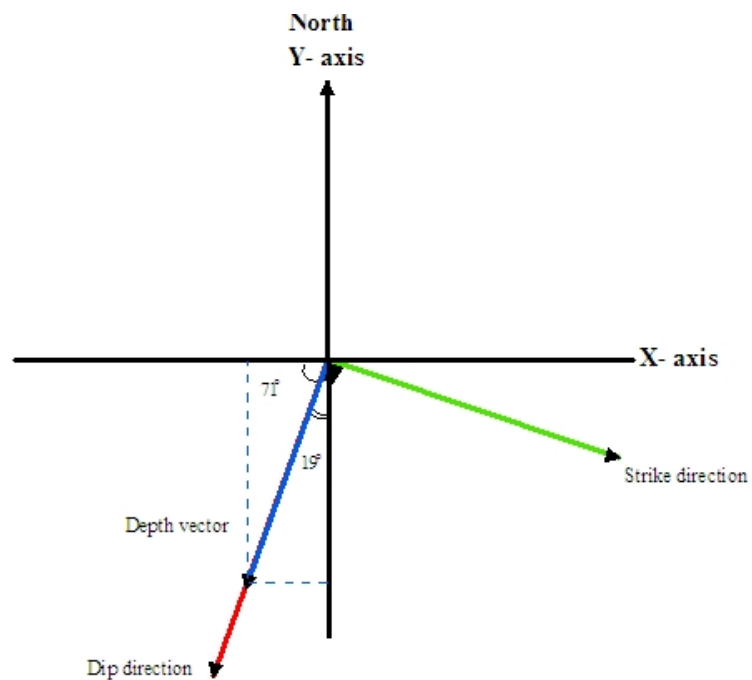


Figure 17: Resolved depth vector at St.3 to Y' and X; $Y' = Y - d \cos 19^\circ$; and $X' = X - d \cos 71^\circ$

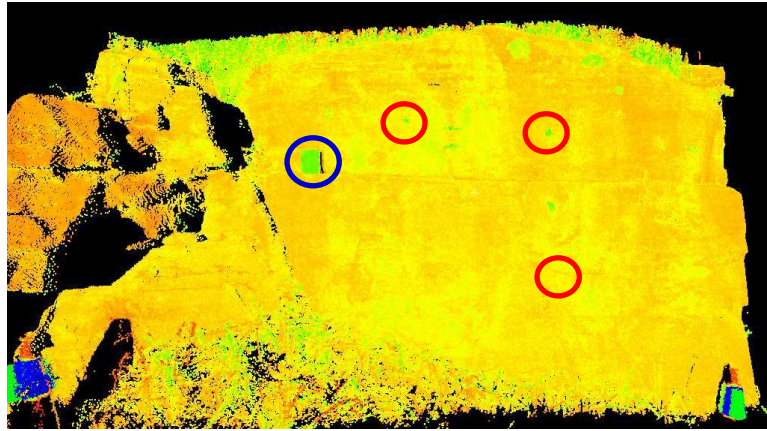


Figure 18: Point cloud image showing the location of the reference object (the blue circle) and the location of the three index points (the red circles) on the rock slope face of St.3.

Table 12: LIDAR geometrical measurements for the detected hidden subvertical joints in St.3 based on the true perpendicular depth vector components analysis and by using the 3-point equation.

		Geometrical measurements of the detected hidden subvertical joints						
Joint No.	Point No.	The 3-corresponding index points coordinates			LIDAR		Field verification	
		X'	Y'	Z'	D.D.	θ	D.D.	θ
1	1	8910.60	15158.96	-936.98	197°	86°	194°	89°
	2	8918.17	15188.34	-486.48				
	3	8100.41	15504.63	-394.12				
2	1	8872.18	15047.38	-936.98	193°	88°	NA	NA
	2	8875.51	15064.48	-486.48				
	3	8038.55	15324.98	-394.12				
3	1	8848.41	14978.36	-936.98	199°	89°	NA	NA
	2	8848.16	14985.05	-486.48				
	3	8039.20	15326.87	-394.12				

SITE 1_STATION 4



The geometry of the GPR survey lines at St.4

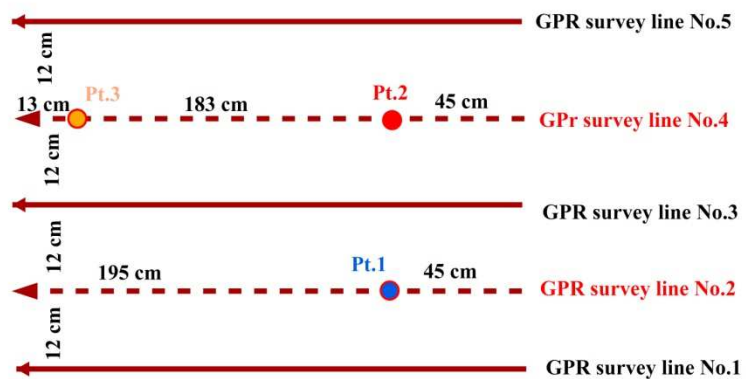


Figure 19: The location of the GPR survey lines (dashed lines are the two index lines) at St.4 and their geometry. The colored circles are the locations of the three index points.

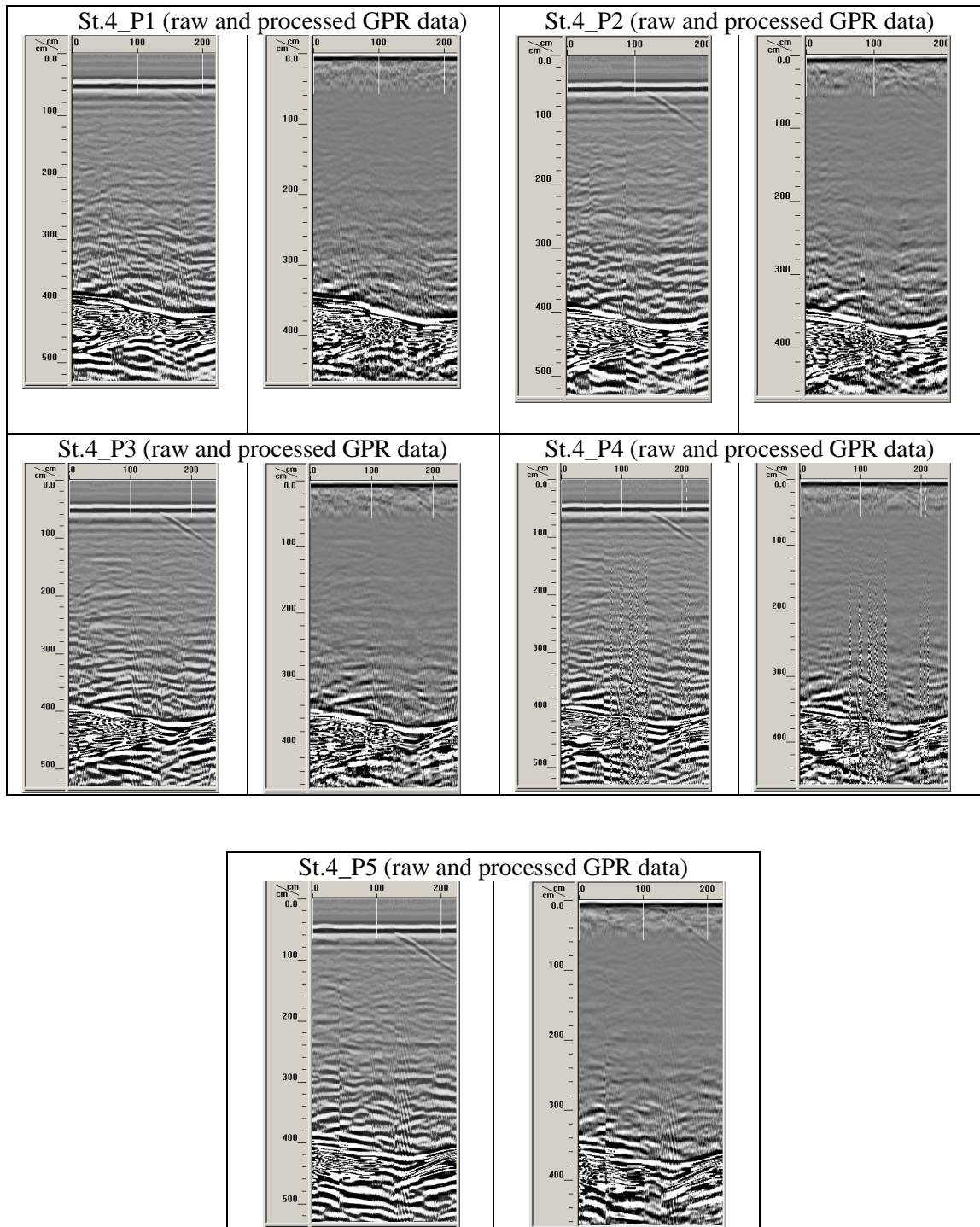


Figure 20: Radiogram images (GPR profiles) show the acquired raw and processed GPR data at St. 4.

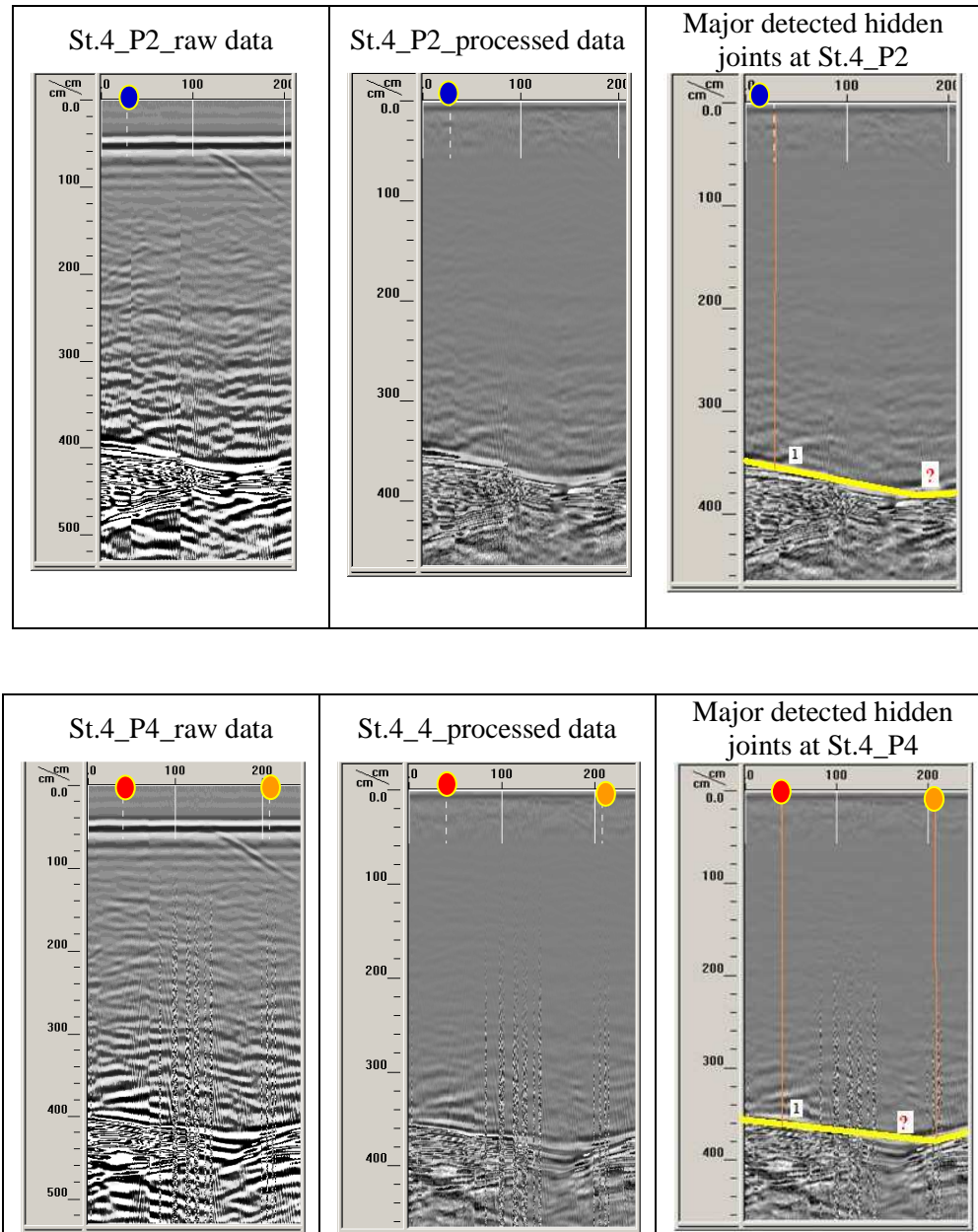


Figure 21: The perpendicular apparent depths (z) to the detected hidden subvertical joints in St.4 after GPR data processing for the two index lines.

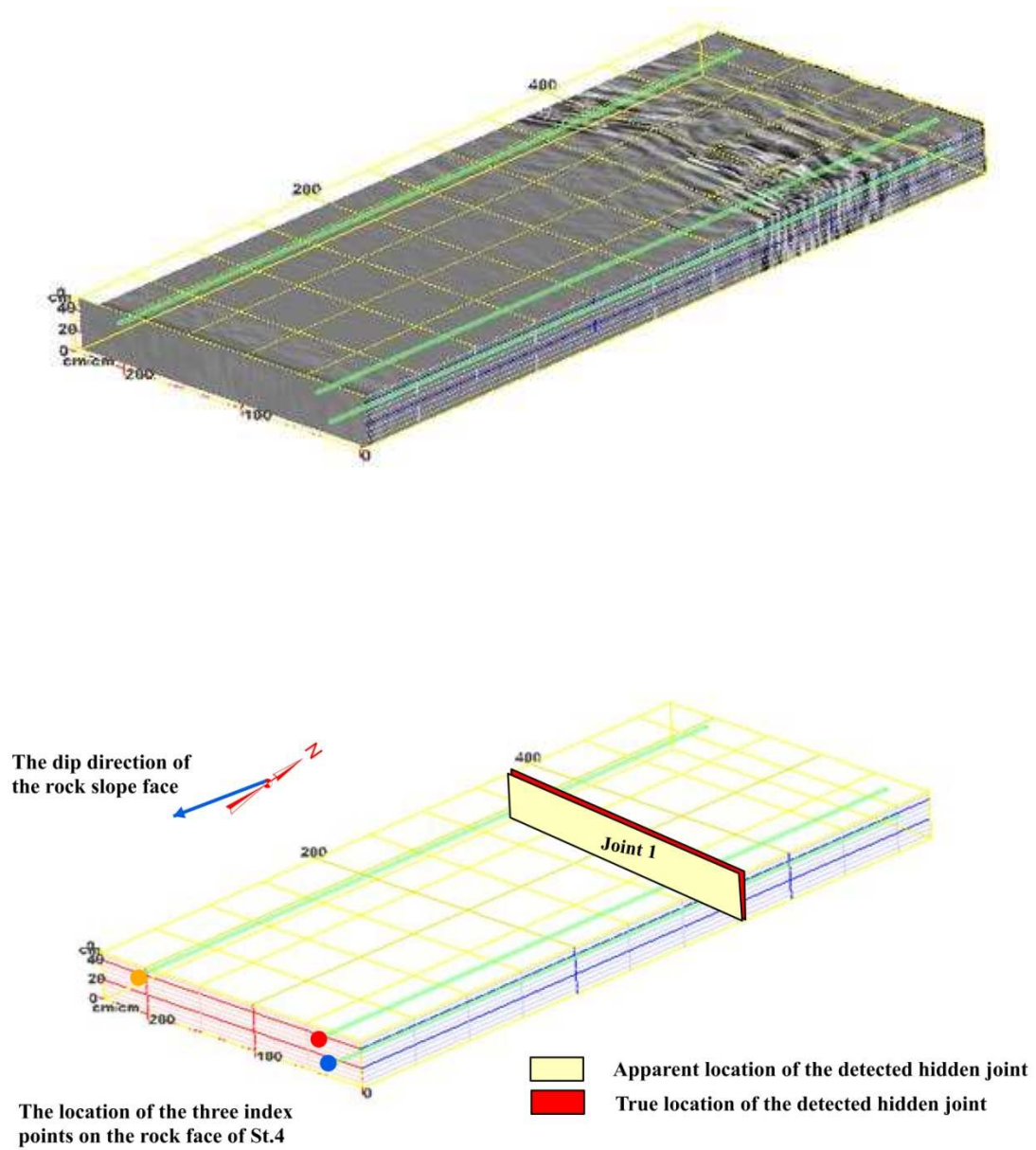


Figure 22: The created 3D image of St.4 using RADAN software (above image) and the 3D-image for the detected hidden subvertical joints with apparent and true strike directions (below image).

Table 13: The apparent and true perpendicular depths from the rock slope face to the detected hidden subvertical joints at St.4.







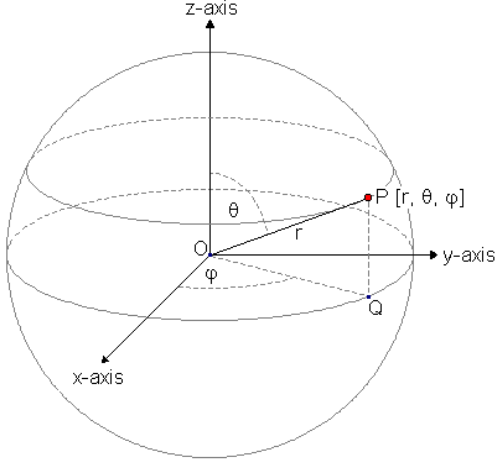
Joint No.	Apparent perpendicular depths (z) from the 3-points on the rock slope face of St.4, in cm.			Apparent (α) and true (β) declination angles of the strike		True perpendicular depths (d) from the 3-points on the rock slope face of St.4, in cm		
	Point 1 	Point 2 	Point 3 	α	β	Point 1 	Point 2 	Point 3 
1	348	355	379	11°	11.2°	355	362	386




Table 14: The coordinate values and geometry of the reference object for LIDAR measurements calibration at the rock slope face of St.4.

3-points coordinates of the reference object				Dip direction (D.D.) and dip angle (θ) measurements			
				Field		LIDAR	
Point	X	Y	Z	D.D.	θ	D.D.	θ
1	2390.76	13728.16	-966.48	196°	88°	196°	86°
2	2319.41	13742.89	-1014.53				
3	2388.97	13720.45	-1074.33				



$\theta = 86^\circ$
 $\phi = 76^\circ$
 The correction of the dip direction rotation = 358° clockwise.

Table 15: Geometrical measurements of the rock face at St. 4 after the calibration for LIDAR.

The three index point coordinates at The rock slope face				Geometry of the rock slope face			
Point	X	Y	Z	Field		LIDAR	
				D.D.	θ	D.D.	θ
1 	4506.50	13003.10	-1057.25	195°	87°	202°	90°
2 	4485.41	13012.93	-821.73				
3 	2804.01	13626.68	-670.18				

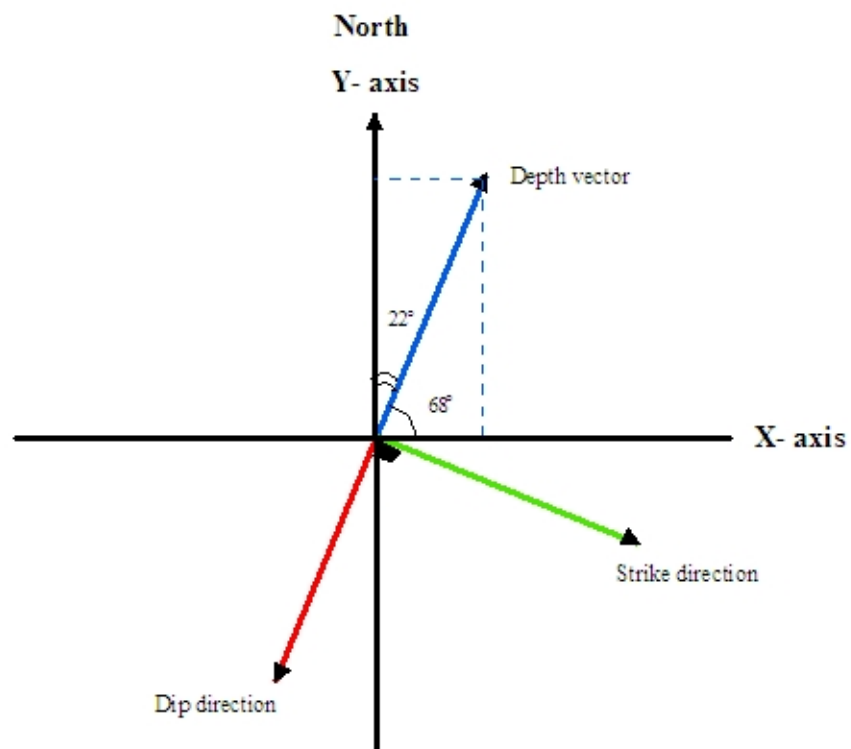


Figure 23: Resolved depth vector at St.4 to Y' and X' ; $Y' = Y - d \cos 22^\circ$; and $X' = X - d \cos 68^\circ$

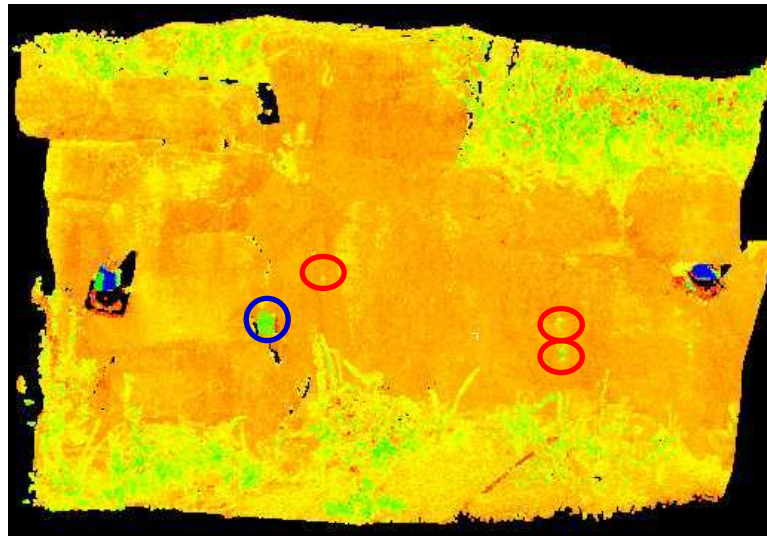
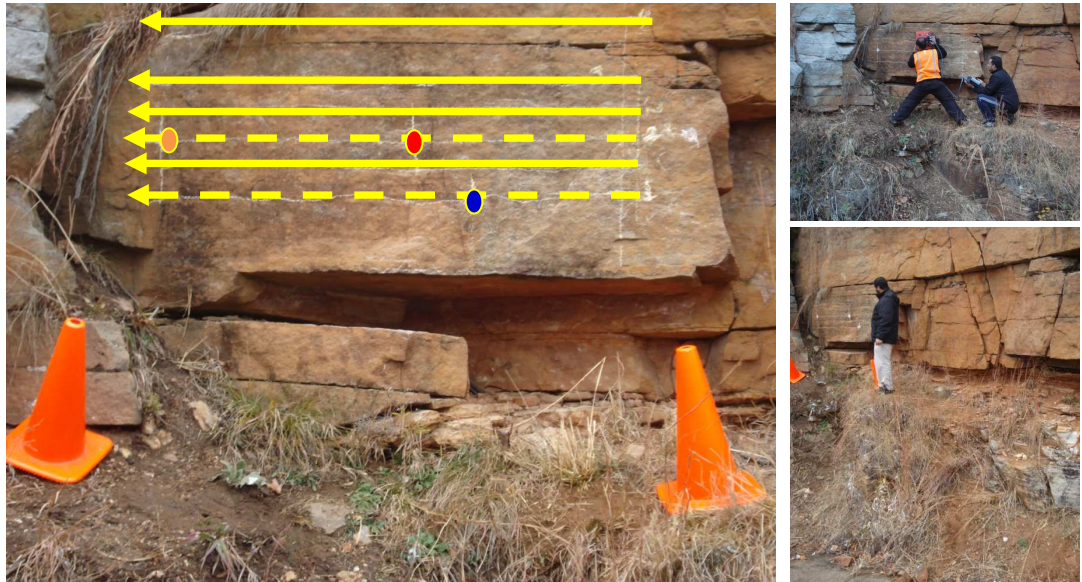


Figure 24: Point cloud image showing the location of the reference object (the blue circle) and the location of the three index points (the red circles) on the rock slope face of St.4.

Table 16: LIDAR geometrical measurements for the detected subvertical hidden joints in St.4 based on the true perpendicular depth vector components analysis and by using the 3-point equation.

Geometrical measurements of the detected hidden subvertical joints								
Joint No.	Point No.	The 3-corresponding index points coordinates			LIDAR		Field verification	
		X'	Y'	Z'	D.D.	θ	D.D.	θ
1	1	4373.52	12673.94	-1057.25	021°	89°	NA	NA
	2	4349.80	12677.28	-821.73				
	3	2659.41	13268.78	-670.18				

SITE 1_STATION 5



The geometry of the GPR survey lines at St.5

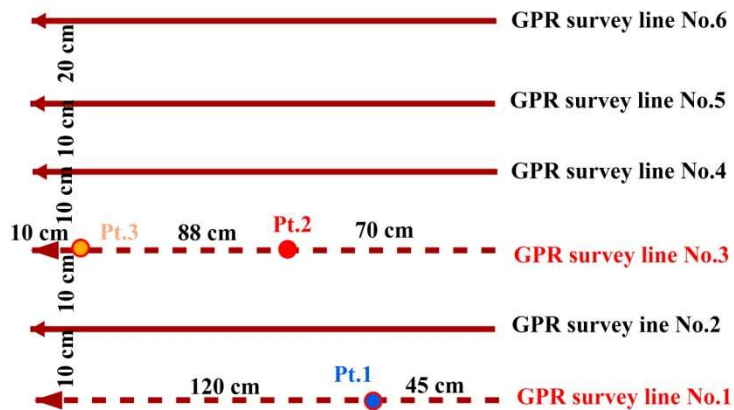


Figure 25: The location of the GPR survey lines (dashed lines are the two index lines) at St.5 and their geometry. The colored circles are the locations of the three index points.

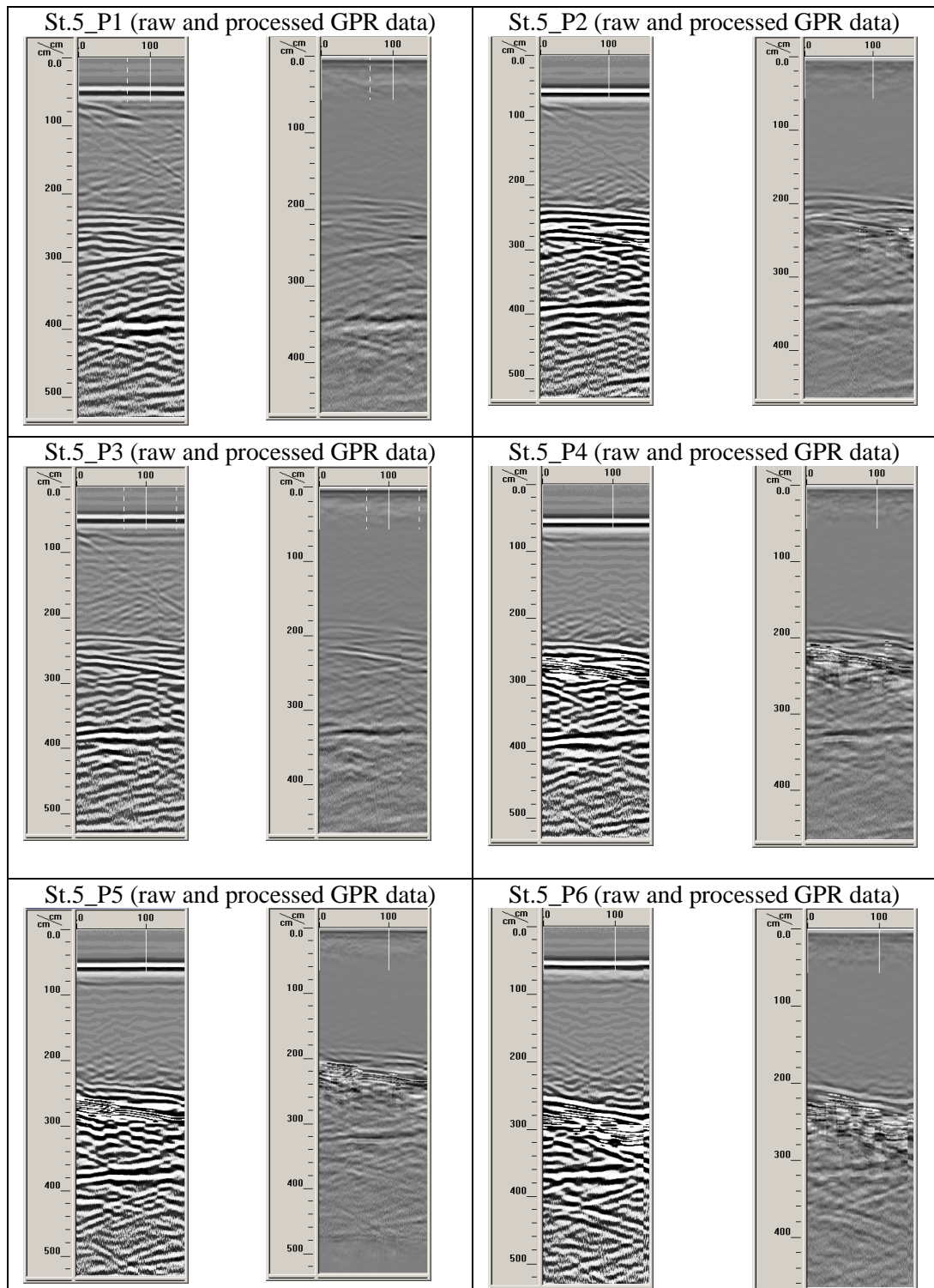


Figure 26: Radiogram images (GPR profiles) show the acquired raw and processed GPR data at St. 5.

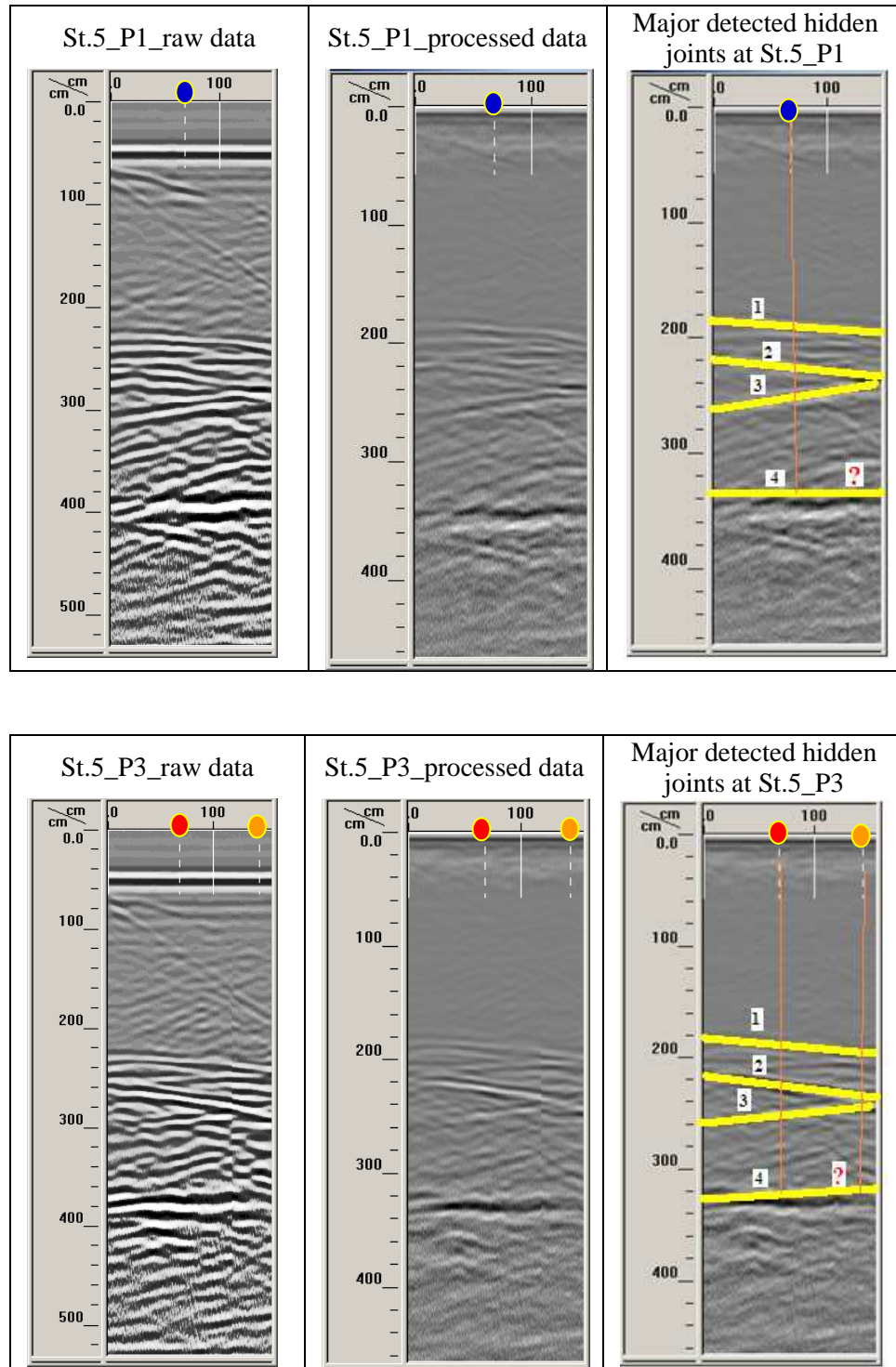


Figure 27: The apparent perpendicular depths (z) to the detected hidden subvertical joints in St.5 after GPR data processing for the two index lines.

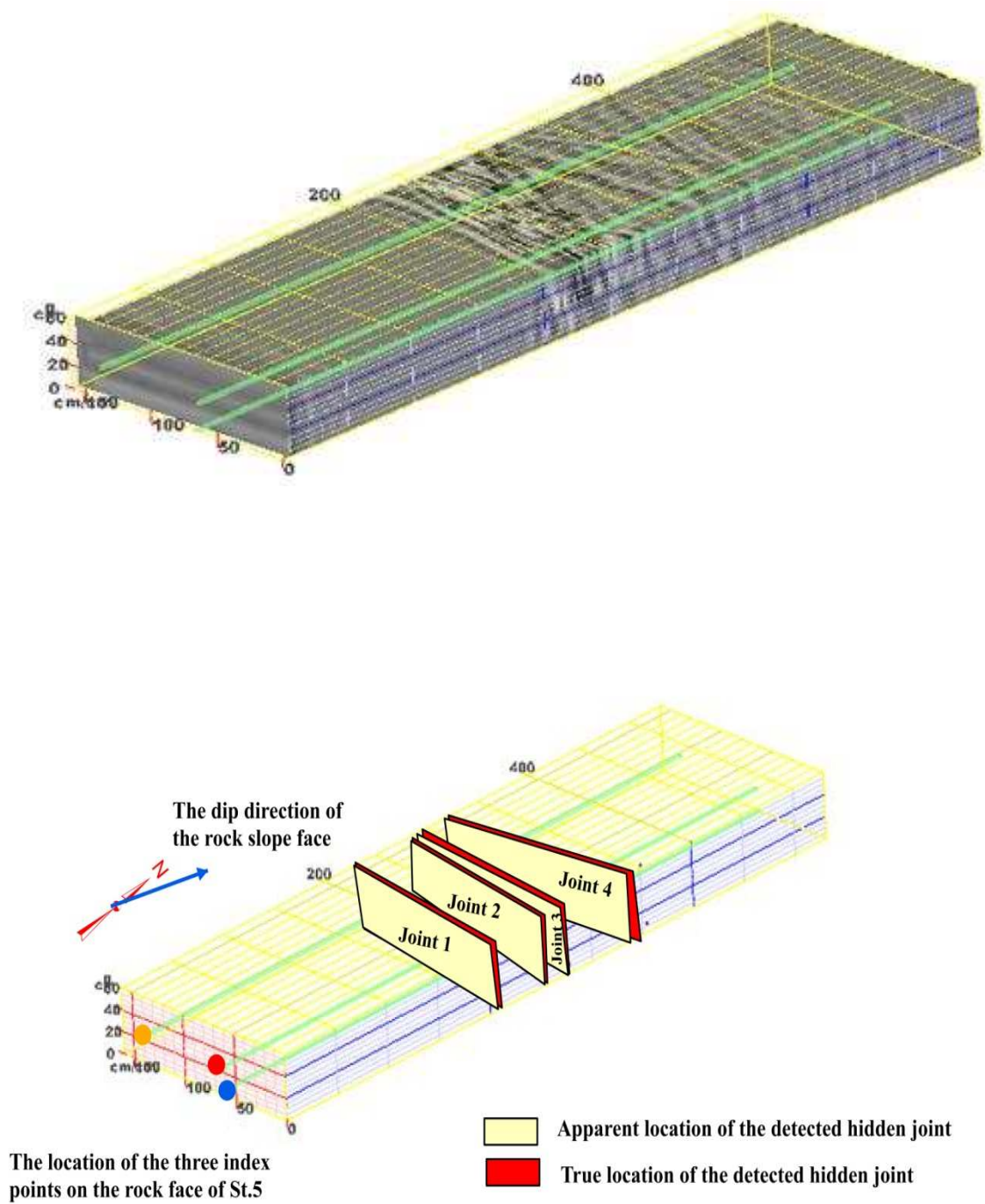


Figure 28: The created 3D image of St.5 using RADAN software (above image) and the 3D-image for the detected hidden subvertical joints with apparent and true strike directions (blow image).

Table 17: The apparent and true perpendicular depths from the rock slope face to the detected hidden subvertical joints at St.5.







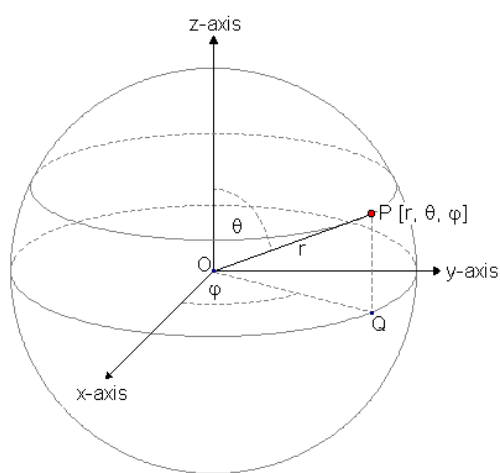
Joint No.	Apparent perpendicular depths (z) from the 3-points on the rock slope face of St.5, in cm.			Apparent (α) and true (β) declination angles of the strike		True perpendicular depths (d) from the 3-points on the rock slope face of St.5, in cm		
	Point 1 	Point 2 	Point 3 	α	β	Point 1 	Point 2 	Point 3 
1	187	189	197	7°	7.1°	188	190	198
2	224	227	240	7°	7.1°	225	229	242
3	248	249	236	9°	9.1°	251	252	239
4	336	323	320	5°	5.1°	338	324	321




Table 18: The coordinate values and geometry of the reference object for LIDAR measurements calibration at the rock slope face of St.5.

3-points coordinates of the reference object				Dip direction (D.D.) and dip angle (θ) measurements			
Point	X	Y	Z	Field		LIDAR	
				D.D.	θ	D.D.	θ
1	2422.82	13994.80	253.29	200°	90°	200°	85°
2	2333.76	14024.61	222.52				
3	2374.55	14015.37	183.12				



$\theta = 85^\circ$
 $\phi = 73^\circ$
 The correction of the dip direction rotation = 177° clockwise.

Table 19: Geometrical measurements of the rock face at St.5 after the calibration for LIDAR.

The three index point coordinates at The rock slope face				Geometry of the rock slope face			
Point	X	Y	Z	Field		LIDAR	
				D.D.	θ	D.D.	θ
1 	2644.17	13969.41	588.63	010°	88°	015°	87°
2 	2599.15	13986.50	741.64				
3 	1629.43	14195.73	775.75				

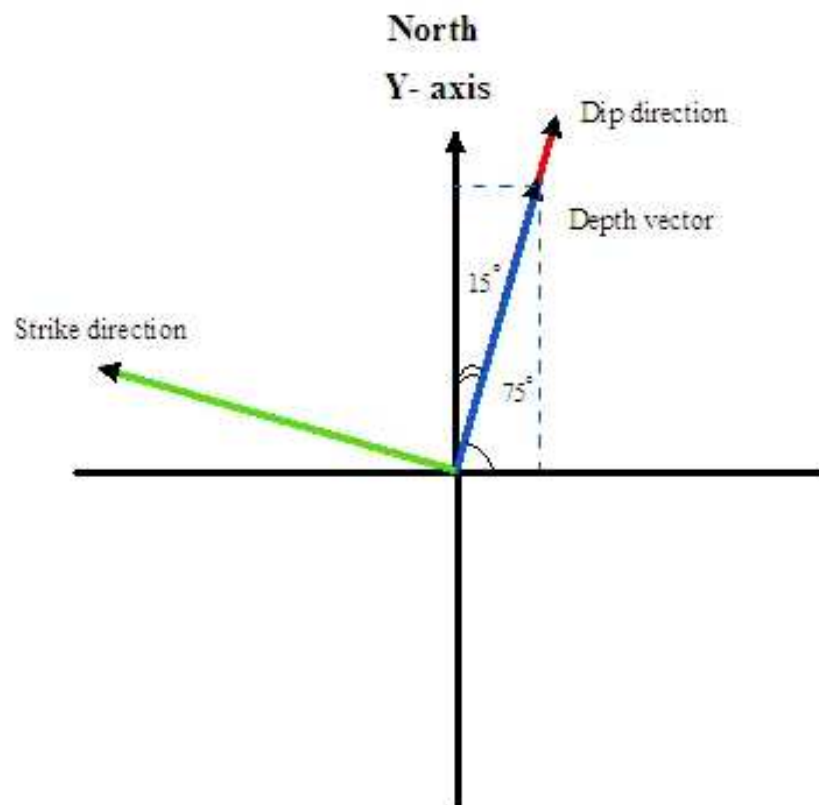


Figure 29: Resolved depth vector at St.5 to Y' and X' ; $Y' = Y - d \cos 15^\circ$; and $X' = X - d \cos 75^\circ$

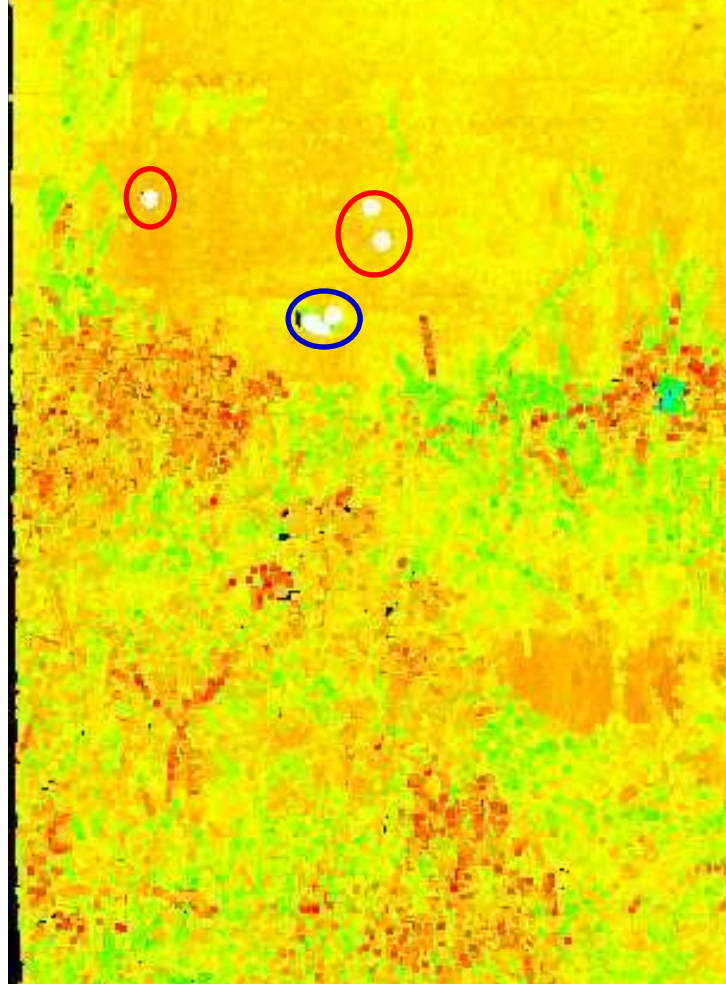


Figure 30: Point cloud image showing the location of the reference object (the blue circle) and the location of the three index points (the red circles) on the rock slope face of St.5.

Table 20: LIDAR (3D TLS) geometrical measurements for detected hidden joints in St. 5 based on the true depths using GPR and 3-point equation.

Geometrical measurements of the detected hidden subvertical joints								
Joint No.	Point No.	The 3-corresponding index points coordinates			LIDAR		Field verification	
		X'	Y'	Z'	D.D.	θ	D.D.	θ
1	1	2595.51	13787.82	588.63	015°	88°	NA	NA
	2	2549.97	13802.97	741.64				
	3	1578.18	14004.48	775.75				
2	1	2585.94	13752.08	588.63	014°	89°	NA	NA
	2	2539.88	13765.30	741.64				
	3	1566.80	13961.97	775.75				
3	1	2579.21	13726.96	588.63	016°	88°	NA	NA
	2	2533.93	13743.09	741.64				
	3	1567.57	13964.87	775.75				
4	1	2556.69	13642.93	588.63	015°	82°	NA	NA
	2	2515.29	13673.54	741.64				
	3	1546.35	13885.67	775.75				

SITE 2_STATION 6



The geometry of the GPR survey lines at St. 6

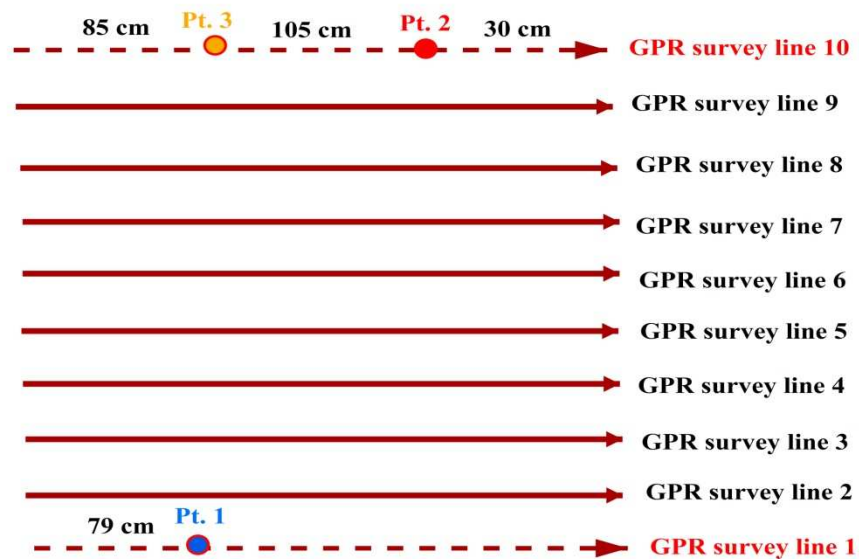


Figure 31: The location of the GPR survey lines (dashed lines are the two index lines) at St.6 and their geometry. The colored circles are the locations of the three index points.

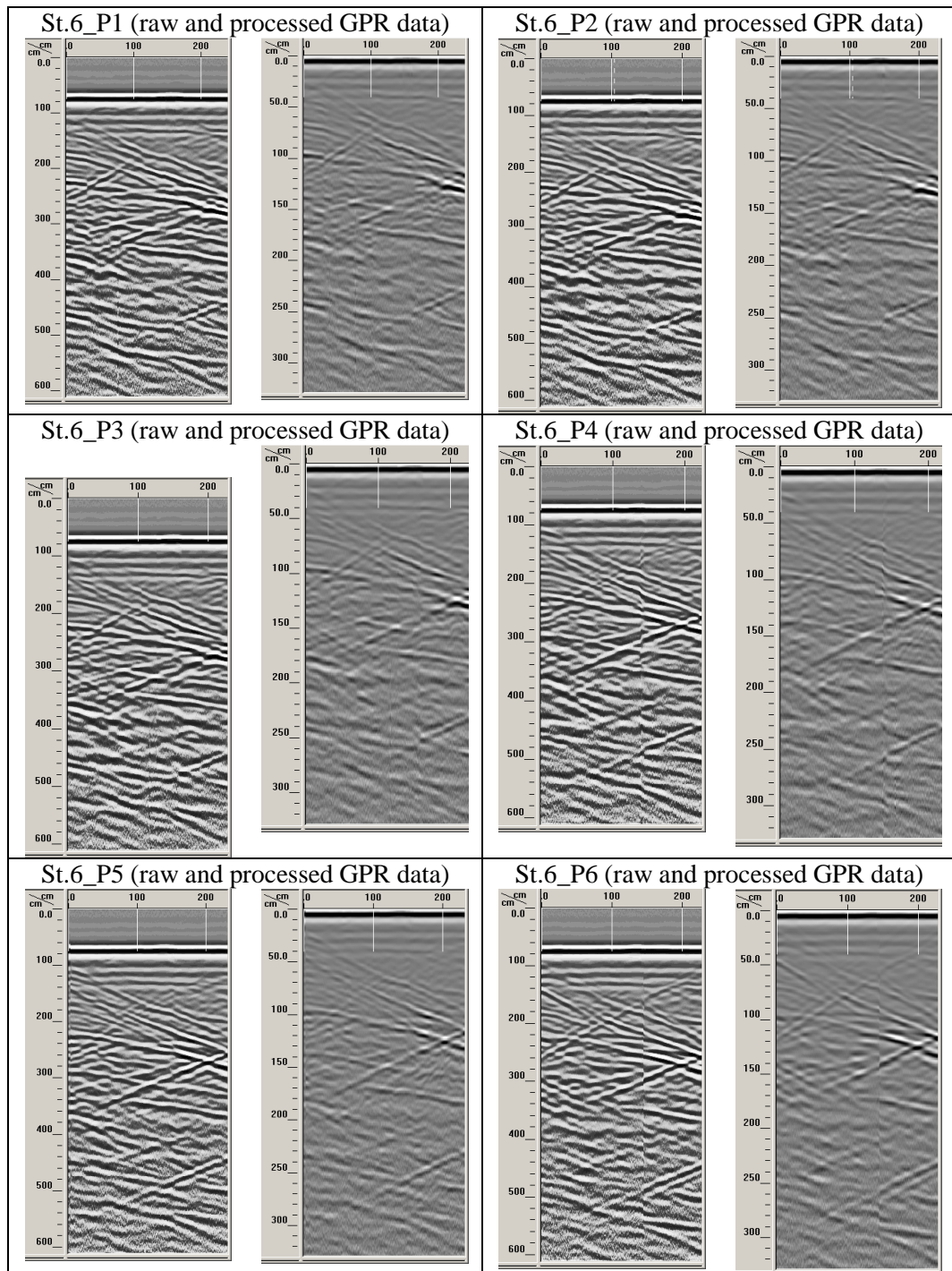


Figure 32: Radiogram images (GPR profiles) show the acquired raw and processed GPR data at St. 6.

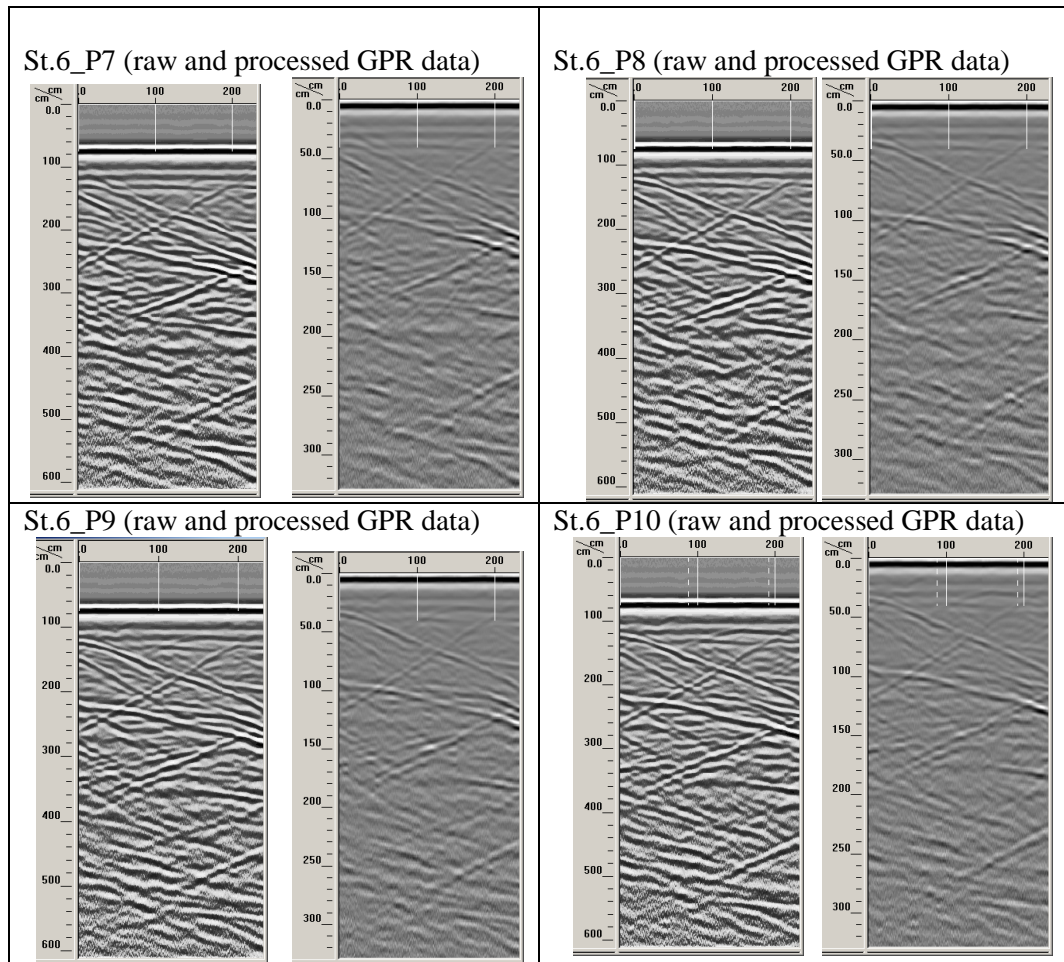


Figure 32 (Cont.): Radiogram images (GPR profiles) show the acquired raw and processed GPR data at St. 6.

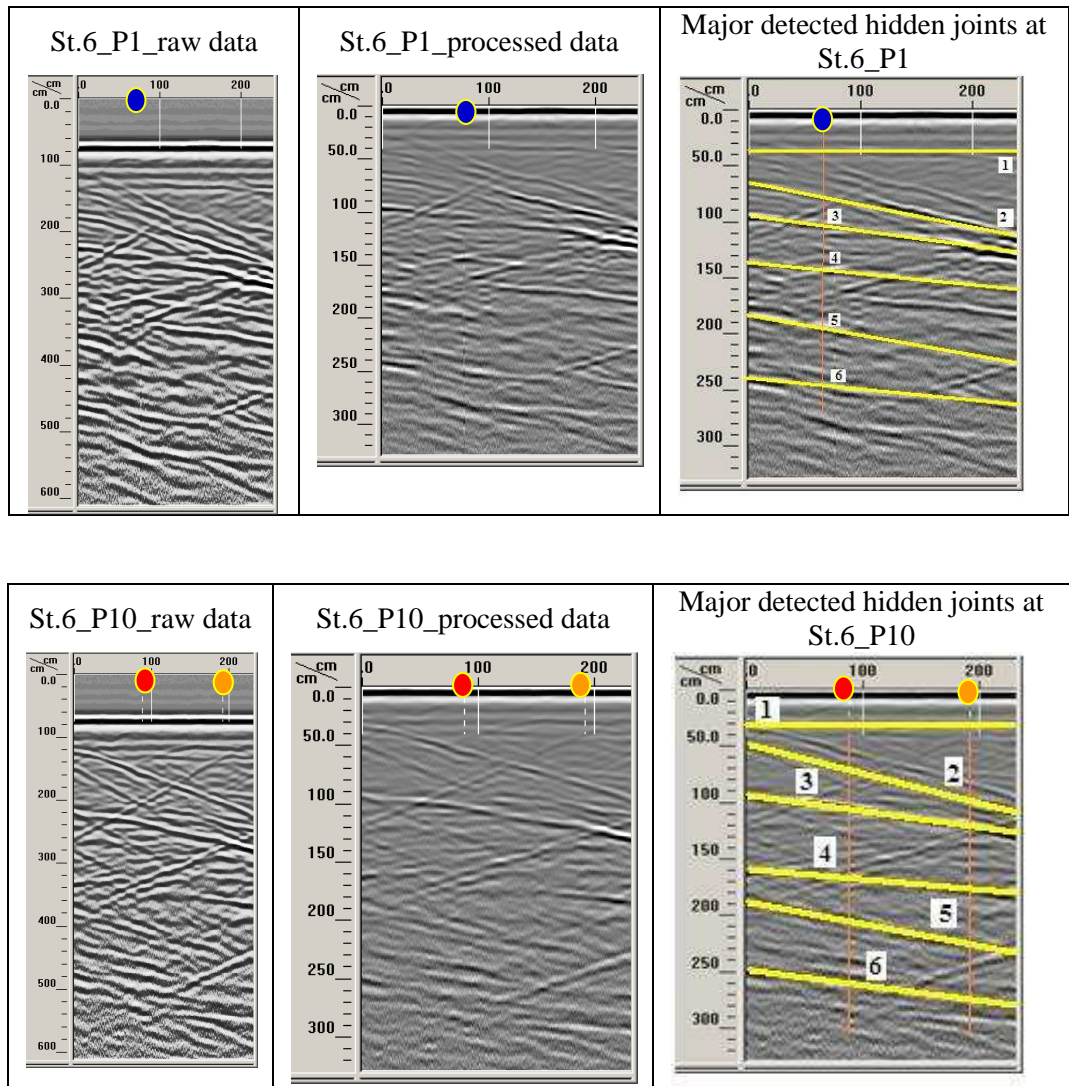


Figure 33: The apparent perpendicular depths (z) to the detected hidden subvertical joints in St.6 after GPR data processing for the two index lines. The vertical scale equals to the horizontal scale.

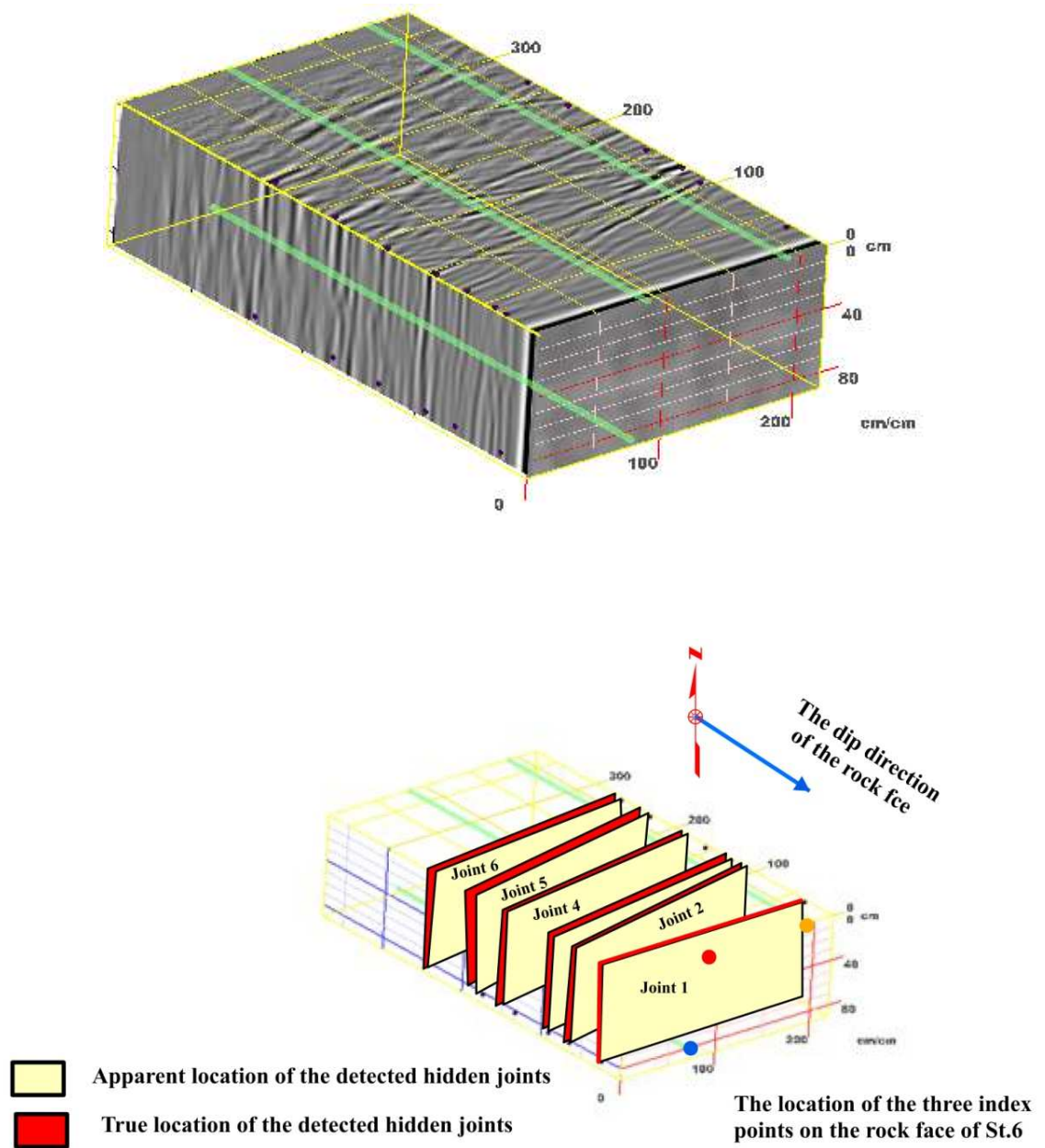


Figure34: The created 3D image of St.6 using RADAN software (above image) and the 3D-image for the detected hidden subvertical joints with apparent and true strike directions (blow image).

Table 21: The apparent and true perpendicular depths from the rock slope face to the detected hidden subvertical joints at St.7.







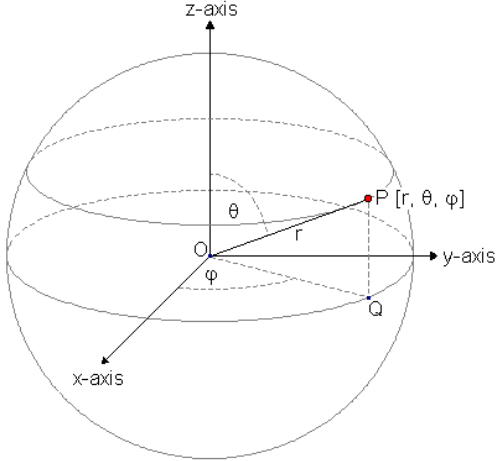
Joint No.	Apparent perpendicular depths (z) from the 3-points on the rock slope face of St.6, in cm.			Apparent (α) and true (β) declination angles of the strike		True perpendicular depths (d) from the 3-points on the rock slope face of St.6, in cm		
	Point 1 	Point 2 	Point 3 	α	β	Point 1 	Point 2 	Point 3 
1	36	36	39	1	1	36	36	39
2	79	83	104	11	11.2	81	85	106
3	102	104	121	10	10.2	104	106	123
4	142	163	174	6	6	142	163	180
5	197	218	239	12	12.3	202	223	245
6	249	264	277	8	8.1	252	267	280




Table 22: The coordinate values and geometry of the reference object for LIDAR measurements calibration at the rock slope face of St.6.

3-points coordinates of the reference object				Dip direction (D.D.) and dip angle (θ) measurements			
				Field		LIDAR	
Point	X	Y	Z	D.D.	θ	D.D.	θ
1	-1835.49	19893.59	875.73	205	81	205	81
2	-2260.37	19968.69	172.37				
3	-1358.82	19581.32	401.48				



$\theta = 81^\circ$
 $\phi = 65^\circ$
 The correction of the dip direction rotation = 0° clockwise.

Table 23: Geometrical measurements of the rock face at St.6 after the calibration for LIDAR.

The three index point coordinates at The rock slope face				Geometry of the rock slope face			
Point	X	Y	Z	Field		LIDAR	
				D.D.	θ	D.D.	θ
1 	-3793.10	19704.89	-395.71	159°	88°	159°	89°
2 	-3221.23	20073.10	501.74				
3 	-3998.90	19603.95	492.64				

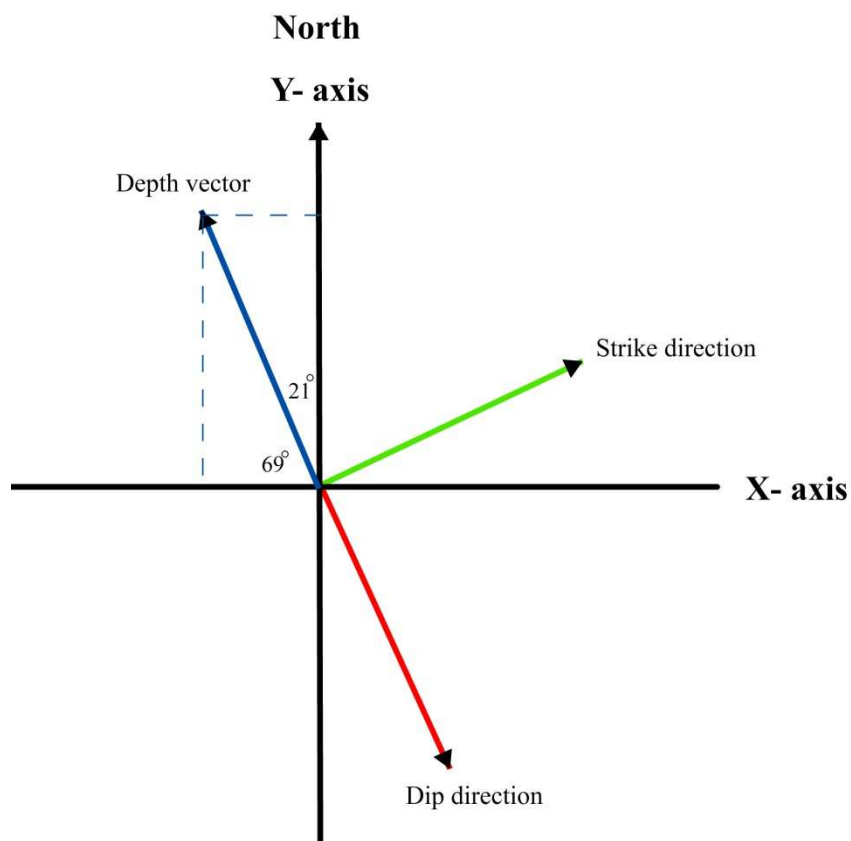


Figure 35: Resolved depth vector at St.6 to Y' and X'; $Y' = Y - d \cos 21^\circ$; and $X' = X - d \cos 69^\circ$.

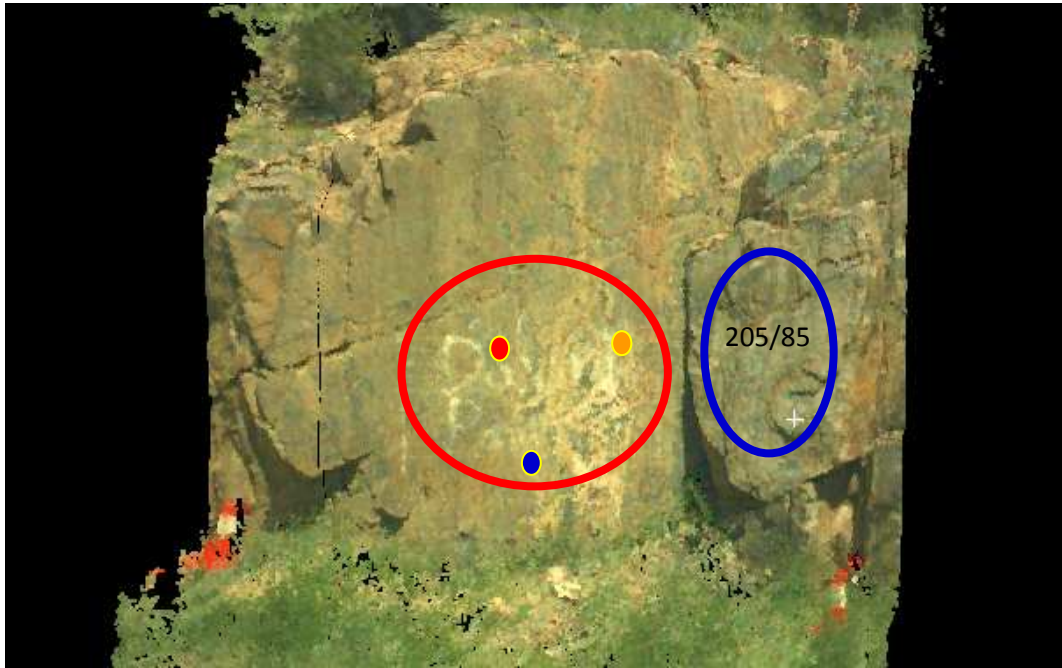


Figure 36: Point cloud image showing the location of the reference object (the blue circle) and the location of the three index points (the red circles) on the rock slope face of St.6.

Table 24: LIDAR (3D TLS) geometrical measurements for detected hidden joints in St. 6 based on the true depths using GPR and 3-point equation.

Geometrical measurements of the detected hidden subvertical joints								
Joint No.	Point No.	The 3-corrospoding index points coordinates			LIDAR		Field verification	
		X'	Y'	Z'	D.D.	θ	D.D.	θ
1	1	-3799.97	19669.55	-395.71	159°	89°	155°	90°
	2	-3228.10	20037.76	501.74				
	3	-4006.34	19565.67	492.64				
2	1	-3808.56	19625.38	-395.71	158°	90°	153°	85°
	2	-3237.45	19989.66	501.74				
	3	-4019.13	19499.90	492.64				
3	1	-3812.94	19602.80	-395.71	158°	89°	152°	88°
	2	-3241.46	19969.05	501.74				
	3	-4022.37	19483.21	492.64				
4	1	-3820.19	19565.50	-395.71	338°	90°	336°	90°
	2	-3252.33	19913.09	501.74				
	3	-4033.25	19427.26	492.64				
5	1	-3813.64	19506.60	-395.71	158°	90°	NA	NA
	2	-3263.78	19854.20	501.74				
	3	-4045.65	19363.45	492.64				
6	1	-3841.18	19457.52	-395.71	158°	90°	NA	NA
	2	-3272.18	19811.01	501.74				
	3	-4052.33	19329.09	492.64				

SITE 2_STATION 7



The geometry of the GPR survey lines at St. 7

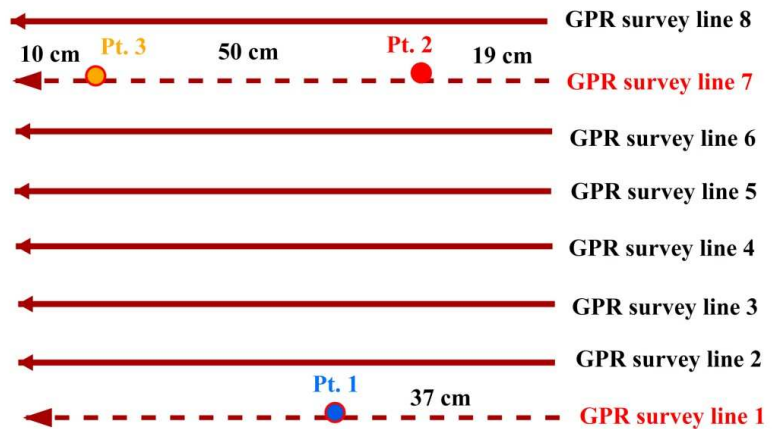


Figure 37: The location of the GPR survey lines (dashed lines are the two index lines) at St.7 and their geometry. The colored circles are the locations of the three index points.

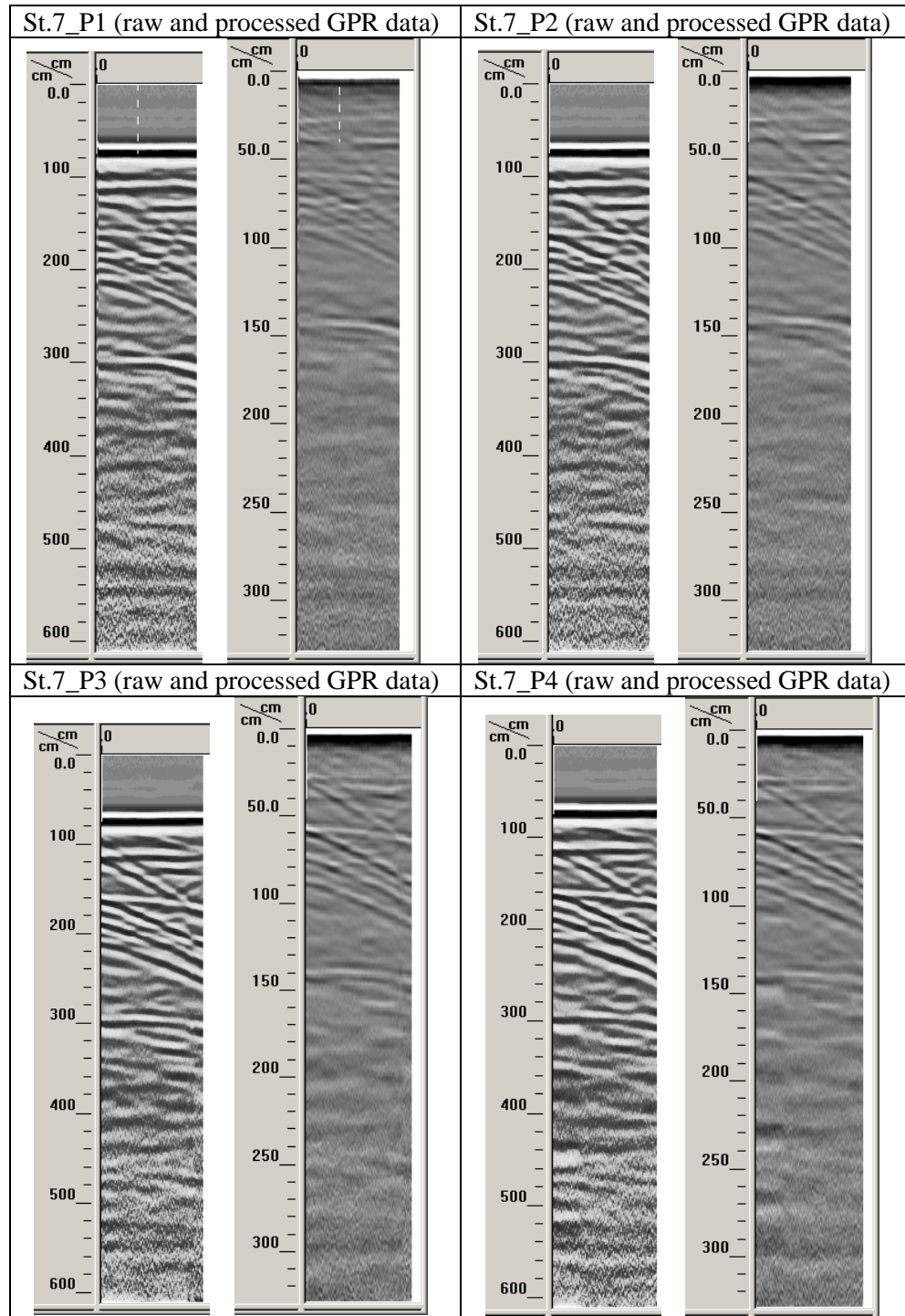


Figure 38: Radiogram images (GPR profiles) show the acquired raw and processed GPR data of profiles 1 to 4 at St. 7.

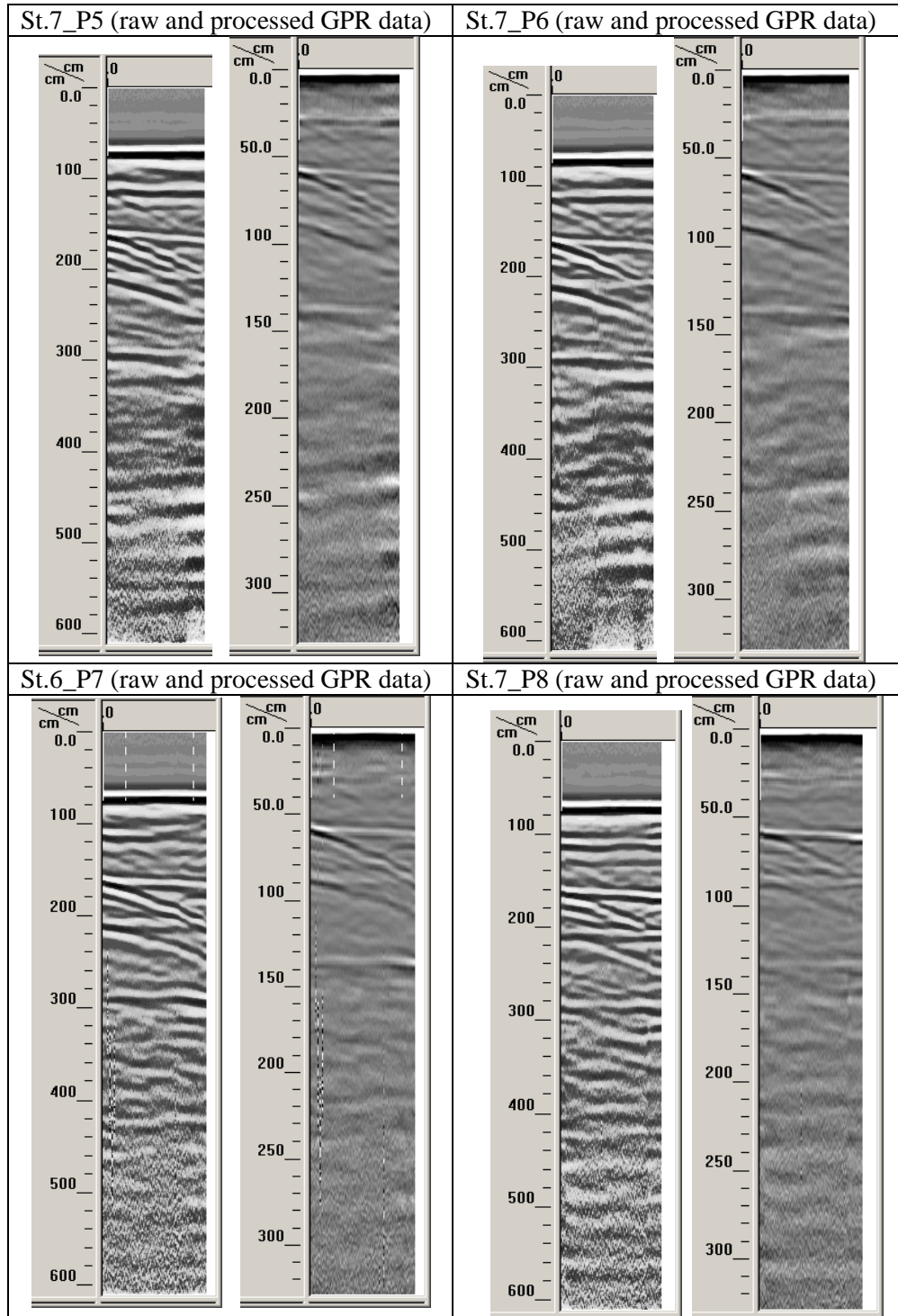


Figure 38 (Cont.): Radiogram images (GPR profiles) show the acquired raw and processed GPR data of profiles 5 to 8 at St. 7.

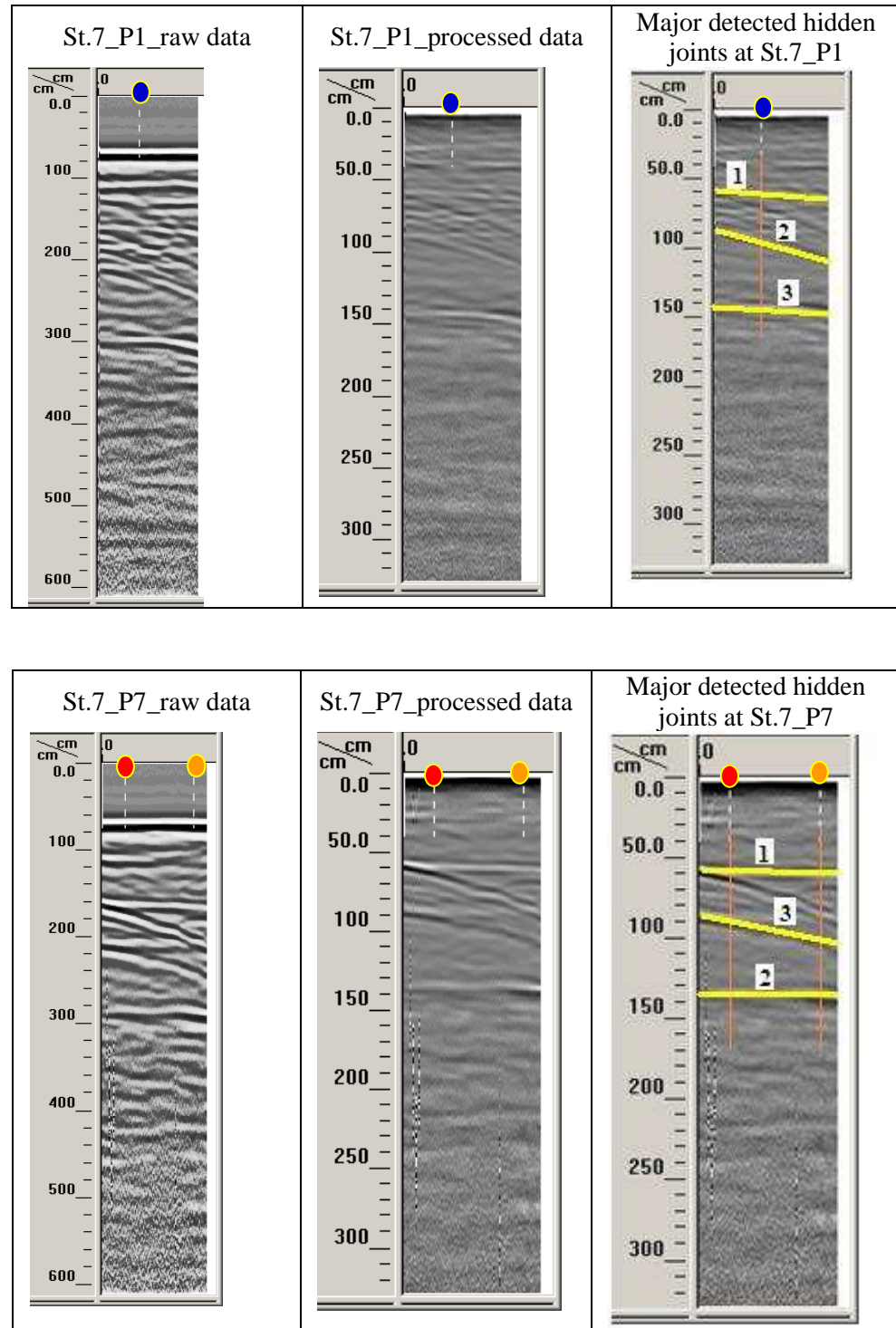


Figure 39: The apparent perpendicular depths (z) to the detected hidden subvertical joints in St.7 after GPR data processing for the two index lines. Note that the vertical scale equals to the horizontal scale.

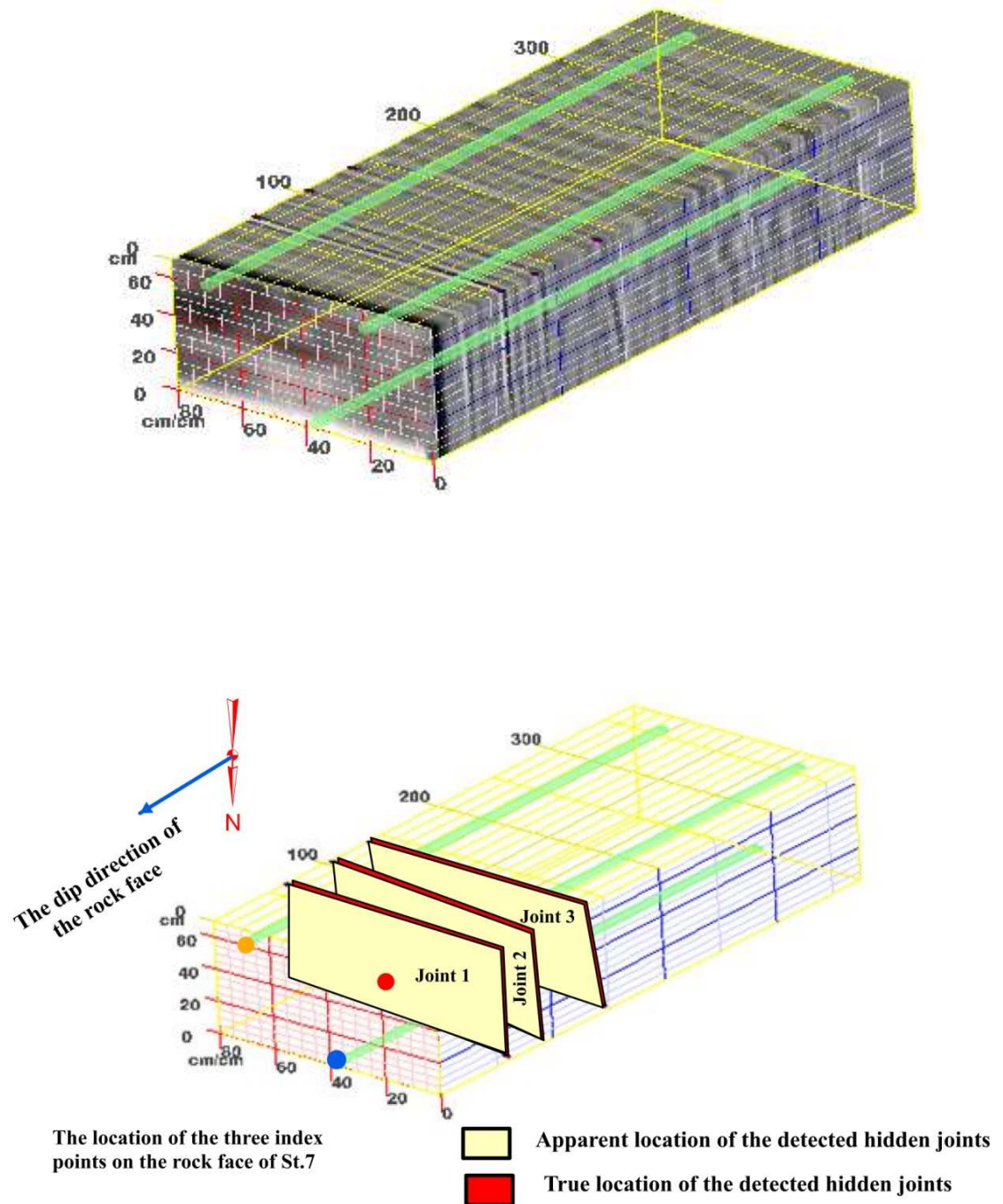


Figure 40: The created 3D image of St.7 using RADAN software (above image) and the 3D-image for the detected hidden subvertical joints with apparent and true strike directions (blow image).

Table 25: The apparent and true perpendicular depths from the rock slope face to the detected hidden subvertical joints at St.7.







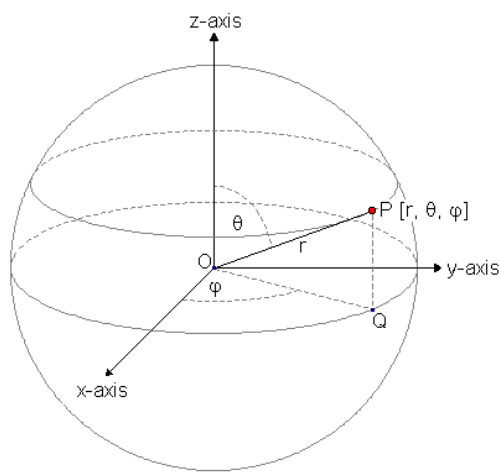
Joint No.	Apparent perpendicular depths (z) from the 3-points on the rock slope face of St.7, in cm.			Apparent (α) and true (β) declination angle of the strike		True perpendicular depths (d) from the 3-points on the rock slope face of St.7, in cm		
	Point 1 	Point 2 	Point 3 	α	β	Point 1 	Point 2 	Point 3 
1	61	60	62	3°	3.1°	61	60	62
2	96	90	103	9°	9.1°	97	91	104
3	144	137	137	2°	2.1°	144	137	137




Table 26: The coordinate values and geometry of the reference object for LIDAR measurements calibration at the rock slope face of St.7.

3-points coordinates of the reference object				Dip direction (D.D.) and dip angle (θ) measurements			
				Field		LIDAR	
Point	X	Y	Z	D.D.	θ	D.D.	θ
1	-0.23755	8.78542	0.45773	243°	89°	243°	89°
2	-0.1159	8.64696	0.36193				
3	-0.18003	8.71774	0.26389				



$\theta = 89^\circ$
 $\phi = 42^\circ$
 The correction of the dip direction rotation = 345° clockwise.

Table 27: Geometrical measurements of the rock face at St.7 after the calibration for LIDAR.

The three index point coordinates at The rock slope face				Geometry of the rock slope face			
Point	X	Y	Z	Field		LIDAR	
				D.D.	θ	D.D.	θ
1 	4489.19	14244.57	-2032.90	065°	90°	065°	89°
2 	4155.09	14221.15	-1410.64				
3 	4637.18	14243.89	-1440.03				

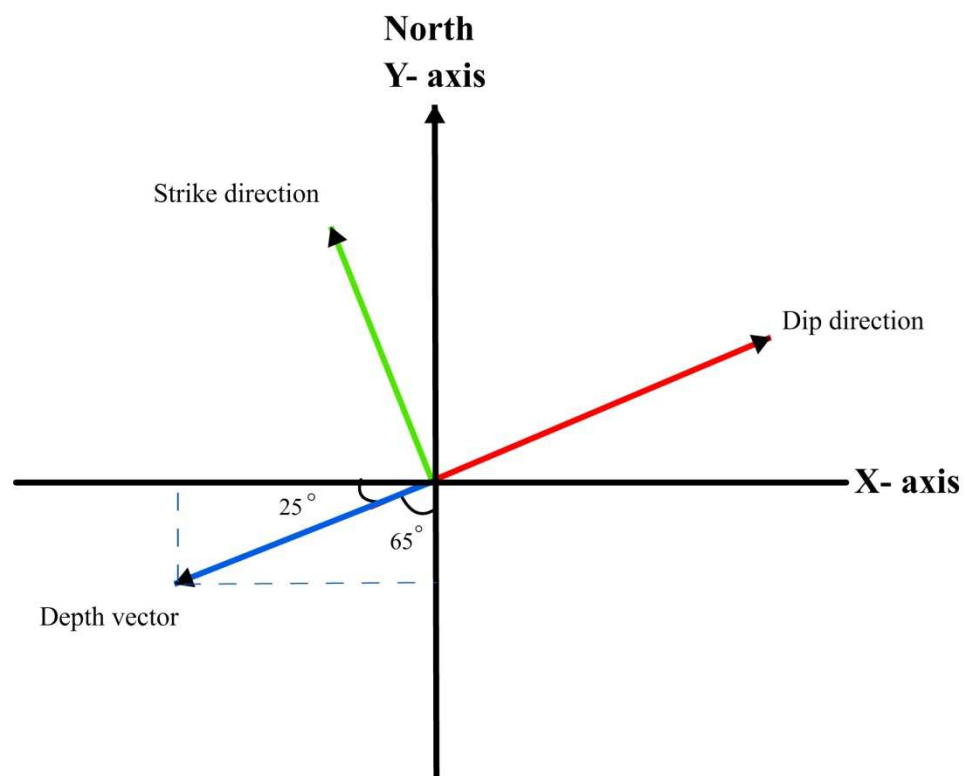


Figure 41: Resolved depth vector at St.7 to Y' and X'; $Y' = Y - d \cos 65^\circ$; and $X' = X - d \cos 25^\circ$

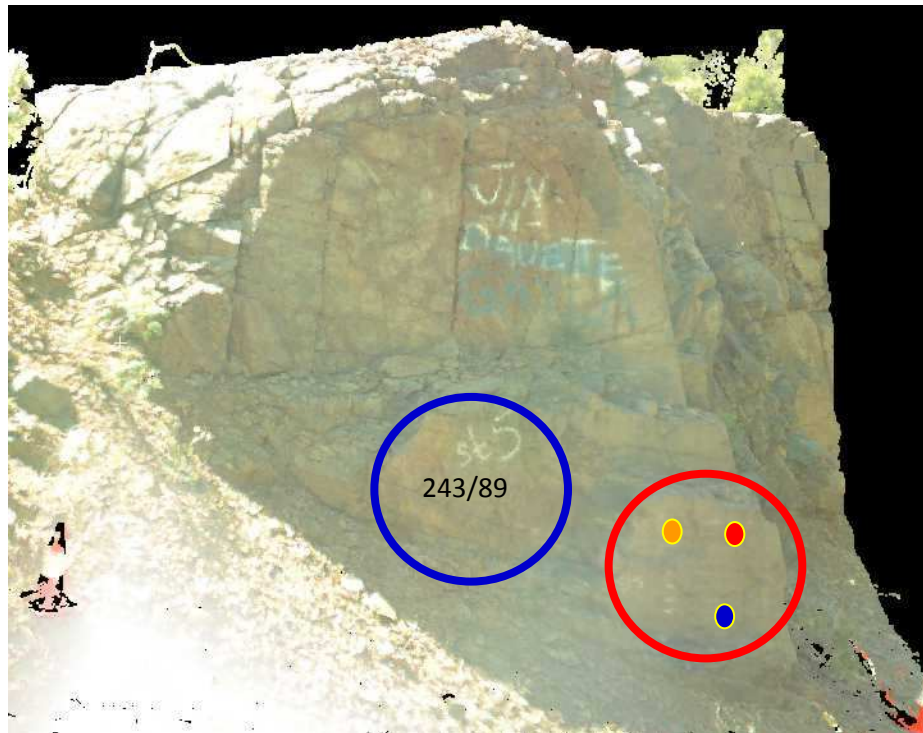


Figure 42: Point cloud image showing the location of the reference object (the blue circle) and the location of the three index points (the red circles) on the rock slope face of St.7.

Table 28: LIDAR (3D TLS) geometrical measurements for detected hidden joints in St. 7 based on the true depths using GPR and 3-point equation.

		Geometrical measurements of the detected hidden subvertical joints						
Joint No.	Point No.	The 3-corrospoding index points coordinates			LIDAR		Field verification	
		X'	Y'	Z'	D.D.	θ	D.D.	θ
1	1	4433.91	14218.79	-2032.90	065°	89°	069°	87°
	2	4100.71	14195.79	-1410.64				
	3	4580.99	14217.69	-1440.03				
2	1	4401.28	14203.58	-2032.90	066°	89°	069°	88°
	2	4072.62	14182.69	-1410.64				
	3	4542.92	14199.94	-1440.03				
3	1	4358.68	14183.71	-2032.90	065°	90°	070°	88°
	2	4030.93	14163.25	-1410.64				
	3	4513.02	14185.99	-1440.03				

REFERENCES

- Abellan, A., Calvet, J., Vilaplana, J., & Balnchard, J. (2010). Detection and spatial prediction of rockfalls by means of terrestrial laser scanner monitoring. (119), 162-171.
- Abellan, A., Calvet, J., Vilaplana, J., & Balnchard, J. (2010). Detection and spatial prediction of rockfalls by means of terrestrial laser scanner monitoring. (119), 162-171.
- Abellan, A., Vilpalana, J., & Martinez, J. (2006). Application of long range terrestrial laser scanner to detailed rockfall study at Val de Nuria, Eastern Pyrenes, Spain. *Engineering Geology* (88), 136-148.
- Abramson, L. W., Lee, T. S., Sharma, S., & Boyce, G. M. (2002). *Slope Stability and Stabilization Methods* (2nd ed.). New York, USA: John Wiley & Sons, Inc.
- Aksoy, H., & Ercanoglu, M. (2007). Fuzzified Kinematic analysis of discontinuity-controlled rock slope instabilities. (89), 206-219.
- Alba, M., & Scaioni, M. (2010). Automatic Detection of Changes and Deformations in Rock Faces by. *Commission V Symposium, UK. 38*, pp. 11-16. Newcastle upon Tyne: International Archives of Photogrammetry, Remote Sensing and Spatial Information Sciences.
- Anderson, N. (2011). Lectures and Notes on GPR. Rolla, Missouri, USA.
- Anderson, N. (2010). Lectures in: Ground Penetrating Radar Applications in Engineering and Environmental Studies. *GE 401* . Rolla, Missouri, USA: Missouri University of Science and Technology.
- Annan, A. P. (2009). Electromagnetic Principles of Ground Penetrating Radar. In H. Jol (Ed.), *Ground Penetrating Radar: Theory and Applications* (pp. 3-40). Solvenia: Elsevier B. V.
- Annan, A. P. (2001). Ground Penetrating Radar Workshop Notes. Mississauga, Ontario, Canada: Sensors & Software, Inc.
- Asahina, D., & Taylor, M. (2011). Geometry of irregular particles: Direct surface measurements by 3-D laser scanner. *Powder Tecnology* (213), 70-78.
- Baillifard, E., Jaboyedoff, M., & Sartori, M. (2003). Rockfall hazard mapping along a mountainous road in Switzerland using a GIS-based parameter rating approach. *Natural Hazards and Earth System Sciences* (3), 431-438.

- Balanis, C. A. (1989). *Advanced Engineering Electromagnetics*. New York, USA: John Wiley & Sons.
- Beres, J. M., & Haeni, F. P. (1991). Application of Ground-Penetrating-Radar Methods in Hydrogeologic Studies. *Ground Water*, 29 (3), 375-386.
- Bieniawski, Z. T. (1989). *Engineering Rock Mass Classification: A Complete Manual for Engineers and Geologists in Mining, Civil, and Petroleum Engineering*. New York, USA: John Wiley & Sons.
- Bloom, A. (2012). *Protecting Roads and Infrastructure from Falling Rocks*. Retrieved February 1, 2012, from US Infrastructure: <http://www.americainfra.com/article/Protecting-Roads-and-Infrastructure-from-Falling-Rocks/>
- Booth, A. D., Endres, A. L., & Murray, T. (2009). Spectral bandwidth enhancement of GPR profiling data using multiple-frequency compositing. *Applied Geophysics* (67), 88-97.
- Bornaz, L., Lingua, A., & Rinaudo, F. (2002). Terrestrial laser scanning: Increasing Automation for engineering and heritage applications. *GIM International*, 17 (3), 5-12.
- Brady, B. H., & Brown, E. T. (2006). *Rock Mechanics for Underground Mining* (3rd ed.). Dordrecht, The Netherlands: Springer.
- Bulut, F., & Tude, S. (1996). Determination of discontinuity traces on inaccessible rock slope using electronic tachaeometer: an example from the Ikizdere (Rize) Region, Turkey. *Engineering Geology* (44), 229-233.
- Capineri, L., Daniels, D. J., Falorni, P., Lopera, O. L., & Windsor, C. G. (2008). Estimation of Relative Permittivity of Shallow Soils by Using the Ground Penetrating Radar Response from Different Buried Targets. *Progress In Electromagnetic Research Letters*, 2, 63-71.
- Cardimona, S. (2002). Subsurface Investigation using Ground Penetrating Radar. *2nd Annual Conference on the Application of Geophysical and NDT Methodologies to Transportation Facilities and Infrastructure* (pp. 63-71). California: FHWA-WCR-02-001.
- Cassidy, N. J. (2009a). Electrical and Magnetic Properties of Rocks, Soils and Fluids. In H. Jol (Ed.), *Ground Penetrating Radar: Theory and Applications* (pp. 41-72). Solvenia: Elsevier B. V.
- Cassidy, N. J. (2009b). Ground Penetrating Radar Data Processing, Modeling and Analysis. In H. Jol (Ed.), *Ground Penetrating Radar: Theory and Applications* (pp. 141-176). Solvenia: Elsevier B. V.
- Chernyshev, S. N., & Dearman, W. R. (1991). *Rock Fractures*. (G. B. Mirovsky, Trans.) London, UK: Butterworth-Heinemann Ltd.

- Chiang, S.-H., & Chang, K.-T. (2009). Application of radar data to modeling rainfall-induced landslides, Taiwan. *Geomorphology* (103), 299-309.
- Chow, K. L. (2007). Engineering Survey Applications of Terrestrial laser Scanner in Highways Department of the Government of Hong Kong Special Administration Region (HKSAR). *FIG Working Week 13-17 May 2007*. Hong Kong SAR: Survey Division, Highways Department - Hong Kong.
- Coe, J. A. (1995). Close-range photogrammetric geological mapping and structural analysis. (*Unpublished Master Thesis*) . USA: Colorado School of Mines.
- Conyers, L. B. (2004). *Ground-Penetrating Radar for Archaeology*. California, USA: ALTAMIRA Press –A division of Rowman & Littlefield Publishers.
- Daniels, D. J. (2004). *Ground Penetrating Radar* (2nd ed.). London, UK: Institution of Electrical Engineers.
- Dérobot, X., & Abraham, O. (2000). GPR and seismic imaging in a gypsum quarry. *Applied Geophysics* (45), 157-169.
- Dezelic, V. (2004). Applications of Ground Penetrating Radar (GPR) in Mapping Mine Roof. (*Unpublished Master Thesis*) . Missouri, USA: Missouri University of Science and Technology.
- DNR-MO. (2008). The Geologic Column of Missouri- Summer 2008. *Department of Natural Resources - MO* , 3 (1) . Missouri, USA.
- Donovan, J., Kemeny, J., & Handy, J. (2005). The Application of Three-Dimensional Imaging to Rock Discontinuity Characterization. *Alaska Rocks 2005: The 40th U.S. Symposium on Rock Mechanics*. Anchorage-Alaska.
- Dot.CA, C. D. (2011). Terrestrial Laser Scanning Specifications: In Survey Manual. California, USA.
- Duan, X., Xiaoling, L., Maerz, N., & Otto, J. (2011). Automatic 3D Facet Orientation from Lidar Imaging. *Proceedings of 2011 NSF Engineering Research and Innovation Conference*. Atlanta-Georgia.
- Dunning, S. A., Massey, C. I., & Rosser, N. J. (2009). Structural and geomorphological features of landslides in the Bhutan Himalaya derived from Terrestrial Laser Scanning. *Geomorphology* (103), 17-29.
- Eberhardt, E. (2003). Rock Slope Stability Analysis – Utilization of Advanced Numerical Techniques. *Lecture Notes* . Vancouver, Canada: Earth and Ocean Sciences at University of British Columbia.
- English, C., Zhu, S., Smith, C., Ruel, S., & Christie, L. (2005). TriDAR: A Hybrid Sensor for Exploiting the Complementary Nature of Triangulation and LIDAR Technologies. *Proceeding of the 8th International Symposium on Artificial*

Intelligence - Robotics and Automation in Space (iSAIRAS) 5-7 Sep. 2005.
Munich - Germany: ESA SP-603.

- Fasching, A., Gaich, A., & Schubert, W. (2001). Data acquisition in Engineering Geology: An improvement of Acquisition Methods for Geotechnical Rock Mass Parameters. *Felsbau*, 19 (5), 93-101.
- Fell, R., MacGregor, P., Stapledon, D., & Bell, G. (2005). *Geotechnical Engineering of Dams*. London, UK: Taylor & Francis Group plc.
- Feng, Q. H., & Roshoff, K. (2004). In-situ Mapping and Documentation of Rock Faces Using a Full-Coverage 3D Laser Scanning Technique. *International Journal of Rock Mechanics and Mining Sciences*, 41 (3), Paper 1A 23.
- Franklin, J. A., & Dusseault, M. B. (1989). *Rock Engineering*. USA: McGraw-Hill Publishing Company.
- Franklin, J. A., & Senior, S. A. (1987). Rockfall Hazards-Strategies for Detection, Assessment, and Remediation. *Proceedings International Symposium on Engineering Geology and The Environment*, (pp. 657-663). Athens-Greece.
- Frohlich, C., & Mettenleiter, M. (2004). Terrestrial Laser Scanning: New Perspective in 3D Surveying. In M. Thies, B. Koch, H. Spiecker, & H. Weinacker (Ed.), *Laser-Scanners for Forest and Landscape Assessment 03-06 October 2004. XXXVI-8/W2*, pp. 7-13. Freiburg-Germany: International Archives of Photogrammetry, Remote Sensing and Spatial Information Sciences.
- Gaich, A., Potsch, M., & Schubert, W. (2006). Basics, principles and application of 3D imaging systems with conventional and high-resolution cameras. In F. Tonon, & J. Kottenstette (Ed.), *Laser and Photogrammetric Methods for Rock Face Characterization, June 17-18, 2006*. Golden-Colorado: The 41st U.S. Symposium on Rock Mechanics (USRMS) - Landmarks and Future Challenges.
- García-Sellés, D., Falivene, O., Arbués, P., Gratacos, O., Tavani, S., & Muñoz, J. A. (2011). Supervised identification and reconstruction of near-planar geological surfaces from terrestrial laser scanning. *Computers & Geosciences* (37), 1584-1594.
- Gigli, G., & Casagli, N. (2011). Semi-automatic extraction of rock mass structural data from high resolution LIDAR point clouds. *International Journal of Rock Mechanics & Mining Sciences* (48), 187-198.
- Gischig, V., Amann, F., Moore, J., Loew, S., Eisenbeiss, H., & Stempfhuber, W. (2011). Composite rock slope kinematics at the current Randa instability, Switzerland, based on remote sensing and numerical modeling. *Engineering Geology* (118), 37-53.

- González-Jorge, H., Riverio, B., Armesto, J., & Arias, P. (2011). Standard artifact of the geometric verification of terrestrial laser scanning systems. *Optics & Laser Technology* (43), 1249-1256.
- Goodman, D., Piro, S., Nishimura, Y., Schneider, K., Hongo, H., Higashi, N., et al. (2009). GPR Archaeometry. In H. Jol (Ed.), *Ground Penetrating Radar: Theory and Applications* (pp. 479-506). Solvenia: Elsevier B. V.
- Goodman, R. E. (1989). *Introduction to Rock Mechanics* (2nd ed.). Toronto, Canada: John Wiley & Sons.
- Grandjean, G., & Gourry, J. C. (1996). GPR data processing for 3D mapping in a marble quarry (Thassos, Greece). *Applied Geophysics* , 36 (1), 19-30.
- Green, A., Maurer, H., Spillmann, T., Björn, H., & Willenberg, H. (2006). High-resolution geophysical techniques for improving hazard assessments of unstable rock slopes. *Society of Exploration Geophysicists-The Leading Edge* , 25 (3), 311-316.
- Grégoire, C. (2001). Fracture Characterization by Ground-Penetrating Radar. (*Unpublished Ph.D. Dissertation*) . Leuven, Belgium: Katholieke University of Leuven.
- Gritzner, M. L., Marcus, W. A., Aspinall, R., & Custer, S. G. (2000). Assessing landslide potential using GIS, soil wetness modeling and topographic attributes, Payette River, Idaho. *Geomorphology* (37), 149-165.
- Gurocak, Z., Alemdag, S., & Zaman, M. (2008). Rock slope stability and excavatability assessment of rocks at the Kapıkaya dam site, Turkey. *Engineering Geology* (96), 17-27.
- Hack, R., Price, D., & Rengers, N. (2003). A new approach to rock slope stability- a probability classification (SSPC). *Bulletin of Engineering Geology and the Environment* , 62 (2), 167-184.
- Haneberg, W. C. (2008). Using close range terrestrial digital photogrammetry for 3-D rock slope modeling and discontinuities mapping in the United States. *Bulletin of Engineering Geology and the Environment* , 67 (4), 457-469.
- Heincke, B., Günther, T., Dalsegg, E., Rønning, J. S., Ganerød, G. V., & Elvebakk, H. (2010). Combined three-dimensional electric and seismic tomography study on the Aknes rockslide in western Norway. *Applied Geophysics* (70), 292-306.
- Hoek, E. (2006). *Prctical Rock Engineering*. Retrieved November 2011, from RocScience: http://www.rocscience.com/hoek/corner/Practical_Rock_Engineering.pdf.
- Hoek, E., & Bray, J. (1981). *Rock Slope Engineering* (3rd ed.). The Institution of Mining and Metallurgy (IMM).

- <http://ahmct.ucdavis.edu/pdf/UCD-ARR-08-06-30-06.pdf>
- <http://eparc.missouri.edu/Data/RCIP/BUSECC/RE-Mo-map.htm>
- <http://ims.missouri.edu/moims2008/step1AOI.aspx?status=NEW>
- http://ookaboo.com/o/pictures/picture/14675384/Location_Lauria__ItalyLandslide_type_Sli
- <http://www.bgs.ac.uk/eqr/SlopeStability.htm>
- <http://www.geographica.hr>
- <http://www.google.com/earth/index.html>
- <http://www.landslideblog.org/2008/09/catastrophic-rockfalls-in-middle-east.html>
- <http://www.rockfalldefence.com>
- <http://www.usgwarchives.org/maps/missouri/images/madison.gif>
- <http://www.usgwarchives.org/maps/missouri/images/phelps.gif>
- http://www.vias.org/comp_geometry/math_coord_sphere.htm
- Hudson, J. A. (1989). *Rock Mechanics Principles*. London, UK: Butterworth-Heinemann.
- Hudson, J. A., & Harrison, J. P. (2007). *Engineering Rock Mechanics: An Introduction to the Principles*. Oxford, UK: Pergamon-Elsevier.
- ISRM. (2004). International Society for Rock Mechanics Commission on Application of Geophysics to Rock Engineering (Suggested Methods for Land Geophysics in Rock Engineering). *International Journal of Rock Mechanics & Mining Sciences* (41), 885-914.
- Jeannin, M., Garambois, S., Grégoire, C., & Jongmans, D. (2006). Multi-configuration GPR measurements for geometric fracture characterization in limestone cliffs (Alps). *Geophysics*, 71 (3), B85-B92.
- Jenyon, M. K., & Fitch, A. A. (1985). *Seismic Reflection Interpretation*. Stuttgart-Berlin, Germany: Gebrüder Borntraeger (Geopublication Associates).
- Kemeny, J., Norton, B., & Turner, K. (2006). Rock slope stability analysis utilizing ground-based LIDAR and digital image processing. *Felsbau*, 24 (3), 8-15.
- Kiliche, C. A. (1999). *Rock Slope Stability*. Littleton, Colorado, USA: Society for Mining, Metallurgy, and Exploration, Inc.
- Kleyn, A. H. (1983). *Seismic Reflection Interpretation*. England: Springer - Elsevier Applied Science Publishers LTD.

- Koch, M., & Kaehler, M. (2009). Combining 3D Laser-Scanning and Close-Range Photogrammetry – An Approach to Exploit the Strength of Both Methods. *Computer Applications to Archaeology - March 22-26, 2009*. Williamsburg-Virginia.
- Koppenjan, S. (2009). Ground Penetrating Systems and Design. In H. M. Jol (Ed.), *Ground Penetrating Radar: Theory and Applications* (pp. 73-98). Solvenia: Elsevier B. V.
- Kovin, O. N. (2010). Ground Penetrating Radar Investigations in Upper Kama Potash Mines. (*Unpublished Ph.D. Dissertation*) . Rolla, Missouri, USA: Missouri University of Science and Technology.
- Kovin, O. N., & Anderson, N. L. (2010). Use of 3-D Ground Penetrating Radar for Fracture Imaging. (*Notes on GPR*) . Rolla, Missouri, USA: Missouri University of Science and Technology.
- Kovin, O. N., & Anderson, N. L. (2006). Use of Ground Penetrating Radar for Fracture Imaging. *Geophysics* , 78 (3 (10)), 91-103.
- Kovin, O., & Anderson, N. (2005). Use of Ground Penetrating Radar for Fracture Imaging. *Applied Geophysics Conference July 2005*, (pp. 566-573).
- Lan, H. X., Zhou, C. H., Wang, L. J., Zhang, H. Y., & Li, R. H. (2004). Labdslide hazard spatial analysis and prediction using GIS in the Xiaojiang watershed, Yunnan, China. *Engineering Geology* (76), 109-128.
- Lana, M. S., & Gripp, M. F. (2003). The use of inclined hemisphere projection for analyzing failure mechanisms in discontinuous rocks. *Engineering Geology* (67), 321-330.
- Lang, S. J. (1996). Lab and Field Investigations using Ground Penetrating Radar (GPR) for Mining and Geotechnical Applications. (*Unpublished Master Thesis*) . Rolla, Missouri, USA: Missouri University of Science and Technology.
- Leucci, G., Persico, P., & Soldovieri, F. (2007). Detection of fractures from GPR data: the case history of the Cathedral of Otranto. *Geophysics and Engineering* , 4, 452-461.
- Lines, L. R., & Newrick, R. T. (2004). *Geophysical Monograph Series (No.13): Fundamentals of Geophysical Interpretation*. Oklahoma, USA: Society of Exploration Geophysicists (SEG).
- Maerz, N. H. (2000). Highway Rock Cut Stability Assessment in Rock Masses Not Conducive to Stability Calculations. *Proceedings of the 51st Annual Highway Geology Symposium, Seattle, WA, Aug. 29 - Sep. 1, 2000*, (pp. 249-259). Seattle.
- Maerz, N. H., & Kim, W. (2000). Potential Use of Ground Penetrating Radar in Highway Rock Cut Stability. *Geophysics Applications*. St. Louis.

- Maerz, N. H., Youssef, A., & Fennessey, T. W. (2005). New risk-consequence rock fall hazards rating for Missouri Highways using digital image analysis. *Environmental and Engineering Geoscience*, 11 (3), 229-250.
- Maerz, N. H., Youssef, A., Otoo, J. N., Kassebaum, T. J., & Duan, Y. (2012). A Simple Method for Measuring Discontinuity Orientations from Terrestrial LIDAR Images. (*Unpublished Document*) . Rolla, Missouri, USA.
- Marescot, L., Monnet, R., & Chapellier, D. (2008). Resistivity and induced polarization surveys for slope instability studies in the Swiss Alps. *Engineering Geology*, 98 (1-2), 18-28.
- Mauldon, M., & Mauldon, J. G. (1997). Fracture sampling on a cylinder: from scanlines to boreholes and tunnels. *Rock Mechanics and Rock Engineering*, 30 (3), 129-144.
- Mellett, J. S. (1995). Ground penetrating radar applications in engineering, environmental management, and geology. *Applied Geophysics*, 33 (1-3), 157-166.
- Morey, R. M. (1974). Continuous subsurface profiling by impulse radar. In N. H. Henniker (Ed.), *Proceedings of the ASCE engineering foundation conference on subsurface exploration for underground excavations and heavy construction*, (pp. 212-232). New York.
- Naghadehi, M., Jimenez, R., Khalokakaie, R., & Jalali, S.-M. (2011). A Probabilistic system methodology to analyze the importance of factors affecting the stability of rock slopes. *Engineering Geology* (118), 82-92.
- Nasrallah, J., Monte, J., & Kemeny, J. (2004). Rock Mass Characterization for Slope/catch Bench Design Using 3D Laser and Digital Imaging. *Gulf Rocks - ARMA - The 6th North American Rock Mechanics Symposium (NARMS), June 5-10, 2004*. Houston - TX: American Rock Mechanics Association (ARMA).
- Otoo, J. N., Maerz, N. H., Duan, Y., & Xiaoling, L. (2011a). 3-D Discontinuity orientations using combined optical imaging and LiDAR techniques. *The 45th U.S. Rock Mechanics & Geomechanics Symposium, June 26-29, 2011*. San Francisco - CA.
- Otoo, J. N., Maerz, N. H., Duan, Y., & Xiaoling, L. (2011b). LiDAR and optical imaging for 3-D fracture orientations. *Proceedings of 2011 NSF Engineering Research and Innovation Conference*. Atlanta - GA.
- Otoo, J. N., Maerz, N. H., Duan, Y., & Xiaoling, L. (2012). Verification of a 3-D LiDAR point cloud viewer for measuring discontinuity orientations. *The 46th U.S. Rock Mechanics & Geomechanics Symposium*. San Francisco - CA.
- Otto, J. C., & Sass, O. (2006). Comparing geophysical methods for talus slope investigations in the Turtmann valley (Swiss Alps). *Geomorphology* (76), 257-277.

- Pernito, M. (2008). Rock Mass Slope Stability Analysis Based on 3D Terrestrial Laser Scanner and Ground Penetrating Radar. (*Unpublished Master Thesis*) . Enschede, The Netherlands: International Institute for Geo-Information Science and Earth Observation (ITC).
- Petley, D. (2008, Sep. 8). *Catastrophic rockfalls in the Middle East* . Retrieved Sep. 2011, from The Landslide Blog: <http://daveslandslideblog.blogspot.com/2008/09/catastrophic-rockfalls-in-middle-east.html>
- Piteau, D. R. (1979d). *Approach and techniques in geological structural analysis*. Part C, Rock Slope Engineering Reference Manual: FHWA Report – FHWATS- 79-208.
- Piteau, D. R. (1979c). *Description of detail line engineering geology mapping method*. Part G, Rock Slope Engineering Reference Manual: FHWA Report – FHWATS- 79-208, 29 pp.
- Piteau, D. R. (1979a). *Engineering geology considerations and basic approach to rock slope stability analysis for highways*. Part A., Rock Slope Engineering Reference Manual: FHWA Report – FHWATS- 79-208, 78 pp.
- Piteau, D. R. (1979b). *Methods of obtaining geological, structural, strength and related engineering geology data*. Part B., Rock Slope Engineering Reference Manual: FHWA Report – FHWATS- 79-208, 147 pp.
- Piteau, D. R. (1979f). *Rock slope stabilization, protection and warning- instrumentation measures and related construction considerations*. Part E, Rock Slope Engineering Reference Manual: FHWA Report – FHWATS- 79-208.
- Piteau, D. R. (1979e). *Slope stability analysis methods*. Part D, Rock Slope Engineering Reference Manual: FHWA Report – FHWATS- 79-208, 78 pp.
- Porsani, J. L., Sauck, W. A., & Ju´nior, A. O. (2006). GPR for mapping fractures and as a guide for the extraction of ornamental granite from a quarry: A case study from southern Brazil. *Applied Geophysics* (58), 177-187.
- Post, R., Kemeny, J., & Murphy, R. (2001). Image Processing for automatic extraction of rock joint orientation data from digital image. *Proceedings of the 38th U.S. Rock Mechanics Symposium*. Washington - DC: American Rock Mechanics Association (ARMA).
- Pratt, W. P., Middendorf, M. A., Satterfield, I. R., & Gerdemann, P. E. (1992). Geological Map of Rolla 1° × 2° Quadrangle, Missouri. USA: The U.S. Geological Survey - The Missouri Geological Survey.
- Priest, S. D. (1993). *Discontinuity Analysis for Rock Engineering* (1st ed.). London, UK: Champan & Hall.
- Rahman, Z., Slob, S., & Hack, R. (2006). Deriving roughness characteristics of rock mass discontinuities from terrestrial laser scan data. *Proceedings on Engineering*

Geology for tomorrow's cities, the 10th IAEG Congress, Nottingham, UK, 6-10 September 2006 (pp. 1-12). Nottingham, UK: The Geological Society of London.

- Rengers, N. (1967). Terrestrial photogrammetry: a valuable tool for engineering geological purposes. *Rock Mechanics and Engineering Geology* , 5 (2-3), 150-154.
- Reynolds, J. M. (1997). *An Introduction to Applied and Environmental Geophysics*. England: John Wiley & Sons.
- Roberts, G., & Propat, G. (2000). Highwall joint mapping in 3D at the Moura mine using SIROJOINT. In J. W. Beeston (Ed.), *Bowen Basin Symposium 2000 Coal and Mining Proceedings*, (pp. 371-377). Rockhampton- Australia.
- Santamarina, J. C., Klein, K., & Fam, A. (2001). *Soils and Waves: Particulate Materials Behavior, Characterization and Process Monitoring*. Sussex, England, UK: John Wiley & Sons.
- Santini, M., Grimaldi, S., Nardi, F., Petroselli, A., & Rulli, M. C. (2009). Pre-processing algorithms and landslide modeling on remotely sensed DEMs. *Geomorphology* , 113 (1-2), 110-125.
- Sass, O. (2007). Bedrock detection and talus thickness assessment in the European Alps using geophysical methods. *Applied Geophysics* , 62 (3), 254-269.
- Scheidegger, A. E. (1978). The Enigma of Jointing. *Rivista Italiana Di Geofisica* , 1-4.
- Sheriff, R. E., & Geldart, L. P. (1995). *Exploration Seismology* (2nd ed.). Cambridge, UK: Cambridge University Press.
- Sitar, N., & MacLaughlin, M. (1997). Kinematic and Discontinuous Deformation Analysis of Landslide Movement. *II Panamerican Symposium on Landslides, Nov. 10-14th, 1997*. Rio De Janeiro.
- Slob, S., & Hack, R. (2004). 3D Terrestrial Laser Scanning as a New Field Measurement and Monitoring Technique. (*Lecture Notes in Earth Sciences- volume 104*) . Heidelberg- German: Springer-Verlag.
- Slob, S., Hack, H. R., Feng, Q., Roshoff, K., & Turner, A. K. (2006). Fracture mapping using 3D laser scanning techniques.
- Slob, S., Hack, R., & Turner, K. (2002). An Approach to Automate Discontinuity Measurements of Rock Faces Using Laser Scanning Techniques. *ISRM International Symposium on Rock Engineering for Mountainous Regions-Eurock, November 25-28th, 2002*. Funchal- Porugal.
- Slob, S., Hack, R., Van Knapen, B., & Kemeny, J. (2004). Automated Identification and characterization of discontinuity sets in outcropping rock masses using 3D terrestrial laser scan survey techniques. *Proceedings of the ISRM regional*

symposium EUROCK, and the 53rd Geomechanics colloquy: Rock engineering and practice, October 7-9,2004, (pp. 439-443).

- Slob, S., Hack, R., Van Knapen, B., Turner, K., & Kemeny, J. (2005). A method for automated discontinuity analysis of rock slopes with 3D laser scanning. *Proceedings of the 84 th Transportation Research Board (TRB) annual meeting, Jnuary 9 – 13, 2005* (pp. 187-194). Washington - DC: Transportation Research Record No. 1913.
- Socco, L., Jongmans, D., Boiero, D., Stocco, S., Maraschini, M., Tokeshi, K., et al. (2010). Geophysical investigation of the Sandalp rock avalanche deposits. *Applied Geophysics* , 70, 227-291.
- Spren, A. C., & Proctor, P. D. (1993). *Guidebook to the Geology of the Waynesville, Rolla, and St. James Areas, Missouri*. Rolla: Missouri University of Science and Technology.
- Stevens, K. M., Lodha, G. S., Holloway, A. L., & Soonawala, N. M. (1995). The application of ground penetrating radar for mapping fractures in plutonic rocks within the Whiteshell Research Area, Pinawa, Manitoba, Canada. *Applied Geophysics* , 33 (1-3), 125-141.
- Sturzenegger, M., & Stead, D. (2009). Close-range terrestrial digital photogrammetry and terrestrial laser scanning for discontinuity characterization on rock cuts. *Engineering Geology* , 106 (3-4), 163-182.
- Sturzenegger, M., Stead, D., & Elmo, D. (2011). Terrestrial remote sensing-based estimation of mean trace length, trace intensity and block size/shape. *Engineering Geology* , 119 (3-4), 96-111.
- Sturzenegger, M., Yan, M., Stead, D., & Elmo, D. (2007). Application and limitations of ground-based laser scanning in rock slope characterization. In E. Eberhardt, D. Stead, & T. Morrison (Ed.), *Proceedings 1st of Canada-USA Rock Mechanics Symposium*, (pp. 29-36). Vancouver - Canada.
- Sucre, E. B., Tuttle, J. W., & Fox, T. R. (2011). The Use of Ground-Penetrating Radar to Accurately Estimate Soil Depth in Rocky Forest Soils. *Forest Science* , 57 (1), 59-66.
- Takahashi, T. (2004). ISRM Suggested Methods for land geophysics in Rock Engineering. *International Journal of Rock Mechanics & Mining Sciences* , 41, 885-914.
- Terzaghi, R. D. (1965). Sources of errors in joint surveys. *Geotechnique* , 15, 287-304.
- Theune, U., Rokosh, D., Sacchi, M. D., & Schmitt, D. R. (2006). Mapping fractures with GPR: A case study from Turtle Mountain. *Geophysics* , 71 (5), B139-B150.

- Thompson, T. L. (1991). *Report of Investigation No. 70: Paleozoic Succession in Missouri – Part 2: Ordovician System*. Rolla: Division of Geology and Land Survey at Missouri.
- Topal, T. (2007). Discussion of “A new approach for application of rock mass classification on rock slope stability assessment” by Liu and Chen, *Engineering Geology*, 89: 129 – 143 (2007). *Engineering Geology*, 95, 99-100.
- Torres, C. A. (2008). Geometric Characterization of Rock Mass Discontinuities Using Terrestrial Laser Scanner and Ground Penetrating Radar. (*Unpublished Master Thesis*). Enschede, The Netherlands: ITC.
- Toshioka, T., Tsuchida, T., & Sasahara, K. (2003). Application of GPR to detecting and mapping cracks in rock slopes. *Applied Geophysics*, 33 (1-3), 119-124.
- Turner, A., Kemeny, J., Slob, S., & Hack, R. (2006). Evaluation, and management of unstable rock slopes by 3-D laser scanning. *JAEG*, Paper No. 404.
- wang, X., & Mauldon, M. (2006). Proportional errors of the Terzaghi correction factor. *Golden Rocks: The 41th U.S. Symposium on Rock Mechanics (USRMS), June 17-21, 2006*. Golden-Colorado: USRMS.
- Weirich, F., & Blesius, L. (2007). Comparison of satellite and air photo based landslide susceptibility maps. *Geomorphology*, 87 (4), 352-364.
- Whitworth, M. Z., Giles, D., Anderson, I., & Clewett, M. (2006). Terrestrial laser scanning for applied geosciences studies in the urban environment. *JAEG* (Paper No. 252), 1-9.
- Wyllie, D., & Mah, C. W. (2004). *Rock Slope Engineering: Civil and Mining* (4th ed.). London & New York: Spon Press: Taylor & Francis Group.
- Yarovoy, A. (2009). Landmine and Unexploded Ordnance Detection and Classification with Ground Penetrating Radar. In H. Jol (Ed.), *Ground Penetrating Radar: Theory and Applications* (1st ed., pp. 445-478). Slovenia: Elsevier B. V.

VITA

Adnan Aqeel was born in Ibb, Yemen. Mr. Aqeel attended the Department of Earth and Environmental Sciences at Sana'a University in September 1993 and graduated with a first rank and honor in June 1997. He worked as a teaching assistant for many different courses until 2002. In the meanwhile he was involved in some funded projects related to soil types and water resources mapping.

In September, Mr. Aqeel got a full paid scholarship from King Abdulaziz University in Saudi Arabia perusing his Master of Science degree in Engineering Geology Field. He graduated in 2007 with an excellent grade .In the meantime; he was involved in some funded projects related to rock engineering.

In April 2008, Mr. Aqeel got a full paid scholarship by European Union to study a prestigious program (GEM Program) which is held in cooperation with four of the most prestigious universities in Europe: Southampton University, Lund University, Warsaw University, and ITC. Mr. Aqeel completed some short concentrated courses in GIS, Remote Sensing, and Environmental Regulations and then had to discontinue his program to attend his Ph.D. program in the USA.

During Ph.D. study, Mr. Aqeel worked as a graduate teaching assistant in Missouri University of Science and Technology. Mr. Aqeel has been always involved in a service of community either back in home or in Rolla in the USA where he worked as a committee member for the Muslim Community. Mr. Aqeel has been a member for Society of Exploration Geophysicists (SEG), and the Association of Environmental and Engineering Geologists (AEG).